Suction recirculation mitigation in a double-suction centrifugal pump

J.P. van der Walt
orcid.org/0000-0002-0356-9097

Dissertation accepted in fulfilment of the requirements for the degree Master of Engineering in Mechanical Engineering at the North-West University

Supervisor: Dr. J.-H. Kruger
Co-supervisor: Prof. C.G. du Toit

Graduation: May 2021
Student number: 21142467

Copyright

This dissertation contains information obtained from authentic and highly regarded sources. Reasonable efforts have been made to publish reliable data and information, but the author and publisher cannot assume responsibility for the validity of all materials or the consequences of their use. The authors and publishers have attempted to trace the copyright holders of all material reproduced in this publication and apologize to copyright holders if permission to publish in this form has not been obtained.

ANSYS, ANSYS Workbench, AUTODYN, CFX, FLUENT and any and all ANSYS, Inc. brand, product, service and feature names, logos and slogans are registered trademarks or trademarks of ANSYS, Inc. or its subsidiaries in the United States or other countries. [ICEM CFD is a trademark used by ANSYS, Inc. under license.] All other brand, product, service and feature names or trademarks are the property of their respective owners.

Abstract

Suction recirculation in centrifugal pumps operating at off-design conditions is an eventual reality for all centrifugal pumps. Various types of modifications to both the pump impeller and/or volute have been implemented in the past, with variable success. The successful implementation of the modifications is often counteracted by either an increase of Net Positive Suction Head Required ($NPSHR$), a narrowing of the band of recirculation-free operation and/or the need for intrusive casing modifications. This study aims to determine if a suitable suction recirculation mitigation method, that restricts the suction recirculation phenomenon while not exhibiting a noticeable increase in $NPSHR$, is possible by means of the implementation of a profiled bulkhead-ring. Suction recirculation can be described as the separation of the flow field and the presence of a separation cell in the suction half of the impeller between-vane cavity with a back-flow of fluid from impeller to suction volute.

Two scenarios were investigated: the unmodified pump, and the modified pump geometry including the modified bulkhead-ring - simulated across the entire operating range. The flow characteristics of both cases were investigated after adequately verifying the numerical simulations and validating these results with analytical and certified experimental methods. The results of the study indicated that the modified bulkhead ring concept was partially effective by successfully restricting the bulk back-flow of fluid from impeller to suction volute, however the separation point and recirculation cells remained largely unaffected. In this particular instance, both the measured and simulated $NPSHR$ showed a noticeable increase after the implementation of the modification. Although the results of this particular study do suggest that the installation of the particular rotating modification used in the current setup is not generally more practical when compared to more conventional methods, further development is needed in order to determine a more optimal ring geometry that would produce more favourable results.

Keywords: Suction Recirculation; Double Suction; Centrifugal Pumps, Off-Design, Cavitation, Computational Fluid Dynamics

Dedication

To my wife, mother and father.

Declaration

I, **Johannes Petrus van der Walt** hereby declare that

1. I understand what plagiarism is and am aware of the University's policy in this regard.
2. I know that "plagiarism" means using another person's work and ideas without acknowledgement, and pretending that it is one's own. I know that plagiarism not only includes verbatim copying, but also the extensive (albeit paraphrased) use of another person's ideas without acknowledgement. I know that plagiarism covers this sort of use of material found in textbooks, journal articles, theses AND on the internet.
3. "SUCTION RECIRCULATION MITIGATION IN A DOUBLE-SUCTION CENTRIFUGAL PUMP" submitted in the fulfilment in the requirement for the Master's degree in Mechanical Engineering (M-Eng) is my own original work.
4. Where other people's work has been used (either from a printed source, Internet or any other source), this has been properly acknowledged and referenced in accordance with departmental requirements.
5. I have not used work previously produced by another student or any other person to hand in as my own.
6. I have not allowed, and will not allow, anyone to copy my work with the intention of passing it off as his or her own work.



STUDENT

14/02/2021

DATE

Acknowledgements

I would like to express my gratitude to my supervisors Dr. J.-H. (Jan-Hendrik) Kruger and Prof. C.G. (Jat) du Toit, without your knowledge, insights, accessibility, patience and your willingness to walk the extra mile for me, this dissertation would not have come to be.

I am forever indebted to Albie Schoombee, my direct line manager, for supporting me and always having an open door. Without your tolerance, patience, lenience, encouragement and motivation, I would not have had the freedom to perform and complete this research. Thank you for providing me with this opportunity to grow, while also making the required tools and time available. You are a spectacular manager and colleague, thank you.

I want to thank Drikus Steenkamp, Callie La Grange and Gert Booyzen (including his team of skilled artisans) for their continued support and providing the equipment, manpower, time and capital that made the experiments a reality. Without your support and trust, this project was doomed to fail. I really valued all your practical insights, technical know-how and the urgency while completing the work successfully, first time.

To my parents, Sonja and Johan van der Walt Snr., I cannot express my gratitude in words. The sacrifices you had made in order to provide me with the opportunities to excel is beyond comprehension. Thank you for always being there, for supporting me in tough times and for your love and encouragement. I am forever thankful.

Lastly, to my wife and pillar, Marelie van der Walt. Thank you for your unwavering love, support and encouragement. You have stood by me through all of my endeavours, mostly casting your own priorities aside. I will never be able to repay you for your selfless love and sacrifice. Thank you for being my team mate.

Contents

Copyright ii

Abstract iii

Dedication iv

Declaration v

Acknowledgements vi

List of figures ix

List of tables xii

Nomenclature xv

1. Introduction 1
- 1.1. Background . . . 1
- 1.2. Rationale . . . 2
- 1.3. Research problem, research purpose and objectives . . . 3
  - 1.3.1. Research Problem . . . 3
  - 1.3.2. Research Purpose . . . 3
  - 1.3.3. Research Objectives . . . 3
- 1.4. Summary of contents . . . 3

2. Literature study 5
- 2.1. Suction recirculation in centrifugal pumps . . . 5
- 2.2. Damaging effects of suction recirculation . . . 7
- 2.3. Prediction of recirculation inception . . . 8
- 2.4. Mitigation of suction recirculation in centrifugal pumps . . . 9
  - 2.4.1. Diffuser upstream of impeller inlet . . . 9
  - 2.4.2. Recirculation break upstream of the impeller inlet . . . 9
  - 2.4.3. Stationary orifice (bull-ring) upstream of the impeller inlet . . . 10
  - 2.4.4. Rotating bulkhead-ring inside the impeller eye . . . 10
  - 2.4.5. Curved inlet disk installation into the suction eye of the impeller . . . 10
  - 2.4.6. Application of a modified bull-ring (Sabini ring) . . . 10
- 2.5. Chapter summary . . . 11

I. Methodology 12

3. Method 13
- 3.1. Design of the method of research . . . 13
- 3.2. Research design . . . 13
  - 3.2.1. Subject of investigation - double suction centrifugal pump . . . 14
  - 3.2.2. Simulation . . . 15

3.2.3. Experiments . . . 16
3.3. Data acquisition . . . 16
3.4. Chapter summary . . . 17

4. Solver theory and description **18**
4.1. Numerical solver . . . 18
4.1.1. Transport equations . . . 18
4.1.2. Solver numeric function . . . 19
4.1.3. Turbulence modeling . . . 21
4.1.4. Solver cavitation modelling . . . 23
4.2. Chapter summary . . . 23

5. Verification methodology **25**
5.1. Code verification . . . 25
5.2. Quantification of the discretization error . . . 25
5.3. Chapter summary . . . 26

6. Validation methodology **27**
6.1. Experiments/Testing . . . 27
6.2. Additional comment on the method of determining pump shaft power and overall efficiency at coupling . . . 30
6.3. Additional method of determining simulation tendency . . . 31
6.4. Chapter summary . . . 31

II. Baseline evaluation of pump **32**

7. Baseline evaluation **33**
7.1. Model assembly . . . 33
7.2. Mesh . . . 34
7.3. Model setup . . . 38
7.3.1. ANSYS® CFX® CEL expression language . . . 39
7.4. Chapter summary . . . 40

8. Verification of baseline case **41**
8.1. Chapter summary . . . 45

9. Validation of the baseline geometry **46**
9.1. Pump performance test for the baseline case . . . 46
9.2. Comment on vibration measurement . . . 48
9.3. Mean-line method for qualitative trend observation . . . 48
9.4. Chapter summary . . . 51

III. Evaluation of modified pump **52**

10. Modification **53**
10.1. Perforated bulkhead ring design methodology . . . 53
10.2. Estimate of point of recirculation onset . . . 54
10.3. Exploration of potential geometric layouts . . . 54
10.3.1. Design considerations . . . 54
10.3.2. Assessment of the range of possible ring geometric features . . . 55
10.3.3. Ring internal diameter design . . . 56

10.3.4. Calculation of required ring inlet drill angle . . . 58
10.4. Implementation of modification . . . 60
10.5. Chapter summary . . . 60

11. Setup of the modified pump **61**
11.1. New model assembly . . . 61
11.2. Mesh . . . 62
11.3. Chapter summary . . . 63

12. Verification of the modified pump case **64**
12.1. Chapter summary . . . 68

13. Validation of the modified geometry case **69**
13.1. Chapter conclusion and summary . . . 71

IV. Analysis of results **73**

14. Analysis of simulation data **74**
14.1. Overall performance assessment . . . 74
14.2. Evaluation of 3D CFD data . . . 78
14.2.1. Geometry . . . 78
14.2.2. Case 1 - Effect of the perforated ring at BEP conditions. . . . 79
14.2.3. Case 2 - Effect of the perforated ring at ring design conditions. . . . 79
14.2.4. Cavitation behaviour at operating conditions . . . 82
14.3. Chapter summary . . . 83

15. Conclusion and recommendations **92**
15.1. Conclusion . . . 92
15.1.1. Evaluation of hypothesis . . . 92
15.1.2. Evaluation of implementation in industrial applications . . . 93
15.2. Recommendations for further study . . . 93

Annexures **103**
A. Reduced Order Model for a rotating internal annular seal leakage path . . . 103
A.1. Introduction . . . 103
A.2. Theoretical model . . . 104
A.2.1. Method requirements . . . 104
A.2.2. Model, as proposed by Gülich . . . 104
A.3. Reduced Order Model (ROM) . . . 106
A.3.1. Variable dependency . . . 106
A.3.2. Data generation . . . 107
A.3.3. Regression . . . 107
A.3.4. Final form of ROM . . . 108
A.4. Verification . . . 108
A.4.1. Calculated data set . . . 108
A.4.2. Flownex-Gülich verification . . . 109
A.4.3. Gülich-ROM verification . . . 110
A.5. Implementation in ANSYS® CFX® . . . 111
A.6. Conclusion . . . 112
B. ANSYS® CFX® CEL implementation . . . 113
B.1. Annular seal Reduced Order Model . . . 113

B.2. Boundary conditions . . . 114
B.3. Torque . . . 114
B.4. Custom monitor points . . . 115
C. Assessment of test pump geometry . . . 116
C.1. Measurement standard . . . 116
C.2. Measurement equipment and analysis software . . . 117
C.3. Impeller . . . 117
C.3.1. Measurement setup . . . 117
C.3.2. Visual evaluation of measurement results of the impeller used during testing 117
C.3.3. Visual evaluation of measurement results of similar impeller after destructive machining . . . 119
C.3.4. Evaluation to set standard . . . 121
C.3.5. Practical evaluation of impeller measurement and geometry . . . 123
C.4. Casing . . . 125
C.5. Chapter summary . . . 127
C.5.1. Matters regarding the impeller geometry . . . 127
C.5.2. Matters regarding the casing geometry . . . 127
D. Methods regarding the design of the back-flow restricting ring . . . 128
D.1. Prediction of flow rate at point of suction- and discharge recirculation inception . . . 128
D.1.1. Discharge recirculation . . . 128
D.1.2. Suction recirculation . . . 128
D.2. Determining the required suction eye diameter . . . 129
D.2.1. Methodology for determining the inlet throat diameter for an inlet bull ring 129
D.2.2. A design methodology for a new impeller design - prior to blade development 130
D.3. Determination of geometrical design limits of ring geometry . . . 131
D.3.1. Design constraints . . . 131
D.3.2. Mathematical formulation . . . 131
D.4. Perforation drill angle design . . . 133
E. Grid Convergence Index formulation . . . 137
F. Additional discussion relating to the analytic calculation of the impeller mean-line 139
F.1. Analytic solution methodology . . . 139
F.1.1. Calculation methodology and principles . . . 139
F.1.2. Slip factor . . . 141
G. Slip factor formulations . . . 144
G.1. Stodola's slip model . . . 144
G.2. Wiesner's slip model . . . 144
G.3. Stanitz slip model . . . 144
G.4. von Backström/SRE slip model . . . 145
G.5. Aungier slip model . . . 145
G.6. Gülich slip model . . . 145
G.7. Paeng-Chung-Visser slip model . . . 146
G.8. Qiu-Japikse slip model . . . 147
H. Example monitor and residual plots . . . 148
I. Best Efficiency Point CFD Data . . . 151

List of Figures

0-1. Important geometry definitions of centrifugal impellers . . . xvi

1-1. An example of a typical API-610 (2011) BB2 centrifugal process pump . . . 1

2-1. Depiction of suction recirculation, (Budris, 1993) . . . 5
2-2. Illustration of expected events at off-design operation, (Karassik and McGuire, 1997) . . . 5
2-3. Illustration of flow deceleration at the impeller suction, (Gülich, 2014) . . . 5
2-4. Inlet velocity triangles, (Sayers, 1990) . . . 5
2-5. Recirculation Break, courtesy of Sloteman et al. (1984) . . . 9
2-6. Standard inlet modifications, courtesy of Hergt et al. (1996) and Gülich (2014) . 9
2-7. Curved inlet disk arrangement (Hermez et al., 2017) . . . 10
2-8. Sabini ring, as per Bradshaw (2012) . . . 10

3-1. Research methodology . . . 13
3-2. Cross sectional drawing of subject pump, with part descriptions. . . . 14
3-3. Drawings depicting the subject pump's impeller and volute layout. . . . 14

4-1. Illustration of the ANSYS® CFX® Release 2019 R2 discretization methodology. 20
4-2. Law of the wall and range of applicable turbulence models, adapted from Pletcher et al. (2016) . . . 22

5-1. Research methodology . . . 25

6-1. Depiction of test station layout. The red arrows indicate the flow direction. . . . 28
6-2. Schematic layout of test station. . . . 29

7-1. Isometric view of the flow field with location of boundary conditions indicated. . 33
7-2. Cross section of the flow field in the $z - x$ plane . . . 34
7-3. Suction volute mesh - fine grid representation. . . . 34
7-4. Discharge volute mesh - fine grid representation. . . . 35
7-5. Impeller fine grid representation. . . . 36
7-6. Surface contour plots of the $y+$ parameter at $Q = 639.361m^3/h$. Vector plots of the node locations are shown to illustrate the boundary layer resolution at the indicated locations. . . . 37
7-7. Isometric view of the flow field with location of boundary conditions indicated. . 38
7-8. Location of annular seal leakage path. Blue arrows indicate discharge to suction leakage represented by an opening boundary condition. Black arrows indicate the inlet of the discharge to suction leakage flow, represented by an inlet boundary condition with a specified mass flow equal to the ROM of the leakage flow. . . . 39

8-1. Total pressure in stationary frame as measured on mid-plane of flow field. . . . 43
8-2. Velocity in stationary frame as measured on mid-plane of flow field. . . . 44

9-1. Test 1; Performance test with original geometry, tolerance ranges as per ISO 9906 49

9-2. Analytic calculation points at various flow rates and slip models at fine grid conditions . . . 50

10-1. Ring modification physical implementation. . . . 53
10-2. Modification design methodology . . . 53
10-3. Comparison of various ring geometric attributes versus a varying β_{1r} and d_r . . . 56
10-4. Calculation of the expected $NPSHR_{3\%}$ at various flow rates and values of d_R . . . 57
10-5. Calculation of the expected $NPSHR_{3\%}$ at various flow rates and values of d_R . . . 58
10-6. Ring modification physical implementation. . . . 60

11-1. Isometric view of the flow field with location of boundary conditions indicated. . 61
11-2. Cross section of the modified flow field in the $z - x$ plane. The green part is the back-flow restricting device. . . . 62
11-3. Ring modification fine grid representation. . . . 62

12-1. Total pressure in stationary frame as measured on mid-plane of flow field. . . . 66
12-2. Velocity in stationary frame as measured on mid-plane of flow field. . . . 67

13-1. Test 2; Performance curve after modification, acceptable tolerance as per ISO 9906 72

14-1. Comparison of CFD results (0° impeller rotation) . . . 77
14-2. Depiction of the location where the CFD data was evaluated. The results reported in this chapter is consistent with the locations shown in this figure. . . . 78
14-3. Comparison of BEP (initial) conditions for Case 2 . . . 79
14-4. Comparison of various parameters on Planes A and B . . . 80
14-5. Comparison of c_{1m} between different Cases and eye configurations . . . 85
14-6. Comparison of μ_t between different Cases and eye configurations . . . 86
14-7. Comparison of impeller inlet flow angle between different Cases and eye configurations . . . 86
14-8. Comparison of area-averaged, circumferential meridional data . . . 87
14-9. Comparison of 2D plane unmodified and modified impeller inlet geometry. . . . 88
14-10 Comparison of flow characteristics of the unmodified and modified impeller inlet geometry. . . . 89
14-11 Comparison of vortex core iso-surface regions between the unmodified and modified impeller inlet geometry. Vortex core regions identified by means of the Q-Criterion method and the generated iso-surfaces are colored by Eddy Viscosity . 90
14-12 Comparison of the conservative liquid vapour fraction free surface interface between different Cases and eye configurations . . . 91

A-1. Geometry of single stage annular seal . . . 104
A-2. Calculated Q_{sp} across a range of data as per section A.2 . . . 109
A-3. Model created in Flownex . . . 109

C-1. The setup at time of 3D scanning. . . . 117
C-2. Illustration of the linear and angular measurements taken on the 3D scanned point cloud of the impeller which was used in the pump test. The point cloud measurements are compared to the model geometry. . . . 118
C-3. Partial scan of shrouded (tested) impeller outlet geometry. . . . 119
C-4. Illustration of the linear and angular measurements taken on the 3D scanned point cloud of a similar impeller which was destroyed for measurement purposes. The point cloud measurements are compared to the model geometry. . . . 119
C-5. Accuracy of in site geometry vs ideal design . . . 120
C-6. Depictions of the volute casing and some critical components. . . . 125

C-7. Representative images showing important casing variables. 126

D-1. Nomenclature useful in the ring design algorithm. 131

F-1. Impeller meanline calculation algorithm 140
F-2. Calculation of slip factor in the range of evaluation with regards to the current geometry of the unmodified impeller. 143

I-1. Comparison of BEP (initial) conditions for Case 1 151
I-2. Comparison of p_{Ts} between different Cases and eye configurations 152
I-3. Comparison of μ_t between different Cases and eye configurations 153
I-4. Comparison of impeller inlet flow angle between different Cases and eye configurations 153
I-5. Comparison of area-averaged, circumferential meridional data 154
I-6. Comparison of 2D plane unmodified and modified impeller inlet geometry. 155

List of Tables

3-1. Information relating to the subject pump . . . 14
3-2. Geometric features of the model pump as used in the study . . . 15

4-1. (ANSYS®, 2019*d*) recommended settings for the Raleigh-Plesset cavitation model. 24

6-1. Test 1 evaluation of the water standard . . . 27
6-2. Permissible values of overall uncertainties as per EN-ISO-9906 (2012) . . . 29
6-3. EN-ISO-9906 (2012) tolerance limits for Grade 1 performance testing . . . 30

7-1. Breakdown of the different elements that the meshes consist of for the current case 35
7-2. Indication of mesh quality for the unchanged geometry, fine mesh . . . 36
7-3. Indication of impeller mesh quality for the unchanged geometry, fine mesh . . . 37

8-1. Grid convergence study of the modified mesh at $\dot{m} = 58.985kg/s$ . . . 41
8-2. Grid convergence study of the modified mesh at $\dot{m} = 127.215kg/s$ . . . 42
8-3. Grid convergence study of the modified mesh at $\dot{m} = 177.245kg/s$ . . . 42

9-1. Test 1 systematic (instrumental) uncertainty evaluation . . . 46
9-2. Results of baseline experiment. . . . 47
9-3. Results of baseline $NPSHR_{3\%}$ experiment . . . 48
9-4. Mean-line calculation as per the rigorous method of par. F.1 for the unmodified geometry . . . 50

10-1. Impeller eye ID vs. Q_{La} at recirculation onset (estimate) . . . 54
10-2. Calculated ring throat inside diameter study . . . 57
10-3. Summary of incidence angles of the various points of interest . . . 59
10-4. Selection of ring geometric features based on the results of the design algorithm . 60

11-1. Breakdown of the different elements that the meshes consist of for the current case 63

12-1. Grid convergence study of the modified mesh at $\dot{m} = 58.985kg/s$ . . . 64
12-2. Grid convergence study of the modified mesh at $\dot{m} = 127.215kg/s$ . . . 65
12-3. Grid convergence study of the modified mesh at $\dot{m} = 177.245kg/s$ . . . 65

13-1. Test 2 systematic (instrumental) uncertainty evaluation . . . 69
13-2. Results of the modified pump's experiment. . . . 70
13-3. Results of the modified pump's $NPSHR_{3\%}$ experiment . . . 71

14-1. Comparison of CFD results for H_{tot}, η and P between the modified and unmodified pump geometries . . . 74
14-2. Comparison of CFD results for H_{tot}, η and P between the modified and unmodified pump geometries . . . 75
14-3. Comparison of CFD results for H_{thL} for ϕ_{2c} between the modified and unmodified pump geometries . . . 76

A-1. Variable dependency . . . 106

A-2. Table of data with fixed geometry and ε . . . 107
A-3. Polynomial regression at every ΔH to find Q_{sp} as a function of T . . . 107
A-4. Polynomial regression of data in table A-3 to find polynomial coefficients as a function of ΔH . . . 108
A-5. Input independent variables to the test case . . . 108
A-6. Variable dependency . . . 110
A-7. Analysis of values; $\frac{\text{Gülich}}{\text{Flownex}}$ . . . 110
A-8. Variable dependency . . . 111
A-9. Analysis of values; $\frac{\text{Gülich}}{\text{ROM}}$ . . . 111

C-1. Adaptation of EN-ISO-8062-3 (2007) Table 2 - Linear Dimensional Casting Tolerances . . . 116
C-2. Adaptation of EN-ISO-8062-3 (2007) Table 4 and 5 - Casting Tolerances . . . 116
C-3. Evaluation of unmachined (cast) geometric impeller features vs. the ideal impeller geometry, as per EN-ISO-8062-3 (2007) by means of laser scanning. . . . 122
C-4. Evaluation of the similar, machined (cast) geometric impeller features vs. the ideal impeller geometry, as per EN-ISO-8062-3 (2007) by means of laser scanning. 123
C-5. Detailed assessment of geometric features of the impeller casting . . . 124
C-6. Assessment of geometric features of the impeller casting - averaged approximation 124
C-7. Evaluation of the cast geometric casing features vs. the ideal geometry, as per EN-ISO-8062-3 (2007) by means of physical measurement. . . . 126
C-8. Assessment of geometric features of casing . . . 126

D-1. Detailed assessment of the inlet eye diameter - new impeller design . . . 130
D-2. Calculated velocity triangles for shockless entry per impeller eye (unmodified) . . . 134
D-3. Calculated perforation velocity triangles for shockless entry (modified) . . . 135
D-4. Calculated perforation outlet velocity triangle angles, and inlet velocity triangles to impeller (modified) . . . 135
D-5. Calculated velocity triangle data for unaffected portion of impeller blades (modified) 136

F-1. Comparison of different slip models . . . 142

Nomenclature

Abbreviations

ANSI	American National Standards Institute	
API	American Petroleum Institute	
ASME	The American Society of Mechanical Engineers	
BEP	Best Efficiency Point	
CEL	CFX® Expression Language	
CEN	Comité Européen de Normalisation / European Committee for Standardization	
CFD	Computational Fluid Dynamics	
DCTG	Dimensional Casting Tolerance Grade	
EN	Europäische Norm / European Standard	
GCTG	Geometrical Casting Tolerance Grade	
GGI	General Grid Interface	
HI	Hydraulic Institute	
ISO	International Organization for Standardization	
NASA	National Aeronautics and Space Administration	
NPSHA	Net Positive Suction Head Available	$[m]$
NPSHR	Net Positive Suction Head Required	$[m]$
OD	Outside Diameter	
OEM	Original Equipment Manufacturer	
OHSAS	Occupational Health and Safety Assessment Series	
PCD	Pitch Circle Diameter	
ROM	Reduced Order Model	
SANAS	South African National Accreditation System	
TIR	Total Indicator Reading	

Physics Constants

π	Circumference/diameter of circle	3.14159...
g	Gravitational acceleration	$9.81\,m/s^2$

Variables

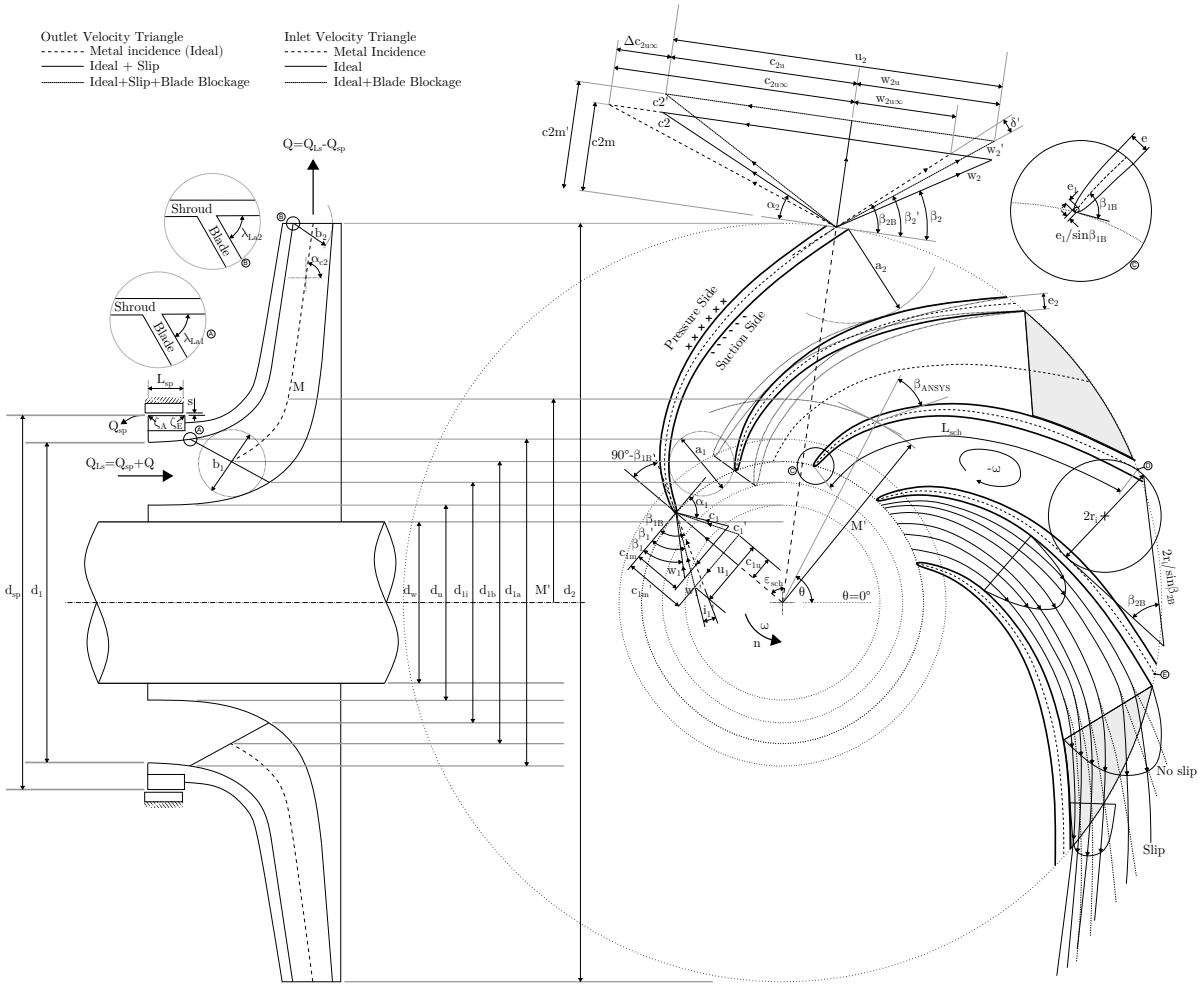


Figure 0-1. Important geometry definitions of centrifugal impellers

α	Individual phase in multi-phase flow	$[-]$
α_{1r}	Inlet swirl flow angle, ring	$[°]$
α_1	Angle between direction of circumferential and absolute velocity	$[°]$
α_{c2}	Angle between the streamline slope and the axial direction at outlet	$[°]$
$\bar{x}$	Arithmetic average of measurements/points taken	
β_{1rB}	Inlet drill angle, ring	$[°]$
β_{1r}	Inlet flow angle, shockless flow, ring	$[°]$
β_{2B}	Outlet blade (metal) angle	$[°]$
β_2	Outlet flow angle	$[°]$
$\boldsymbol{U}_\alpha$	Velocity vector of phase α	$[m/s]$
Δc_{2u}	Slip velocity	$[m/s]$
ΔH	Static head difference across annular seal	$[m]$
ΔH_{stat}	Static differential head produced by pump	$[m]$
ΔH_{tot}	Total differential head produced by pump	$[m]$

δ	Deviation- or slip angle	$[^\circ]$
δ_b	boundary layer thickness	$[m]$
$\dot{m}$	Mass flow rate measured at pump suction/discharge	$[kg/s]$
$\dot{m}_{fg}$	Total inter-phase mass transfer rate per unit volume	$[kg/m^3 \cdot s]$
η	Pump efficiency	$[\%]$
η_m	Efficiency of electric motor	$[\%]$
γ	Slip factor (discharge coefficient of impeller)	$[-]$
Γ_α	Diffusivity of phase α	$[kg/ms]$
λ	Annular seal friction coefficient	$[-]$
λ_{La}	Blade lean angle at shroud	$[rad]$
λ_t	Thermal conductivity	$[W/(m \cdot K)]$
μ	Dynamic viscosity of fluid	$[N \cdot s/m^2]$
μ_t	Turbulent/Eddy viscosity	$[Pa \cdot s]$
ν	Kinematic viscosity of fluid	$[m^2/s]$
ω	Rotational velocity of the impeller	$[rad/s]$
ϕ	Placeholder in GCI calculation for measured variable per grid	$[x]$
ρ	Density of fluid	$[kg/m^3]$
ρ_α	Material density of phase α	$[kg/m^3]$
ρ_g	Density of gas in bubble	$[kg/m^3]$
σ	Standard deviation of a data set	$[-]$
σ_{st}	Surface tension coefficient between the liquid and vapor	$[-]$
ε	Equivalent sand surface roughness	$[m]$
ε_{sch}	Blade wrap angle	$[^\circ]$
φ	Arbitrary scalar value in transport equation	$[-]$
φ_1	Flow coefficient	
ζ_A	Exit pressure loss coefficient	$[-]$
ζ_{EA}	Total hydraulic pressure loss coefficients	$[-]$
ζ_E	Entrance pressure loss coefficient	$[-]$
A	Roughness compensation factor	$[-]$
A_{1q}	Passage inlet throat area	$[m^2]$
a_1	Passage inlet minimum throat circle diameter - radial	$[m]$
a_2	Passage outlet minimum circle diameter - radial	$[m]$
a_{3a}	Minimum distance between cutwater and outer volute in radial plane	$[m]$
a_{3i}	Minimum distance between cutwater and inner volute in radial plane	$[m]$

A_a	Empirical factor - Antoine's Equation	$[-]$
A_{flow}	(Total eye flow area) - (Ring flow restriction area)	$[m^2]$
$A_{h_{all}}$	Total perforation flow area	$[m^2]$
A_{in}	Remaining eye flow area without perforations	$[m^2]$
A_{or}	Eye flow area, no modification	$[m^2]$
A_{ratio}	Area ratio, A_{flow}/A_{or}	$[m^2]$
AR	Asymptotic range, as per Roache (1998*a*, 2009): $GCI^{21}_{coarse} = r^{p_o} GCI^{21}_{fine}$	$[-]$
B	Empirical factor - Antoine's Equation	$[-]$
b_1	Inlet minimum throat circle diameter - meridional	$[m]$
b_2	Passage outlet minimum circle diameter - meridional	$[m]$
b_{3a}	Outer volute channel width at a_{3a}	$[m]$
b_{3i}	Inner volute channel width at a_{3i}	$[m]$
C	Empirical factor - Antoine's Equation	$[-]$
c_{1m}	Meridional component of the absolute fluid flow velocity at the inlet	$[m/s]$
c_{1r}	Absolute velocity at ring inlet	$[m/s]$
c_{1ur}	Circumferential component of absolute velocity, ring	$[m/s]$
c_{1u}	Circumferential component of the absolute fluid flow velocity at the inlet	$[m/s]$
c_1	Absolute fluid flow velocity at the inlet	$[m/s]$
c_{2m}	Meridional component of the absolute fluid flow velocity at the outlet	$[m/s]$
$c_{2u\infty}$	Circumferential absolute blade congruent fluid flow velocity component at the outlet	$[m/s]$
c_{2u}	Circumferential component of the absolute fluid flow velocity at the outlet	$[m/s]$
c_2	Absolute fluid flow velocity at the outlet	$[m/s]$
c_{ax}	Axial velocity in annular seal	$[m/s]$
c_a	Average axial flow velocity in impeller eye	$[m/s]$
c_{sa}	Average axial flow velocity at ring perforation inlet	$[m/s]$
d_h	Perforation diameter	$[m]$
d_n	Internal diameter (shaft side) of impeller eye flow area	$[m]$
d_{rPCD}	PCD of perforations	$[m]$
d_r	Internal diameter of the insert ring	$[m]$
d_{sp}	OD of rotating inner cylinder of annular seal	$[m]$
$e(x)$	Blade thickness as a function of x in $[x, y]$ plane	$[m]$
e_η	Overall pump efficiency uncertainty if computed from pump power input	$[\%]$
e_η	Overall uncertainty of overall efficiency	$[\%]$
e_a	Approximate relative error	$[\pm\%]$

e_c	The calculation uncertainty of the analytic solution	$[\pm\%]$
e_{ext}	Extrapolated relative error	$[\pm\%]$
e_H	Overall total pump head uncertainty	$[\%]$
e_n	Overall speed of rotation uncertainty	$[\%]$
e_{Pgr}	Overall driver power input uncertainty	$[\%]$
e_P	Overall pump power input uncertainty	$[\%]$
e_Q	Overall flow rate uncertainty	$[\%]$
e_R	Random uncertainty	$[\%]$
e_S	Instrumental uncertainty	$[\%]$
e_T	Overall torque uncertainty	$[\%]$
F_{cond}	Empirical factor - condensation	$[-]$
f_q	Number of impeller suction eyes	$[-]$
F_s	Safety factor for GCI study	$[-]$
F_{vap}	Empirical factor - vaporisation	$[-]$
GCI_{coarse}	Grid Convergence Index for the coarse grid solution	$[\pm\%]$
GCI_{fine}	Grid Convergence Index for the fine grid solution	$[\pm\%]$
H	The Head per stage - measured in test	$[m]$
h	Representative grid size	$[-]$
H_{thL}	Total head produced by impeller - with calculated losses	$[m]$
H_{th}	Theoretical total head produced by impeller - no losses	$[m]$
h_{tot}	Total enthalpy	$[J/kg]$
i'_{1r}	Inlet flow incidence angle, ring	$[^\circ]$
i'_1	Inlet flow incidence angle - unaffected by ring outlet, impeller	$[^\circ]$
i''_1	Inlet flow incidence angle - affected by ring outlet, impeller	$[^\circ]$
k_n	Blockage caused by hub	
L_{sch}	Blade 3D arc length	$[m]$
L_{sp}	Annular seal axial length	$[m]$
m_B	Mass of gas bubble	$[kg]$
N	Number of elements in a specific grid	$[-]$
n	Rotational velocity of the impeller	$[RPM]$
n_q	Specific speed	$[RPM, m^3/s, m]$
N_B	Volume of bubbles per unit volume	$[1/m^3]$
n_h	Number of perforations	$[-]$
n_m	Number of measurements/points taken	

N_p	Total number of phases	$[-]$
n_{ss}	Suction specific speed	
n_{ss}^{**}	Normalized suction specific speed	
$O(x, y)$	The axis of impeller rotation in the Cartesian plane, located at any $[x, y]$	$[m]$
P	Pump shaft power	$[W]$
p	Absolute pressure of fluid	$[Pa_{(a)}]$
P_{mes}	Measured motor input power	$[W]$
P_{mloss}	Pump mechanical losses	$[W]$
p_o	Apparent order of convergence	$[-]$
p_{Ts}	Total (stagnation) pressure in the stationary reference frame	$[kPa]$
p_v	Vapor pressure of liquid	$[Pa_{(a)}]$
Q	Volume flow rate measured at pump suction/discharge	$[m^3/s]$
Q_{dr}	Flow rate at discharge recirculation	$[m^3/s]$
Q_{La}	Total volume flow through impeller	$[m^3/s]$
Q_{sp}	Annular seal leakage volumetric flow rate	$[m^3/s]$
Q_{sr}	Flow rate at suction recirculation	$[m^3/s]$
R	Radius from $O(x, y)$ to evaluated point on curve	$[m]$
r	Grid refinement factor	$[-]$
r_α	Volume fraction of phase α	$[-]$
R_c	Arbitrary radius of curvature	$[m]$
r_g	Volume fraction of bubbles	$[-]$
R_{nuc}	Nucleation site radius	$[m]$
r_{nuc}	Volume fraction of nucleation sites	$[-]$
R_{slip}	Radius from $O(x, y)$ to point on blade curve where slip will initiate	$[m]$
Re	Axial Reynolds number in annular seal	$[-]$
Re_u	Reynolds number for circumferential flow	$[-]$
S	Arbitrary source term transport equation	$[-]$
s	Radial annular seal clearance	$[m]$
S_E	Energy source term transport equation	$[J/kg]$
S_M	Momentum source term transport equation	$[kg \cdot m/s]$
T	Temperature of fluid	$[^\circ K]$
u_1	Circumferential velocity at the impeller inlet	$[m/s]$
u_2	Circumferential velocity at the inpeller outlet	$[m/s]$
U_η	EN-ISO-9906 (2012) efficiency tolerance	$[-\%]$

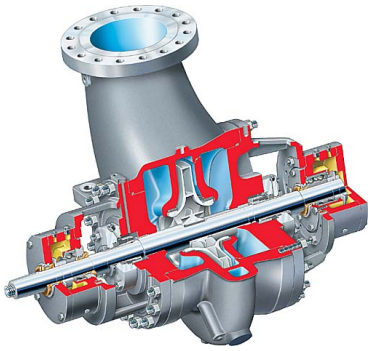
U_H	EN-ISO-9906 (2012) head tolerance	$[\pm\%]$
U_P	EN-ISO-9906 (2012) power tolerance	$[+\%]$
U_Q	EN-ISO-9906 (2012) flow rate tolerance	$[\pm\%]$
u_{rPCD}	Radial velocity at perforation PCD	$[m/s]$
u_{sp}	Wear ring tip velocity	$[m/s]$
V_α	Volume occupied by phase α	$[m^3]$
V_B	Volume of gas bubble	$[m^3]$
w_{1a}	Outer streamline relative flow velocity at the inlet	$[m/s]$
w_{1i}	Inner streamline relative velocity at the inlet	$[m/s]$
w_{1q}	Average flow velocity in the throat of the impeller	$[m/s]$
w_{1r}	Relative velocity at inlet, ring	$[m/s]$
w_{1ur}	Circumferential component of relative velocity, ring	$[m/s]$
w_{1u}	Circumferential component of the relative fluid flow velocity at the inlet	$[m/s]$
w_1	Relative fluid flow velocity at the inlet	$[m/s]$
$w_{2u\infty}$	Circumferential relative blade congruent fluid flow velocity component at the outlet	$[m/s]$
w_{2u}	Circumferential component of the relative fluid flow velocity at the outlet	$[m/s]$
w_2	Relative fluid flow velocity at the outlet	$[m/s]$
$yB_h(x)$	Blade radial y values at hub as a function of x in $[x, y]$ plane	$[m]$
$yB_m(x)$	Blade radial y values at mean line as a function of x in $[x, y]$ plane	$[m]$
$yB_s(x)$	Blade radial y values at shroud as a function of x in $[x, y]$ plane	$[m]$
z_{La}	Number of impeller blades per eye	$[-]$
$zM_h(R)$	Hub meridional z values as a function of R in $[z, R]$ plane	$[m]$
$zM_m(R)$	Mean line meridional z values as a function of R in $[z, R]$ plane	$[m]$
$zM_s(R)$	Shroud meridional z values as a function of R in $[z, R]$ plane	$[m]$

1. Introduction

1.1. Background



(a) Typical API610 BB2 single stage, double suction, between bearings, radially split, centrifugal process pump. (Image courtesy of Flowserve®Corp, https://www.flowserve.com/)



(b) Sectional view of an API610 BB2 pump. The shaft assembly, bearings, pump casing and mechanical seals are visible. (Image courtesy of Flowserve®Corp, https://www.flowserve.com/)



(c) An example of a closed double suction impeller commonly used in API610 BB2 type pumps.

Figure 1-1. An example of a typical API-610 (2011) BB2 centrifugal process pump

Centrifugal pumps are generally classified as process critical equipment in most fluid handling industries world-wide. The efficient and reliable operation of centrifugal pumps is desired in order to ensure safe, predicable, cost efficient and stable operations. In the event that process pumps experience functional failure; the pump driven process, in turn, cannot function and financial implications to the net capital gain of the institution becomes an obvious reality. An example of a typical double suction centrifugal process pump is shown in Figure 1-1.

The successful selection, procurement, installation and satisfactory operation of process pumps are dependent on the consideration and integration of a host of complex factors. These factors are critically evaluated during the basic engineering phase of capital-, green- and brownfields projects. The basic engineering study is then further scrutinized during the detail engineering phase in order to ensure optimal machine-system matching prior to the procurement of equipment.

The optimal (business orientated/financial) solution for a process critical, high risk, single point of failure machine would have significantly more stringent requirements when compared to a lower criticality, lower risk machine with built in system redundancy (i.e. is installed along with a standby machine). Unfortunately, this approach to equipment and auxiliary system selection is not always sufficient with regards to ultimate equipment performance after commissioning; especially when taking older installations (i.e. circa pre 1980) into account where absolute clarity regarding the process parameters were often not enjoyed prior to initial plant commissioning and subsequent beneficial operation date.

Due to changing process conditions, fluid composition over time, production requirements and/or deviation from the expected process/equipment design limits; a host of operational difficulties

can arise during the functional life of process pumps. Among a host of other possible process deviations a very common pumping system constraint is the low flow condition, also commonly referred to as: part-load operation conditions. Low flow conditions in a process system containing a centrifugal pump as process driver will impose potentially strenuous effects on the operation and reliability of the turbomachine in question if the machine is sensitive to the potentially negative effects of suction recirculation.

1.2. Rationale

The current installed asset base of many older industrial sites still comprise of original process pump installations that utilized design practices that date back to the late 1980's and earlier. Many pumps still currently operate with suction recirculation that can be effectively managed using proven methods as mentioned in section 2.4 (apart from costly and time consuming impeller redesign - the use of numerical methods has enabled modern impeller designs to operate satisfactorily at high suction specific speeds without generating excessive suction recirculation at the outer streamlines), however; the application of many of the accepted mitigation methods are impossible to implement due to various geometric reasons relating to the pump.

The implementation of a suction diffuser, as per section 2.4.1, at the suction of the pump has to be built into the suction nozzle of the casing to be effective; if such modifications are not incorporated in the initial design of the casing it will be extremely problematic to implement after initial pump installation. The installation of a recirculation break mechanism, as per 2.4.2, is considered to be extremely effective but this option requires a straight inlet section at the inlet of the impeller - this restricts the application to end suction designs only, with the addition of potentially costly piping and casing modifications. The installation of Sabini rings (preferred over the more common bull-ring variant) as per 2.4.6 is considered effective, but the permanent modification of the pump casing will have to be undertaken, additionally; extended plant downtime will be required in order to finish the casing modification along with potential vendor involvement due to the reduction of the casing thickness. The installation of curved discs as per 2.4.5 is promising, apart from the potential installation difficulties relating to specialized welding during installation that will escalate the cost of this modification.

The least intrusive method to modify the suction capability of centrifugal pumps is bulkhead-rings, as described in 2.4.4. Bulkhead-rings can be cheaply manufactured and easily installed and removed during pump maintenance activities. The drawback relating to this solution is the modification of the pump characteristics when operating over a range of flow rates.

A cost effective solution that allows for significant mitigation of suction recirculation intensity while ensuring minimal influence on operating characteristics, will benefit users that operate centrifugal pumps at off design conditions in the following ways:

1. Ensure continued safe operation of centrifugal pumps across a wide operating range by reducing vibration magnitude (and material erosion damage) caused cavitation due to excessive suction recirculation at the impeller eye
2. Enable extended mean time between failure/repair rates without costly system and/or equipment modification

1.3. Research problem, research purpose and objectives

1.3.1. Research Problem

Currently there is no cost effective method for the mitigation of destructive suction recirculation in centrifugal pumps that concurrently ensures minimal increase of $NPSHR$ (Net Positive Suction Head Required) across a wide operating range, without extensive system and/or equipment modifications/redesign.

1.3.2. Research Purpose

The research will be executed in order to determine the effect on centrifugal pump performance due to impeller suction eye geometry modification by means of a profiled bulkhead-ring, as well as determining the feasibility of applying the technology in an industrial environment.

1.3.3. Research Objectives

The objective of the research is to prove the following hypothesis:

A profiled bulkhead-ring aids in suppressing excessive suction recirculation, and thus aids in relieving the intensity of damaging suction recirculation cavitation.

1.4. Summary of contents

The summary of the contents of this dissertation is discussed below:

1 Introduction: The introduction describe the background, rationale research problem and the hypothesis that are relevant to this work.

2 Literature study: Various sources of literature that relates to the subject of suction recirculation have been consulted and the results of this study are presented here.

I Methodology: This part discusses the general methodology followed during the course of the research. It is applicable to all parts where the relevant topics are discussed.

3 Method: The research design and methodology is discussed and outlined with a flow chart.

4 Solver theory and description: A description of the numeric solver and its capabilities are discussed.

5 Verification methodology: The general verification methodology is discussed. The method and process is used in later verification sections.

6 Validation methodology: The general validation methodology is discussed. The method and process is used in later verification sections.

II Baseline evaluation of pump: The unmodified baseline case is considered and explained in this part.

7 Baseline evaluation: The construction of the 3D model, solver setup and constraint, mesh generation and quality assessment and other model related matters are discussed.

8 Verification of baseline case: The CFD (Computational Fluid Dynamics) results are scrutinized and a structured mesh refinement study is completed.

9 Validation of the baseline geometry: The CFD model results are validated against a rigorous analytical method and a certified pump performance test.

III Evaluation of modified pump: The unmodified baseline case is considered and explained in this part.

10 Modification: The description, design and implementation of the proposed modification is discussed and illustrated.

11 Setup of modified pump: The implementation of the modification into the original 3D setup is discussed and executed.

12 Verification of the modified pump case: The CFD results of the modified geometry are scrutinized and a structured mesh refinement study is completed.

13 Validation of the modified geometry: The CFD model results of the modified geometry are validated against a certified pump performance test.

IV Analysis of results: The CFD results are analysed in this part.

14 Analysis of data: The CFD cases are compared with each other and the results are analysed. Other data such as cavitation and recirculation in the suction eye is discussed as a result of the numerical analysis.

15 Conclusion and recommendations: The conclusions are made that frame the outcome of the study. Recommendations of further study are also made.

Annexures: Various annexures are included that contain important data that is required to understand the contents of the dissertation better.

2. Literature study

2.1. Suction recirculation in centrifugal pumps

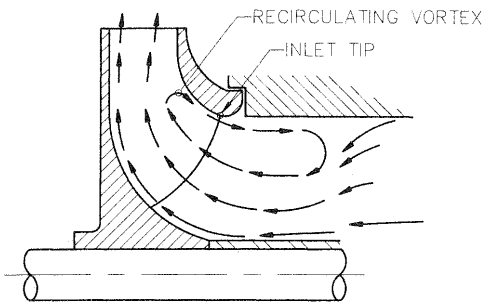


Figure 2-1. Depiction of suction recirculation, (Budris, 1993)

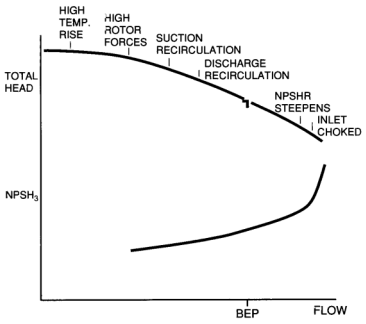


Figure 2-2. Illustration of expected events at off-design operation, (Karassik and McGuire, 1997)

Suction recirculation (Figure 2-1) in centrifugal pumps can be described as the flow reversal of the outer streamline in the impeller suction eye during operation at a reduced flow rate with regards to the BEP (see Figure 2-2).

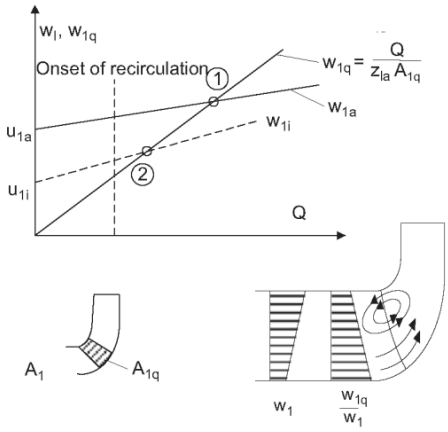


Figure 2-3. Illustration of flow deceleration at the impeller suction, (Gülich, 2014)

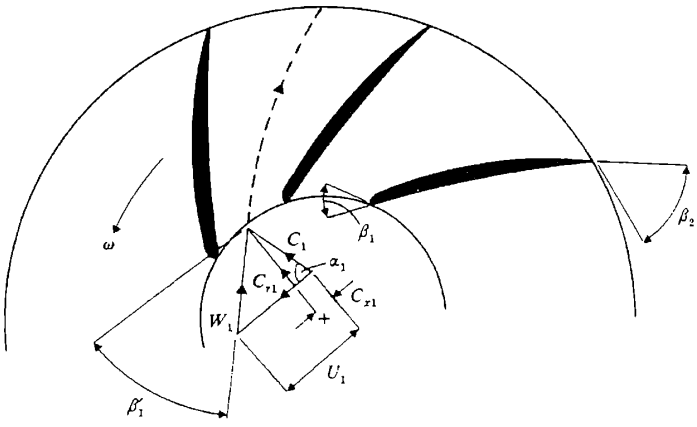


Figure 2-4. Inlet velocity triangles, (Sayers, 1990)

The phenomenon of suction recirculation is described very well by Gülich (2014) (see Figure 2-3 and Figure 2-4): The flow along a curved streamline is dependent on the centrifugal force generated by the rotation of the impeller geometry in conjunction with the centripetal force enabling the fluid particle to move along a curved streamline. At lower flow rates the relative fluid flow velocity into the eye, w_1 (with w_{1i} = inner- w_{1a} = outer streamline relative velocity) as described by Sayers (1990), tends to grow (radially) with respect to the average flow velocity

in the throat of the impeller, w_{1q}. The ratio between the average throat flow velocity and the resultant relative flow velocity at outer inlet radii, (w_{1q}/w_{1a}), will tend to decrease at lower flow rates, subsequently indicating a deceleration of the outer streamline as it passes through the throat. As the relative inlet velocity grows in relation with the average throat velocity; large pressures are developed at the outer streamlines due to streamline curvature and Coriolis forces. At some point during operation at reduced capacity; separation of the flow will take place on the pressure side of the vane, at the outer streamline. This describes a partial stall situation. The streamlines that experience separation decelerate rapidly, thus Coriolis force development is restricted and the centrifugal force dominates the flow. The stalled fluid is transported towards the outer streamline due to centrifugal force in the meridional section. The streamlines located in the upper part of the inlet leading edge is decelerated earlier and more intensely than the streamlines on the inner part of the leading edge due to the fact that the relative speed is greater at the outer radius relative to the mean velocity (and subsequently the inner radius). A back-flow of liquid is induced at the outer streamline. The blade-fluid interaction at the outer streamline also imparts a radial velocity to the incoming fluid and subsequently alters the incoming fluid velocity profile.

It is very likely that ventrifugal impellers will experience some form of recirculatory flow as the operating point of the pump changes in order to adapt to the process requirements in such a manner as to operate way from BEP (Karassik, 1987). In order for suction recirculation to initialize; flow separation at the pressure surface of the vane must occur concurrently with the development of significant pressure gradients in a direction that is normal to the streamline curvature in the vicinity of flow separation (Gülich, 2014).

The initialization and intensity of recirculation is influenced primarily by the following factors:

1. The difference between the inner and outer suction eye flow area diameter, cited by among others Karassik (1987), Fraser (1981*b*), Gülich (2014) and Hirschberger and James (2009). As the ratio between the outer and inner eye diameters increases, the relative velocities (and pressure gradients normal to streamline curvature) at the inlet between the extreme streamlines also increase. The phenomenon of suction recirculation will occur earlier and with greater intensity as the impeller eye diameter increases. The specific speed (n_q) coincidently increases as the eye diameter increases. The inlet flow velocity is critical to the performance of impellers with larger inlet eye diameters; generally a flow rate close to BEP is required to minimize the risk of suction recirculation. Additionally, at lower flow rates the blade-fluid interaction at the outer streamline imparts a tangential velocity to the fluid; this tangential velocity induces a pre-rotation in the incoming fluid that extends many diameters into the suction piping. This pre-rotation alters the incoming fluid's velocity profile and affects the pump performance (Breugelmans and Sen, 1982).

2. The geometry of the throat in the meridional section of the impeller (Gülich, 1999). The deceleration of the outer streamline increases as the meridional throat section enlarges. Thus, the tendency to recirculate is decreased with a smaller meridional flow area. The outer streamline velocity is decelerated to a lesser extent relative to the average velocity in the throat. The geometry of the shroud in the meridional section is also important; a larger curvature radius decreases the pressure gradient generated due to body forces and thus aids in suppressing tendency to recirculate.

3. The geometry of the vane layout and the number of vanes. The vane layout in the blade-to-blade view (back-swept, radial or forward-swept) will have an influence on the flow through the impeller channels with regards to the flow streamlines and the deflection thereof by secondary flow effects. Back-swept vanes are generally preferred. The number of vanes per impeller should be optimized in order to ensure proper fluid acceleration and blade

loading while ensuring relatively even flow streamlines and velocity profiles that are not prone to excessive flow separation and secondary flows at part load (Gülich, 1999).

4. Other geometric aspects of the impeller that contribute, but are mostly of secondary importance, include: the leading edge incidence angle, the radial wear ring clearance, impeller roughness and the leading edge profile (Balasubramanian et al., 2011).

It can be stated that the evaluation of the initialization point of suction recirculation is a complex problem and is completely dependent on the geometry of the impeller.

2.2. Damaging effects of suction recirculation

As described by Yedidiah (1986) and in paragraph 2.1, at flow rates less than BEP; the inlet vane tips transfer a peripheral velocity to the incoming streamlines. In conjunction with this periphery velocity; the effects of suction recirculation tends to expel fluid at the outer streamline back out of the eye of the impeller. The peripheral velocity in conjunction with the change in flow direction creates a pressure differential between the outer and inner streamlines, at a certain point the outer streamline will change direction once more and will flow back to the inlet of the impeller in a newly created flow path located closer to the hub of the impeller. This motion creates a vortex flow at the eye of the impeller, originating from reverse flow at the outer streamline, which acts on the pressure side of the suction vane. The intensity and size of the vortex depends on factors already discussed in paragraph 2.1. With increasing intensity of the vortex, the outer vortex streamlines continuously accelerate; with acceleration of the outer vortex streamlines a large pressure gradient is generated from the outer to inner vortex streamlines. The pressure inside the eye of the vortex can drop below the vapour pressure of the process fluid. When the pressure drops below the vapour pressure of the process fluid; evaporation occurs. The evaporation of process fluid manifests itself in the form of vapour bubbles inside the process fluid, as the bubbles move to a zone of higher pressure inside the pump the vapour inside the bubble abruptly condenses and the bubble collapses on itself. When the bubble collapses; the flow of liquid caused by the sudden volume change creates a focused micro jet of liquid directed at the surface of the impeller. The force of impingement of this micro jet can amount to immense magnitudes; as a result the material that is impinged will over time be eroded by this phenomenon (Brennen, 1995). Cavitation can be mitigated by raising the $NPSHA$ (Net Positive Suction Head Available) to a value sufficiently higher than the fluid vapour pressure at the point of vaporization but in order to achieve satisfactory results in this case will be very difficult as the local pressure at the core of the vortex changes with the severity of recirculation (Budris, 2010).

The potential damage ranges from mild to catastrophic, depending on the fluid and operating conditions. Damage originating from this phenomenon can be observed on the pressure side of the impeller in the form of cavitation erosion and pitting. In extreme cases the pump can experience cavitation surge events relating to this flow phenomenon according to Gülich (2001), Karassik and McGuire (1997) and Fraser (1981*b*). Other inevitable effects include shaft vibration caused by unsymmetrical erosion of impeller material causing an unbalance force in conjunction with the associated vibration caused by the cavitation itself. Mean time between maintenance and failure will become shorter and the total cost of ownership will escalate if not treated. Possible mitigation of vaporization damage include; effective material selection and/or the alteration of $NPSHA$ by means of the installation of a booster pump or system modifications (Schiavello and Visser, 2007).

2.3. Prediction of recirculation inception

The prediction of the suction recirculation inception point has been the subject of numerous studies in the past. The landmark papers by Fraser (1981*a*) and Fraser (1981*b*) sensitized the pump industry to the effects of suction recirculation which was previously only treated as an anomaly of off design performance. Fraser presented a simplified graphical method that enabled pump users and designers to estimate the point of recirculation inception – known as the critical flow rate. Fraser related a combination of the suction specific speed, specific speed and the impeller hub to eye outside diameter ratio values as a function of the BEP in order to determine the point of suction recirculation inception using a set of quick reference tables – while neglecting most of the impeller geometry. He also published a more detailed method requiring more specific knowledge of the impeller inlet and outlet diameters, inlet and outlet flow areas, throat flow areas and a built in empirical assumption relating to the average geometric proportions and the related average flow rates of "normal" impellers of the time in order to predict the onset of suction recirculation – while neglecting the rated flow rate and head generation at BEP. The methods proposed by Fraser, after extensive observation of a large number of pumps, was catered to account for standard impeller design methods used between the 1950's and 1970's, the method was proven to be accurate for machines of that era. The point of suction recirculation initialization was thus linked to the suction specific speed and thus to the impeller eye outer streamline diameter. The findings of Fraser and various industry reliability studies relating pump reliability to the suction specific speed value had a profound effect on the pump industry, various authors embraced his proposal Karassik (1987) and Lobanoff and Ross (1992); Standards Organizations such as the Hydraulic Institute and the American Petroleum Institute (API) issued the option to users to enforce set limits for new machines bought after the latest edition of their standards after 1981 API-610 (1981), API-610 (2011) and American National Standards Institute ANSI-HI-14 (1982).

Gopalakrishnan (1988) proposed a modification to the method proposed by Fraser (1981*b*). Gopalakrishnan modified the empirical assumption built into the Fraser method in order to better represent blade angles smaller than 15° as the original method predicted the onset of recirculation at lower than experienced flow values.

Budris (1993) proposed another modification to the method introduced by Fraser; Budris argued that the overly simplified approach outlined by Fraser did not sufficiently take all factors into account that affects suction recirculation inception. Budris proposed that inlet tip speed, specific gravity of the fluid, basic pump types and vane overlap be taken into account. He introduced a series of graphs that (incorporates the mentioned factors) that assists the user in determining the estimated safe operation zone with regards to suction recirculation.

Many authors – including Gülich (2014), Stoffel and Jaeger (1996) and Schiavello (1993) – motivated that the method proposed by Fraser (1981*b*) is too simplified in order to accurately predict the recirculation point of modern pump impellers from a general design perspective. Relating the suction specific speed to a recirculation point without taking critical dimensions into account might be effective for a family of similar machines (or older impellers designed more than 30 years ago) but will ultimately not yield accurate general results. Modern design techniques and computational power enable designers to develop impellers with high suction specific speeds that function without suction recirculation well below the Fraser (1981*b*) predicted critical flow rate. Despite the recent paper (Bradshaw et al., 2013) claiming that the Fraser (1981*b*) document yields accurate results; due consideration should be given when applying the Fraser method in its original form.

2.4. Mitigation of suction recirculation in centrifugal pumps

Various methods to mitigate the effect of suction recirculation can be practically implemented in industry. Some effective methods are discussed here.

2.4.1. Diffuser upstream of impeller inlet

A diffuser upstream of the impeller inlet (see Figure 2-6c) decelerates the recirculation flow at the outer streamline Hergt et al. (1996) and Gülich (2014), this deceleration minimizes the effect of the vortex outer streamline acceleration and subsequently minimizes the pressure gradient toward the vortex core. A smaller pressure gradient will assist in mitigating vaporization and subsequently cavitation in the core of the vortex.

2.4.2. Recirculation break upstream of the impeller inlet

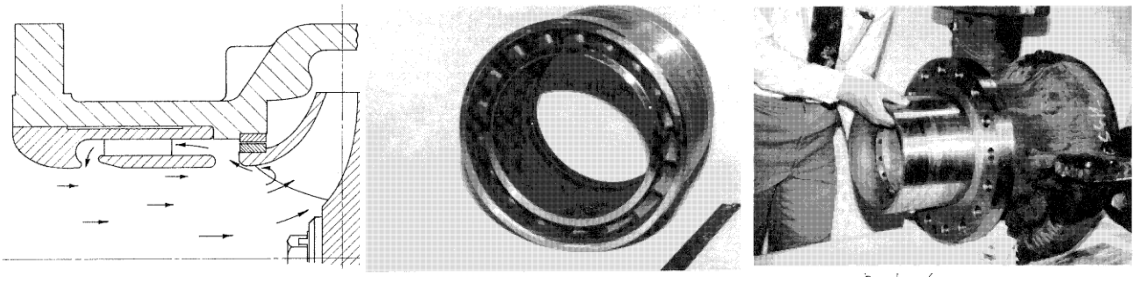
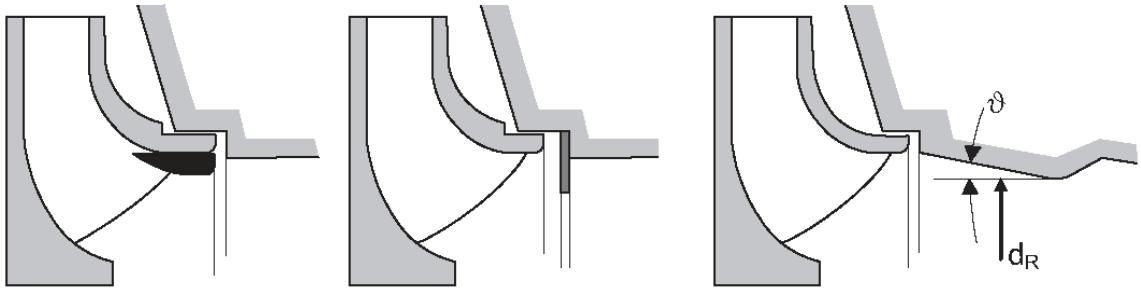


Figure 2-5. Recirculation Break, courtesy of Sloteman et al. (1984)

Sloteman et al. (1984) introduced the concept of a backflow recirculator (see Figure 2-5). This device is fitted at the suction flange of the impeller; when the liquid streamline flow direction at the outer radius is reversed, the backflow recirculator extracts the swirling backflow out of the suction line and removes the induced swirl and re-introduces the extracted liquid back into the suction line. Vortex formation is arrested. This device effectively eliminates pump surge and stabilizes the pump operation at reduced flow rates. Due to its size it is sometimes difficult to retrofit to existing machines.



(a) Bulkhead ring **(b)** Bull ring **(c)** Diffuser

Figure 2-6. Standard inlet modifications, courtesy of Hergt et al. (1996) and Gülich (2014)

2.4.3. Stationary orifice (bull-ring) upstream of the impeller inlet

The stationary orifice (see Figure 2-6b) mentioned by Hergt et al. (1996) and Gülich (2014) suppresses the propagation of the backflow of the liquid in the outer flow streamline. The backflow length is kept short and subsequently the intensity of the recirculation and power consumption is kept low. The BEP of the pump is affected. Similar effects to the $NPSHR$ are experienced as per paragraph 2.4.4

2.4.4. Rotating bulkhead-ring inside the impeller eye

The installation of a bulkhead-ring (see Figure 2-6a) that extends into the flow passage of the impeller eye effectively reduces the impeller eye diameter. The point of recirculation is shifted to lower flow rates (see 2.1.(1)) while the eye diameter has a negative effect on the $NPSHR$ for higher flow rates (as per normal pump design guidelines), increasing the risk of cavitation in low $NPSHA$ installations. The use of a bulkhead-ring is mentioned and has been successfully implemented by numerous authors including Budris (2010), Hergt et al. (1996), Gülich (2014) and Pembroke et al. (1998). The installation of bulkhead-rings is easy and offers effective suction recirculation mitigation if sized for operation within a specified flow margin.

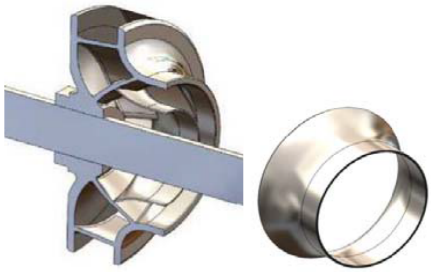


Figure 2-7. Curved inlet disk arrangement (Hermez et al., 2017)

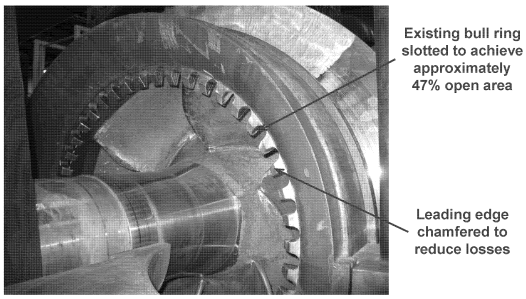


Figure 2-8. Sabini ring, as per Bradshaw (2012)

2.4.5. Curved inlet disk installation into the suction eye of the impeller

Hermez et al. (2016) proposed the installation of a curved disc arrangement into the flow region of an impeller eye (see Figure 2-7). This geometry essentially creates a second flow passage (or additional throat area in the meridional section of the impeller). The difference between the inner and outer flow radii of the individual flow passages now emulate various flow regions in the meridional section that does not have a large pressure and velocity profile gradient. As per 2.1.(2); this is beneficial to the suction recirculation tendency of the impeller eye and shifts the critical flow where recirculation takes place to a lower percentage of BEP. The numerical simulation of the design also predicts improvements in head production and power consumption. This design still requires a field test to verify the findings.

2.4.6. Application of a modified bull-ring (Sabini ring)

Bradshaw (2012) tested the application of a modified bull ring concept (a.k.a. Sabini ring, see Figure 2-8), to an API610 BB1 arrangement pump that was experiencing severe suction

recirculation during operation. The author sanctioned the profiling of the stationary ring by removing approximately 47% of the restricted annular area of the bull ring by means of slotting. The ring design proved to be extremely effective: suction recirculation was suppressed adequately (proven by the reduction in vibration readings) and adverse effects on the $NPSHR$ were not observed during testing. The performance enhancement of the Sabini ring can be attributed to the fact that the flow area of the impeller eye was impacted in a less extreme way than with a bull-ring configuration while still restricting the axial propagation of the recirculating fluid at the outer streamline whereby minimizing the intensity of the recirculation vortex.

2.5. Chapter summary

A literature survey was completed that focused on the phenomenon of suction recirculation in centrifugal pumps and ways to mitigate the occurrence thereof in practical industrial applications. Various options were noted, all of which in various grades of applicability. All of the noted solutions have their own particular strengths and weaknesses, however; the most effective of these was, in the author's opinion, the Sabini ring as described in par. 2.4.6. The weakness of this design is the requirement for casing modification. The following chapters are dedicated to research and develop a potential modification with similar properties to the Sabini ring, but will have the added benefit of being installed in the eye of the impeller, thus being less intrusive.

Part I.

Methodology

3. Method

3.1. Design of the method of research

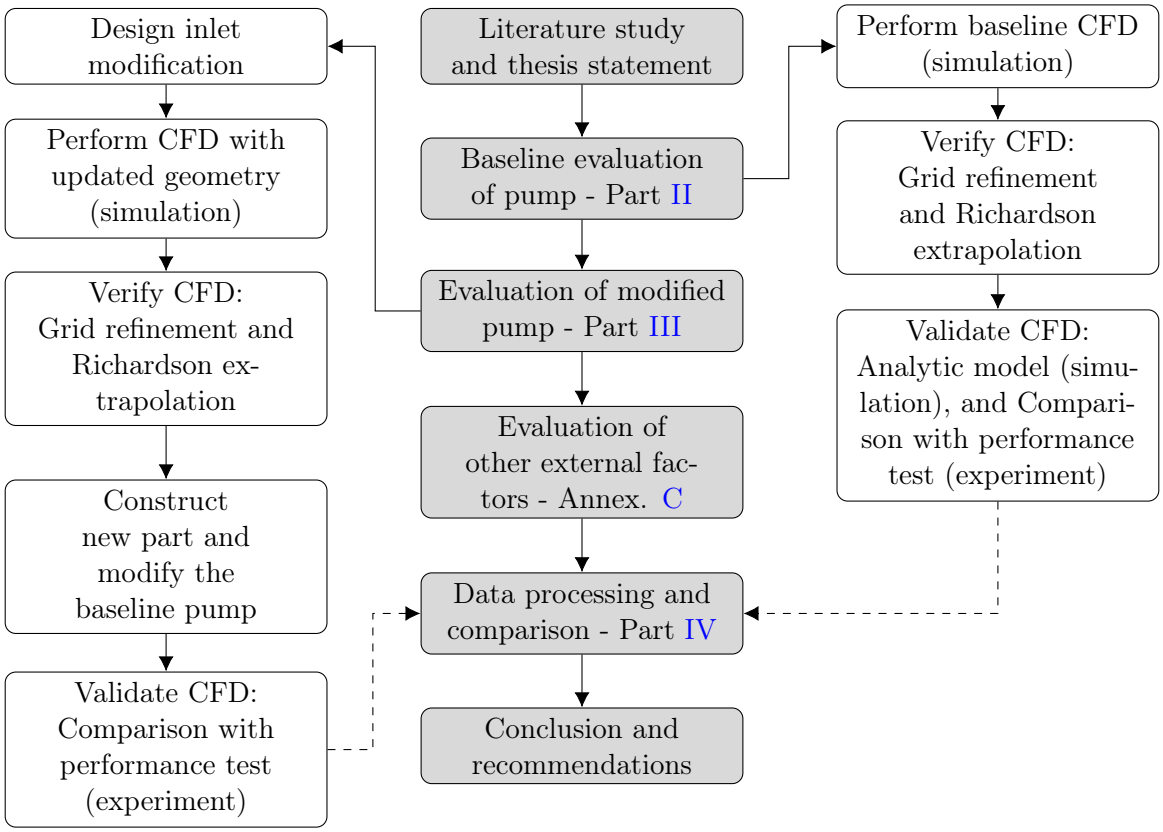


Figure 3-1. Research methodology

The execution of the current research will be completed as per the highlighted methodology in Figure 3-1. The grey blocks highlight the main path of the methodology. The white blocks indicate a sub-function of the attached upstream grey block. Dashed lines indicate that the outcome of the related task/method is transferred to the downstream block for further analysis. The different main blocks relate to parts of this text and should be read in the shown order in order to maintain a coherent flow of information.

3.2. Research design

The different research designs intended for use in this work is briefly mentioned and discussed below.

3.2.1. Subject of investigation - double suction centrifugal pump

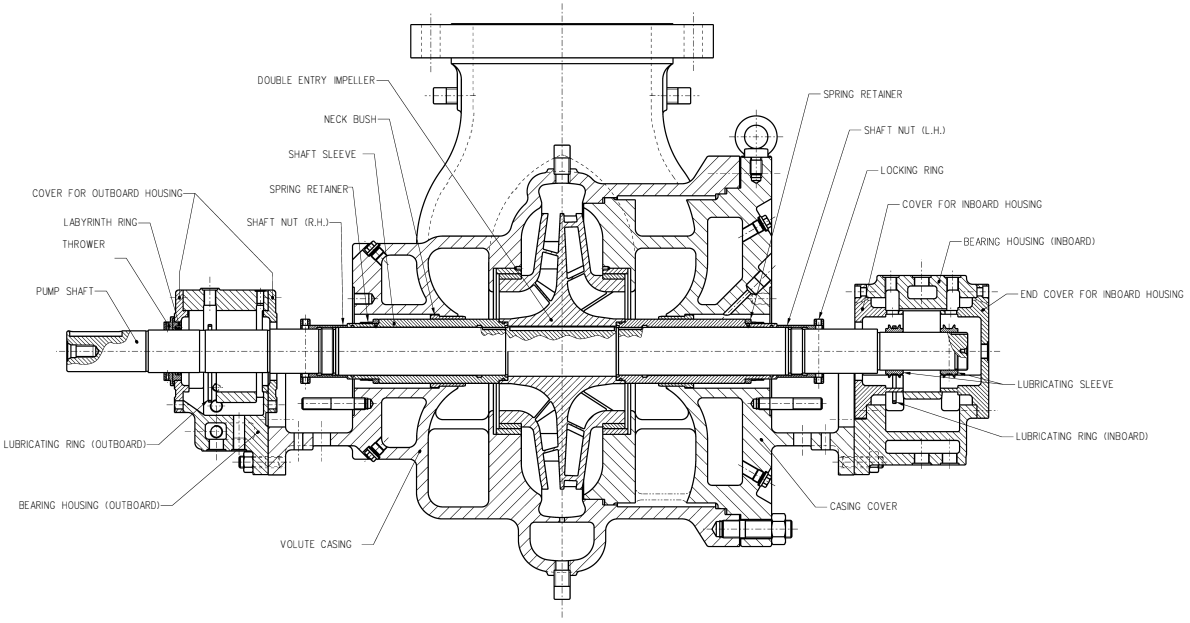
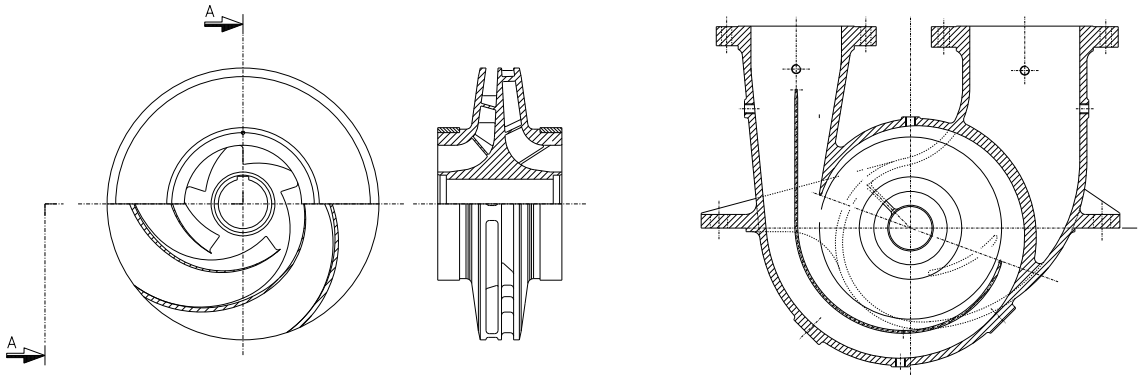


Figure 3-2. Cross sectional drawing of subject pump, with part descriptions.



(a) Double suction impeller. **(b)** Double volute casing.

Figure 3-3. Drawings depicting the subject pump's impeller and volute layout.

Table 3-1. Information relating to the subject pump

Materials[1]		Data at BEP[2]			Additional[3]		
Component	Material	Var.	Value	Unit	Var.	Value	Unit
Impeller	GX6CrNiN26-7	$\text{NPSHR}_{3\%}$	9	$[m]$	z_{La}	5	$[-]$
Casing	GX6CrNiN26-7	Q	1150	$[m^3/h]$	f_q	2	$[-]$
Shaft	X4-CrNiMoNb-25-7	H	286.55	$[m]$	n	2985	$[RPM]$
Wear Rings	GX40-CrNi27-4	η	82.77	$[\%]$	n_q	17.14	$[-]$
Test fluid	Water	P	1084.8	$[kW]$	n_{ss}	228.97	$[-]$

[1] Original materials as per OEM supplied pump drawings.
[2] These values were derived from the original pump data book.

Table 3-2. Geometric features of the model pump as used in the study

Var.	Value	Unit	Var.	Value	Unit	Var.	Value	Unit	Var.	Value	Unit
d_1	211	$[mm]$	a_1	41.62	$[mm]$	e_1	4	$[mm]$	L_{sch}	450.38	$[mm]$
d_2	473	$[mm]$	a_2	68.95	$[mm]$	e_2	7	$[mm]$	d_{1b}	189.24	$[mm]$
b_1	38.9	$[mm]$	β_{1B}	14.18	$[°]$	d_n	111	$[mm]$	λ_{La}	39.63	$[°]$
b_2	20.25	$[mm]$	β_{2B}	14.18	$[°]$	s	0.275	$[mm]$	ε	4	$[\mu m]$

[1] The values listed in this table are as per the 3D model of the impeller, as used in the CFD analysis.

3.2.2. Simulation

The primary research methodology that will be used to evaluate the thesis statement during this study is computer-based numerical simulation. Simulation by means of Computational Fluid Dynamics (CFD) will be used to calculate the complex flow fields inside a double suction centrifugal pump across a range of operation points, with a particular focus on the low flow operating condition.

A high density spacial grid is constructed of the flow field (including the suction- and discharge volute, the impeller and any secondary flow volumes), and the Navier-Stokes equations are numerically approximated at each node. The output of this numerical method provides detailed information regarding the flow field at any discrete node element, thus providing a good representation of the observed physics regarding the considered problem.

The success of a CFD simulation is highly dependent on accurate geometry, the generation of a high quality mesh/grid, the application of the most representative boundary conditions for the problem and the selection of an appropriate turbulence model. The simulation is also critically dependent on the fluid characteristics, the chosen thermodynamic model and any simplification assumptions either imposed by the analyst or inherent simplifications present in the code itself.

Due to the large amount of simulation runs and cases that needed to be evaluated in this study, and considering the limited time and the available computational resources available to the author to complete this study; the preferred numerical solving methodology was chosen. The solving methodology will be assumed to be steady state, frozen rotor type analysis. The study will consider half of the pump geometry, the split plane will be represented with a symmetry boundary condition (in order to ease the computational strain). The assumption was considered valid due to the setup of the impeller (completely split passages) and due to the area of interest not residing in the volutes themselves. Additionally; no account is taken of the relative movement between the impeller mesh and the stationary volute and thus the interaction between these components are not modeled (ANSYS®, 2019*d*). The flow is incompressible and generally well mixed out in the particular application under consideration and thus it can be considered feasible to apply the frozen rotor method if the convergence is stable and the residuals are shown to have reduced to within the desired order of magnitude. The methodology can also be considered an approximation of the unsteady flow solution (transient) at the exact position of the impeller at a specific time period.

3.2.3. Experiments

Experimental work was also conducted in order to generate reliable physical data that will be used to compare the simulation work with experimental results. Successful experimental work depends largely on the accuracy of the instrumentation used therein. It is very important to use calibrated instrumentation and execute the testing to a recognised standard (if applicable/possible) in order to ensure that the testing is considered reliable and repeatable. The test setup is also somewhat sensitive to external influences such as ambient temperature and working fluid properties.

The execution of experiments by utilising internationally standardised test methods are convenient as performance test methodology and test setup are well documented and their accuracy is well accepted in the turbomachinery community. The pump testing was executed in accordance with EN-ISO-9906 (2012) and ANSI-HI-1.6 (2000), as is recommended by various industrial pump standards and Codes of Practice, including API-610 (2011).

One potentially prohibitive factor when considering industry standard tests as certified experiments is the cost involved; the execution of these tests are potentially expensive and the successful execution thereof also greatly relies on the capacity of the test bench itself with regards to the size of the electrical motor used to drive the pump in question, and also of the pump design (the bearing and seal arrangements).

Alternatives to the mentioned standard testing methodologies, is the use of much more involved testing methodologies such as measurement of flow internal velocities (e.g. at the outlet of the impeller) by means of laser velocimetry (widely used in laboratory testing and also mentioned by Gülich (2014)) and the measurement of internal pressures by means of custom installed probes through the pump casing at the outlet of the impeller as done by Memardezfouli and Nourbakhsh (2009). Experiments using transparent casings and impeller arrangements have also been used in literature in order to investigate the flow fields in centrifugal pumps. Although these methods are well justified, it will be impossible to implement in the current study as the pump under investigation is currently used in industry and no modifications to the pressure envelope and parts (in order to apply the intrusive methods described above) have been approved by the equipment owner. No experimental pump units are available for modifications and the cost of constructing such a test pump is not considered feasible from an economic perspective.

3.3. Data acquisition

The data relating to the geometry of the pump impeller and casing were acquired historically by owner funded reverse engineering initiatives (3D modelling of actual parts). The geometry was re-constructed by utilising the previously acquired geometric data into usable 3D CAD part files and further refined into acceptable flow field solid models.

Later comparative measurements of the impeller was completed (by the author) via 3D scanning of similar impellers that were destructively modified in order to render the internal features of the impeller accessible for measurement. The scanned data and the reverse engineered geometry is compared later in this text.

The operating regimes and machine specific construction/clearance data were extracted from both the operating and maintenance manual, maintenance quality control protocols (QCP) and actual on-site operating data.

3.4. Chapter summary

The proposed research methodology and techniques were discussed and outlined in this chapter. The research will be conducted with a focus on the numeric simulation of the flow field of a physical pump. The validation of the simulated models will be accomplished by experimental work coupled with an analytical approach. The next chapter will discuss the numerical solver and turbulence modeling in greater detail.

4. Solver theory and description

4.1. Numerical solver

Analytical solutions to the Navier-Stokes equations does not currently exist for the overwhelming majority of complex fluid flow problems, however; a method of approximating the the solution by means of numeric methods can be achieved. The Navier-Stokes equations can be replaced by algebraic approximations (in each dimension) for a specific measured variable, and solved numerically by using the appropriate solving algorithm.

In order to solve the current flow field, the commercial software package ANSYS® CFX® Release 2019 R2 (ANSYS®, 2019*a*) had been selected as the numerical solver of choice for the current research.

Upon consultation with the Journal of Fluids Engineering's Editorial Policy Statement on the Control of Numerical Accuracy (Freitas, 1993) and its later addendum (Andrews, 2011), it is important for the commercial code user to adequately describe the solver that is utilised in the simulation. An acceptable explanation of the underlying methods, mathematical models and code accuracy is required. A swift explanation is thus presented below.

4.1.1. Transport equations

The governing equations that are solved for – to determine the flow field at each point in the discretized 3D spacial grid – are obtained from the incompressible form of the Reynolds Averaged Navier-Stokes (RANS) equations. The conservation equations for mass, momentum and energy is presented in derived form, for full derivation the reader is referred to the works of Versteeg and Malalasekera (2007) and Pletcher et al. (2016). The annotated equations are shown in Einstein's notation for clarity and for continuity with the ANSYS® CFX® Release 2019 R2 solver theory guide (ANSYS®, 2019*d*). All overbars for averaged terms are removed, except for the fluctuating terms. The continuity equation (conservation of mass) has the following form, as shown in Equation 4.1:

$$\underbrace{\frac{\partial \rho}{\partial t}}_{\substack{\text{Density}\\ \text{rate of}\\ \text{change}\\ \text{wrt}\\ \text{time}}} + \underbrace{\frac{\partial}{\partial x_j}(\rho U_j)}_{\substack{\text{Net mass}\\ \text{flow out of}\\ \text{element}\\ \text{(Convective}\\ \text{term)}}} = 0 \tag{4.1}$$

After inserting the Reynolds decomposition into the Navier-Stokes equations, the Reynolds Averaged form of the Navier-Stokes equations are obtained (for the conservation of momentum,

derived from Newton's second law of motion) as per Equation 4.2:

$$\underbrace{\underbrace{\underbrace{\frac{\partial \rho U_j}{\partial t}}_{\substack{\text{Momentum}\\ \text{rate of}\\ \text{change}\\ \text{term wrt}\\ \text{time}}} + \underbrace{\frac{\partial}{\partial x_j}(\rho U_i U_j)}_{\substack{\text{Convective}\\ \text{term}}}}_{\substack{\text{Material derivative:}\\ \text{describes acceleration}}} = \underbrace{\underbrace{-\underbrace{\frac{\partial p}{\partial x_i}}_{\substack{\text{Rate of}\\ \text{pressure}\\ \text{change}}} + \underbrace{\frac{\partial}{\partial x_j}\Big(\underbrace{\tau_{ij}}_{\substack{\text{Viscous}\\ \text{stress}\\ \text{tensor}}} - \underbrace{\rho\overline{u_i u_j}}_{\substack{\text{Reynolds}\\ \text{stress}\\ \text{tensor}}}\Big)}_{\text{Viscosity term}}}_{\text{Diffusive term}} + \underbrace{S_M}_{\substack{\text{Momentum}\\ \text{source}\\ \text{term}}}}_{\text{Sum of all forces}} \tag{4.2}$$

The Reynolds Averaged Energy Equation (based and derived from the first law of thermodynamics) is described by Equation 4.3:

$$\underbrace{\underbrace{\underbrace{\frac{\partial \rho h_{tot}}{\partial t}}_{\substack{\text{Enthalpy}\\ \text{rate of}\\ \text{change}\\ \text{wrt}\\ \text{time}}} + \underbrace{\frac{\partial}{\partial x_j}(\rho U_j h_{tot})}_{\substack{\text{Convective}\\ \text{term}}}}_{\text{Rate of energy change}} = \underbrace{\underbrace{\underbrace{\frac{\partial p}{\partial t}}_{\substack{\text{Pressure}\\ \text{rate of}\\ \text{change}\\ \text{wrt}\\ \text{time}}} + \underbrace{\frac{\partial}{\partial x_j}\Big(\underbrace{\lambda_t \frac{\partial T}{\partial x_j}}_{\substack{\text{Rate of}\\ \text{heat}\\ \text{addition}\\ \text{due to}\\ \text{conduc-}\\ \text{tion}}} - \underbrace{\rho\overline{u_j h}}_{\substack{\text{Turbu-}\\ \text{lence}\\ \text{(Rey-}\\ \text{nolds)}\\ \text{flux}\\ \text{term}}}\Big)}_{\text{Diffusive term}} + \underbrace{\frac{\partial}{\partial x_j}\left[U_j(\tau_{ij} - \rho\overline{u_i u_j})\right]}_{\substack{\text{Viscous work}\\ \text{term}}}}_{\text{Sum of the rate of change of applied energy and work}} + \underbrace{S_E}_{\substack{\text{Energy}\\ \text{source}\\ \text{term}}} \tag{4.3}$$

The randomly fluctuating tensors in the above formulations, namely the Reynolds flux and -stress tensors, do not have a known formulation for their normal and shear components. The closure of the Navier-Stokes equations require that these terms be solved - this is widely known as the closure problem. The approximation of the normal and shear elements of the fluctuating viscous tensor can be achieved by the use of an adequate turbulence model.

4.1.2. Solver numeric function

As the simulation of a cavitating centrifugal pump in clean cold water service can be performed with the assumption that all fluids (liquid and gas phases) can be accurately described as being homogeneous (ANSYS®, 2019*d*), the mathematical formulation can be derived.

The bulk transport equations for homogeneous multi-phase fluids are derived in ANSYS® CFX® Release 2019 R2 by evaluating the sum of the individual transport equations of each of the fluid phases that are present in the evaluated flow field for a general scalar variable, φ, as per Equation 4.5.

$$\frac{\partial}{\partial t}(\rho\varphi) + \nabla \cdot (\rho \boldsymbol{U} \varphi) = \nabla \cdot (\Gamma \nabla \varphi) + S \tag{4.4}$$

where the following variables are defined by Equation 4.5:

$$\rho = \sum_{\alpha=1}^{N_p} r_\alpha \rho_\alpha \tag{4.5a}$$

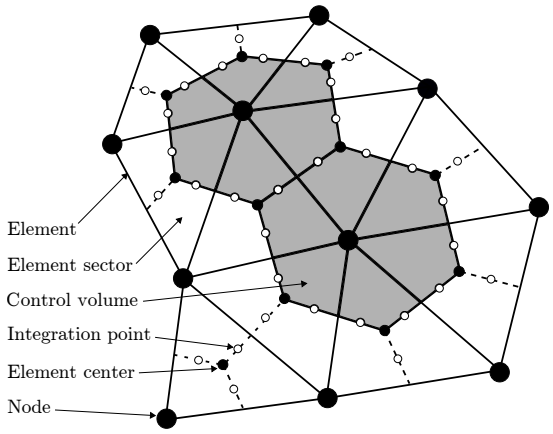
$$\boldsymbol{U} = \sum_{\alpha=1}^{N_p} r_\alpha \rho_\alpha \boldsymbol{U}_\alpha \tag{4.5b}$$

$$\Gamma = \sum_{\alpha=1}^{N_p} r_\alpha \Gamma_\alpha \boldsymbol{U}_\alpha \tag{4.5c}$$

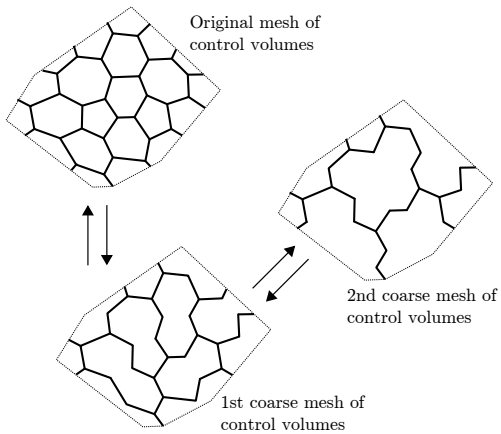
In accordance with the ANSYS® CFX® Release 2019 R2 solver theory guide (ANSYS®, 2019*d*), ANSYS® CFX® Release 2019 R2 (ANSYS®, 2019*a*) utilises an element-based finite volume numeric method, see Figure 4-1a. The governing equations are discretized (in accordance with a spacial 3D grid of the flow field) and solved by a fully implicit, pressure-based numeric methodology.

The solver utilises a pseudo transient algorithm in which a physical time step is utilised in order to advance the problem to the converged steady-state and time independent solution. The time step can be seen as a means to "under-relax" the solution during the solver run, where a smaller time step is similar to a large under-relaxation factor in other (e.g. SIMPLE based) solver algorithms. A fully time dependent, fully transient solver mode is also available.

The coupled (mass and momentum), fully implicit linear solver has been programmed to incorporate the accelerated Incomplete Lower-Upper factorization technique. The coupled solving methodology enables the hydrodynamic equations in all dimensions to be solved as a single system, this results in a more rapid convergence rate.



(a) Schematic (convenient) 2D illustration of the vertex based discretization that is implemented in the ANSYS® CFX® Release 2019 R2 solver.



(b) Illustration of the algebraic multi grid methodology, as implemented in the ANSYS® CFX® Release 2019 R2 solver.

Figure 4-1. Illustration of the ANSYS® CFX® Release 2019 R2 discretization methodology.

The geometric discretization of the flow field yields a finite amount of elements with a finite volume. The element types accepted by the solver include: tetrahedral, hexahedral, wedge and pyramid shapes (ANSYS®, 2019*d*). Due to the fact that all calculated properties of the solution are stored at the grid node points, control volumes are constructed around each node by employing a strategy as depicted in Figure 4-1a. Polyhedral control volumes are mathematically constructed around each node (grey shaded areas in Figure 4-1a), which enables the efficient

calculation of the flow field hydraulic characteristics by means of a conservative 3D finite volume approach. Surface fluxes are evaluated at each integration point, as shown in Figure 4-1a. This methodology ensures that mass, momentum and energy are adequately conserved.

In addition to the mentioned numeric solver features, the Additive Correction Multigrid method (as rigorously explained by Raw (1996) and Hutchinson and Raithby (1986)) is implemented in the solver algorithm. The Additive Correction Multigrid method, see Figure 4-1b, is an algebraic multigrid method and enables the rapid reduction of long wavelength errors (typically errors that manifest along the entire flow volume) on fine meshes where short wavelength errors are typically reduced easily (Roache, 1998*a*). This is achieved by the algebraic addition of control volumes across several grid coarsening levels before interpolating the coarse solution back onto the fine mesh. No additional geometric discretization of the 3D spacial grid is required as the operation is entirely mathematical. The method is extremely robust and is reliable across a wide range of applications (Raw, 1996).

4.1.3. Turbulence modeling

In order to successfully simulate turbo pumps using CFD; it is imperative that the analyst take into account that large pressure gradients are inherently present in the flow field. The accurate simulation of the boundary layer is important in order to accurately predict the separation point of the fluid from the impeller blades at various operating points. The geometry of turbomachines is also inherently complex; variable solid body/streamline curvature and rotation are standard design characteristics. Although most available turbulence models were validated for use in flat plate type simulations, Japikse and Baines (1997) stated that the applicability of standard turbulence modeling methods can be motivated when the ratio of the boundary layer thickness (δ_b) vs. the radius of curvature (R_c) - the blade curve radius, etc. - was small ($\delta_b << R_c$).

Recent published works by Spence and Amaral-Teixeira (n.d.), Vyavahare et al. (2017), S Muttalli et al. (2014) describe the full simulation of centrifugal pumps using the k-ϵ turbulence model of Launder and Spalding (1973) for analysis, but notably; most of the papers reviewed using this approach were published prior to 2010, including the works by Baumgarten et al. (2001), Cheah et al. (2007), Park and Morrison (2009), Sun and Tsukamoto (n.d.). The results that were published ranged in accuracy when compared with actual test data. The robustness of the model itself and the relatively more economical computer requirements of the k-ϵ (when compared with the k-ω SST model of the time) were large factors in the selection thereof.

Various papers have been published that compare different turbulence models (used to close RANS based CFD scripts) typically used for industrial turbomachinery simulation. Recent papers including the works by Chalghoum et al. (2016), Feng et al. (2010) and Liu and Pan (2012) have compared various turbulence models, including the k-ϵ turbulence model of Launder and Spalding (1973) and the k-ω SST model of Menter (1994), when implemented in turbo pump CFD simulations. The general preference among the mentioned authors reside with the k-ω SST model; this model generally predicts boundary layer flows and separation accurately while being implemented in simulations with wide ranges of flow and pressure gradients. The k-ω SST model of Menter (1994) combines the superior near wall modelling capabilities of the Wilcox (2008) k-ω model with the robust and accurate representation of the free stream region as modelled by the k-ϵ model. The two models are linked by means of a transition model in order to enable accurate general simulation results for most industrial flow applications. Recent publications detail notable accuracy of pump simulations when implementing the k-ω SST model, notably works by Chalghoum et al. (2016), Kagawa and Matsushita (2017), Kim et al. (2017) and Strongin (2015).

In addition to the above mentioned; the ERCOFTAC best practice guidelines for single phase

flows (Casey and Wintergerste, 2000) have listed a range of known problems with the k-ϵ turbulence model. Some important deficiencies such as the model's inefficient prediction of separation and reattachment in areas of large pressure gradients are concerning. The ERCOFTAC best practice guidelines does promote the use of the k-ω SST model as a more suitable method for these applications. (ANSYS®, 2019*d*) also promotes the k-ω SST model as being able to accurately predict the onset and amount of flow separation as it takes the transport of turbulent shear stresses into account (hence the name).

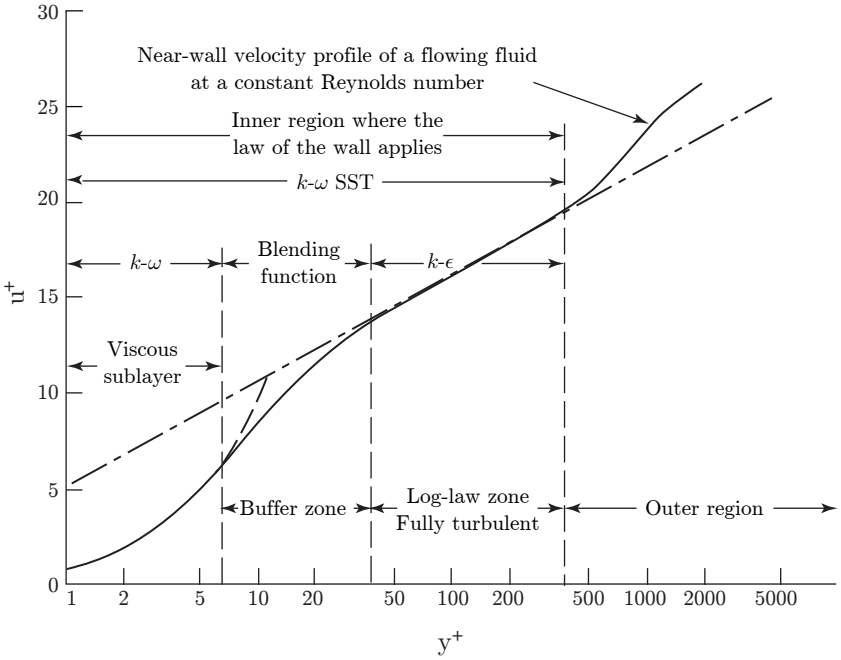


Figure 4-2. Law of the wall and range of applicable turbulence models, adapted from Pletcher et al. (2016)

Due to the fact that the k-ω SST model, as implemented in the ANSYS® CFX® Release 2019 R2 (ANSYS®, 2019*a*) solver, combines the k-ϵ and k-ω models by means of a sophisticated blending function (ANSYS®, 2019*d*); the strict constraint on grid generation of near wall cells (the y^+ value) is somewhat relieved. It is widely acknowledged (Casey and Wintergerste, 2000) that the required grid resolution (y^+) cannot always be strictly attained for all flow areas, specially at areas of separation and reattachment. The k-ω SST model thus automatically switches to the most suitable turbulence numerics, and maintains accuracy through the validated blending approach. See Figure 4-2 for the applicable ranges of the stated turbulence models.

Regarding the near-wall meshing constraints for low Reynolds number turbulence model simulation: The ERCOFTAC best practice guidelines for single phase flows (Casey and Wintergerste, 2000) specifies (more practically) that the analyst should attempt to restrict the first node $y^+ \sim 4$. Additionally, the analyst should attempt to abide by the minimum of ∼10 grid nodes located between the wall and $y^+ = 20$, and close to 30 points inside the boundary layer. The ANSYS® CFX® Release 2019 R2 solver modeling guide (ANSYS®, 2019*c*) recommends a minimum of 15 nodes inside the boundary layer in order to effectively utilise the automatic wall treatment developed for low-Reynolds number based turbulence models, and a minimum of 10 for models utilising the wall function approach in ANSYS® (2019*a*).

Regarding the aspect ratio allowed for grid elements located close to the wall in ANSYS® CFX® Release 2019 R2 (ANSYS®, 2019*a*); The CFX® modeling guide (ANSYS®, 2019*c*) suggests that the upper limit of mesh aspect ratio is 1000 (for double precision methods) with

a warning that aspect ratios greater than 1000 will lead to round-off errors and convergence difficulties. The CFX® reference guide's general best practice guidelines for grid generation (ANSYS®, 2019*b*) however acknowledges the fact that near wall meshes should have a much greater aspect ratio in the range of 1000 for single precision runs and 10000 for double precision runs in order to capture the boundary layer adequately, it further suggests that the aspect ratio of elements away from the boundary region should be kept within 50 for the best results.

The k-ω SST model will be implemented in this study. The impeller mesh would be constructed in order to capture the boundary layer adequately, in order to accurately determine the separation on the vanes. The volute mesh will be constructed to utilise the wall function approach - as the available computing power available to the researcher (during this study) restricted the generation of dense near-wall meshes across large flow areas (especially considering the amount of solver runs to be executed).

4.1.4. Solver cavitation modelling

The solver applies the Rayleigh-Plesset cavitation model (the method was first derived by Rayleigh (1917) and applied by Plesset (1949) for a cavitation problem) in order to model the vaporization and condensation of liquids. The method is explined by Equation 4.6:

$$\dot{m}_{fg} = \underbrace{F_{cond}\frac{3r_g\rho_g}{R_{nuc}}\sqrt{\frac{2}{3}\left(\frac{|p_v - p|}{\rho} - \frac{2\sigma_{st}}{\rho R_{nuc}}\right)}\cdot sign(p_v - p)}_{\text{Expression for bubble condensation}} \tag{4.6a}$$

$$\dot{m}_{fg} = \underbrace{F_{vap}\frac{3r_{nuc}(1 - r_g)\rho_g}{R_{nuc}}\sqrt{\frac{2}{3}\left(\frac{|p_v - p|}{\rho} - \frac{2\sigma_{st}}{\rho R_{nuc}}\right)}\cdot sign(p_v - p)}_{\text{Expression for rapid localized liquid evaporation}} \tag{4.6b}$$

Where the inter-phase mass transfer rate, $\dot{m}_{fg}$, is defined as per Equation 4.7:

$$\dot{m}_{fg} = \underbrace{N_B\frac{dm_B}{dt}}_{\substack{\text{Rate of}\\ \text{bubble mass}\\ \text{change}}} = \underbrace{N_B\rho_g\frac{dV_B}{dt}}_{\substack{\text{Rate of}\\ \text{bubble volume}\\ \text{change}}} = \underbrace{N_B\rho_g\frac{d}{dt}\left(\frac{4}{3}\pi R_{nuc}^3\right)}_{\substack{\text{Rate of bubble}\\ \text{volume change wrt}\\ \text{nucleation radius}}} \tag{4.7}$$

The variable values that is required to be specified in Equation 4.6 are shown in Table 4-1:

4.2. Chapter summary

This chapter briefly discussed the Navier-Stokes equations and presented the main transport equations related to the successful completion of any CFD analysis based on the finite volume method. The preferred numerical solver for this research was selected: ANSYS® CFX® Release 2019 R2. The solver theory, turbulence modeling and cavitation modeling had been discussed briefly. The next chapter will outline the project verification methodology.

Description	Variable	Quantity	Unit
Nucleation site radius	R_{nuc}	1	μm
Volume fraction of nucleation sites	r_{nuc}	5×10^{-4}	–
Empirical factor - vaporisation	F_{vap}	50	–
Empirical factor - condensation	F_{cond}	0.01	–
Water vapour pressure [1][2]	p_v	$10^5 \cdot 10^{A_a-(B/(C+T))}$	$Pa_{(a)}$
Interface length scale [3]	–	1	mm
Multi-phase model [3]	–	Homogeneous	–

[1] Calculated as per the Antoine (1888) equation.
[2] Constants as per *NIST Standard Reference Database Number 69* (2018) for water:
$A_a = 5.40221,\ B = 1838.675,\ C = -31.737,\ T =$ Temperature $[°K]$
[3] Solver selection/value

Table 4-1. (ANSYS®, 2019*d*) recommended settings for the Raleigh-Plesset cavitation model.

5. Verification methodology

5.1. Code verification

The verification of the CFD solver itself is sometimes of much importance, i.e. for nuclear reactor safety calculations, the development of new CFD codes, new developments in existing codes etc. (Roache, 1998*b*), but practically this requirement was not considered to be of crucial importance for the current study. A commercially well known and accepted (especially for turbomachinery related applications) numerical solver was chosen and accepted to be well validated. ANSYS® CFX® Release 2019 R2 solver theory guide (ANSYS®, 2019*d*) claims that the code is at least second order accurate in space when utilising the high accuracy discretization scheme; this scheme utilises a second order upwind discretization methodology and blends this scheme with a first order upwind formulation in areas that causes high numerical difficulties for the second order formulation.

5.2. Quantification of the discretization error

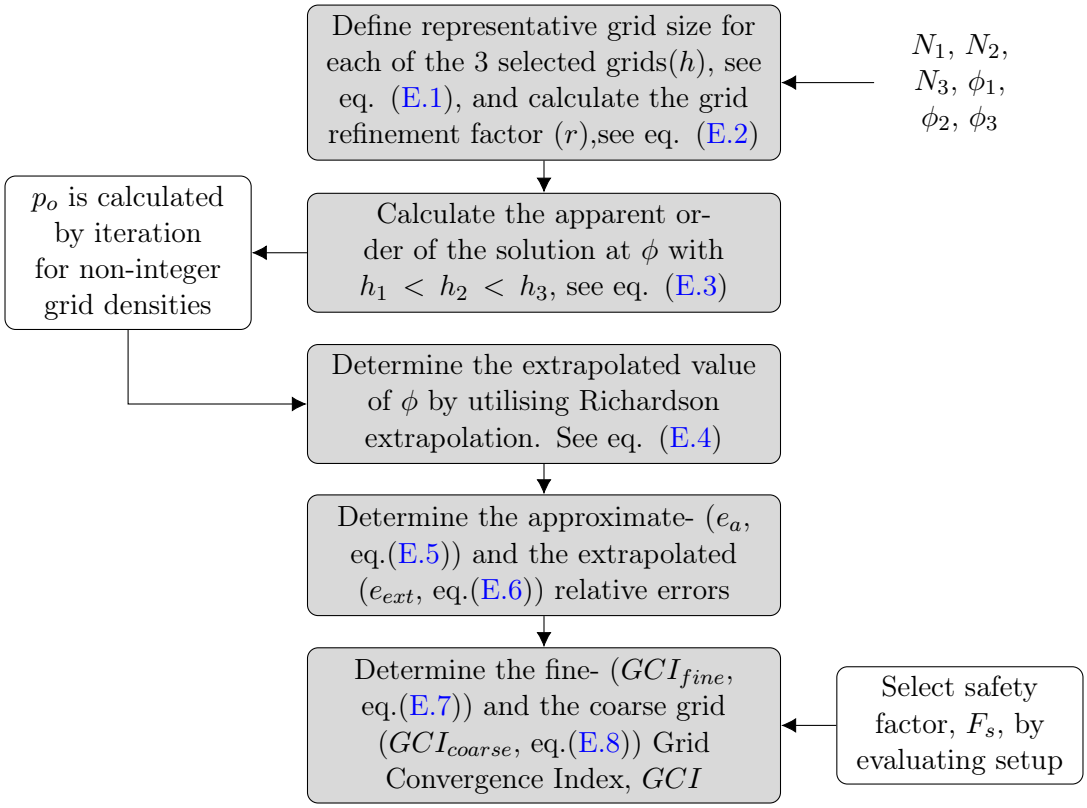


Figure 5-1. Research methodology

In order to determine the discretization error, the Grid Convergence Index (GCI) was developed by Roache (1998*b*) and has since been accepted as the standard practice by The American Society

of Mechanical Engineers (ASME) Standard ASME-V&V-20 (2009). The *GCI* methodology will be implemented as per fig. 5-1. An explanation of the underlying mathematical formulation is presented in Annex. E.

5.3. Chapter summary

The method of solution verification and grid Independence had been described in this chapter. The GCI method enables the analyst to determine discretization error and a conservative uncertainty range for the investigated numerical problem, if implemented correctly. The next chapter will discuss the validation methodology that was used in this study.

6. Validation methodology

In order to validate the accuracy of the constructed CFD model of the noted pump, a multitude of tests and calculations can be performed that can accurately approximate the behaviour of a centrifugal pump operating at a specific operating point.

6.1. Experiments/Testing

In order to enable a meaningful evaluation of the executed experiments, clear guidelines as to the acceptable uncertainty tolerance for each variable should be outlined. Due to the fact that the testing of the actual pump was executed in accordance with EN-ISO-9906 (2012) Grade 1, the analysis of the test uncertainty and measurement tolerance will be done as per the mentioned International Standard's requirements and guidelines. EN-ISO-9906 (2012) had been selected as the preferred test standard due to the fact that the pump design had been completed in accordence with API-610 (1981), the latest revision of this standard, API-610 (2011), refers the reader to select either EN-ISO-9906 (2012) or ANSI-HI-1.6 (2000) for pump performance test completion. ANSI-HI-1.6 (2000) is slightly more forgiving in its prescribed tolerance ranges, in order to enforce stricter tolerances the preferred test standard was chosen to be EN-ISO-9906 (2012).

Table 6-1. Test 1 evaluation of the water standard

Fluid property evaluated	Unit of measure-ment	ISO 9906:1999 Table 5 [1]	Reported value
T	$°C$	40	21
ν	m^2/s	1.75×10^{-6}	1.0×10^{-6}
ρ	kg/m^3	1050	998.6
Free Solids	kg/m^3	2.5	-[2]
Dissolved Solids	kg/m^3	50	-[2]

[1] Although EN-ISO-9906 (2012) does not comment on what qualifies as "cold clean water", ISO-9906 (1999) does provide guidance in Table 5: Specification of "clean cold water. The test fluid was compared with the stated guidelines of the old revision.
[2] Value negligible.

The witnessed testing of the pump in question was completed by qualified professionals at an accredited testing facility owned, constructed and operated by a prominent and respected turbo pump Original Equipment Manufacturer (OEM). The works are ISO-9001 (2015), ISO-14001 (2004) and OHSAS-18001 (2007) certified. After testing had been completed, a pump performance curve and completion certificate stating compliance with EN-ISO-9906 (2012) Grade 1 was issued for both instances. Compliance with the mentioned standard ensures that full

compliance with all measurement procedures had been upheld throughout the testing work, furthermore; all published assumptions relating to the validity of overall measurement uncertainty and performance tolerances are implicitly validated.

Although no guarantee point with regards to pump performance is specified for the current design, the principles of the EN-ISO-9906 (2012) standard can still be applied to different point measurements.

The test bench and layout is shown in fig. 6-1. The red arrows show the fluid flow path, in sequence: Fig. 6-1a shows the suction vessel and distribution system - the piping contains the suction throttle valve as shown in 6-2. Fig. 6-1b shows the test pump with connecting piping - note that the piping is not optimally supported on the discharge side. Fig. 6-1c depicts the (underground) return line to the suction vessel - which contains the flow meter. Fig. 6-1d shows the main instrument panel of the test bench - flow readings are read here, also a schematic representation of the facility is shown.



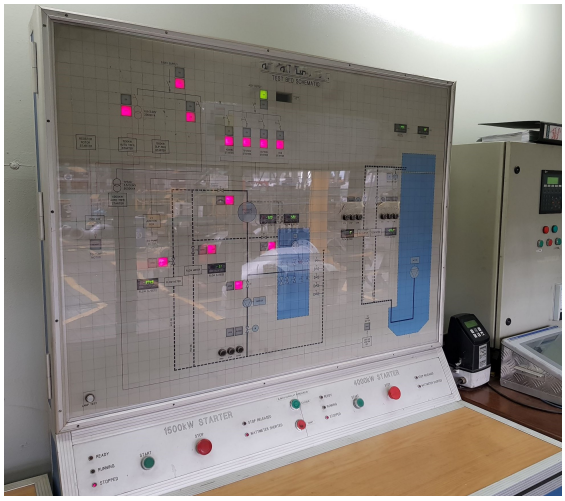
(a) Suction vessel setup.



(b) Pump connection and flow direction.



(c) Return line containing flow meter.



(d) Main instrument panel and layout.

Figure 6-1. Depiction of test station layout. The red arrows indicate the flow direction.

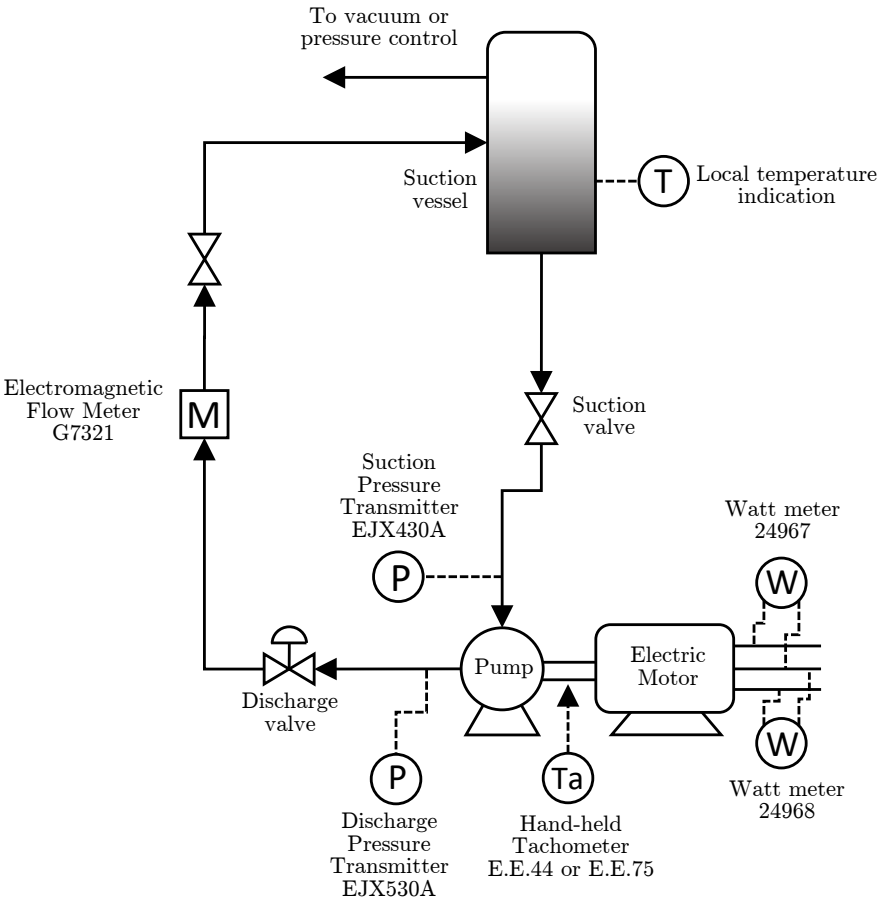


Figure 6-2. Schematic layout of test station.

Table 6-2. Permissible values of overall uncertainties as per EN-ISO-9906 (2012)

Quantity	Symbol	Grade 1 $k = 2, norm$ [%]	Grade 2,3 [2] $k = 2, norm$ [%]
Flow rate	e_Q	±2.0	±3.5
Speed of rotation	e_n	±0.5	±2.0
Torque	e_T	±1.4	±3.0
Pump total head	e_H	±1.5	±3.5
Driver power input	e_{Pgr}	±1.5	±3.5
Pump power input[1]	e_P	±2.0	±4.0
Pump efficiency[3]	e_η [4]	±3.2	±6.4
Overall efficiency [3]	$e_{\eta gr}$ [5]	±2.9	±6.1

[1] Calculated by using the driver power and motor efficiency.
[2] Included for reference purposes.
[3] EN-ISO-9906 (2012) Table 7: Resulting greatest values of the overall uncertainties of efficiency.
[4] $e_{\eta gr} = \sqrt{e_Q^2 + e_H^2 + e_{Pgr}^2}$
[5] $e_\eta = \sqrt{e_Q^2 + e_H^2 + e_P^2}$

Figure 6-2 depicts the test bench layout and location and instrument identification numbers. The system utilised were a closed loop configuration, one of the most accurate standard setups. Table 9-1 outlines the instrumental uncertainties related to the installation at the time of the test execution; as can be seen, all the components were accurately and timely calibrated. All instrumental uncertainty levels fall well inside the EN-ISO-9906 (2012) Grade 1 required limits with a coverage factor of $k = 2$ translating to a 95% confidence level. Table 6-1 also confirms that the test fluid conforms to the requirements for "clean cold water" as per ISO-9906 (1999). Note that no data is provided on the free- nor dissolved solid content, this will have an impact on the interpretation of the $NPSHR$ test and also the CFD cavitation modeling accuracy. The entertained solids act as a nucleation point for the cavitation bubbles to start forming - the current assumption is that the water conforms to the set standards.

Table 6-3. EN-ISO-9906 (2012) tolerance limits for Grade 1 performance testing

Test Grade	U_Q [±%]	U_H [±%]	U_η [%]	U_P [%]
Grade 1, 1B	4.5	3	-3	4
Grade 1, 2B	8	5	-5	8
Grade 1, 3B	9	7	-7	8

6.2. Additional comment on the method of determining pump shaft power and overall efficiency at coupling

The pump shaft power, P, is determined in the experiment by calculation; The measured motor input power is multiplied by the motor's characteristic efficiency curve value at the given operating point. Additionally, the pump's mechanical losses are subtracted from the power calculation - this yields P.

$$P = P_{mes}\eta_m - P_{mloss} \tag{6.1}$$

The formulation of the measured shaft power is detailed in equation 6.1, above.

The pump mechanical losses, P_{mloss}, are influenced by two angular contact ball bearings (acting as a thrust and journal combination arrangement on the shaft non-drive end) and a single anti-friction deep groove ball bearing at the drive end.In addition to the bearing arrangements losses due to the flexible coupling and two mechanical face seals are taken into account. The sum of the expected losses, P_{mloss}, of the individual components (as specified by the individual part OEM's) equates to approximately $8.2kW$ in total.

Note that the alignment between the pump and the motor will also have an effect on the expected power loss of the coupling - however, this loss effect will be minimal if the alignment between the driver and the pump is executed within allowable alignment specification/standards. Also note that the mechanical losses in the pump and motor bearings are a function of the alignment and the lubrication applied (grease in the case of the motor). The mechanical face seal losses are a function of the seal compression (seal tension) values, a function of the setting/assembly of the seals. The values are thus estimated as per standard tests performed by the individual

part OEM's.

$$\eta = \frac{\rho g H Q}{P} \tag{6.2}$$

The pump overall efficiency, ρ, is subsequently calculated as per equation 6.2, above.

6.3. Additional method of determining simulation tendency

An additional 1D meanline method was developed as a qualitative screening tool. Although it is acknowledged that 1D meanline methods cannot explicitly be seen as equivalent (or higher) in accuracy when compared to full 3D CFD simulations, it can be useful to qualitatively compare certain projected performance aspects (such as H_{th} and H_{thL} vs Q) related to impeller geometry characteristics. Large deviations between the 1D meanline- and the baseline 3D CFD simulation results (at BEP) will aid in highlighting any major modelling errors. An explanation of the methodology and assumptions of the method is presented in Annex. F.

6.4. Chapter summary

The validation strategy of CFD simulations were discussed and the strategy outlined in this chapter.

The experimental setup and standards for acceptance in accordance with EN-ISO-9906 (2012) was also presented. The experimental standard is applicable to all experiments executed during this study.

The proposal, development and implementation of a 1D mean-line impeller flow analysis algorithm was also presented. This 1D tool was successfully implemented on the unmodified impeller later in this study.

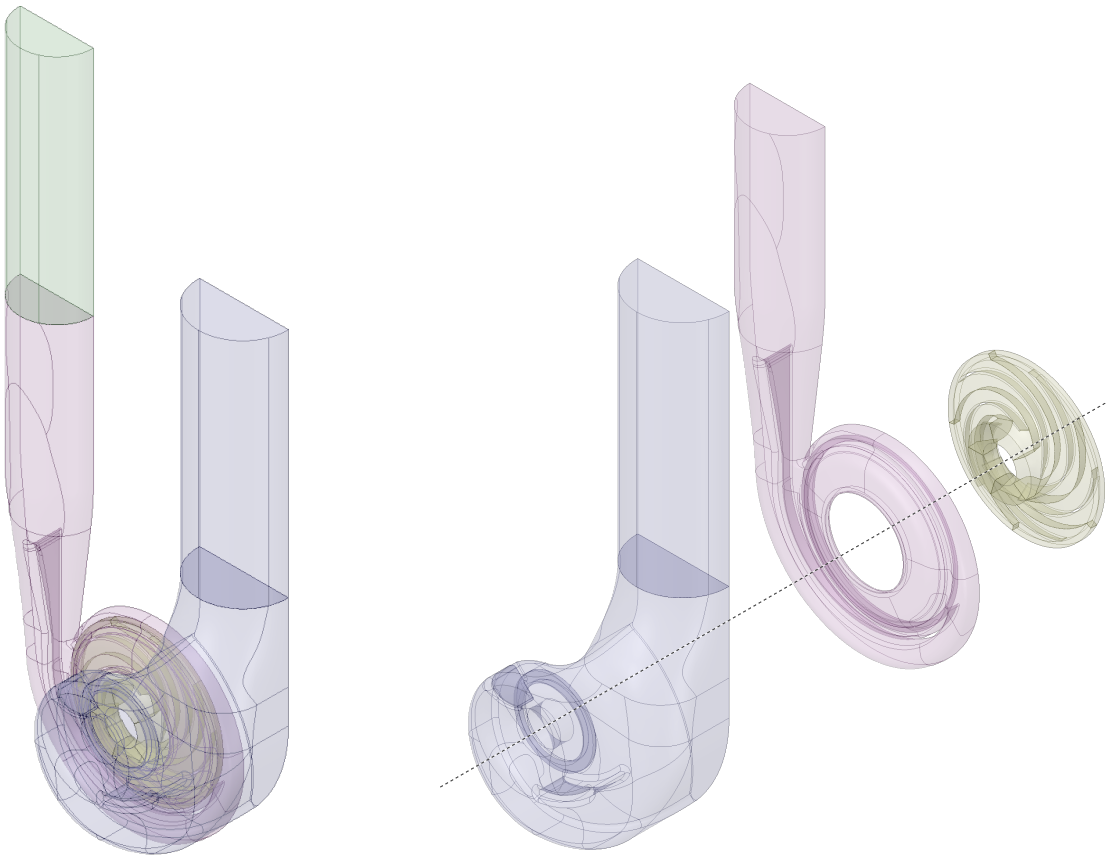
The next chapter will form part of Part II, where the baseline analysis of the unmodified pump geometry will be presented.

Part II.

Baseline evaluation of pump

7. Baseline evaluation

7.1. Model assembly



(a) Assembly of complete flow field. Transparency is activated in order to see components.

(b) Exploded isometric view of the unmodified mesh arrangement. The discharge volute's extension (green portion in Figure 7-1a) is omitted in favour of favourable image layout. The z axis (dashed line) is the axis of impeller rotation.

Figure 7-1. Isometric view of the flow field with location of boundary conditions indicated.

The flow field of the baseline pump is shown, as modeled, in Figure 7-1. The exploded view of Figure 7-1b shows the impeller mesh (full) in gold, the suction volute in blue and the discharge volute in pink. The meshes are assembled from the impeller mesh, stacked from back to front. The assembly is shown in Figure 7-1a.

A more detailed depiction of the impeller-suction volute interface is shown in Figure 7-2. It can be seen that the suction of the impeller mesh is very closely matched with the outlet of the suction volute. Geometry consistent with the original pump suction and discharge volute has been maintained, thus the areas of leakage flow addition (wear ring cavity) is included adjacent to the impeller eye.

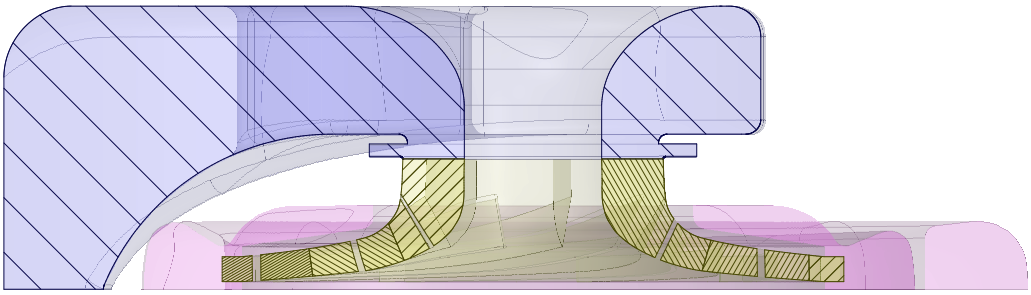
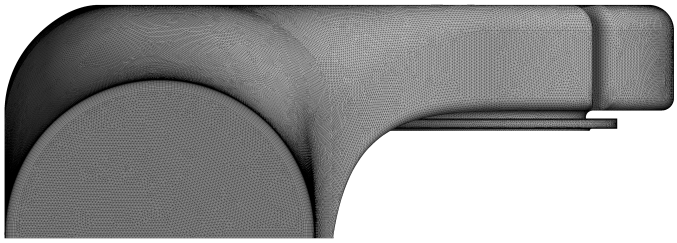


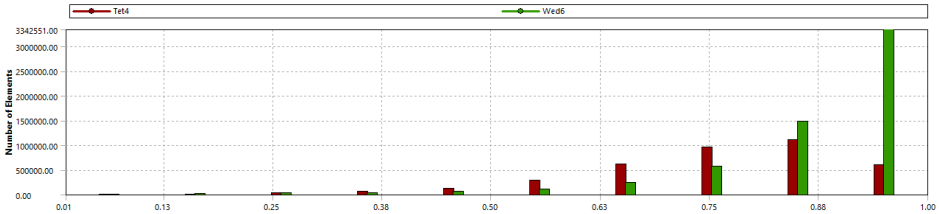
Figure 7-2. Cross section of the flow field in the $z - x$ plane

Both the suction and discharge volute meshes are defined to be stationary while the impeller mesh is defined to be rotating in an anti-clockwise direction at a rotational speed of 2985RPM. A single passage could have been modeled while implementing periodic boundary conditions between the neighbouring impeller passages and the corresponding pitch points on the suction and discharge volute meshes, but it was decided that the complete impeller mesh should be modeled in order to ensure the capture of individual separation cells.

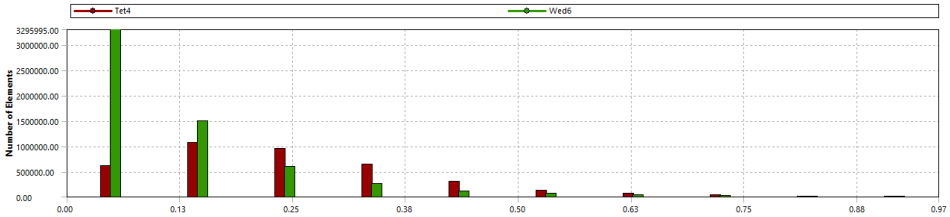
7.2. Mesh



(a) The top view of the suction volute mesh



(b) Orthogonality property analysis graph for the suction volute mesh



(c) Skewness property analysis graph for the suction volute mesh

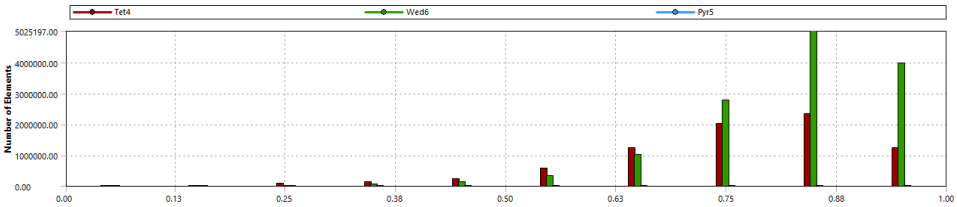
Figure 7-3. Suction volute mesh - fine grid representation.

As can be observed from fig. 7-3b and 7-3c; the overall quality metrics for orthogonality and skewness is favourable with a small fraction of cells falling just short of the 0.1 lower recom-

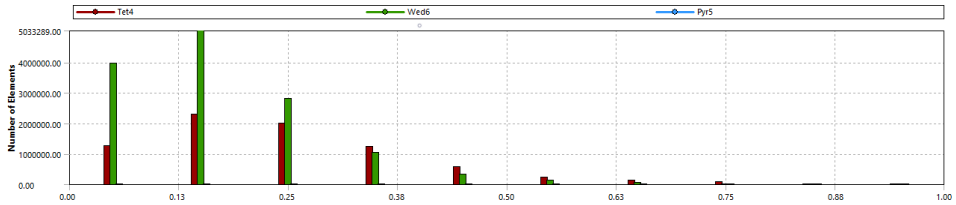
mended value for orthogonality. The mesh itself is comprised on mainly tetrahedral elements with prism boundary layer inflation. Higher density grid definitions are present at the GGI interfaces. Overall the mesh is seen as acceptable.



(a) The top view of the discharge volute mesh



(b) Orthogonality property analysis graph for the discharge volute mesh



(c) Skewness property analysis graph for the discharge volute mesh

Figure 7-4. Discharge volute mesh - fine grid representation.

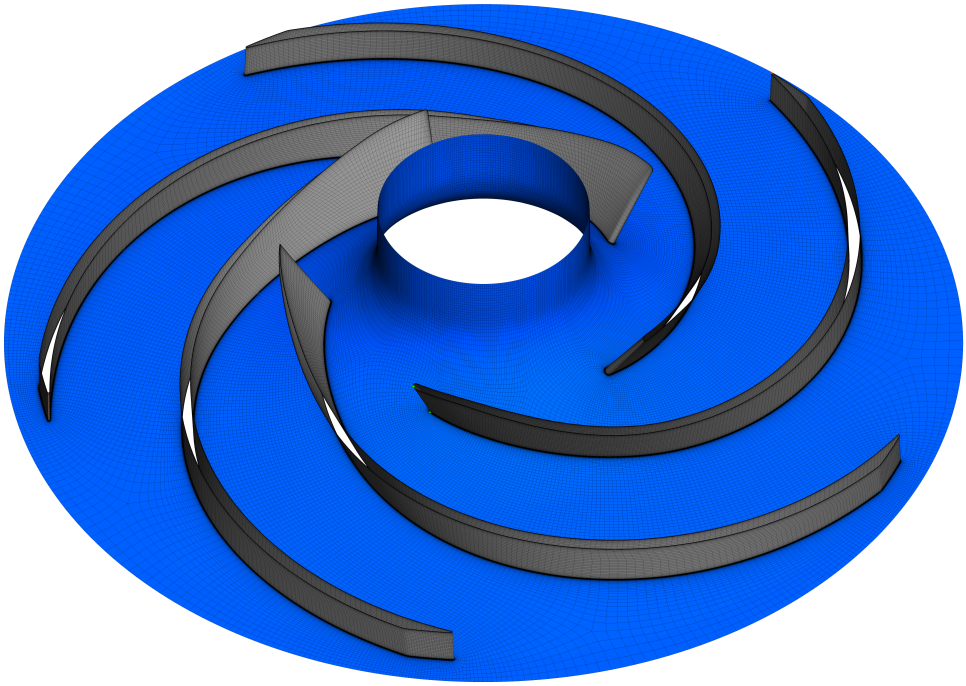
The discharge volute mesh metrics are presented in figs. 7-4b and 7-4c. The overall quality metrics for orthogonality and skewness is favourable with a minute fraction of cells falling just short of the developer recommended 0.1 lower value for orthogonality and 0.95 for skewness (ANSYS®, 2019*c*).The same meshing methodology is followed as per the suction volute.

The impeller grid had been generated by using the purpose built turbomachinery rotating element grid generator, ANSYS® TurboGrid™ Release 2019 R2 (ANSYS®, 2019*a*) which utilises the ANSYS® ICEM CFD™ Release 2019 R2 (ANSYS®, 2019*a*) as grid generating engine. High quality structured grids are generated and this enables the use of comparatively less dense grids to achieve good results in turbomachinery applications. Due to the nature of the application, high turbulence levels can be expected. The proper boundary layer mesh does become very stretched close to the walls, but as mentioned in par. 4.1.3, mesh aspect ratios close to the wall (in the laminar sub-layer) can be in the vicinity of 10000 with double precision. The impeller mesh, as described in fig. 7-5 and table 7-3, is thus considered of high quality and will be used as the fine grid mesh for the component.

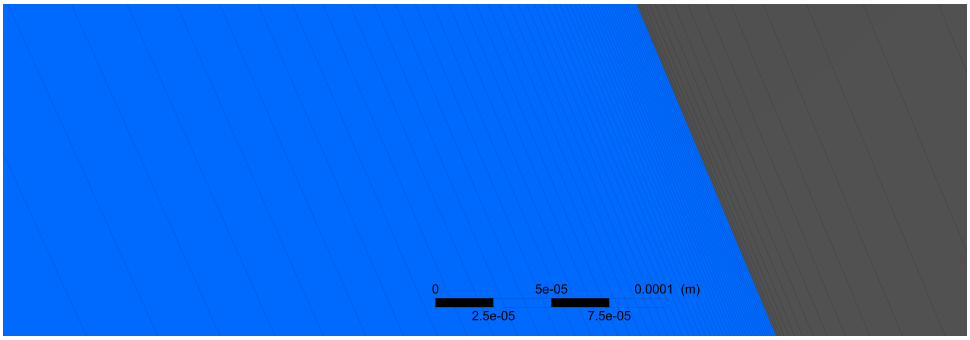
Table 7-1. Breakdown of the different elements that the meshes consist of for the current case

Domain	Nodes	Elements	Tetrahedra	Wedges	Pyramids	Hexahedra
Impeller	11712690	11439350	0	0	0	11439350
Volute Discharge	8646196	22373265	8489819	13881356	2090	0
Volute Suction	3795324	9970005	3924385	6045620	0	0
All Domains	24154210	43782620	12414204	19926976	2090	11439350

The mesh refinement study was executed by generating three different meshes of varying density.



(a) A high quality structured grid was generated for the impeller, as shown in this figure for the fine grid variant.



(b) The near wall resolution, note the ruler for reference to the scale. The boundary resolution is required in order to properly model the low-Re section of the boundary layer.

Figure 7-5. Impeller fine grid representation.

Table 7-2. Indication of mesh quality for the unchanged geometry, fine mesh

Domain	Average orthogonality	σ	Recom.	Average skewness	σ	Recom.
Volute Discharge	0.80399	0.12864	≥ 0.1	0.19523	0.12882	≤ 0.95
Volute Suction	0.83407	0.14322	≥ 0.1	0.16384	0.1404	≤ 0.95

The methodology that was followed is as discussed in fig. 5-1. The quality of the generated grids was very similar to the stated parameters and is deemed to be adequate meshes in order to complete the mesh convergence study. The near wall resolutions were maintained in all cases in order to ensure that the implementation of the turbulence model does not skew the results on grids with varying near wall resolution.

Table 7-3. Indication of impeller mesh quality for the unchanged geometry, fine mesh

Limit Measure	Minimum	Maximum	Actual	% Bad
Face Angle [°]	15	165	35.245-144.761	0
Element Volume ratio	-	12	3.18762	0
Minimum Volume $[m^3]$	-	20	$1.69529 \cdot 10^{-16}$	0
Edge-Length Ratio	-	10000	11899.7 [1]	12.2221

[1] All bad elements are located in the first 3 layers of the boundary layer mesh

In order to ensure that the generated mesh complies with the requirements of the selected turbulence model and solver requirements, contour plots of the $y+$ parameter was completed and is presented in fig. 7-6. The indications describe that the impeller geometry near wall mesh is generally within the $y+ \leq 5$ limit for laminar sub-layer modelling.

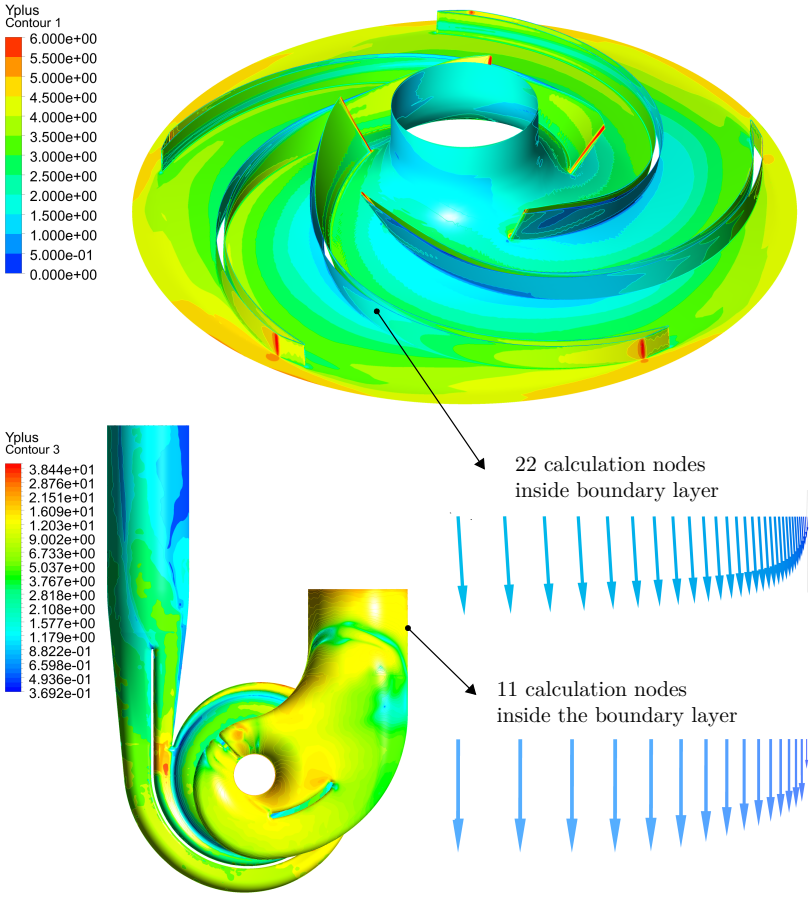


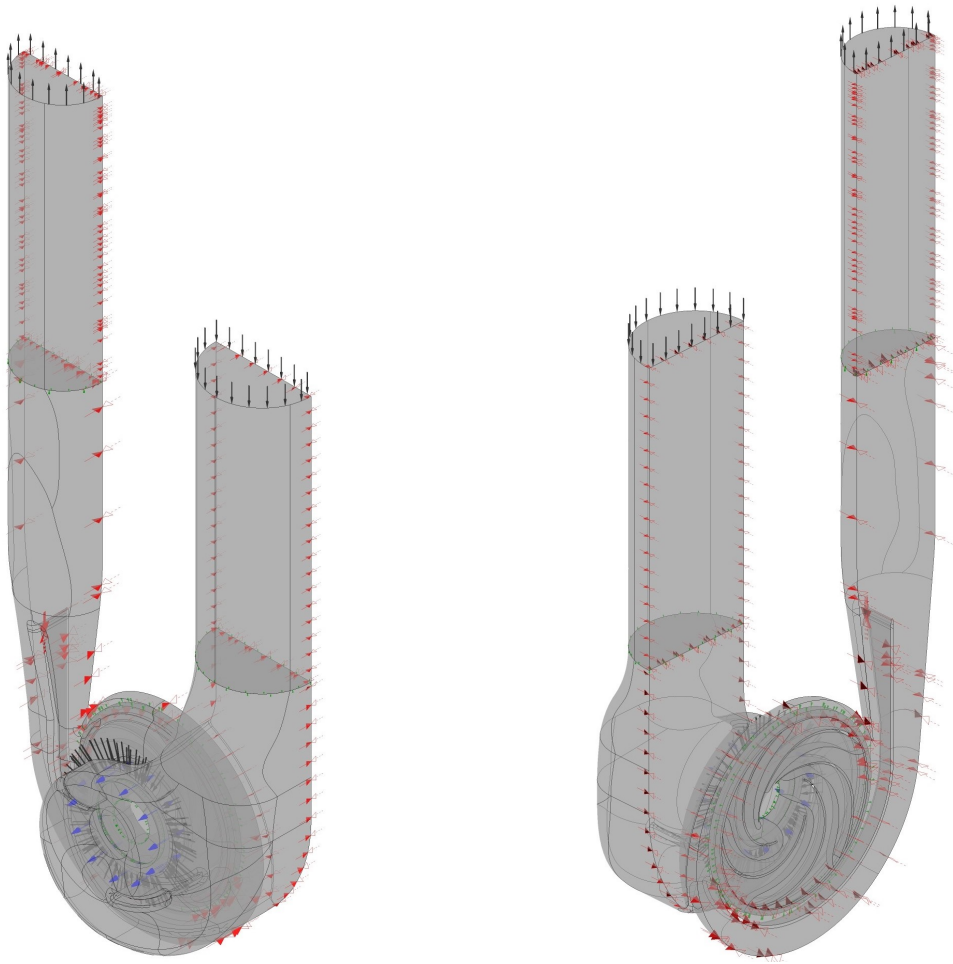
Figure 7-6. Surface contour plots of the $y+$ parameter at $Q = 639.361m^3/h$. Vector plots of the node locations are shown to illustrate the boundary layer resolution at the indicated locations.

The vector plot of the impeller flow field confirms that 22 nodes lie within the boundary layer at the observed point, well within the ANSYS® CFX® Release 2019 R2 solver theory guide (ANSYS®, 2019*d*) recommended value of a minimum of 15 nodes in the boundary layer for low-Re turbulence modeling.

The inlet- and outlet volute flow fields maintains a $y+ \leq 50$ on all walls. This near wall resolution is very much acceptable for the implementation of wall function based near wall modeling. The

scalable nature of the $k-\omega$ SST turbulence model ensures that intermediate values of $y+$ are well resolved.

7.3. Model setup



(a) Isometric view of the flow field, from the $+z$ direction

(b) Isometric view of the flow field, from the $-z$ direction

Figure 7-7. Isometric view of the flow field with location of boundary conditions indicated.

The model is comprised of 50% of the total flow volume of the pump. The mid-plane is set as a symmetry boundary condition; the wall is thus modeled as a free slip, frictionless surface. This emulates a symmetry plane. It is important to note that the flow field had been chosen to have a symmetry plane in order to accommodate the available computing power.

The suction casing inlet is set to an inlet boundary condition that is governed by a static pressure inlet value. No gradients are specified, thus a Zero Gradient case is selected. The discharge outlet is defined by a mass flow outlet boundary condition. The connection between all meshes, moving or static is achieved by using the GGI interface (General Grid Interface), this boundary condition enables the interpolation between meshes in order to enable seamless carry over between grids in any reference frame. All walls (except the annular seal) are defined as rough walls, with an equivalent sand surface roughness of $4\mu m$.

The annular seal is modeled by a user defined ROM, defined by CFX® Expression Language

(CEL) expression language and extensively discussed in Annexures A and B and par. 7.3.1 and fig. 7-8.

7.3.1. ANSYS® CFX® CEL expression language

Internal leakage path through rotating annular seal

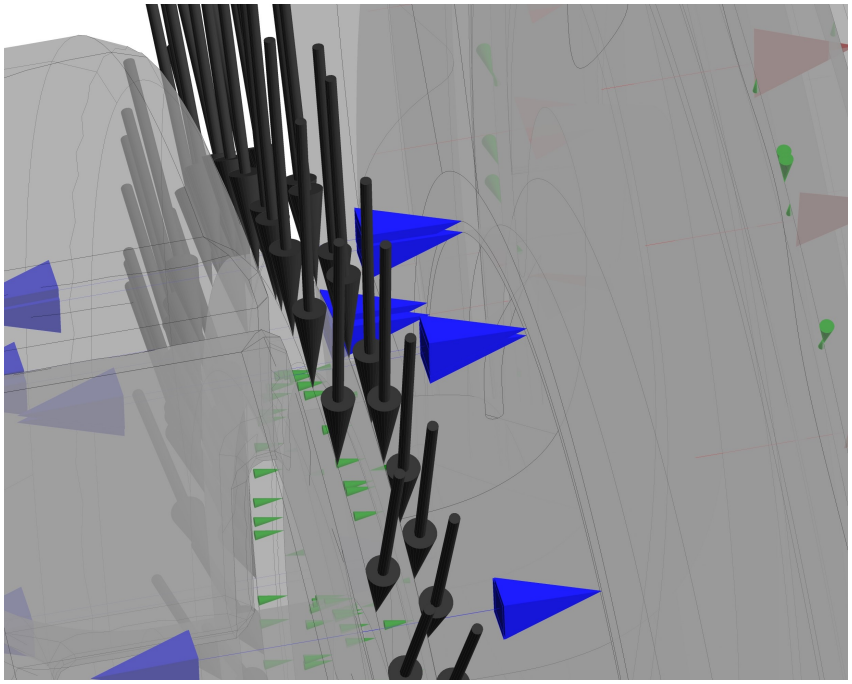


Figure 7-8. Location of annular seal leakage path. Blue arrows indicate discharge to suction leakage represented by an opening boundary condition. Black arrows indicate the inlet of the discharge to suction leakage flow, represented by an inlet boundary condition with a specified mass flow equal to the ROM of the leakage flow.

In order to separate the high pressure and low pressure volumes in a centrifugal pump, rotating annular seal arrangements are used. These annular seals function by maintaining a close running clearance between the stationary (casing) and rotating (impeller eye Outside Diameter(OD), in this case) surfaces. The close running clearance essentially functions as a throttling device and thus ensures that the flow of liquid from the high pressure discharge side to the low pressure suction side of the impeller is restricted by means of a predetermined flow area reduction. For a detailed discussion on this matter, the reader is directed to Annexure A, and additionally to Figure A-1 in the same section.

In order to include the effect of this unavoidable parasitic loss, an analytic model was constructed as per the methodology outlined in Annexure A. The construction of a Reduced Order Model (ROM) to calculate the internal leakage rate was pursued due to the inconvenience of including a very dense mesh (compared with the rest of the model) in order to represent a very narrow annular flow path; the addition of this mesh geometry has a negative effect on solution convergence rate and stability. It has been proven in Annexure A that the internal leakage flow can be very accurately modeled using analytic methods.

7.4. Chapter summary

The setup of the 3D flow field is discussed in this chapter as implemented in ANSYS® CFX® Release 2019 R2 solver setup.

A study of the mesh construction and quality was completed and the mesh arrangement was accepted as being of acceptable quality and resolution. The mesh was considered acceptable to facilitate the implementation of low-Re turbulence modeling methods as facilitated by the implemented $k - \omega$ SST turbulence model. Adequate boundary layer resolution was obtained with approximately 22 nodes within the flow area of interest (the impeller) and approximately 11 nodes inside the casing boundary layer (which will be approximated by the wall function methodology).

The implementation of an intricate ROM, constructed to represent the rotating annular seal leakage path between the outlet volute casing and the suction casing through the wear ring arrangement is implemented in the ANSYS® CFX® Release 2019 R2 setup via the solver CEL. The ROM was also subjected to a verification study.

The next chapter will describe the verification study and the results of the CFD simulations regarding the unmodified geometry.

8. Verification of baseline case

Table 8-1. Grid convergence study of the modified mesh at $\dot{m} = 58.985kg/s$

Variable	η	ΔH_{stat}	ΔH_{tot}	ΔH_{thL}	P [1]	$\dot{m}_{sp}$ [1]
	[%]	[m]	[m]	[m]	[kW]	[kg/s]
ϕ_1	55.194	314.66	314.84	389.57	328.45	5.7044
ϕ_2	54.934	312.7	312.93	388.45	329.38	5.711
ϕ_3	55.504	310.22	310.54	386.14	324.52	5.6379
ϕ_{ext}^{21}	55.405	320.88	321.2	390.53	328.24	5.7038
	[−]	[−]	[−]	[−]	[−]	[−]
p_o	3.3913	1.1569	1.109	3.26045	7.182	10.472
AR [4]	1.036	1.0063	1.0061	1.0029	1.0195	1.0135
	[±%]	[±%]	[±%]	[±%]	[±%]	[±%]
e_a^{21}	0.47107	0.62289	0.60666	0.2875	0.28315	0.1157
e_{ext}^{21}	0.38055	1.9372	1.9789	0.24617	0.063215	0.010564
GCI_{coarse}^{21}	2.5592	7.7952	7.8766	1.6028	1.039	0.37879
GCI_{fine}^{21}	1.146	5.9265	6.0567	0.74035	0.18953	0.03169

[1] For all cases: Simulated $\dot{m} = 58.985kg/s$, $Q = 212.772m^3/h$, for full pump flow apply Note 5.
[2] For all cases: $N_1 = 49808780$, $N_2 = 23777244$, $N_3 = 16692124$.
[3] For all cases: $r_{21} = 1.2795$, $r_{32} = 1.1252$, $F_s = 3$.
[4] Asymptotic range achieved if $AR \approx 1$
[5] Multiply the indicated column values of $\phi_1, \phi_2, \phi_3, \phi_{ext}^{21}$ and the total $\dot{m}, Q$ by 2. All other values will remain unchanged as the proportional change will not affect the calculation method.

A three grid mesh independence study was completed as per the method outlined in the Journal of Fluids Engineering Editorial Policy Statement on the Control of Numerical Accuracy, as per Freitas (1993) and subsequently by the referenced work by Celik et al. (2008) which is based on the ground breaking work by Roache (2009). Richardson extrapolation of the three grid solution was also completed for all cases in order to approximate the exact solution for the considered value ϕ.

Tables 8-1, 8-2 and 8-3 highlights the results of the study. It is noteworthy to state that all cases have exhibited good grid independence and the resulting GCI_{fine} has resulted in narrow error bars (Roache, 2003) used in other graphs. The value of p_o have in some cases been far away from 1, however it can be argued that two of the three grids produce similar results for the measured quantity to motivate that the asymptotic region have already been reached.

Figures 8-1 and 8-2 depict contour plots of the total pressure and velocity in the stationary frame for all operating cases across all grids. Satisfactory solution stability is observed. All RMS residuals converged to less than 4 orders of magnitude. For an example convergence case see Annexure H.

Table 8-2. Grid convergence study of the modified mesh at $\dot{m} = 127.215 kg/s$

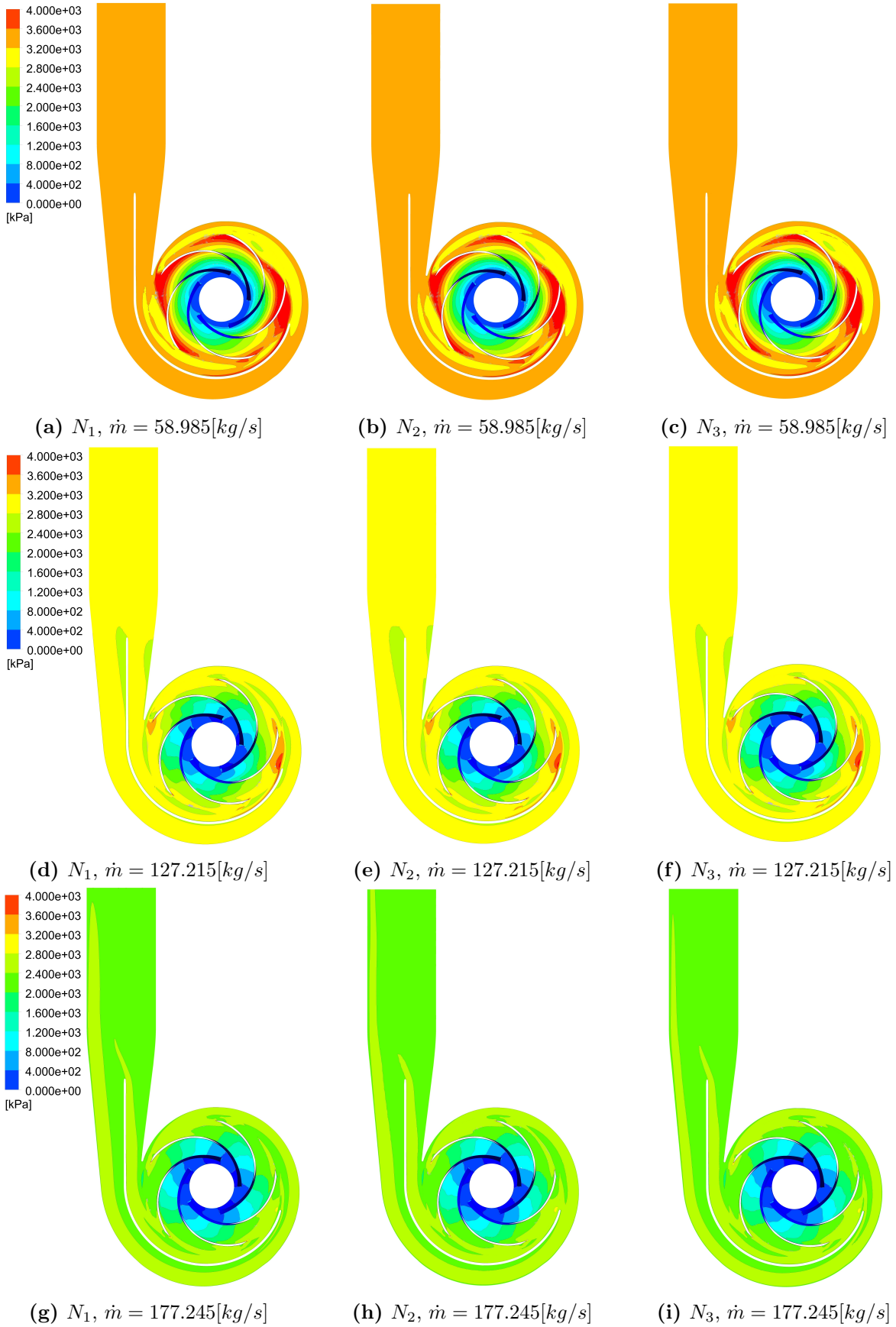
Variable	η	ΔH_{stat}	ΔH_{tot}	ΔH_{thL}	P [1]	$\dot{m}_{sp}$ [1]
	[%]	[m]	[m]	[m]	[kW]	[kg/s]
ϕ_1	78.879	287.06	288.23	312.98	455.250	5.1248
ϕ_2	78.738	286.83	288.75	313	456.16	5.2255
ϕ_3	79.338	287.71	289.62	313.3	455.42	5.2093
ϕ_{ext}^{21}	78.92	287.14	287.54	312.98	451.21	5.1043
	[−]	[−]	[−]	[−]	[−]	[−]
p_o	6.2833	5.8185	2.3588	11.854	0.85715	7.4991
AR [4]	1.0264	1.0266	0.9982	0.99994	0.68772	0.96064
	[±%]	[±%]	[±%]	[±%]	[±%]	[±%]
e_a^{21}	0.17875	0.080123	0.18041	0.0063902	0.19989	4.0969
e_{ext}^{21}	0.052078	0.026981	0.24158	0.00041016	0.89575	5.7758
GCI_{coarse}^{21}	0.69258	0.32133	1.2642	0.020401	3.2631	28.672
GCI_{fine}^{21}	0.15631	0.080966	0.72298	0.0012305	2.6634	16.381

[1] For all cases: Simulated $\dot{m} = 127.215 kg/s$, $Q = 458.892 m^3/h$, for full pump flow apply Note 5.
[2] For all cases: $N_1 = 43782620$, $N_2 = 21509931$, $N_3 = 10821486$.
[3] For all cases: $r_{21} = 1.2673$, $r_{32} = 1.2573$, $F_s = 3$.
[4] See Note 4, Table 12-1.
[5] See Note 5, Table 8-1.

Table 8-3. Grid convergence study of the modified mesh at $\dot{m} = 177.245 kg/s$

Variable	η	ΔH_{stat}	ΔH_{tot}	ΔH_{thL}	P [1]	$\dot{m}_{sp}$ [1]
	[%]	[m]	[m]	[m]	[kW]	[kg/s]
ϕ_1	78.852	235.28	236.84	259.88	522.27	4.7327
ϕ_2	79.356	235.89	240.22	260.25	524.69	4.853
ϕ_3	79.558	238.26	239.99	260.85	524.32	4.7835
ϕ_{ext}^{21}	78.485	235.09	236.57	259.35	521.81	4.5636
	[−]	[−]	[−]	[−]	[−]	[−]
p_o	3.6465	5.9949	11.003	2.2243	7.7065	2.2683
AR [4]	0.17655	0.99741	0.0054394	0.99858	0.026378	0.3439
	[±%]	[±%]	[±%]	[±%]	[±%]	[±%]
e_a^{21}	0.63917	0.25927	1.4271	0.14237	0.46336	2.5419
e_{ext}^{21}	0.46793	0.082688	0.1138	0.20564	0.089063	3.7049
GCI_{coarse}^{21}	3.3148	1.0257	4.6224	1.0428	1.657	18.343
GCI_{fine}^{21}	1.3972	0.24786	0.34103	0.61565	0.26695	10.718

[1] For all cases: Simulated $\dot{m} = 177.245 kg/s$, $Q = 639.361 m^3/h$, for full pump flow apply Note 5.
[2] For all cases: $N_1 = 43782620$, $N_2 = 21509931$, $N_3 = 10821486$.
[3] For all cases: $r_{21} = 1.2673$, $r_{32} = 1.2573$, $F_s = 3$.
[4] See Note 4, Table 8-1.
[5] See Note 5, Table 8-1.

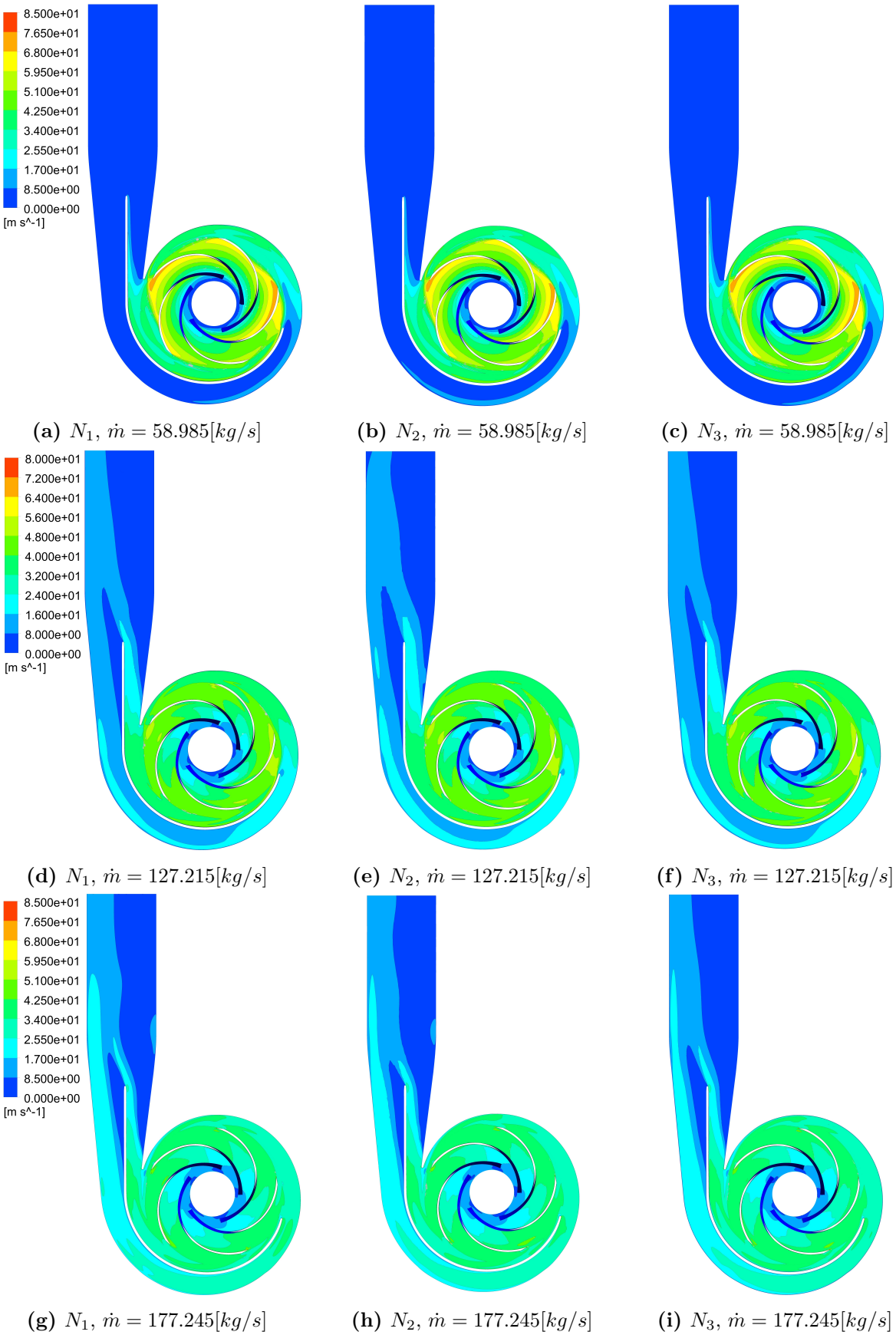


(a) N_1, $\dot{m} = 58.985[kg/s]$ **(b)** N_2, $\dot{m} = 58.985[kg/s]$ **(c)** N_3, $\dot{m} = 58.985[kg/s]$

(d) N_1, $\dot{m} = 127.215[kg/s]$ **(e)** N_2, $\dot{m} = 127.215[kg/s]$ **(f)** N_3, $\dot{m} = 127.215[kg/s]$

(g) N_1, $\dot{m} = 177.245[kg/s]$ **(h)** N_2, $\dot{m} = 177.245[kg/s]$ **(i)** N_3, $\dot{m} = 177.245[kg/s]$

Figure 8-1. Total pressure in stationary frame as measured on mid-plane of flow field.



(a) N_1, $\dot{m} = 58.985[kg/s]$ **(b)** N_2, $\dot{m} = 58.985[kg/s]$ **(c)** N_3, $\dot{m} = 58.985[kg/s]$

(d) N_1, $\dot{m} = 127.215[kg/s]$ **(e)** N_2, $\dot{m} = 127.215[kg/s]$ **(f)** N_3, $\dot{m} = 127.215[kg/s]$

(g) N_1, $\dot{m} = 177.245[kg/s]$ **(h)** N_2, $\dot{m} = 177.245[kg/s]$ **(i)** N_3, $\dot{m} = 177.245[kg/s]$

Figure 8-2. Velocity in stationary frame as measured on mid-plane of flow field.

8.1. Chapter summary

A detailed study of the grid independence and discretization error estimate was completed in this chapter. It was demonstrated after the procedure to determine the GCI had been completed, that the solution generated by the fine grid setup was well converged and was approaching the solution obtained by Richardson Extrapolation for all measured cases.

The next chapter will describe the completed validation actions.

9. Validation of the baseline geometry

9.1. Pump performance test for the baseline case

Table 9-1. Test 1 systematic (instrumental) uncertainty evaluation

Instrument description	Instrument number	ISO 9906 Table C.1 [1] [Month]	Previous calibr. [2] [Month]	ISO 9906 Table 5[3] [%]	e_S, $k = 2$ norm [4] [%]
Watt meter	24967	12	4	±1.0	±0.1
Watt meter	24968	12	4	±1.0	±0.1
Tachometer	E.E.44	36	4	±0.35	±0.001
Pressure Transmitter	EJX530A	4	4	±1.0	±1.0
Pressure Transmitter	EJX430A	4	4	±1.0	±0.6
Flow meter	G7321	12	12	±1.5	±0.2

[1] EN-ISO-9906 (2012), Table C.1: Instrument calibration intervals, indicated in months.
[2] The amount of months since the previous calibration and certification was completed.
[3] EN-ISO-9906 (2012), Table 5: Permissible relative values of the instrumental uncertainty, e_S. The limits correspond to the Grade 1 (most stringent) certification level.
[4] The reported instrumental uncertainty, e_S, based on a standard uncertainty multiplied by a coverage factor of $k = 2$, which unless specifically stated otherwise, provides a confidence level of 95%.

A baseline experiment was completed in order to determine the pump performance prior to implementing the proposed modifications. The test was completed as per the detailed explanation in par. 6.1. The experiment was certified to be compliant with 2012 Grade 1.

Table 9-1 shows the uncertainty related to the instrumentation that were utilised during the test. Note that the recommended EN-ISO-9906 (2012) calibration periods for the mentioned instruments had been achieved in full. The uncertainties and tolerances related to the test were assumed to be the maximum allowable values allowed by EN-ISO-9906 (2012) in order to fulfill the requirements of the Grade 1 performance test.

The experimental results are shown in tables 9-2 and 9-3. The measured values are plotted in fig. 9-1, on the solid black curves. The test points are additionally marked with solid black bi-lateral error bars. Due to the fact that design points are not specified, the selected points of comparison were selected after the experiment was completed; the blue shaded zones represent the bi-lateral uncertainty, the green shaded areas depict the Grade 1B bi-lateral tolerance range, the orange areas show the Grade 2B bi-lateral error tolerance and the red areas illustrate the Grade 3B bi-lateral error tolerance ranges. The stated range limits are discussed in detail in par. 6.1. In order for the pump to be certified to be compliant within a certain accuracy grade, the curve connecting the test points need to dissect at least one of the bi-lateral error tolerance bars.

The CFD results and uncertainty error bars are also plotted on fig. 9-1 in the shape of bold

Table 9-2. Results of baseline experiment.

	ΔH			P			η		
Q $[m^3/h]$	Test $[m]$	ϕ_{2c} $[m]$	Δ [%]	Test $[kW]$	ϕ_{2c} $[kW]$	Δ [%]	Test [%]	ϕ_{2c} [%]	Δ [%]
0	317.35	-	-	506.65	-	-	-	-	-
215.496	318.53	326.09	2.32	574.47	566.95	-1.33	32.42	33.91	4.39
288	-	320.37	-	-	607.61	-	-	41.44	-
360	-	314.83	-	-	633.48	-	-	48.88	-
424.692	314.11	311.41	-0.87	683.84	671.25	-1.87	52.93	53.51	1.08
504	-	313.50	-	-	715.10	-	-	60.66	-
504	-	325.52	-	-	741.13	-	-	60.22	-
576	-	315.86	-	-	743.04	-	-	66.53	-
576	-	320.02	-	-	767.03	-	-	65.4	-
648	-	311.17	-	-	778.91	-	-	70.49	-
685.08	299.32	308.24	2.89	817.22	800.16	-2.13	68.08	71.95	5.38
720	-	305.19	-	-	821.06	-	-	72.93	-
792	-	300.85	-	-	851.78	-	-	76.37	-
864	-	294.11	-	-	887.91	-	-	77.92	-
915.912	273.34	288.62	5.29	946.19	914.54	-3.46	71.8	78.64	8.70
915.912	273.34	292.88	6.67	946.19	933.94	-1.42	71.8	78.15	9.068
1008	-	277.70	-	-	956.28	-	-	79.37	-
1080	-	268.19	-	-	986.49	-	-	79.83	-
1158.696	238.19	259.62	8.26	1036.37	1013.30	-2.28	72.26	80.20	9.90
1158.696	238.19	264.46	9.93	1036.37	1032.88	-0.34	72.26	79.320	9.089
1224	-	249.34	-	-	1037.36	-	-	79.94	-
1276.2	217.69	240.82	9.61	1069.92	1051.16	-1.78	70.45	79.50	11.38

[1] The teal entries indicate CFD results obtained by rotating the impeller mesh by 26°.
[2] $\Delta = 100(\text{Test}/\phi_{2c})$
[3] Q indicates the full pump flow rate in order to easily compare the test and CFD results.
[4] P = Motor Shaft Power. The total motor input power is measured and compensated for by the supplied motor overall efficiency.

black vertical error bars and a red point where the value is programmed to be as per the testing done in par. 8. The simulation points are connected via the dashed curves, calculated by using a B-spline interpolation technique. A shaded area is also shown, indicating the range obtained when rotating the impeller mesh by 26°.

As can be observed, the experiment and the CFD results match within industry acceptable standards for actual pump testing of new designs and comparison between two similar physical pumps. The results of the CFD analysis are thus deemed to be validated after complying with the accuracy requirements of EN-ISO-9906 (2012) for performance certification to a set standard.

Overall validation of the CFD results could be motivated after the successful completion of the experiment.

Table 9-3. Results of baseline $NPSHR_{3\%}$ experiment

	$NPSHR_{3\%}$		
Q $[m^3/h]$	Test $[m]$	ϕ_{2c} $[m]$	Δ [%]
216.14	-	3.40	-
269.10	5.07	3.49	-45.27
425.97	-	3.70	-
668.00	6.13	6.91	11.29
687.14	-	9.20	-
918.67	-	9.54	-
935.50	7.70	10.93	29.55
1282.40	9.83	19.79	50.33

[1] The coral colored entries indicate interpolated values using a best fit exponential regression line.

9.2. Comment on vibration measurement

Fig. 6-1b illustrates the setup of the pump in the test bay. As noted in par. 6.1, the piping arrangement is not ideal as there exists long unsupported pipe lengths with multi-plane bends. The available piping in the test center can only accommodate this layout due to the pump configuration (vertical inlet and outlet nozzles). Due to this limitation, the setup is prone to flow excited piping vibration - as observed during the pump test. Sub-synchronous vibration signatures were measured across a range of operating flow rates.

In addition to the piping layout limitations, dedicated/custom mounting pedestals were not available for the test pump and a makeshift mounting frame was assembled to enable the pump to be mounted for the test run. The anchor bolts were not secured as per OEM standard and the mounting pedestal was not stiff. A more pronounced vibration characteristic was observed due to resonance and soft foot related defects during the run.

Due to the noted deficiencies in the physical setup of the pump on the test bench, and the absence of displacement vibration probes (only acceleration based monitoring from external surfaces), the vibration data was not included in the analysis as the vibration frequencies of interest were contaminated by external factors.

9.3. Mean-line method for qualitative trend observation

The analytic calculation of the total differential head produced exclusively by the impeller (presented and treated extensively in Annex. F), including losses and leakage flow, (as per Annex. A) can be implemented in order to qualitatively evaluate the general trajectory of the CFD solution and to represent some impeller characteristics accurately within reasonable limits (close to BEP for example) - even though the model does not take three dimensional fluid structures into account. The intent of this method is not to validate the full 3D CFD simulation using a 1D calculation algorithm.

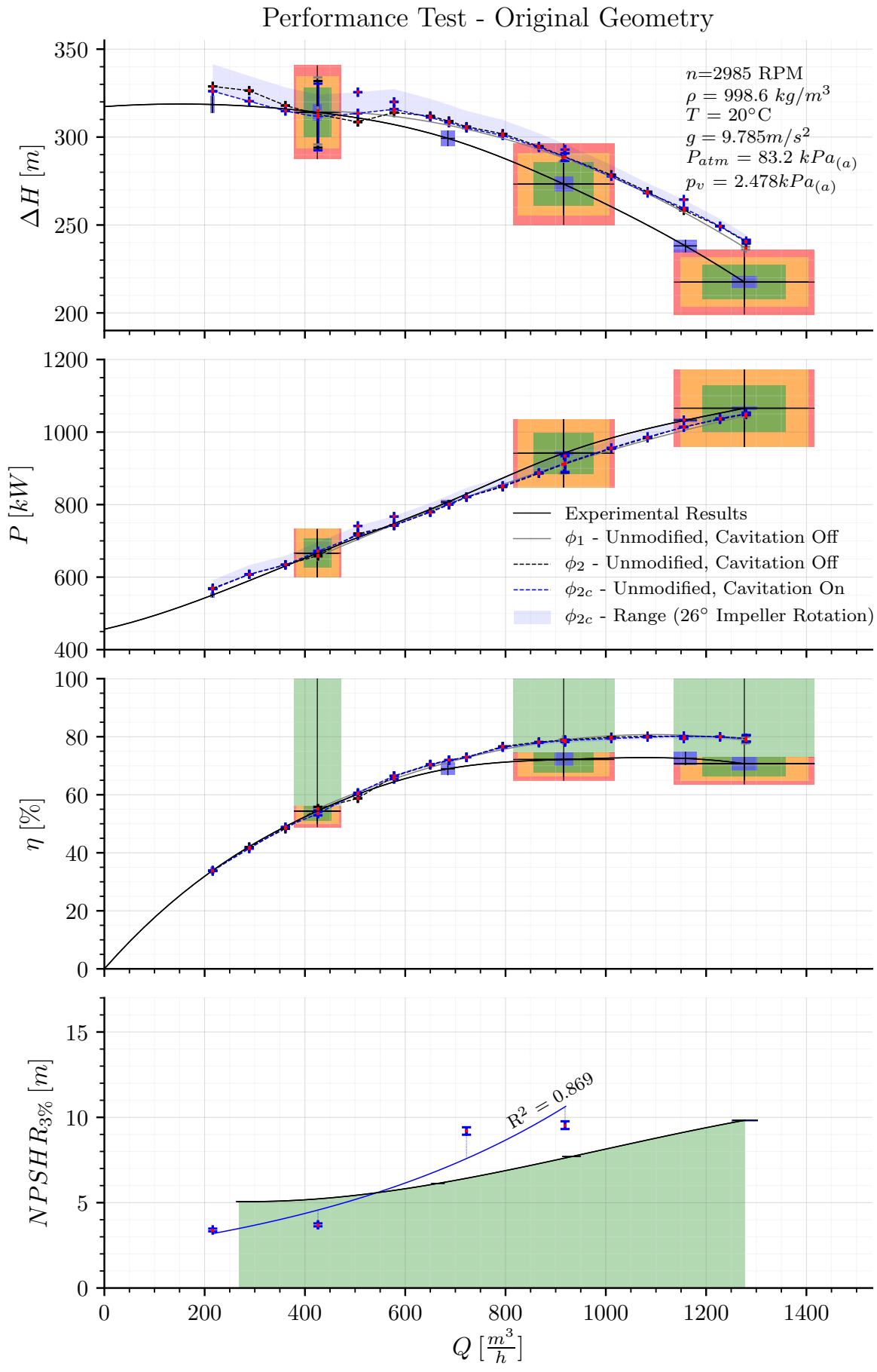


Figure 9-1. Test 1; Performance test with original geometry, tolerance ranges as per ISO 9906

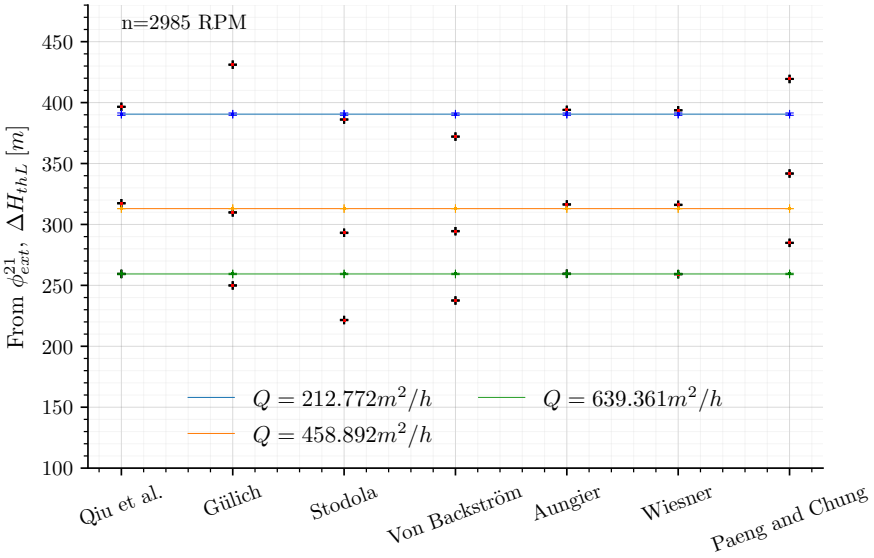


Figure 9-2. Analytic calculation points at various flow rates and slip models at fine grid conditions

Table 9-4. Mean-line calculation as per the rigorous method of par. F.1 for the unmodified geometry

	$Q = 212.772[m^3/h]$ $Q_{sp} = 20.595[m^3/h]$ $Q_{La} = 233.367[m^3/h]$			$Q = 458.892[m^3/h]$ $Q_{sp} = 18.431[m^3/h]$ $Q_{La} = 477.323[m^3/h]$			$Q = 639.361[m^3/h]$ $Q_{sp} = 16.478[m^3/h]$ $Q_{La} = 655.839[m^3/h]$		
Data[1]	ΔH_{thL} [m]	e_c [±%]	Δ [%]	ΔH_{thL} [m]	e_c [2] [±%]	Δ [%]	ΔH_{thL} [m]	e_c [±%]	Δ [3] [%]
ϕ^{21}_{ext}	390.53	-	-	312.98	-	-	259.35	-	-
Qiu et al.	396.539	$5.45 \cdot 10^{-5}$	1.54	317.393	0.047	1.41	259.386	0.040	0.01
Gülich	431.110	$7.69 \cdot 10^{-5}$	10.39	309.864	0.058	-1.00	249.927	0.042	-3.63
Stodola	386.114	$6.75 \cdot 10^{-5}$	-1.13	293.147	0.067	-6.34	221.546	0.067	-14.58
von Backström	372.084	$6.49 \cdot 10^{-5}$	-4.72	294.465	0.055	-5.92	237.576	0.046	-8.40
Aungier	394.025	$5.47 \cdot 10^{-5}$	0.89	316.406	0.047	1.09	259.517	0.040	0.06
Wiesner	393.701	$5.48 \cdot 10^{-5}$	0.81	316.082	0.047	0.99	259.193	0.040	-0.06
Paeng and Chung	419.393	$4.41 \cdot 10^{-5}$	7.39	341.774	0.039	9.20	284.885	0.033	9.85

[1] As per the rigorous analytical method, see par. F.1. The slip factor model used in the execution of the method is shown as row name. The fine grid solution of the CFD model, ϕ^{21}_{ext} is the reference value.
[2] The calculation uncertainty, e_c, is derived from the uncertainty of the wear ring leakage flow rate, as determined in the CFD analysis and its subsequent grid refinement study.
[3] Δ represents the difference between the analytic and CFD generated results, neglecting the uncertainties.
[4] All flow rates are per single impeller eye. The BEP is taken at $Q = 575[m^3/h]$.

The accuracy of the analytic method (as explained in F.1) has been proven in table 9-4, after applying Richardson Extrapolation to determine the most accurate ΔH_{thL} and $\dot{m}_{sp}$ values. The uncertainty values of the analytic solution is based on the uncertainty of the $\dot{m}_{sp}$ for which the uncertainty is e^{21}_{ext} for the Richardson Extrapolation, as per tables 8-1,8-2 and 8-3.

9.4. Chapter summary

The validation study included the comparison of the entire CFD flow field's results to an EN-ISO-9906 (2012) certified performance test. The results were satisfactory as all considered calculation points satisfy an EN-ISO-9906 (2012) standard and is illustrated in the produced performance curve, fig. 9-1.

A qualitative comparison between a first principle 1D algorithm and the full 3D impeller solution was completed by comparing the CFD results of the impeller differential head production vs volume flow rate to the results of the mentioned rigorous analytic technique. The resulting comparative results fall within close margins across a wide flow range.

The CFD model could be motivated to be adequately validated across a wide operating range of the pump (for the purposes of this study).

The next part will illustrate the evaluation of the modified geometry, while following the same procedures as highlighted in the presented baseline study.

Part III.

Evaluation of modified pump

10. Modification



(a) Ring modification, prior to installation. Direction of rotation: clockwise



(b) Ring modification installed in one of the suction eyes. Direction of rotation: clockwise

Figure 10-1. Ring modification physical implementation.

The proposed modification intended to enable the restriction of the mentioned back-flow condition has been conceptualised to be a modified bulkhead ring design. The profiled ring consists of a generously filleted inlet profile in combination with a series of designed perforations that are oriented in the direction of rotation at a specified drill angle. The ring will then be manufactured and installed in the eye of the impeller by means of a 0.05mm interference fit and secured by welding. The (implemented) physical concept is illustrated in fig. 10-1.

10.1. Perforated bulkhead ring design methodology

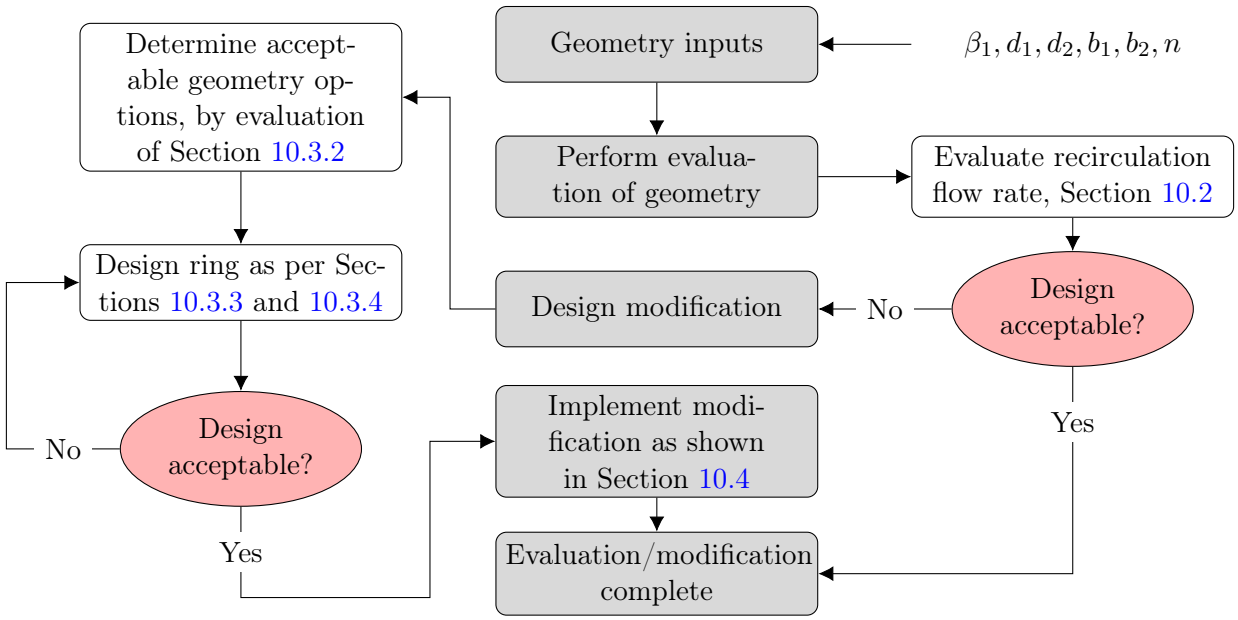


Figure 10-2. Modification design methodology

Figure 10-2 shows a schematic diagram that explains the design process; the grey blocks highlight the main design steps and the red blocks indicate a logic decision that the designer has to take in order to complete the design.

The optimum design of the device shown in 10-1 could be achieved by using a design exploration (design of experiment) methodology with CFD as the main development tool. Unfortunately, due to the nature of operational production facilities - rapidly changing availability of the pump (originally earmarked for testing purposes) concerned, coupled with budgetary restrictions at the time of development (influencing the timeline initially allocated for testing and preparation) - necessitated a rapid geometry generation and part fabrication effort.

The design of the perforation drill angle (β_{1rB}) was based on a trade-off between the idealised principles of velocity triangle theory and geometrical limitations. A variation in d_1 was conceptually evaluated by utilising the adapted (and potentially oversimplified) methodology of Fraser (1981*a*) and Gopalakrishnan (1988) as an initial screening tool, while implementing and adapting the inlet ring sizing methodologies proposed by Gülich (2019) within the boundaries of the physical geometry limitations of the impeller eye and ring.

10.2. Estimate of point of recirculation onset

Table 10-1. Impeller eye ID vs. Q_{La} at recirculation onset (estimate)

Location of recirculation	Q_{La}[1]	d_1 $211mm$	d_1 $204mm$	d_1 $190mm$	d_1 $170mm$
Suction	$[m^3/h]$	766.099	673.614	508.775	316.695
Discharge	$[m^3/h]$	873.518	873.518	873.518	873.518

[1] The flow rates mentioned in this column are equivalent to 100% of the total measured flow rate of the entire pump, 50% this value represents the flow through a single eye.
[2] The estimated points of recirculation onset (suction and discharge recirculation) was calculated using the methodology of Fraser (1981*b*) and Gopalakrishnan (1988), as explained in Annex. D.

As can be seen from table 10-1, according to the methods of Fraser (1981*b*) and Gopalakrishnan (1988): with the current geometry, discharge recirculation could possibly be initiated at a relatively high flow rate (compared to the measured and originally stated BEP). With the current d_1 of $211mm$, suction recirculation can be expected at a flow rate of $\leq 766.099m^3/h$ (total flow rate - 2 eyes); this is high for the application. With the variation of eye diameter it can be seen that the expected point of suction recirculation inception changes quite rapidly.

10.3. Exploration of potential geometric layouts

10.3.1. Design considerations

The methodology of design stated in fig. 10-2 was followed. The internal diameter of the perforated ring design was influenced by multiple factors. With reference to fig. 10-4, the following design constraints are in place:

1. The NPSHA of the test rig and the site installation would constrain the $NPSHR_{3\%}$ increase at the maximum (normal) operating flow rate.
2. It is to be noted that the normal operating range is well away from the BEP for the current geometry. The ring sizing should ensure that re-circulations are not expected across the stated operating range - the ring should thus be designed to operate reliably at the lower flow rate in the normal operating range.
3. An important consideration is to ensure that the drilled holes do not compromise the structural integrity of the ring, thus avoiding the penetration of the inner diameter (d_r) when drilling the holes, while maintaining a substantial ligament thickness between perforations, in order to provide some structural resilience/strength in the case of cavitating flow - this is to ensure that undue mechanical damage caused by potential cavitation does not prematurely consume the ring material and cause unbalance and flowing debris.
4. The ring should be rapidly manufactureable using standard methods and tooling, this ensures an economical design. The material should be weldable and corrosion resistant (to on site process).
5. The perforation drill angle should be designed to ensure a minimal incidence to the incoming flow in order to minimise the possibility of local flow separation and potentially cavitation - especially at the higher flow rates in the range.
6. The amount of perforations should be equal for all flow passages, in order to minimise asymmetry of the flow field.

10.3.2. Assessment of the range of possible ring geometric features

In order to determine the possible perforation layout, an algorithm was constructed (as per the methodology in par. D.3) which generates a range of plausible design iterations. The algorithm determines the maximum perforation drill radius (r_h) at a certain drill angle (β_{1rB}) corresponding to a selected d_r. The results of the method is depicted by fig. 10-3.

Fig. 10-3a depicts the relationship between β_{1rB}, d_r and the ratio A_{ratio}. The data shows that as d_r decrease, the ratio of the modified vs original eye flow area (A_{ratio}) tend to increase. Another relationship exists where A_{ratio} decreases as β_{1rB} decrease. A stepped tendency is exhibited (especially with smaller values of d_{1r}) - this is due to the abrupt changes of d_h and n_h as per the available drill sizes as per ASME-B94.11M (1993).

Fig. 10-3c illustrates that a definite point exists where the maximum allowable d_h starts to exhibit an accelerated reduction compared with a reduction in β_{1rB} for all d_r. The rapid reduction in d_h is attributed to the restriction in t_{ir} as the drill angle β_{1rB} increases.

The ratio of ring perforation throat flow area ($A_{h_{all}}$) versus the flow area reduction brought about by a solid bulkhead ring of d_r is shown in 10-3b. A_{flow2} tends to increase as d_r decrease, also it shows the same tendency with an increase of β_{1rB}. This tendency is logical as the total flow area increases with an increase of n_d and d_h.

As the drill angle is reduced and the available space for perforation addition reduce, a subsequent reduction of n_h is observed with a reduction in both β_{1rB} and d_r, as per fig. 10-3d.The rapid change in the amount of allowable perforations is attributed to the constraints detailed in D.3) and above.

The red dots in all graphs shown in 10-3 depict the selected ring design - this will be further elaborated on in later paragraphs.

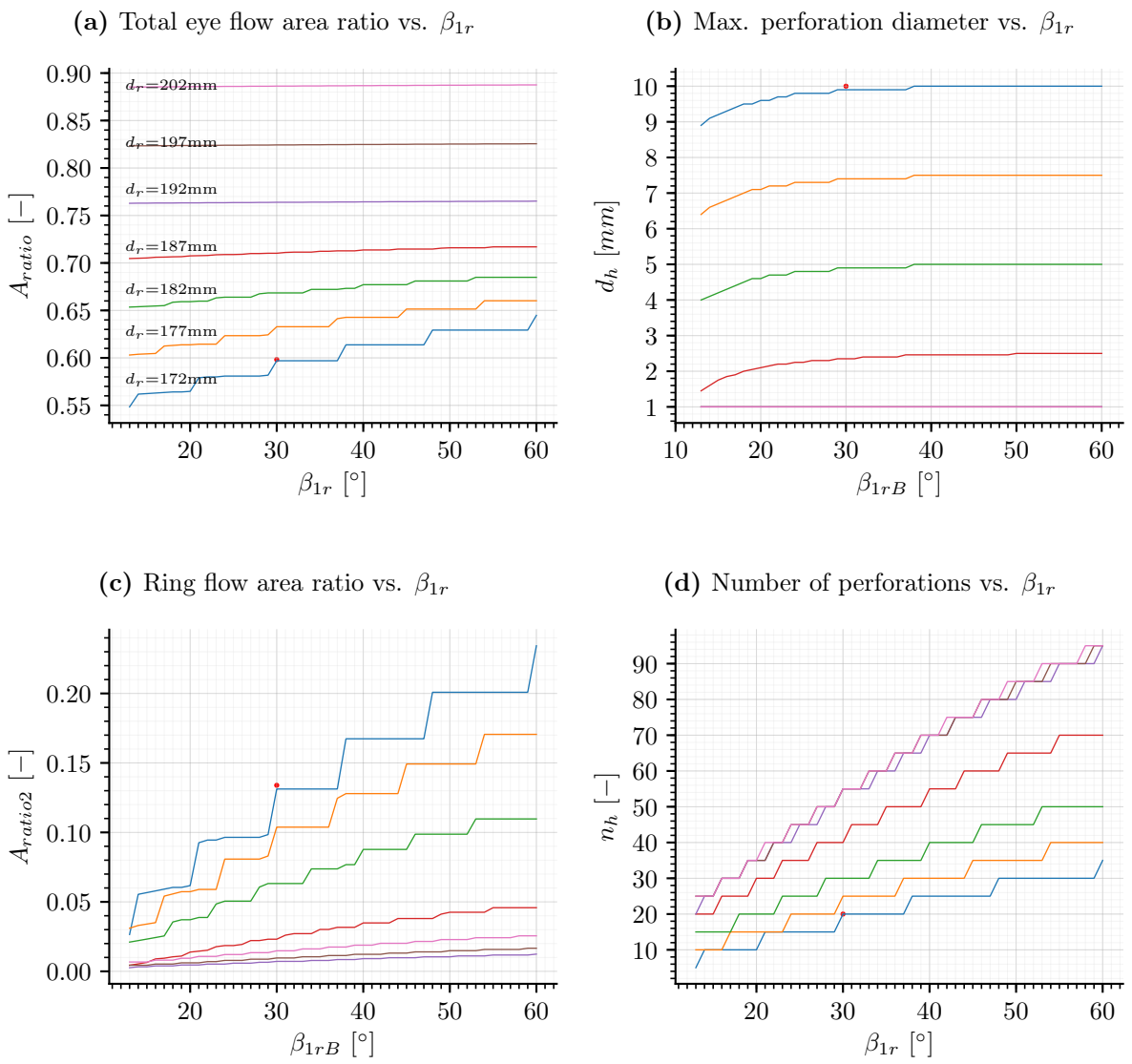


Figure 10-3. Comparison of various ring geometric attributes versus a varying β_{1r} and d_r

10.3.3. Ring internal diameter design

The iterative design methodology detailed in fig. 10-2 was implemented. With reference to fig. 10-4; the site NPSHA limit at the maximum expected site Q_{La} in conjunction with the test bench NPSHA limit at BEP was taken as the limiting design criteria. Incorporating the geometrical design possibilities discussed in 10.3 - with the intent to maximize A_{ratio} and A_{ratio2} without compromising the ring structural integrity - it was determined that the ring should be designed for a flow rate of $Q = 250m^3/h$ per eye and geometric attributes as per table 10-4.

A study which compares some performance characteristics related to the selected perforated ring geometry and a corresponding solid ring variant with the same d_r is shown in table 10-2 - a numerical representation of fig. 10-4. Note that the (projected) gain in NPSHR performance of the perforated ring could potentially aid in the application of the geometry with a reduced impact on the suction performance of the pump - most notably in the higher flow rate operating regimes.

Admittedly, the β_{1rB} angle could be made to be more acute, however as per fig. 10-3 the

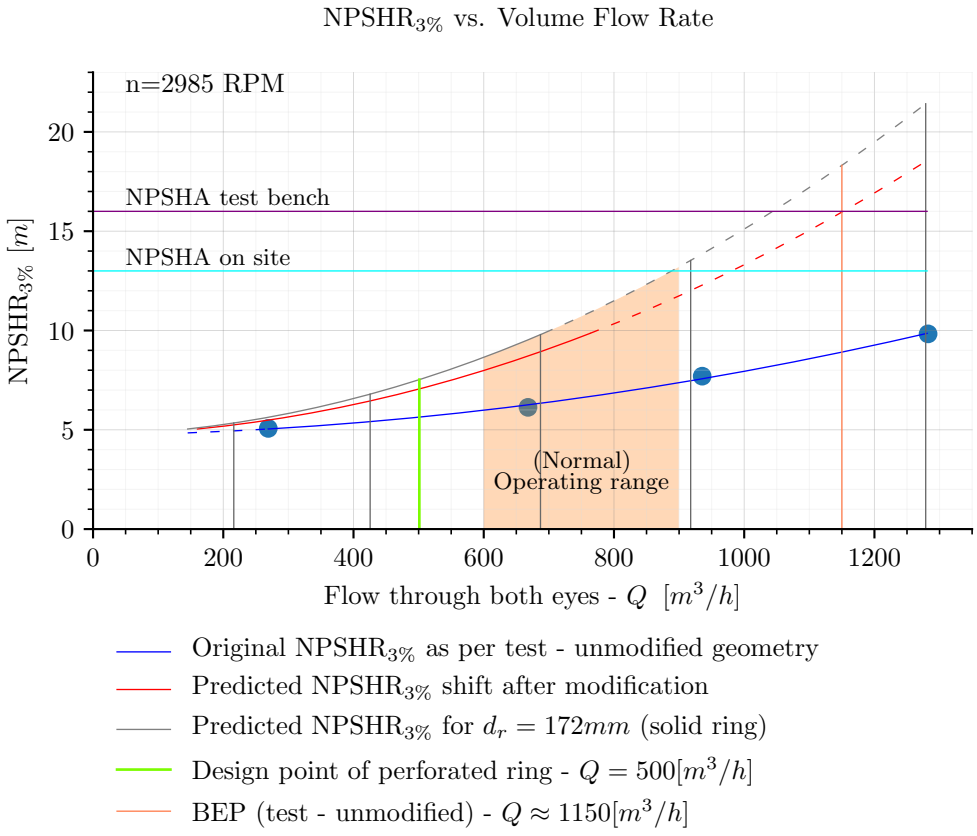


Figure 10-4. Calculation of the expected $NPSHR_{3\%}$ at various flow rates and values of d_R

Table 10-2. Calculated ring throat inside diameter study

Flow rate	Unit			Design	Normal operating flow range					BEP	
$Q^{[1]}$	$[m^3/h]$	216.14	425.54	500	600	685.08	687.14	900	917.78	1150	1278.72
$Q^{[2]}$	$[m^3/h]$	108.07	212.77	250	300	342.54	343.57	450	458.89	575	639.36
Analysis of expected $NPSHR_{3\%}$ at the specified flow rates/operating points, see fig. 10-4 [3]											
Blue[4]	$[m]$	4.95	5.41	5.63	5.98	6.33	6.34	7.37	7.47	8.91	9.84
Red[5]	$[m]$	5.24	6.45	7.05	7.99	8.91	8.93	11.74	12.01	15.96	18.52
Grey[6]	$[m]$	5.34	6.79	7.51	8.65	9.76	9.79	13.20	13.53	18.32	21.42
Analysis of expected deviation ratios at the specified flow rates/operating points [3]											
Grey/Red	$[-]$	1.02	1.05	1.07	1.08	1.10	1.10	1.12	1.13	1.15	1.16
Red/Blue	$[-]$	1.06	1.19	1.25	1.33	1.41	1.41	1.59	1.61	1.79	1.88
Grey/Blue	$[-]$	1.08	1.26	1.33	1.45	1.54	1.54	1.79	1.81	2.06	2.18

[1] The total measured flow through both impeller eyes.
[2] The total measured flow through a single impeller eye, in order to adapt the data to the CFD results.
[3] The ratio of between the different data sets vs the volume flow rates per column.
[4] The blue data set is the $NPSHR_{3\%}$ of the unmodified pump as per the test data
[5] The red data set is the projected $NPSHR_{3\%}$ for the modified pump - perforated ring with $d_R = 172mm$. This ring is considered to be geometrically similar to a plain bull-ring with $d_R = 177.72mm$ - as per the method proposed by Gülich (2019), as detailed in Annex. D
[6] The grey data set is the projected $NPSHR_{3\%}$ for a modified pump with a plain bull-ring with $d_R = 172mm$ - as per the method proposed by Gülich (2019), as detailed in Annex. D

implication of a reduced d_r, a reduction of perforations and/or the reduction of d_h indicate that any further pursuit of β_{1rB} reduction would likely be counter-productive for the current layout, promoting increased ring solidity and subsequently reduce the influence of the perforations to a noticeable degree. Fig. 10-3 shows a sharp decline in favourable geometric attributes after β_{1rB} is reduced past the 30° point, this attribute was subsequently deemed the geometric constraint for the current layout.

10.3.4. Calculation of required ring inlet drill angle

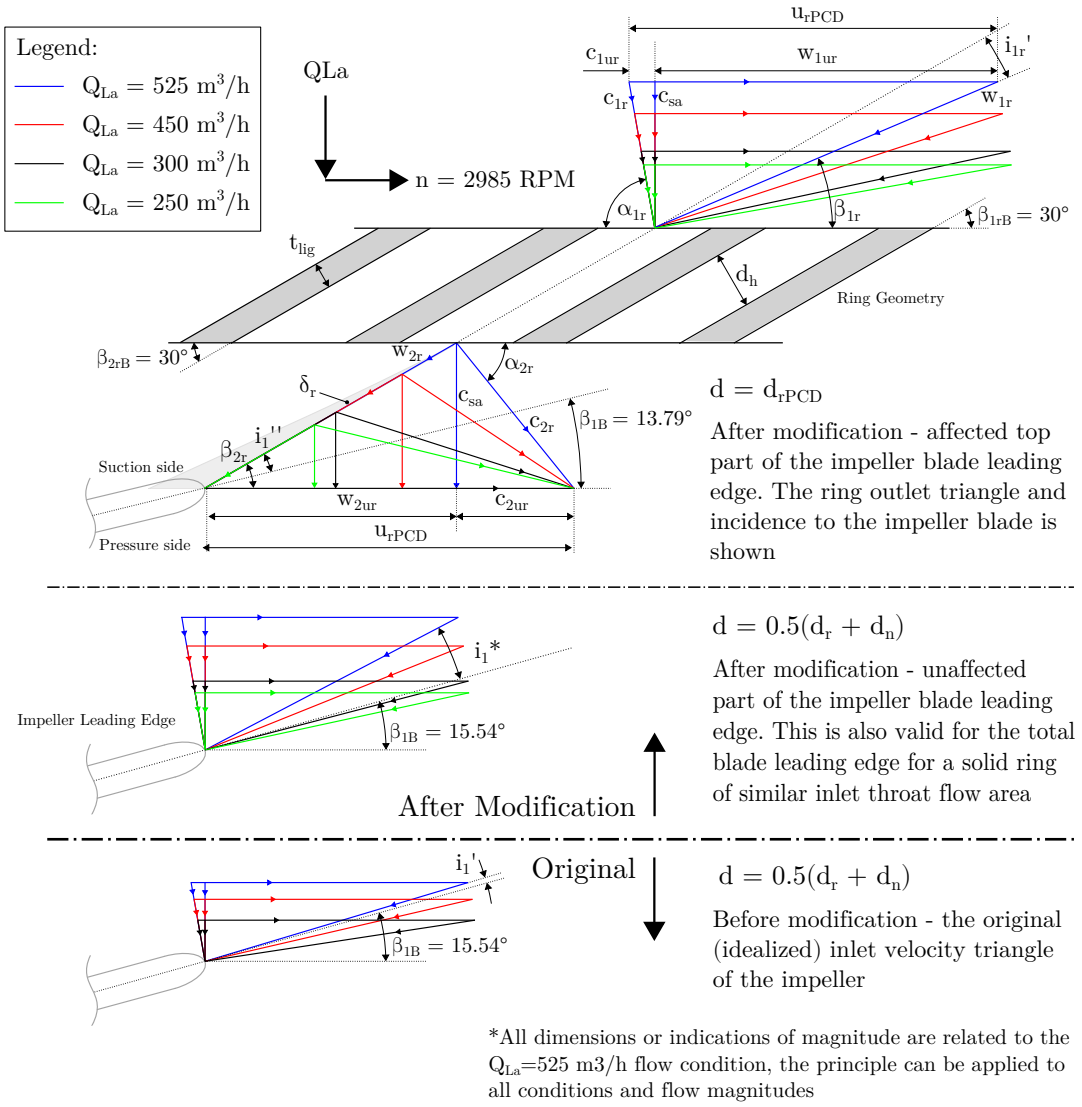


Figure 10-5. Calculation of the expected $NPSHR_{3\%}$ at various flow rates and values of d_R

Fig. 10-5 depicts the idealised inlet and outlet velocity triangle diagrams constructed for the proposed modification. The flow rates correspond to the design value ($250m^3/h$), the expected operating minimum ($300m^3/h$), maximum ($450m^3/h$) and BEP ($575m^3/h$) values of Q_{La}. Refer to Annex. D par. D.4 for detailed data and methodology relating to fig. 10-4.

The relative flow velocities - w_1 and w_{2r} - between the ring outlet and impeller vane leading edge could not be exactly tangentially aligned, resulting in a negative incidence of $i_{1r}'' = -16.21°$. Global alignment of the idealised perforation outlet relative- (w_{2r}) and absolute flow velocities (c_{2r}), to the bulk impeller inlet free stream flow - and specifically to the impeller inlet relative

Table 10-3. Summary of incidence angles of the various points of interest

			$d = d_{rPCD}$ $\beta_{1B} = 13.79°$		$d = 0.5(d_r + d_n)$ $\beta_{1B} = 15.54°$	
Q_{La}[2] $[m^3/h]$	$\dot{m}$[3] $[kg/s]$	α_1 [°]	i'_{1r} [°]	i''_1 [°]	i_1* [°]	i'_1 [°]
250	69.24	80	21.00	-16.21	3.33	8.33
250	69.24	90	21.24	-16.21	3.77	8.49
250	69.24	100	21.47	-16.21	4.17	8.64
300	83.08	80	19.18	-16.21	0.88	6.88
300	83.08	90	19.52	-16.21	1.5	7.1
300	83.08	100	19.85	-16.21	2.07	7.31
450	124.63	80	13.74	-16.21	-6.35	2.49
450	124.63	90	14.49	-16.21	-5.03	2.99
450	124.63	100	15.18	-16.21	-3.85	3.45
575	159.24	80	9.29	-16.21	-12.1	-1.13
575	159.24	90	10.48	-16.21	-10.07	-0.34
575	159.24	100	11.55	-16.21	-8.31	0.38

[1] These variable magnitudes are applicable to all considered cases as the impeller geometry remains constant.
[2] This value represents the flow through a single eye, for total pump: $2Q_{La}$
[3] Mass flow calculated at $\rho = 997kg/m^3$ - this corresponds to test conditions.

flow velocity (w_1) and impeller inlet flow angle β_1 - was not possible without outlet guide vanes.

Table 10-3 summarises the calculated incidences as shown and calculated in fig. 10-5. It can be observed that the ring inlet flow incidence, i'_{1r}, is large at low flows but decreases as the flow rate increases - the same trend is observable for all incidences measured, except for i''_1. The incidence i''_1 remains constant, however the effect of flow deviation, δ_2, was omitted - as per par. D.3.2.

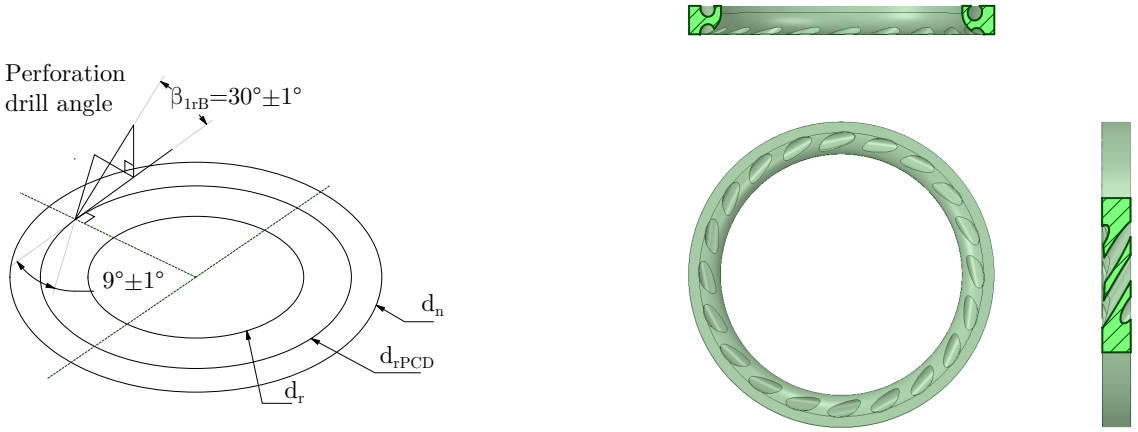
It seems apparent from table 10-3 that the ring element will reach on optimum flow rate at a value substantially higher than the original impeller BEP. Upon consideration of the inlet flow area throat restriction; the point of operation at optimum flow incidence of the impeller blades areas not directly affected by the ring is approximately $300m^3/h$. Thus, the optimal ring flow incidence was not achieved, however, if cavitation can be omitted - even with separated flow at the inlet there should exist a measurable amount of fluid flow through the ring at all flow rates.

Taking all the above-mentioned factors and calculations into account, the selected geometric layout of the perforated ring design as specified as per table 10-4.

Table 10-4. Selection of ring geometric features based on the results of the design algorithm

Variable	Unit	Value	Variable	Unit	Value	Variable	Unit	Value
n	$[RPM]$	2985	d_{rPCD}	$[mm]$	191.72	A_{or}	$[m^2]$	0.025343
d_1	$[mm]$	211.44	β_{1rB}	$[°]$	30	$A_{h_{all}}$	$[m^2]$	0.0015708
d_n	$[mm]$	111.53	n_h	$[-]$	20	A_{flow}	$[m^2]$	0.015036
d_r	$[mm]$	172	d_h	$[mm]$	10	A_{ratio}	$[-]$	0.59331

[1] These variable magnitudes are applicable to all considered cases as the impeller geometry remains constant.



(a) Ring modification, prior to installation. Direction of rotation: clockwise

(b) Ring modification installed in one of the suction eyes. Direction of rotation: clockwise

Figure 10-6. Ring modification physical implementation.

10.4. Implementation of modification

Figure 10-6 illustrates the final ring modification design. Rings situated in each of the impeller eye inlets will have inverted geometric features.

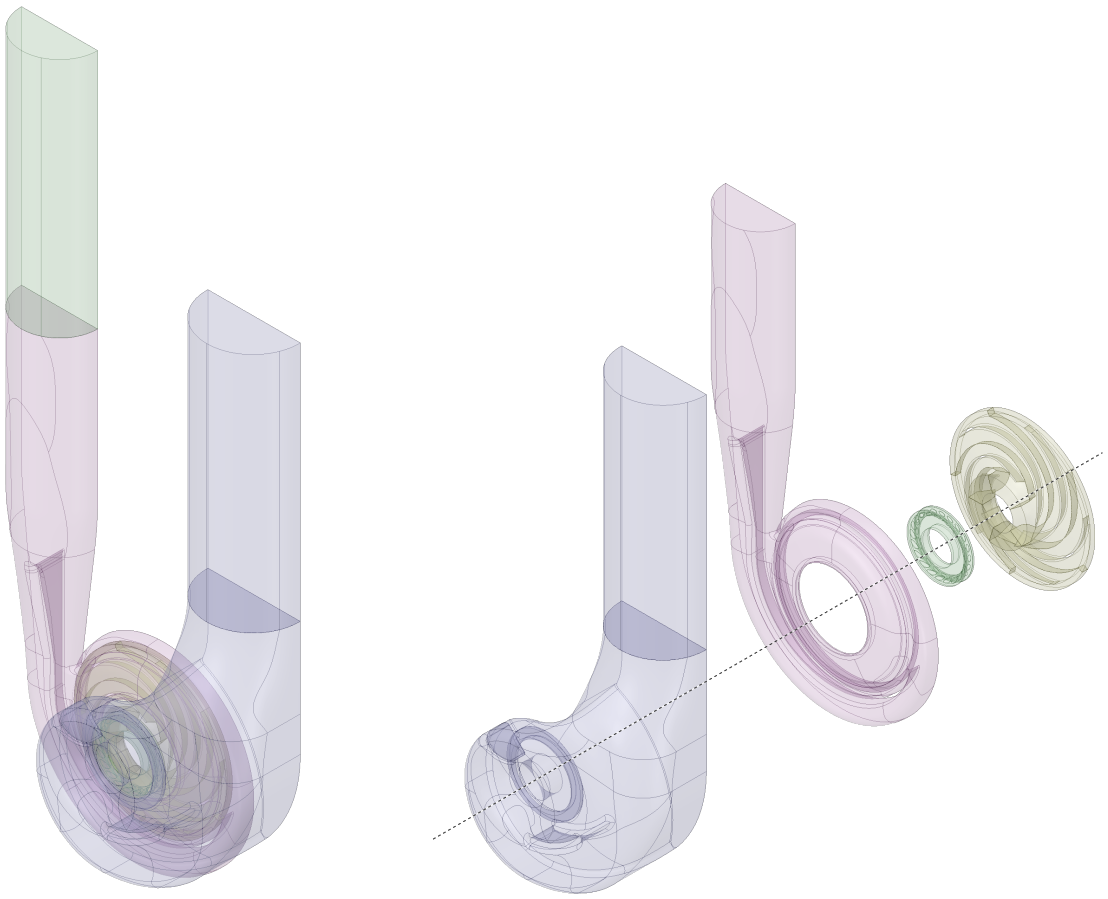
Figure 10-1a shows the final design of the modification after physical manufacture by means of milling from a SA-240 Type 304L austenitic stainless steel plate. This particular material of construction was selected in order to ensure weldability between the impeller casting and the ring and to mitigate material cost, as this particular grade of stainless steel is readily available. The installation of the ring into the eye of the test pump is also shown in fig. 10-1b.

10.5. Chapter summary

The design of the proposed impeller inlet eye modification was discussed. Due to geometric constraints, the resulting β_{1rB} angle results in greater than optimal bulk flow incidence, across all flow rates. Sub-optimal efficiency operation can be expected from the current conceptual design, however the design should still be effective at flow rates with adequate $NPSH_{3\%}$. The manufacture and installation of the physical ring was also briefly discussed. The next chapter discussed and describes the impact of the modification on the model setup and mesh.

11. Setup of the modified pump

11.1. New model assembly



(a) Assembly of complete flow field. Transparency is activated in order to see components.

(b) Exploded isometric view of the modified mesh arrangement. The discharge volute's extension (green portion in Figure 11-1a) is omitted in favour of favourable image layout. The z axis (dashed line) is the axis of impeller rotation. The back-flow restricting device is shown in green.

Figure 11-1. Isometric view of the flow field with location of boundary conditions indicated.

The implementation of the ring modification on the 3D solid pump model is minimal, by design, In order to incorporate the change the impeller inlet area was trimmed and a small area at the inlet volute connection to the impeller was recessed. The ring geometry was the fitted to the area that was made available through the 3D model modification.

In order to ensure that the physics of the problem are adequately represented, the setup is kept identical to the original pump model, as described by par.7.1. The connection of the ring to the original parts is achieved by using GGI interfaces at all connection points. The ring domain is also specified to be rotating, at the same velocity as the impeller. See 11-2 for a section of

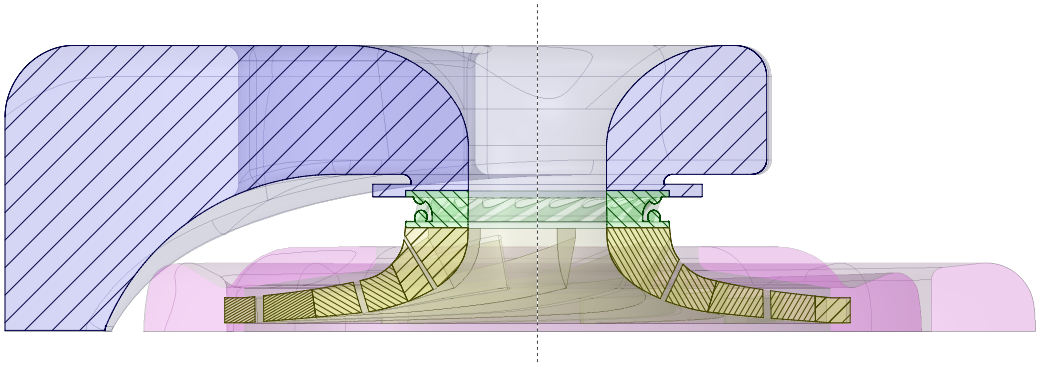
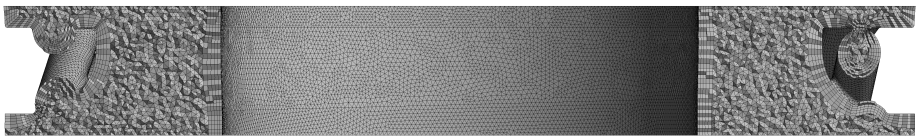


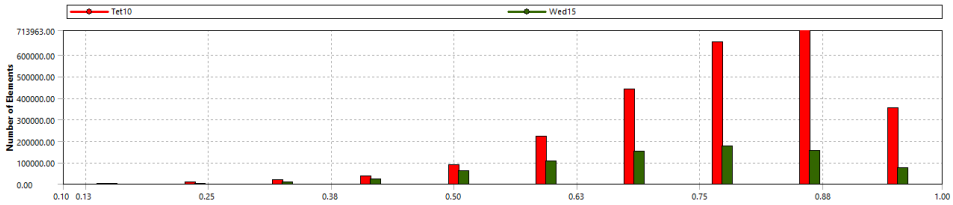
Figure 11-2. Cross section of the modified flow field in the $z - x$ plane. The green part is the back-flow restricting device.

domains.

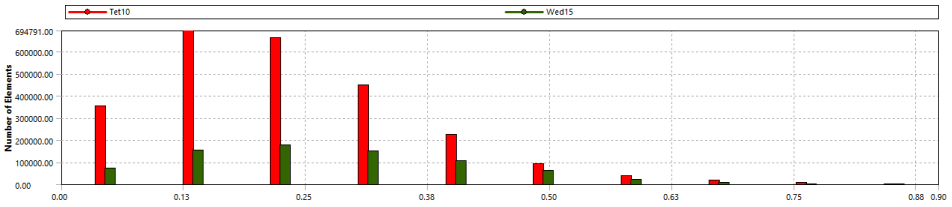
11.2. Mesh



(a) The mesh as constructed for the ring modification



(b) Orthogonality property analysis graph for the ring modification mesh



(c) Skewness property analysis graph for the ring modification mesh

Figure 11-3. Ring modification fine grid representation.

As discussed in par. 11.1, an additional 3D part/mesh has to be incorporated into the final mesh assembly. All parameters of the other meshes are kept constant, but the ring's mesh was once again considered for the mesh independence study. The mesh metrics can be seen in the tables contained in this chapter.

As described in figs. 11-3a, 11-3c and the analysis in table 11-1; it is evident that the meshes are of good quality and can be used with confidence.

Table 11-1. Breakdown of the different elements that the meshes consist of for the current case

Domain	Nodes	Elements	Tetrahedra	Wedges	Pyramids	Hexahedra
Ring	862952	3273927	2530582	743345	0	0
Impeller	12147770	11860530	0	0	0	11860530
Volute Discharge	8646196	22373265	8489819	13881356	2090	0
Volute Suction	4887411	12301058	4258258	8042800	0	0
All Domains	26544329	49808780	15278659	22667501	2090	11860530

11.3. Chapter summary

The modification of the mesh and the 3D setup was also discussed and the modifications described and presented. The mesh and the setup had not been fundamentally changed when compared to the original setup, thus the complete mesh and setup was not discussed again. The mesh quality of the ring geometry was shown to be of high quality and is acceptable for the simulation to be accurate. The next chapter discusses the CFD results relating to the modified geometry and the verification thereof.

12. Verification of the modified pump case

Table 12-1. Grid convergence study of the modified mesh at $\dot{m} = 58.985kg/s$

Variable	η	ΔH_{stat}	ΔH_{tot}	ΔH_{thL}	P [1]	$\dot{m}_{sp}$ [1]
	$[\%]$	$[m]$	$[m]$	$[m]$	$[kW]$	$[kg/s]$
ϕ_1	54.865	304.81	304.98	375.66	321.540	5.802
ϕ_2	53.912	307.47	307.73	376.28	331.150	6.0397
ϕ_3	52.816	309.8	310.27	396.76	344.450	6.21
ϕ_{ext}^{21}	55.246	302.82	303.18	375.66	318.910	5.4852
	$[-]$	$[-]$	$[-]$	$[-]$	$[-]$	$[-]$
p	5.0860	3.4453	3.7602	29.905	6.2364	2.271
AR [4]	1.0177	0.99135	0.99106	0.99835	0.97098	0.96064
	$[\pm\%]$	$[\pm\%]$	$[\pm\%]$	$[\pm\%]$	$[\pm\%]$	$[\pm\%]$
e_a^{21}	1.737	0.87267	0.9017	0.16504	2.9887	4.0969
e_{ext}^{21}	0.68915	0.6566	0.59421	0.0001039	0.82525	5.7758
GCI_{coarse}^{21}	7.2928	4.575	4.4772	0.49544	11.422	28.672
GCI_{fine}^{21}	2.0818	1.957	1.7721	0.0003117	2.4555	16.381

[1] For all cases: Simulated $\dot{m} = 58.985kg/s$, $Q = 212.772m^3/h$, for full pump flow apply Note 5.
[2] For all cases: $N_1 = 49808780$, $N_2 = 23777244$, $N_3 = 16692124$.
[3] For all cases: $r_{21} = 1.2795$, $r_{32} = 1.1252$, $F_s = 3$.
[4] Asymptotic range achieved if $AR \approx 1$
[5] Multiply the indicated column values of $\phi_1, \phi_2, \phi_3, \phi_{ext}^{21}$ and the total $\dot{m}, Q$ by 2. All other values will remain unchanged as the proportional change will not affect the calculation method.

Similar to par. 8, a three grid mesh independence study was completed as per the method outlined in the Journal of Fluids Engineering Editorial Policy Statement on the Control of Numerical Accuracy, as per Freitas (1993) and subsequently by the referenced work by Celik et al. (2008) which is based on the ground breaking work by Roache (2009). Richardson extrapolation of the three grid solution was also completed for all cases in order to approximate the exact solution for the considered value ϕ.

Tables 12-1, 12-2 and 12-3 highlight the results of the study. It is noteworthy to state that all cases have exhibited good grid independence and the resulting GCI_{fine} has resulted in narrow error bars (Roache, 2003) used in other graphs. The values of p_o have in some cases been far away from 1, however it can be argued that two of the three grids produce similar results for the measured quantity to motivate that the asymptotic region have already been reached.

Figures 12-1 and 12-2 depict contour plots of the total pressure and velocity in the stationary frame for all operating cases across all grids. Satisfactory solution stability is observed. All RMS residuals converged to less than 4 orders of magnitude. For an example convergence case see Annexure H.

Table 12-2. Grid convergence study of the modified mesh at $\dot{m} = 127.215kg/s$

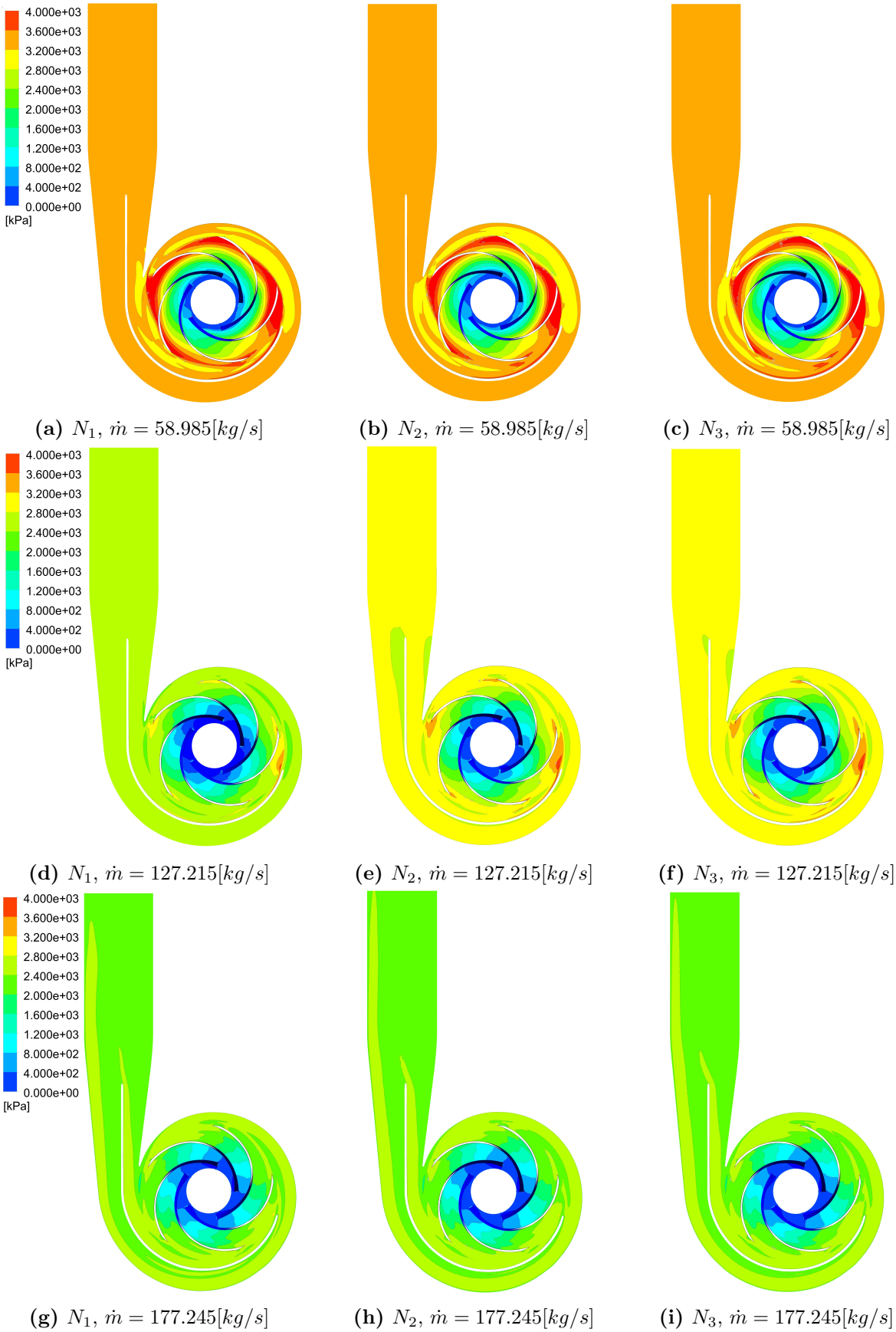
Variable	η	ΔH_{stat}	ΔH_{tot}	ΔH_{thL}	P [1]	$\dot{m}_{sp}$ [1]
	[%]	[m]	[m]	[m]	[kW]	[kg/s]
ϕ_1	77.738	285.1	285.87	311.7	460.37	5.2588
ϕ_2	78.354	283.23	284.94	311.57	453.68	5.235
ϕ_3	79.583	282.09	285.13	311.48	447.98	5.2217
ϕ_{ext}^{21}	77.654	289.84	286.29	311.89	465.74	5.3596
	[−]	[−]	[−]	[−]	[−]	[−]
p	8.5941	1.3493	4.7176	2.0738	3.2817	0.8602
AR [4]	0.99214	1.0066	0.1893	1.0004	1.0147	1.0045
	[±%]	[±%]	[±%]	[±%]	[±%]	[±%]
e_a^{21}	0.79241	0.65591	0.32532	0.041707	1.4532	0.45257
e_{ext}^{21}	0.10841	1.6352	0.14772	0.062469	1.1534	1.8802
GCI_{coarse}^{21}	2.7021	6.9548	1.4198	0.31264	7.86	7.1063
GCI_{fine}^{21}	0.32487	4.9871	0.44382	0.18752	3.5005	5.7486

[1] For all cases: Simulated $\dot{m} = 127.215kg/s$, $Q = 458.9m^3/h$, for full pump flow apply Note 5.
[2] For all cases: $N_1 = 49808780$, $N_2 = 23777244$, $N_3 = 16692124$.
[3] For all cases: $r_{21} = 1.2795$, $r_{32} = 1.1252$, $F_s = 3$.
[4] See Note 4, Table 12-1.
[5] See Note 5, Table 12-1.

Table 12-3. Grid convergence study of the modified mesh at $\dot{m} = 177.245kg/s$

Variable	η	ΔH_{stat}	ΔH_{tot}	ΔH_{thL}	P [1]	$\dot{m}_{sp}$ [1]
	[%]	[m]	[m]	[m]	[kW]	[kg/s]
ϕ_1	78.156	233.58	235.44	259.21	523.62	4.7151
ϕ_2	78.192	230.47	233.96	258.81	520.13	4.705
ϕ_3	78.998	230.26	233.73	258.46	515.7	4.682
ϕ_{ext}^{21}	78.156	234.48	236.5	259.51	524.76	4.7162
	[−]	[−]	[−]	[−]	[−]	[−]
p	26.719	6.0741	3.5404	3.4389	5.6956	9.475
AR [4]	0.99954	0.050743	0.17569	1.0015	1.0067	1.0021
	[±%]	[±%]	[±%]	[±%]	[±%]	[±%]
e_a^{21}	0.046062	1.3314	0.62861	0.15432	0.66651	0.21421
e_{ext}^{21}	6.3645e-05	0.38233	0.44915	0.11553	0.21656	0.022943
GCI_{coarse}^{21}	0.13838	5.1457	3.2394	0.80994	2.6506	0.71146
GCI_{fine}^{21}	0.00019094	1.1514	1.3535	0.347	0.65109	0.068845

[1] For all cases: Simulated $\dot{m} = 177.245kg/s$, $Q = 639.361m^3/h$, for full pump flow apply Note 5.
[2] For all cases: $N_1 = 49808780$, $N_2 = 23777244$, $N_3 = 16692124$.
[3] For all cases: $r_{21} = 1.2795$, $r_{32} = 1.1252$, $F_s = 3$.
[4] See Note 4, Table 12-1.
[5] See Note 5, Table 12-1.

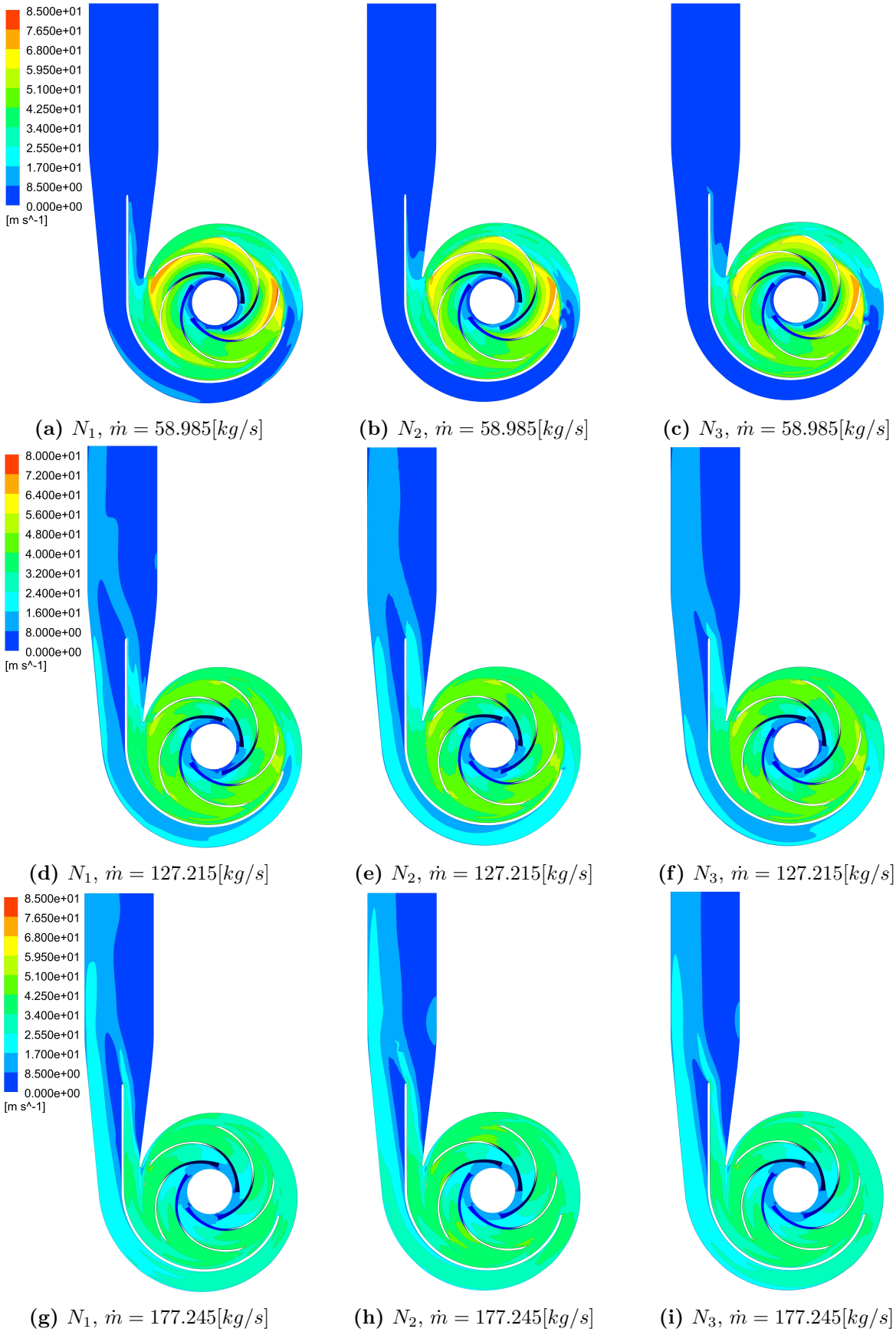


(a) N_1, $\dot{m} = 58.985[kg/s]$ **(b)** N_2, $\dot{m} = 58.985[kg/s]$ **(c)** N_3, $\dot{m} = 58.985[kg/s]$

(d) N_1, $\dot{m} = 127.215[kg/s]$ **(e)** N_2, $\dot{m} = 127.215[kg/s]$ **(f)** N_3, $\dot{m} = 127.215[kg/s]$

(g) N_1, $\dot{m} = 177.245[kg/s]$ **(h)** N_2, $\dot{m} = 177.245[kg/s]$ **(i)** N_3, $\dot{m} = 177.245[kg/s]$

Figure 12-1. Total pressure in stationary frame as measured on mid-plane of flow field.



(a) N_1, $\dot{m} = 58.985[kg/s]$ **(b)** N_2, $\dot{m} = 58.985[kg/s]$ **(c)** N_3, $\dot{m} = 58.985[kg/s]$

(d) N_1, $\dot{m} = 127.215[kg/s]$ **(e)** N_2, $\dot{m} = 127.215[kg/s]$ **(f)** N_3, $\dot{m} = 127.215[kg/s]$

(g) N_1, $\dot{m} = 177.245[kg/s]$ **(h)** N_2, $\dot{m} = 177.245[kg/s]$ **(i)** N_3, $\dot{m} = 177.245[kg/s]$

Figure 12-2. Velocity in stationary frame as measured on mid-plane of flow field.

12.1. Chapter summary

A detailed study of the grid independence and discretization error estimate was completed in this chapter. It was demonstrated after the procedure to determine the GCI had been completed, that the solution generated by the fine grid setup was well converged and was approaching the solution obtained by Richardson Extrapolation for all measured cases.

The next chapter will describe the completed validation methodology and the appropriate outcome.

13. Validation of the modified geometry case

Table 13-1. Test 2 systematic (instrumental) uncertainty evaluation

Instrument description	Instrument number	ISO 9906 Table C.1 [1] [Month]	Previous calibr. [2] [Month]	ISO 9906 Table 5[3] [%]	e_S, $k = 2$ norm [4] [%]
Tachometer	E.E.75	36	5	±0.35	±0.001
Pressure Transmitter	EJX530A	4	13	±1.0	±0.01
Pressure Transmitter	EJX430A	4	13	±1.0	±0.04
Flow meter	G7321	12	32	±1.5	±0.2

[1] EN-ISO-9906 (2012), Table C.1: Instrument calibration intervals, indicated in months.
[2] The amount of months since the previous calibration and certification was completed.
[3] EN-ISO-9906 (2012), Table 5: Permissible relative values of the instrumental uncertainty, e_S. The limits correspond to the Grade 1 (most stringent) certification level.
[4] The reported instrumental uncertainty, e_S, based on a standard uncertainty multiplied by a coverage factor of $k = 2$, which unless specifically stated otherwise, provides a confidence level of 95%.
[5] Recommended re-calibration intervals according to EN-ISO-9906 (2012) not met, however, all calibration certificates are still valid in accordance with SANAS.

The validation experiment was completed after the appropriate modifications were completed to the impeller inlet geometry, as per par. 10.4. A full performance test was completed in order to determine the operating characteristics of the modified geometry across a wide operating range. The experiment was completed as an industrial pump performance test as per EN-ISO-9906 (2012) Grade 1.

Table 13-1 shows the uncertainty related to the instrumentation that were utilised during the test. Note that the recommended EN-ISO-9906 (2012) calibration periods for the mentioned instruments had lapsed, however these suggested time periods are for guidance only and the recommended values as set forth by a set standard or the OEM can also be used should the client accept the proposal. Due to the fact that the calibrations are still (theoretically) valid as per the mentioned alternative arrangements, the test was accepted in solidarity with the standard (due to production pressure and limited test bench and technical personnel availability) - guidance is provided in Appendix C of EN-ISO-9906 (2012). The uncertainties and tolerances related to the test were assumed to be the maximum allowable values allowed by EN-ISO-9906 (2012) in order to fulfill the requirements of the Grade 1 performance test rules/guidelines.

The experimental results are shown in tables 13-2 and 13-3. The measured values are plotted in fig. 13-1, on the solid black curves. The test points are additionally marked with solid black bi-lateral error bars. Due to the fact that design points are not specified, the selected points of comparison were selected after the experiment was completed; the blue shaded zones represent the bi-lateral uncertainty, the green shaded areas depict the Grade 1B bi-lateral tolerance range,

Table 13-2. Results of the modified pump's experiment.

	ΔH			P			η		
Q $[m^3/h]$	Test $[m]$	ϕ_{2c} $[m]$	Δ [%]	Test $[kW]$	ϕ_{2c} $[kW]$	Δ [%]	Test [%]	ϕ_{2c} [%]	Δ [%]
0.00	314.4	-	-	412.31	-	-	0.00	-	-
215.50	-	313.66	-	-	531.25	-	-	33.91	-
235.44	322.35	312.56	-3.13	542.22	542.75	0.1	37.98	36.46	-4.17
288.00	-	309.67	-	-	573.03	-	-	43.16	-
360.00	-	308.21	-	-	617.41	-	-	49.21	-
424.69	-	301.45	-	-	660.52	-	-	53.31	-
504.00	321.46	288.12	-11.57	716.93	716.22	-0.1	61.32	56.31	-8.9
504.00	321.46	306.25	-4.97	716.93	681.41	-5.21	61.32	63.75	3.81
576.00	-	288.16	-	-	766.78	-	-	59.03	-
576.00	-	303.14	-	-	706.16	-	-	68.66	-
649.08	-	305.26	-	-	783.42	-	-	69.70	-
720.00	-	299.69	-	-	819.83	-	-	72.06	-
756.00	307.16	297.37	-3.29	873.07	833.72	-4.72	72.17	73.59	1.93
792.00	-	295.06	-	-	847.62	-	-	75.12	-
864.00	-	289.58	-	-	884.15	-	-	77.19	-
907.20	293.08	285.04	-2.82	944.41	905.91	-4.25	76.39	77.76	1.76
915.91	-	284.12	-	-	910.30	-	-	77.88	-
915.91	-	282.02	-	-	903.27	-	-	78.04	-
1008.00	-	272.97	-	-	951.50	-	-	78.77	-
1054.80	208.39	266.29	21.74	887.73	970.67	8.54	67.19	78.82	14.76
1080.00	-	262.70	-	-	980.98	-	-	78.85	-
1158.70	-	252.55	-	-	1010.11	-	-	79.03	-
1158.70	-	255.37	-	-	1018.66	-	-	79.04	-
1224.00	-	241.90	-	-	1030.15	-	-	78.99	-
1276.20	-	233.59	-	-	1042.04	-	-	77.94	-

[1] The teal entries indicate CFD results obtained by rotating the impeller mesh by 26°.
[2] The coral entries indicate linearly interpolated values.
[3] The grey entries indicate test point data that is considered to be incorrect - the data is included for the sake of completeness.
[4] $\Delta = 100(\text{Test}/\phi_{2c})$
[5] Q indicates the full pump flow rate in order to easily compare the test and CFD results.
[6] P = Motor Shaft Power. The total motor input power is measured and compensated for by the supplied motor overall efficiency.
[5] Calculation methodology as per Annex. B

the orange areas show the Grade 2B bi-lateral error tolerance and the red areas illustrate the Grade 3B bi-lateral error tolerance ranges. The stated range limits are discussed in detail in par. 6.1. In order for the pump to be certified to be compliant within a certain accuracy grade, the curve connecting the test points need to dissect at least one of the bi-lateral error tolerance bars.

The CFD results and uncertainty error bars are also plotted on fig. 13-1 in the shape of bold black vertical error bars and a red point where the value is programmed to be as per the testing done in par. 12. The simulation points are connected via the dashed curves. A shaded area is

Table 13-3. Results of the modified pump's $NPSHR_{3\%}$ experiment

	$NPSHR_{3\%}$		
Q $[m^3/h]$	Test $[m]$	ϕ_{2c} $[m]$	Δ $[\%]$
216.14	-	2.64	-
425.97	-	4.97	-
522.00	4.70	5.7	17.54
687.14	-	10.36	-
748.80	8.10	9.17	11.67
903.60	10.55	12.69	16.86
918.67	-	10.86	-
1015.20	10.95	16.04	31.73

[1] The coral colored entries indicate interpolated values using a best fit exponential regression line.

also shown, indicating the range obtained when rotating the impeller mesh by 26°.

Note: The outlet control valve of the test setup became compromised and had to be replaced with a gate valve mid-way through the performance test - the initial test was aborted and recommenced the following evening. The outlet pressure indication was unstable after the valve change - high piping vibrations were also noted after the change (see par. 9.2). The vacuum pump connected to the suction pressure vessel also exhibited some operational difficulties and could not maintain adequate suction pressure at the high flow experimental point on this particular instance - the final experimental test point (high flow) was excluded from the analysis as this point is believed to have been recorded in a cavitation state. Due to the long time since re-calibration, the outlet pressure gauge is suspected to have been defective - as a result, the $\Delta H - Q$ and $\eta - Q$ curves in fig. 13-1 is not seen as accurate and is subsequently faded out. The $NPSHR_{3\%} - Q$ and $P - Q$ graphs are unaffected by the outlet pressure gauge and can be seen as accurate.

Fig. 13-1 and table 13-3 indicates good correlation between the CFD predicted $NPSHR_{3\%}$ data regression vs the test results and the analytic prediction discussed in par. 10.3.3. Due to the computing time, only four points were simulated.

13.1. Chapter conclusion and summary

The second CFD validation study included the comparison of the entire modified CFD flow field's results to a second EN-ISO-9906 (2012) certified performance test. Although the considered calculation points satisfy the EN-ISO-9906 (2012) standard, the adapted CFD model can only be motivated to be partially validated across the entire operating range of the pump. Apart from the suspected inaccuracy of the outlet pressure gauge - the experimental results relating to $NPSH_{3\%}$ and P could considered as satisfactory (due to the measurement technique).

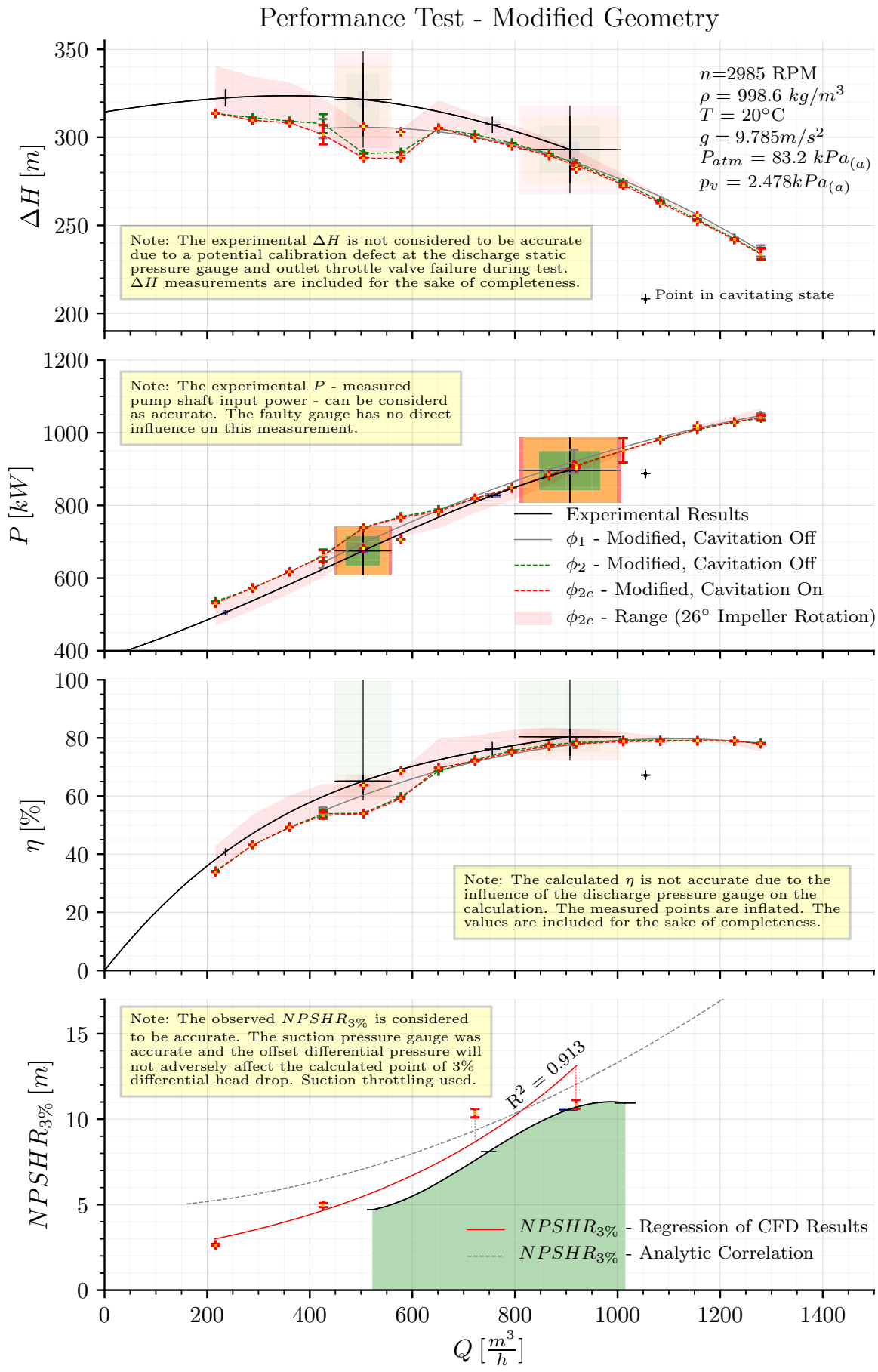


Figure 13-1. Test 2; Performance curve after modification, acceptable tolerance as per ISO 9906

Part IV.

Analysis of results

14. Analysis of simulation data

14.1. Overall performance assessment

Note: All values presented in all graphs and tables were generated by the formulae/methods included in Annex. B in the form of user CEL language (as programmed into the solver algorithm). All flow cavities, secondary flow paths and rotating and/or stationary walls were evaluated.

Table 14-1. Comparison of CFD results for H_{tot}, η and P between the modified and unmodified pump geometries

	ΔH and ϕ_{2c}			P and ϕ_{2c}			η and ϕ_{2c}		
Q $[m^3/h]$	Original $[m]$	Perf. Ring $[m]$	Δ [%]	Original $[kW]$	Perf. Ring $[kW]$	Δ [%]	Original [%]	Perf. Ring [%]	Δ [%]
215.496	326.09	313.54	-4.00	566.95	535.94	-5.79	33.91	33.91	0.01
288	320.37	311.18	-2.95	607.61	572.50	-6.13	41.44	43.16	3.99
360	314.83	309.17	-1.83	633.48	617.41	-2.60	48.88	49.21	0.67
424.692	311.41	307.73	-1.20	671.25	662.30	-1.35	53.51	53.31	-0.37
504	313.50	290.81	-7.80	715.10	740.30	3.40	60.66	53.92	-12.51
504	325.52	306.25	-6.29	741.13	681.41	-8.76	60.22	63.75	5.54
576	315.86	291.45	-8.37	743.04	768.90	3.36	66.53	59.03	-12.71
576	320.02	303.14	-5.57	767.03	706.16	-8.62	65.40	68.66	4.75
648	311.17	304.87	-2.07	778.91	788.23	1.18	70.49	69.70	-1.13
685.08	308.24	303.15	-1.68	800.16	803.96	0.47	71.95	70.91	-1.47
720	305.19	301.54	-1.21	821.06	818.79	-0.28	72.93	72.06	-1.21
792	300.85	296.72	-1.39	851.78	848.53	-0.38	76.37	75.12	-1.66
864	294.11	290.69	-1.18	887.91	881.01	-0.78	77.92	77.19	-0.94
915.912	288.62	284.94	-1.29	914.54	907.36	-0.79	78.64	77.88	-0.98
915.912	292.88	282.02	-3.85	933.94	903.27	-3.4	78.15	78.04	-0.14
1008	277.70	274.08	-1.32	956.28	950.75	-0.58	79.37	78.77	-0.76
1080	268.19	263.83	-1.65	986.49	981.25	-0.53	79.83	78.85	-1.25
1158.696	259.62	253.25	-2.52	1013.30	1008.33	-0.49	80.20	79.03	-1.48
1158.696	264.46	255.37	-3.56	1032.88	1018.66	-1.4	79.32	79.04	-0.35
1224	249.34	242.57	-2.79	1037.36	1029.36	-0.78	79.94	78.99	-1.20
1276.2	240.82	233.96	-2.93	1051.16	1040.26	-1.05	79.50	77.94	-2.00

[1] The teal entries indicate CFD results obtained by rotating the impeller mesh by 26°.
[2] The coral entries indicate linearly interpolated values.
[3] The grey entries indicate questionable test point data - included for completeness.
[4] $\Delta = 100(\text{Test}/\phi_{2c})$
[5] Q indicates the full pump flow rate in order to easily compare the test and CFD results.
[6] P = Motor Shaft Power. The total motor input power is measured and compensated for by the supplied motor overall efficiency.

Table 14-2. Comparison of CFD results for H_{tot}, η and P between the modified and unmodified pump geometries

	Comparison of best fit regression $NPSHR_{3\%}$ and ϕ_{2c}			Perf. Ring regression vs Gülich correlation $NPSHR_{3\%}$ and Gülich		
Q $[m^3/h]$	Original $[m]$	Perf. Ring $[m]$	Δ [%]	Perf. Ring $[m]$	Gülich $[m]$	Δ [%]
215.496	3.19	3.00	-6.23	3.00	5.24	42.80
288	3.61	3.49	-3.31	3.49	5.58	37.46
360	4.08	4.06	-0.49	4.06	6.00	32.34
424.692	4.56	4.65	1.98	4.65	6.45	27.87
504	5.22	5.49	4.93	5.49	7.08	22.48
576	5.90	6.38	7.52	6.38	7.75	17.57
648	6.68	7.43	10.05	7.43	8.49	12.56
685.08	7.12	8.03	11.32	8.03	8.91	9.90
720	7.56	8.64	12.50	8.64	9.32	7.34
792	8.55	10.04	14.89	10.04	10.23	1.81
864	9.67	11.68	17.21	11.68	11.22	-4.11
915.912	10.57	13.02	18.85	13.02	11.98	-8.67

[1] The comparisons are made between regression lines.
[2] $\Delta = 100$(Original/Perf. Ring)
[3] Q indicates the full pump flow rate in order to easily compare the test and CFD results.

As can be understood from the table 14-1 and illustrated in fig. 14-1 (considering the ΔH, P, and η parameters vs. Q): the addition of the ring modification did not have a profound impact on the performance of the pump within the normal operating boundaries when the $NPSHA$ is maintained significantly higher than the $NPSHR_{3\%}$ at the measured flow rate. The calculated performance parameters of the modified pump were, however, slightly worse overall compared to the unaltered design. The most affected parameter was the differential head produced at a set flow rate, particularly at low flow rates of $Q \leq 650m^3/h$. The comparison of the CFD data in fig. 14-1 was based on a fixed 0° rotation of the impeller mesh (in order to ensure consistency in result reporting). The flow rates $400m^3/h \leq Q \leq 650m^3/h$ could be considered to be more unstable (transient) when compared to higher values of Q due to the growing deviation between the simulated impeller rotation positions as Q decreases. The normal operating range indicated in fig. 14-1 shows a less pronounced deviation for the largest percentage of the normal operating range.

The prominent kink in the $\Delta H, P$ and η curves observed at flow rates $400m^3/h \leq Q \leq 650m^3/h$ will be discussed in later paragraphs but the phenomenon can be attributed to a stalled flow field in one of the two volute passages. The kink is more pronounced in the simulations that included the perforated ring geometry. Considering the data presented in table 14-1, the effect of the impeller mesh position when considering the angle of rotation is significant - especially at lower flow rates. The kink in the ΔH curves are still prominent with impeller rotation, however generally higher values of ΔH and η are computed, while P tends to compute at a lower value considering impeller rotation values of 26°.

When considering the $NPSHR$ characteristics as presented in table 14-2, more notable differences between the two configurations are observed. The modified geometry's predicted $NPSHR_{3\%}$ curve shows a tendency to diverge from the original geometry's computed trend.

Considering the data presented in table 14-2 and illustrated in fig. 14-1: the $NPSHR_{3\%}$ curve tends (within reasonable limits) to the predicted curve as presented in par. 10.3.3. The presented results implies that the modification could be reasonably predicable and could potentially be feasible in a centrifugal pump setup with adequate $NPSHA$ and favourable geometry and operating parameters.

Table 14-3. Comparison of CFD results for H_{thL} for ϕ_{2c} between the modified and unmodified pump geometries

	Comparison of CFD results ΔH_{thL} and ϕ_{2c}		
Q $[m^3/h]$	Original $[m]$	Perf. Ring $[m]$	Δ [%]
215.496	500.13	464.51	-7.67
288	443.17	421.18	-5.22
360	411.83	392.90	-4.82
424.692	388.90	374.53	-3.84
504	372.75	360.36	-3.44
576	363.15	345.78	-5.02
648	348.70	343.54	-1.50
685.08	342.01	338.65	-0.99
720	336.47	334.05	-0.72
792	328.17	325.86	-0.71
864	319.15	317.54	-0.51
915.912	312.68	311.37	-0.42
1008	298.18	296.68	-0.51
1080	287.62	286.00	-0.56
1158.696	277.64	274.98	-0.97
1224	267.80	265.70	-0.79
1276.2	260.13	258.24	-0.73

[1] The coral entries indicate linearly interpolated values.
[2] $\Delta = 100(\text{Original}/\text{Perf. Ring})$
[3] Q indicates the full pump flow rate in order to easily compare the test and CFD results.

The simulated comparison of the total theoretical head (including losses), H_{thL}, produced by the impeller (with the inlet and outlet volutes and all secondary flows and subsequent hydraulic losses included in the evaluation) corresponding to both the original and modified impeller suction geometry is presented in table 14-3. As determined from the current simulation results; the modified geometry is negatively affected (in terms of head production at the corresponding total flow rate) at flow rates corresponding to $Q \leq 648m^3/h$ when compared to the unmodified impeller geometry's simulation results.

From the overall performance data produced in this section it can be stated that the modification brought about by the addition of the perforated ring seems to have amplified the transient flow effects observed at low flow rates.

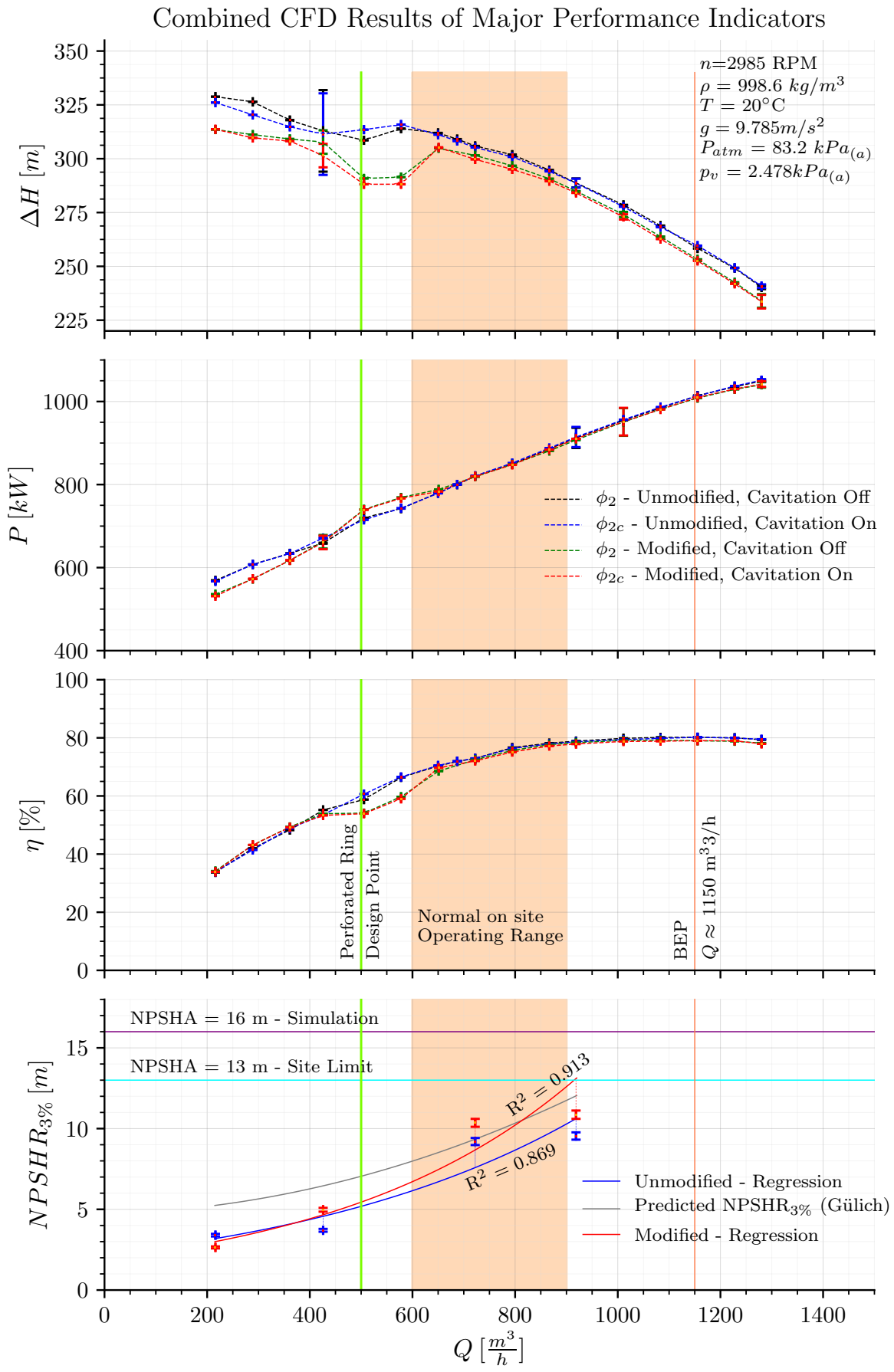


Figure 14-1. Comparison of CFD results (0° impeller rotation)

14.2. Evaluation of 3D CFD data

14.2.1. Geometry

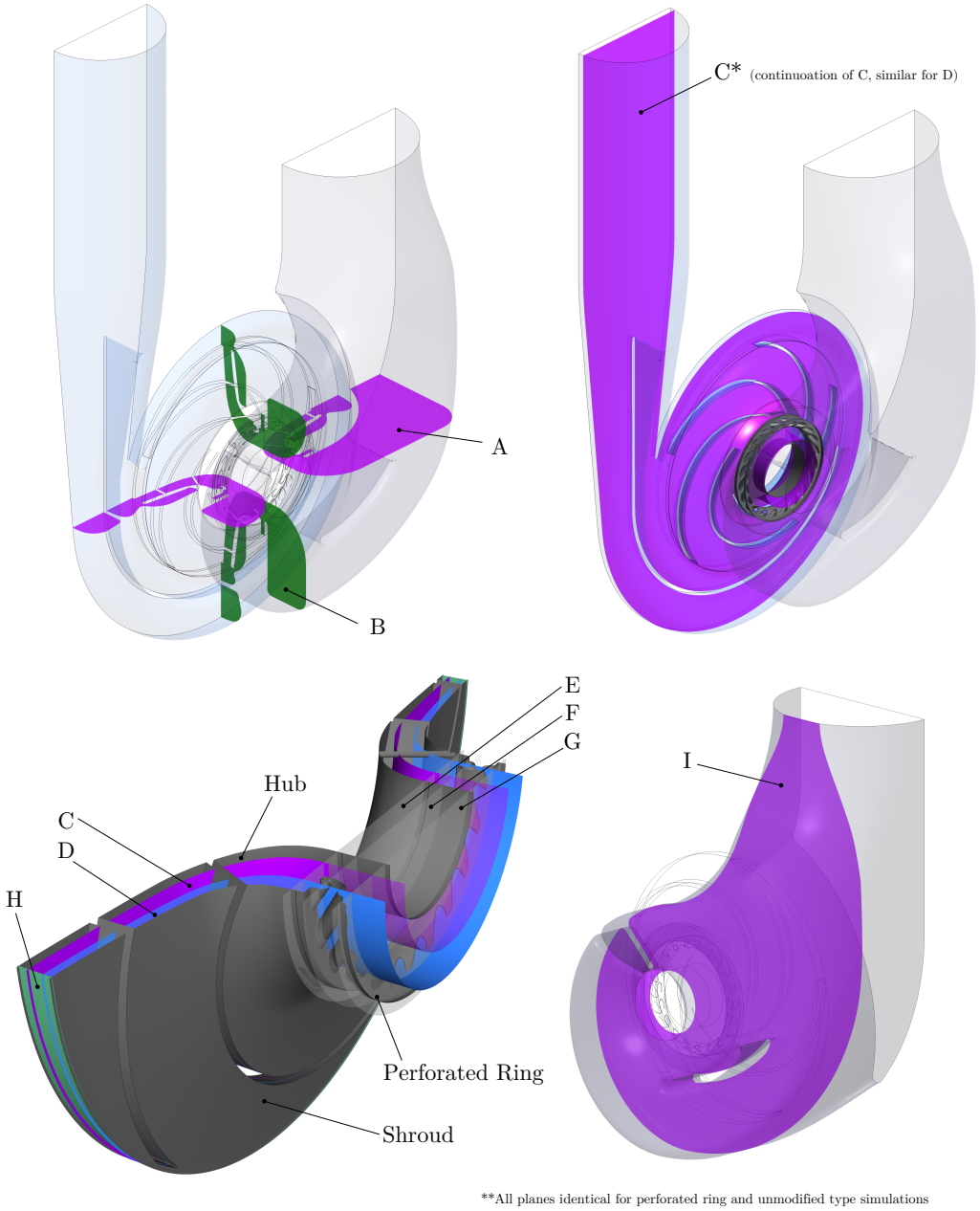


Figure 14-2. Depiction of the location where the CFD data was evaluated. The results reported in this chapter is consistent with the locations shown in this figure.

Fig. 14-2 shows all the considered planes for data analysis. The planes are referenced consistently throughout the current section. Note that Planes C, D, Hub and Shroud are meridional turbo surfaces representing a stream-wise impeller cut at a constant span-wise percentage. Planes which are depicted with an asterisk (*) indicate a continuation of the stream-wise impeller surface area into a parallel surface dissecting either the outlet and/or suction volute at the same axial position (Z-axis) of the impeller exit meridional surface span.

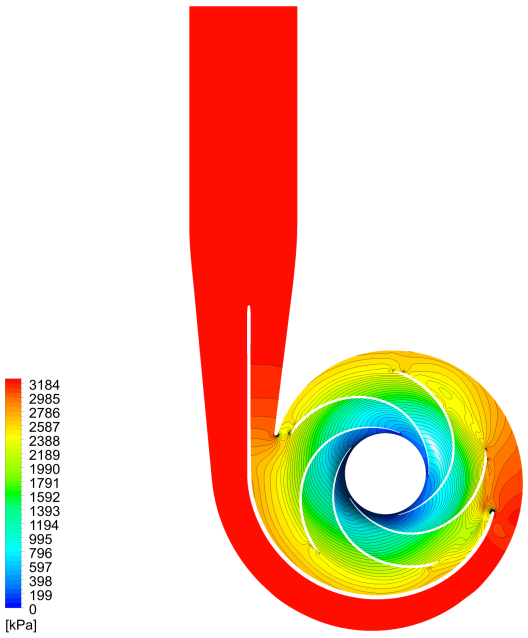
The geometry in fig. 14-2 also applies to all model variations relating to naming, position and application thereof.

14.2.2. Case 1 - Effect of the perforated ring at BEP conditions.

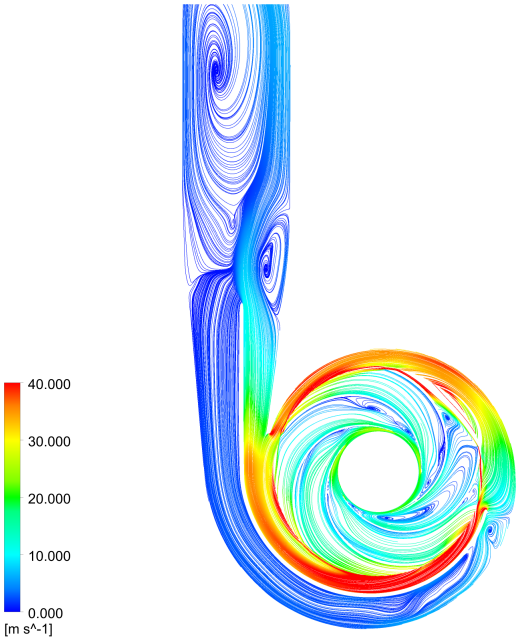
In order to economise the layout of this document, the results of the CFD analysis at the BEP operating conditions have been presented in Annex. I. References to the BEP simulation data are made throughout and the reader is urged to study the output data of Case 1 as a prerequisite to evaluating the results reported in Case 2.

14.2.3. Case 2 - Effect of the perforated ring at ring design conditions.

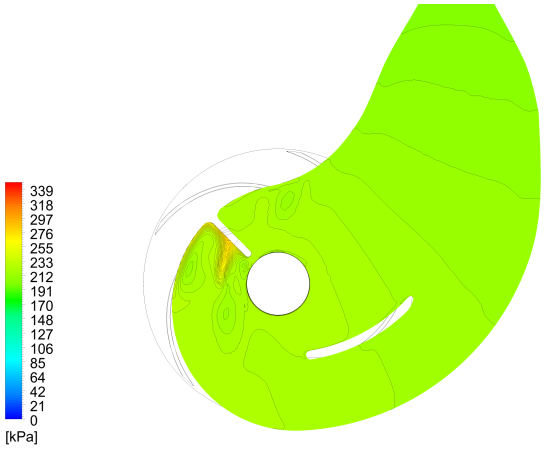
Case 2: Ring design point flow rate
$n = 2985RPM$ (clockwise), $Q = 250m^3/h$ ($Q = 500m^3/h$ for full pump)



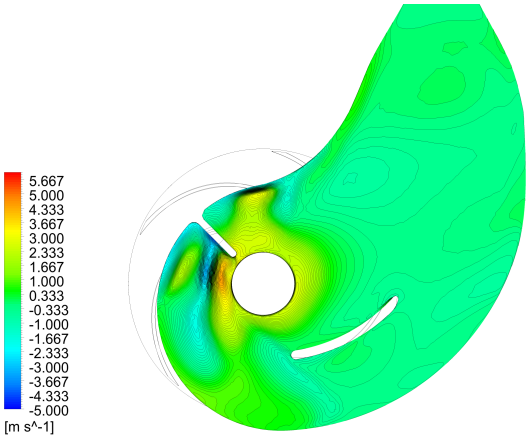
(a) Absolute pressure, Plane C*



(b) Velocity magnitude (Impeller: Relative/Volute: Stationary), Plane C*



(c) Total pressure in stationary frame, Plane I

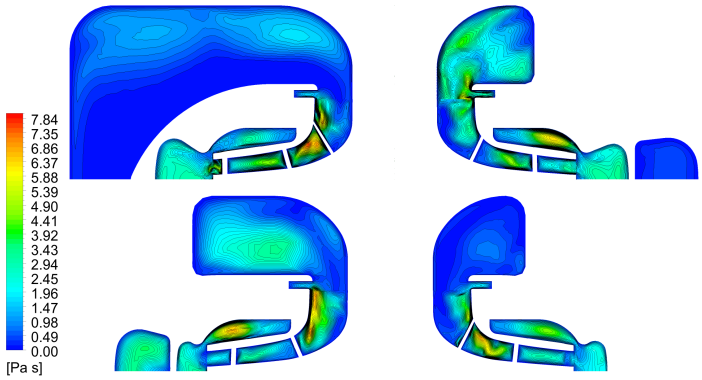


(d) Axial flow velocity in stationary frame, Plane I

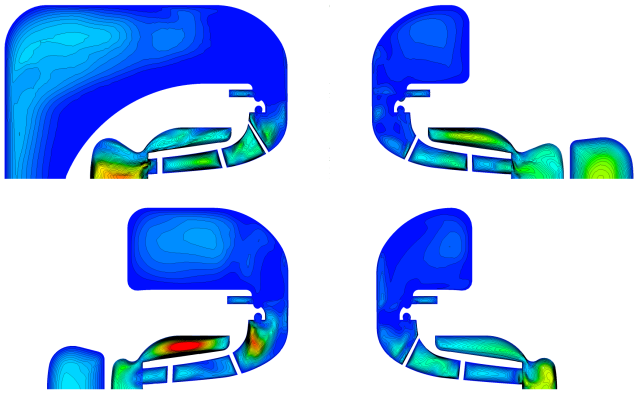
Figure 14-3. Comparison of BEP (initial) conditions for Case 2

No Ring installed	Ring Installed

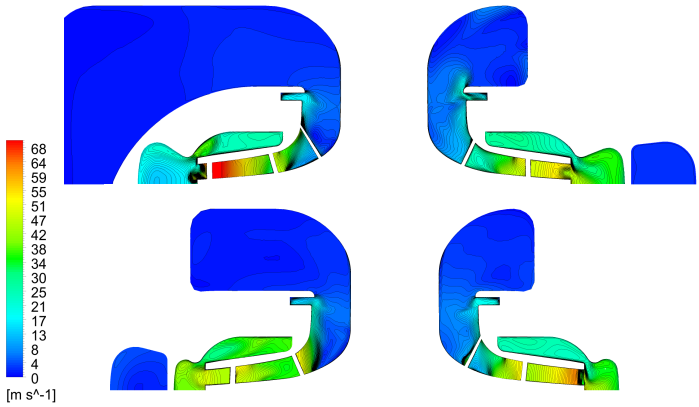
Case 2: Ring design flow rate
$n = 2985RPM$ (clockwise), $Q = 250m^3/h$ ($Q = 500m^3/h$ for full pump)



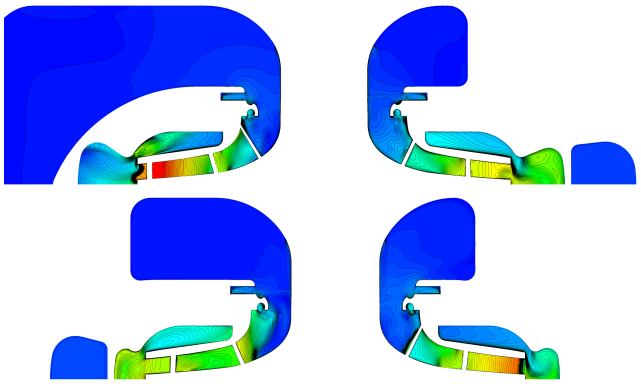
(a) Eddy Viscosity, Plane A top, Pane B bottom



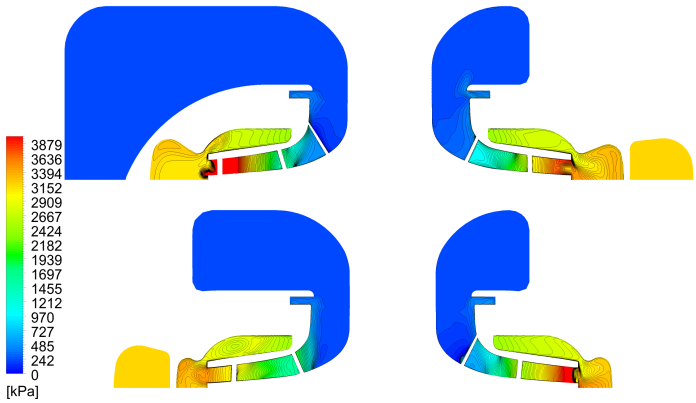
(b) Eddy Viscosity, Plane A top, Pane B bottom



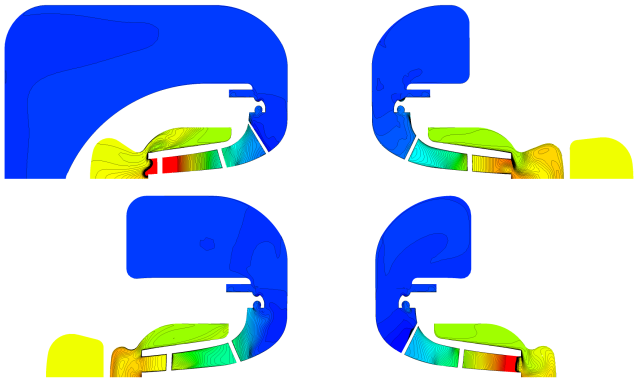
(c) Velocity in Stationary Frame, Plane A top, Pane B bottom



(d) Velocity in Stationary Frame, Plane A top, Pane B bottom



(e) Total Pressure in Stationary Frame, Plane A top, Pane B bottom



(f) Total Pressure in Stationary Frame, Plane A top, Pane bottom

Figure 14-4. Comparison of various parameters on Planes A and B

General comments on the 3D CFD data

In this section; various surface plots are provided at the evaluation flow rate of $Q = 250m^3/h$ (single eye flow rate). The Author intends to sketch a tangible state of the test pump for Cases

1 and 2 by means of the evaluation of numerous useful plots.

By evaluation of fig. 14-4, initial observations regarding the addition of the perforated ring and the impact thereof on the Case 2 flow field can be made on Planes A and B. Fig. 14-4 indicates that the addition of the perforated ring did alleviate areas of higher (calculated) Eddy Viscosity in the suction casing, upstream of the impeller inlet - this indicates a potential reduction of more turbulent flow structures in the bulk flow rate in these areas. The impact on the bulk total fluid flow velocity (observed in the stationary frame) is also evident - the ring addition seems to have altered the magnitude of the observed total flow velocity somewhat, especially in the impeller eye region. The impact on the total pressure had been slightly less obvious, with volute total pressure change being evident - as observed by a reduced volute total outlet volute pressure for the ring configuration.

The impeller inlet flow had been further investigated by the evaluation of c_{1m} at the inlet cross sectional flow areas depicted by Planes E, F and G as per figs. 14-5 and 14-6. Figs. 14-5a through 14-5c indicate a notable reverse flow region at the outer circumference of the evaluated planes (shown as a flow magnitude of value less than $0m/s$, indicating a flow rate opposite to the expected axial flow direction). The inner (forward-flowing) annulus exhibited an increase of c_{1m} due to the partial restriction of the total impeller inlet flow area by the outer fluid portion flowing in an apposed axial direction when compared with the bulk c_{1m} flow rate. With the addition of the perforated ring in figs. 14-5d through 14-5f, the reverse flow that had been observed in the outer diameter of the inlet were removed - however, a new area of low/reversed flow were created as a consequence. The new reverse flow area is located in the lower left quadrant of the inlet flow annulus. The conditioning of the inlet flow is also supported by the results contained in figs. 14-5g through 14-5i for the total (or stagnation) pressure, p_{Ts}. A higher total pressure was observed in the unmodified geometry at the design flow rate of the ring - this indicates the presence of strong secondary flows in conjunction with the bulk mass flow rate. The situation (regarding p_{Ts}) was mitigated by the "normalisation" of the p_{Ts} structure by the ring. A dramatic decrease in eddy viscosity, as observed in the annular flow areas of Planes E,F and G, μ_t, had been recorded in 14-6 after the addition of the perforated ring - this was also observed in fig. 14-4. In addition to the results obtained above, the ring design assumptions were supported by the results obtained from the Case 1 results at Planes E and G respectively, refer to figs. I-2d and I-2f (BEP conditions) - see the notes in tables D-3 and D-5.

Fig. 14-7 indicates the expected flow angles (β_1) at Plane C, D and Shroud. It can be seen from the images that there exits areas with negative flow angles within the impeller passages - indicating a reverse flow. A similar plot for Case 1, ref. fig. I-4 however shows favourable flow angle predictions. The accuracy of the calculated flow angles used in the calculation of the perforated ring design for the unaffected portion of the blades (Plane C) to be in good agreement with the CFD data as presented in fig. I-4b - see comments section in table D-5.

Fig. 14-8 illustrates various plots of meridional area averaged (about the axis of rotation) data of the impeller at the specified ring design flow rate Q - comparisons are also made between the unmodified and the modified inlet eye geometry. As can be seen in the figure, the addition of the ring does, in fact, assist in greatly reducing the level of calculated eddy viscosity in the meridional section of the impeller - indicating a reduction of bulk flow fluid mixing, figs. 14-8a and 14-8d. The addition of the ring also seems to be effective in ensuring a more even distribution of inlet flow velocity in the streamwise direction to the impeller blade leading edges, figs. 14-8b and 14-8e. The apparent gain in flow field uniformity seems to be offset by an increase of predicted vapour volume fraction at the leading edge of the vanes, see fig. 14-8c and 14-8f - the increase of the predicted cavitation zone will be discussed later in this section.

Recirculation flow

The recirculatory flow was investigated by means of blade-to-blade plots of the flow vectors at various meridional span locations as shown in previous paragraphs. The graphical layout of the results of the investigation is presented in ig. 14-9. The figure contains vector plots and streamline representations of the calculated flow vectors in order to aid the reader in interpretation of the results.

From the data shown in fig. 14-9, it is clear that there is indeed recirculatory behaviour present during operation at low flow rates (flow rates in the vicinity of $Q = 250m^3/h$ in this case). The vector plots of the unmodified geometry shows clear evidence of reverse flow and ejection of fluid out of the eye of the impeller into the bulk inflow to the impeller and the blades. The 2D streamlines also depict clear areas of separation in both the modified and unmodified impeller geometries - it should be noted that the level of recirculatory behaviour is somewhat alleviated by the addition of the perforated ring in this particular instance, with a reduction of observable separation cells and recirculatory flows visible in the mentioned graphs.

The recirculatory flows were further investigated using 3D rendering of the results. Plane G was used as the reference to plot the 3D streamlines and to generate the axially projected flow vectors, as per figs. 14-10a through 14-10d. Clear recirculation was illustrated by the combination of streamline and vector depictions, also, the effect of the perforated ring could be illustrated.

As a final probe into the extent of the calculated recirculation induced reverse flow, a vortex core iso-surface were constructed by means of the Q-Criterion and were colored by the Eddy Viscosity at those points. The iso-surface of the unmodified and modified pump geometry is presented in fig. 14-11. From the stated figure it is clear that extensive secondary flows are present in the pump setup prior to the installation of the perforated ring. After the ring was installed, the backflow-induced vortex cores were eliminated, with the exception of other secondary flows generated by the inflow of fluid from the suction of the pump casing.

It must however be noted that the suppression of the overall recirculation phenomena (restriction of back-flow of fluid out of the impeller eye) has not been fully achieved. there exist a back-flow close to the hub region, causing a portion of the impeller to become partially unloaded during the revolution, refer figs. 14-10. This behaviour of the impeller flow field will likely result in unintended performance over an extended operating period due to the potential cyclic mechanical and hydrodynamic loading of the blades.

14.2.4. Cavitation behaviour at operating conditions

The modeling of the cavitation as experienced during normal operation is presented. The presence of moderate cavitation during normal operation, above the $NPSH_{3\%}$ point is an unavoidable certainty for most pump installations operating with relatively low $NPSHA$ (Gülich, 2014; Karassik et al., 2008). The possibility of the suppression of unwanted cavitation by means of the installation of a modified suction ring was investigated.

It is known that the cavitation point (as calculated by the Raleigh-Plesset method) is very sensitive to the fluid properties such as entrained gasses and the presence of solids in the stream (Plesset, 1949). Solids or impurities do act as nucleation zones for cavitation bubbles and the concentrations of such elements should be known. The water tests completed for the test purpose did not disclose the solid particle count, nor air entrainment data. Differences between the experimental data and the CFD results are thus likely and even expected. The presence of these elements will also effect the CFD model itself, however these values were kept constant between

the simulation setups, and any deviation caused due to the stated fact would be normalized between the simulation results.

The expected cavitation clouds are shown as the green iso-surface plots of the water vapour volume fraction at a value of 0.5 (50%) at any given cell. Note that the physical size and location of the cavitation zones shown in fig. 14-12 have been slightly altered by the addition of the ring geometry. Additional cavitation zones have been introduced to the pump suction flow field inside and in close proximity to the perforations, fig. 14-12g and 14-12h.

As per earlier discussions regarding predicted vapour fractions, see fig. 14-8c and 14-8f - the increase of the predicted cavitation zone size is likely attributed to the reduction of streamwise flow velocity to the blade leading edge at lower flow rates where recirculation is present (increased flow velocity is present in the unmodified impeller due to the large recirculation zones at the impeller eye inside diameter, causing an obstruction in positive axial flow, which thus increases the streamwise flow velocity and subsequently reduces the leading edge incidence angle and the likelihood of premature cavitation during operation). The opposite is true regarding the streamwise velocity for Case 1, see fig. I-5 - at BEP conditions the ring tends to accelerate the flow unsymmetrically into the impeller eye (the higher velocity is shown to impinge on the area closest to the impeller hub, with the shroud area of the blade leading edge being provided lower inflow velocity) - this can also lead to premature cavitation during operation at BEP flow due to increased blade and flow incidence mismatch. The addition of the ring will likely bring about cavitation zones to form on or in close proximity to the ring geometry itself, at the inlet and at the outlet of some of the perforations - leading to a blockage of the perforations and a further acceleration of the bulk inlet flow rate to the blades. The cumulative effect on the $NPSH_{3\%}$ is detrimental as a greater possibility of cavitation is induced at most flow rates. The cavitation behaviour of the ring geometry would likely be improved in this instance with more acute drill angles - which is not attainable in the current setup due to the geometric constraints discussed at length in 10.3.

14.3. Chapter summary

The overall performance of the CFD vs the verification and validation actions were accepted to be in close agreement. The CFD results were accepted as accurate for the purposes of this study. The CFD data can be considered as clinical data which is as close as practically attainable in this instance (compared with the experimental data), thus these results were considered to be the data that would be used for the analysis of the study. After extensive simulations at closely spaced flow rate points, it was discovered that the pump characteristic curve possesses a slight saddle zone in between tested values.

The impact of the modification was investigated by comparing the CFD results of the unmodified and the modified geometry to each other, at exactly the same mass flow rates and impeller rotational speeds.

After evaluation of the 3D geometry and after due consideration of all the other results of this study, including the 2D plots and other investigations, it was shown that the axial reverse flow of fluid out of the impeller eye could likely be restricted by the addition of the perforated ring.

From the simulation results it can be stated that the modification did not have an unexpectedly large impact on the performance characteristics (e.g. η, P and ΔH_{tot}) of the machine, when adequate $NPSHA$ and flow rates above $600m^3/h$ were maintained. The modified geometry did not have an unexpected detrimental impact on the calculated (and measured) $NPSHR_{3\%}$, as a preliminary calculation predicted similar values to the test and simulation data. The modified

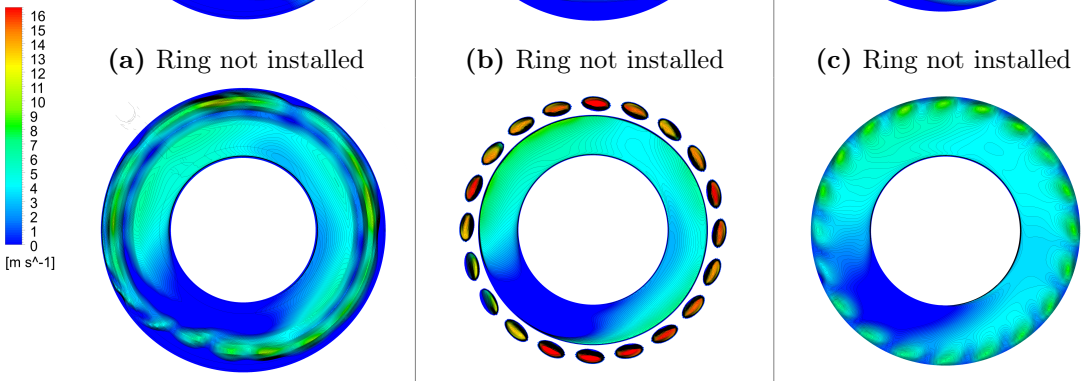
geometry impacted the $NPSHR_{3\%}$ between -6% and 18% as per the calculated values. A slight improvement was realised regarding the separation cell number in the impeller passage, with the trade-off of a slightly negatively impacted performance level and a newly generated (although not high in intensity) back-flow region near the impeller hub - a possible instability in the pump operation could be induced at low flows due to this phenomenon, this effect is not prevalent during operation at more reasonable flow rates close to BEP.

The modification was deemed successful in restricting the back-flow of fluid from the impeller eye to the suction volute.

The next chapter discusses the outcome and further study recommendations.

Plane E	Plane F	Plane G

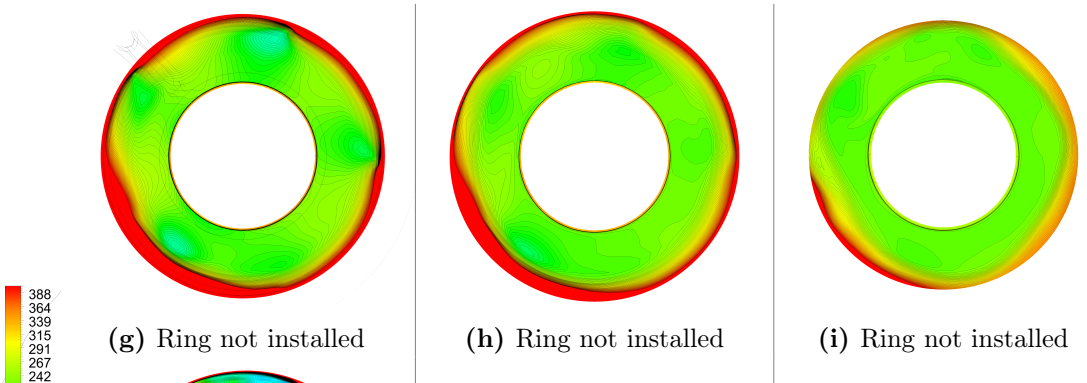
Case 2: Ring design flow rate
$n = 2985RPM$ (clockwise), $Q = 250m^3/h$ ($Q = 500m^3/h$ for full pump)
Measured variable: c_{1m}, direction of normal flow: into page



(a) Ring not installed **(b)** Ring not installed **(c)** Ring not installed

(d) Ring installed **(e)** Ring installed **(f)** Ring installed

Case 2: Ring design flow rate
$n = 2985RPM$ (clockwise), $Q = 250m^3/h$ ($Q = 500m^3/h$ for full pump)
Measured variable: p_{Ts}, direction of normal flow: into page



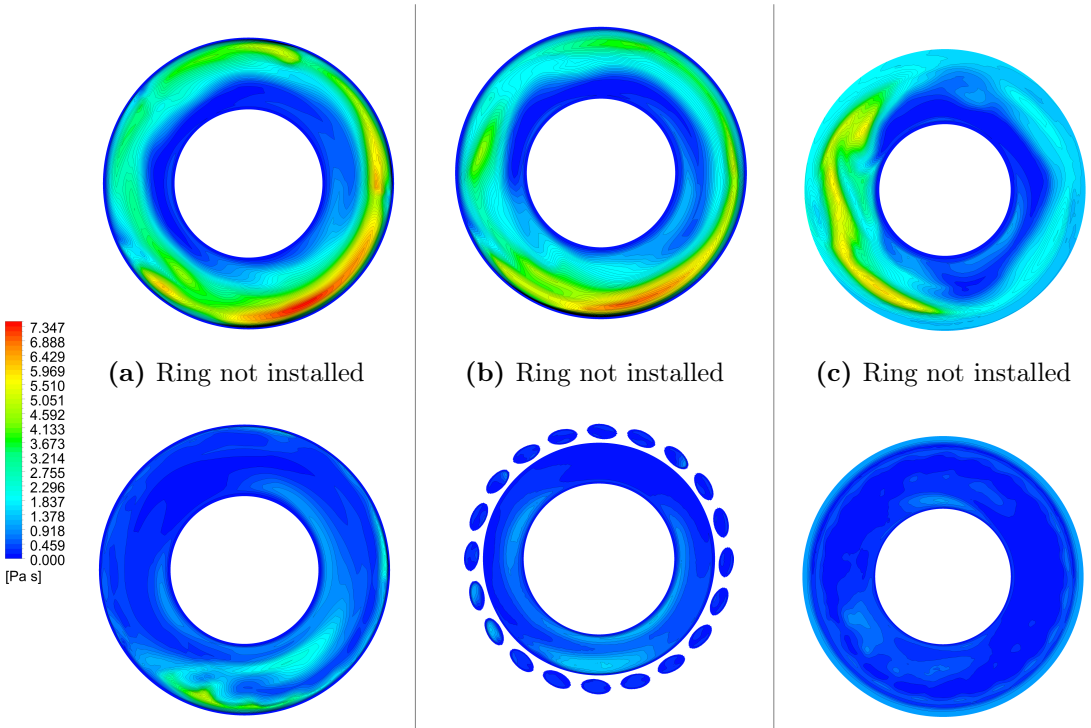
(g) Ring not installed **(h)** Ring not installed **(i)** Ring not installed

(j) Ring installed **(k)** Ring installed **(l)** Ring installed

Figure 14-5. Comparison of c_{1m} between different Cases and eye configurations

Plane E	Plane F	Plane G

Case 2: Ring design flow rate
$n = 2985RPM$ (clockwise), $Q = 250m^3/h$ ($Q = 500m^3/h$ for full pump)
Measured variable: μ_t, direction of normal flow: into page



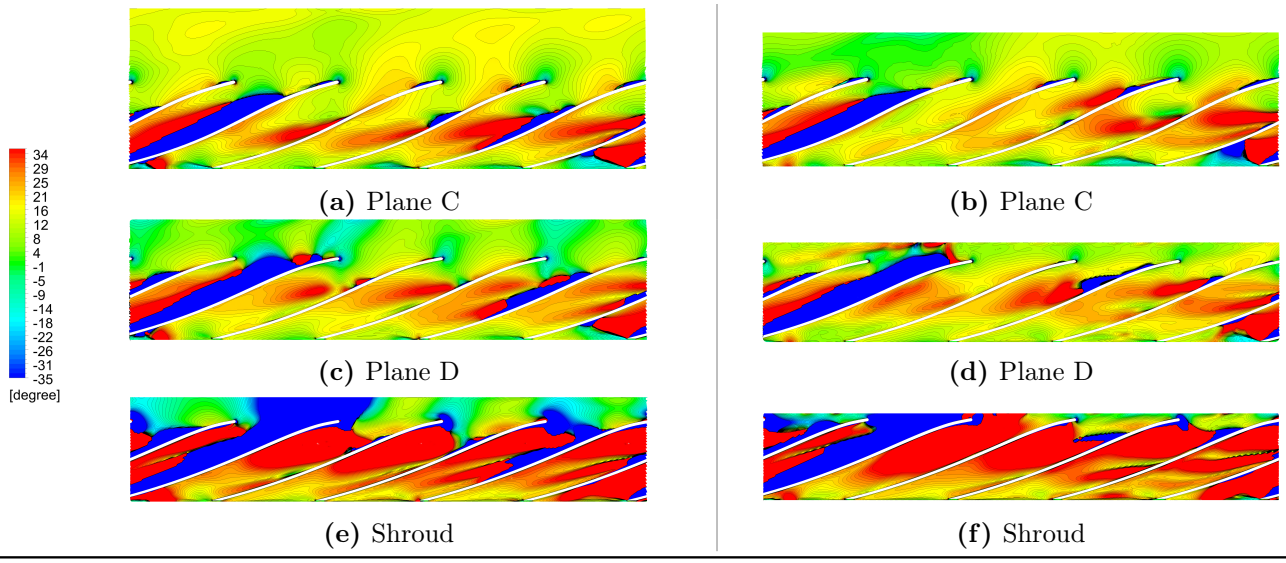
(a) Ring not installed **(b)** Ring not installed **(c)** Ring not installed

(d) Ring installed **(e)** Ring installed **(f)** Ring installed

Figure 14-6. Comparison of μ_t between different Cases and eye configurations

No Ring installed	Ring Installed

Case 2: Ring design flow rate: $Q = 250m^3/h$ ($Q = 500m^3/h$ for full pump), Flow: top to bottom,
$n = 2985RPM$ (clockwise, left-to-right in stationary frame),
Measured variable: Inlet flow angle, β_1



(a) Plane C **(b)** Plane C

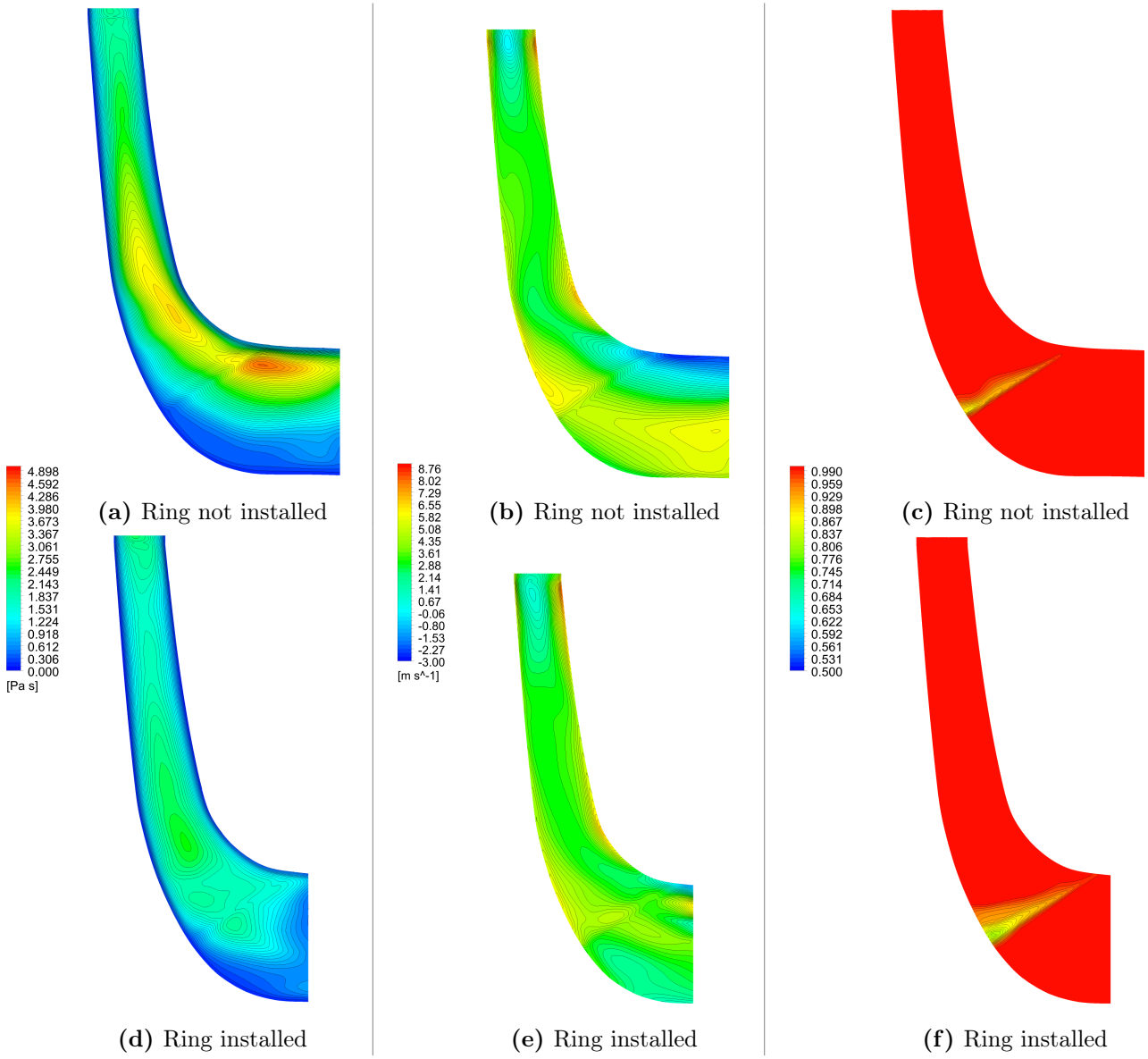
(c) Plane D **(d)** Plane D

(e) Shroud **(f)** Shroud

Figure 14-7. Comparison of impeller inlet flow angle between different Cases and eye configurations

Case 2: Ring design flow rate
$n = 2985RPM$ (clockwise), $Q = 250m^3/h$ ($Q = 500m^3/h$ for full pump)
Measured variable: μ_t, direction of normal flow: into page

Eddy Viscosity	Streamwise velocity	Conservative liquid volume fraction

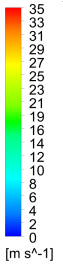


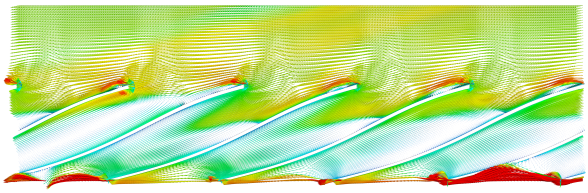
(a) Ring not installed **(b)** Ring not installed **(c)** Ring not installed

(d) Ring installed **(e)** Ring installed **(f)** Ring installed

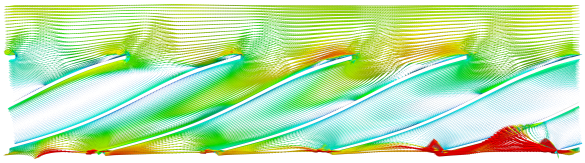
Figure 14-8. Comparison of area-averaged, circumferential meridional data

Case 2: Perforated ring not installed $Q = 250m^3/h$ ($Q = 500m^3/h$), Flow: top to bottom $n = 2985RPM$ (clockwise, left-to-right in stn frame)	Case 2: Perforated ring installed $Q = 250m^3/h$ ($Q = 500m^3/h$), Flow: top to bottom $n = 2985RPM$ (clockwise, left-to-right in stn frame)

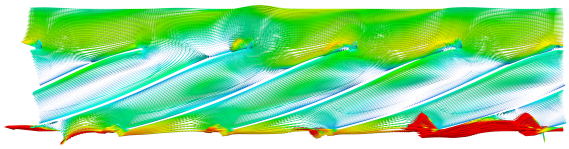




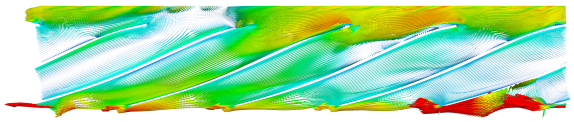
(a) w_1 magnitude 2D, plane C



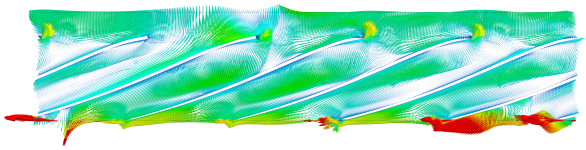
(b) w_1 magnitude 2D, plane C



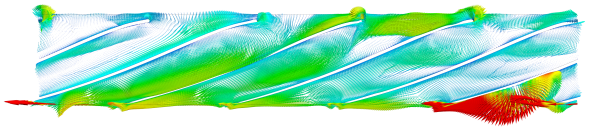
(c) w_1 magnitude 2D, plane D



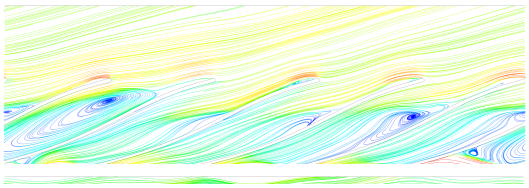
(d) w_1 magnitude 2D, plane D



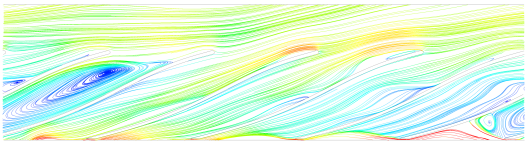
(e) w_1 magnitude 2D, Shroud



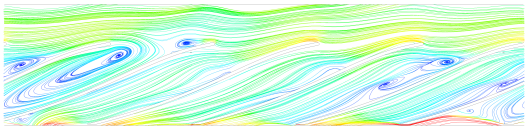
(f) w_1 magnitude 2D, Shroud



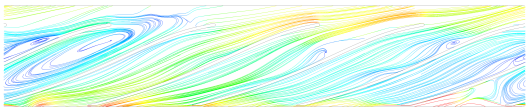
(g) Velocity magnitude 2D streamline, plane C



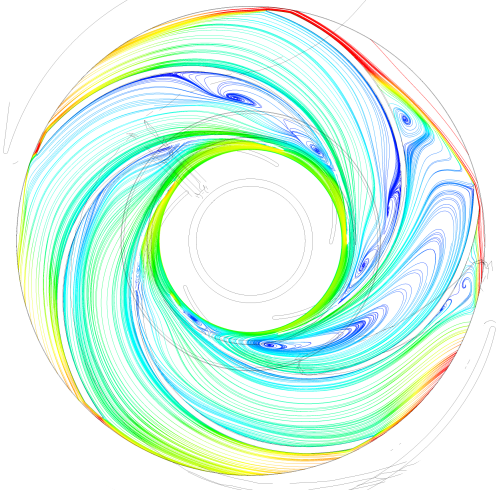
(h) Velocity magnitude 2D streamline, plane C



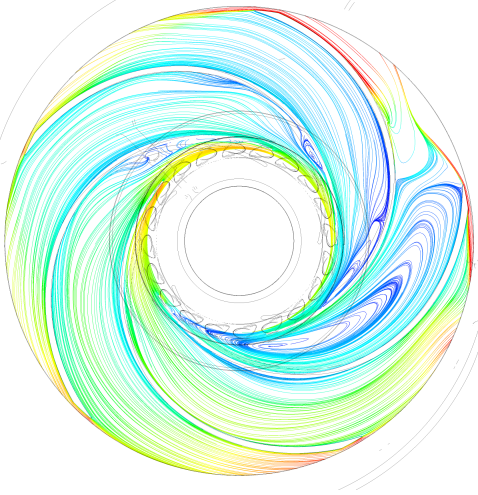
(i) Velocity magnitude 2D streamline, plane D



(j) Velocity magnitude 2D streamline, plane D



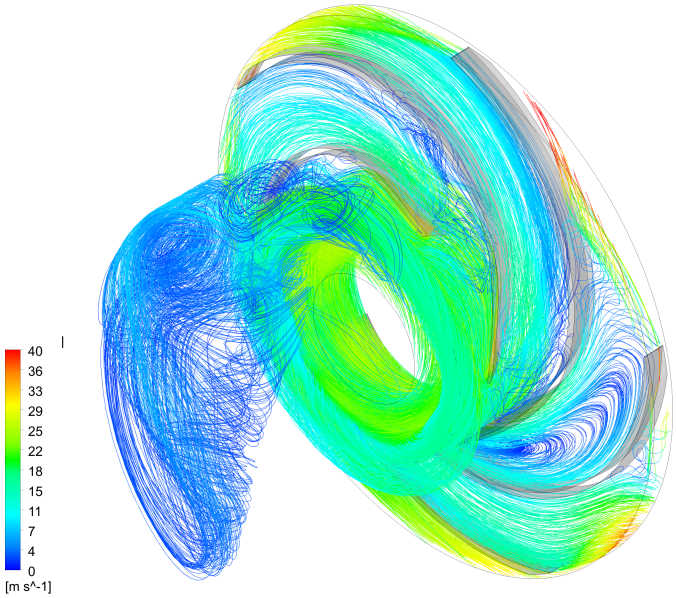
(k) Velocity magnitude 2D streamline, plane C



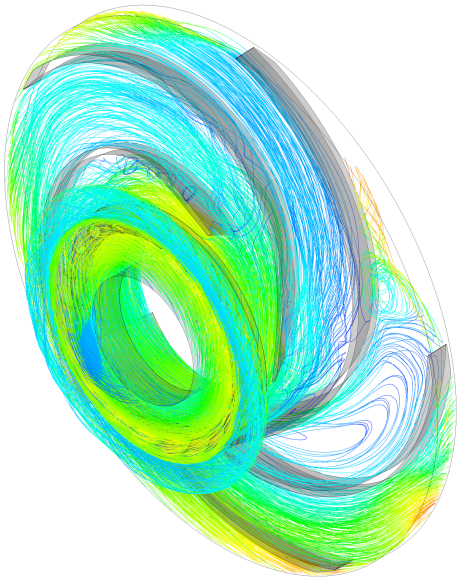
(l) Velocity magnitude 2D streamline, plane C

Figure 14-9. Comparison of 2D plane unmodified and modified impeller inlet geometry.

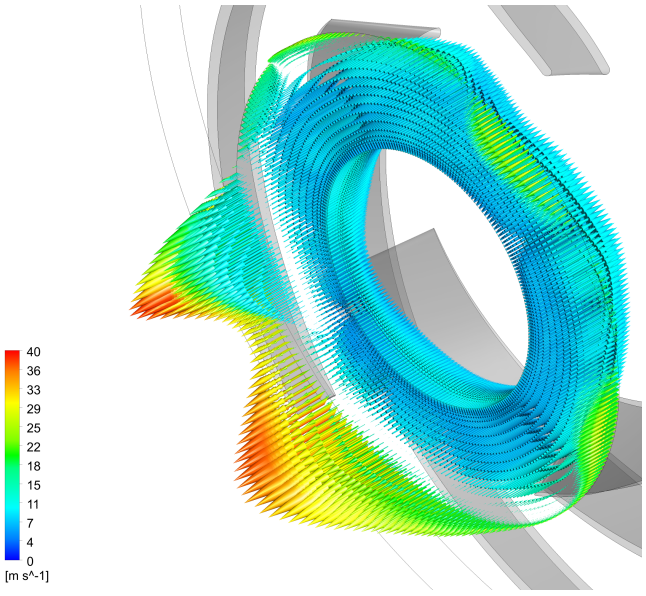
Case 2: Perforated ring not installed $Q = 250m^3/h$ $(Q = 500m^3/h)$ $n = 2985RPM$ (clockwise)	Case 2: Perforated ring installed $Q = 250m^3/h$ $(Q = 500m^3/h)$ $n = 2985RPM$ (clockwise)



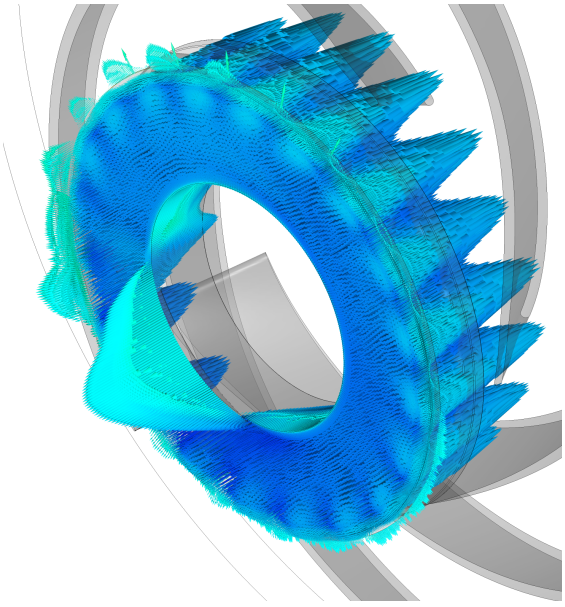
(a) Relative velocity magnitude 3D streamline



(b) Relative velocity magnitude 3D streamline



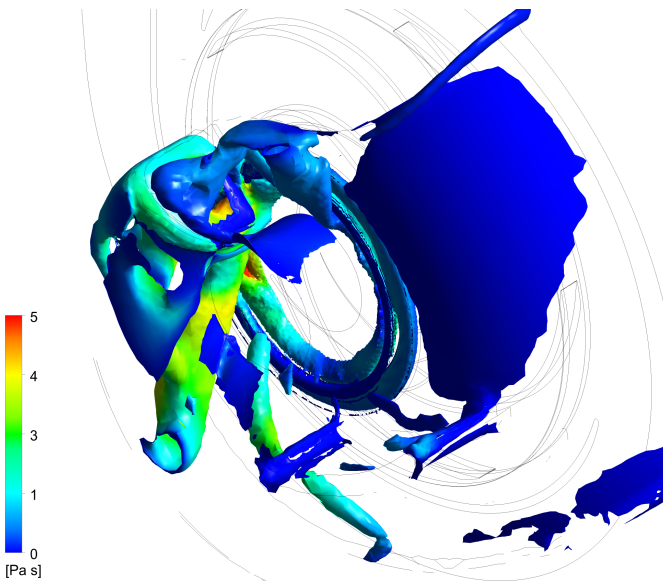
(c) Stream-wise (axial, c_{1m}) 3D velocity vector plot



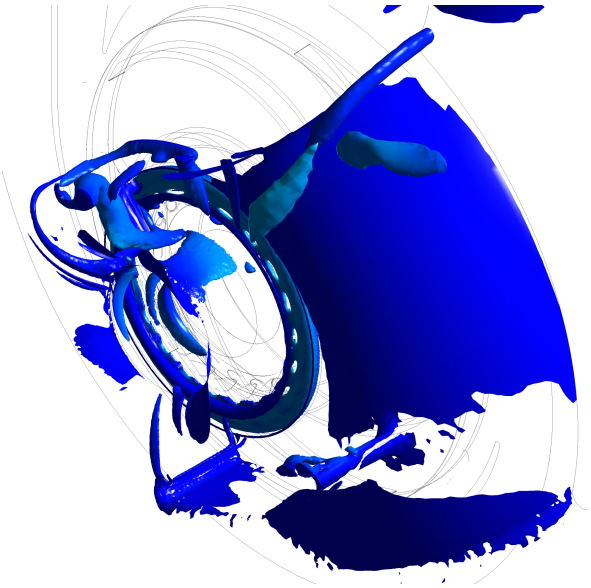
(d) Stream-wise (axial, c_{1m}) 3D velocity vector plot

Figure 14-10. Comparison of flow characteristics of the unmodified and modified impeller inlet geometry.

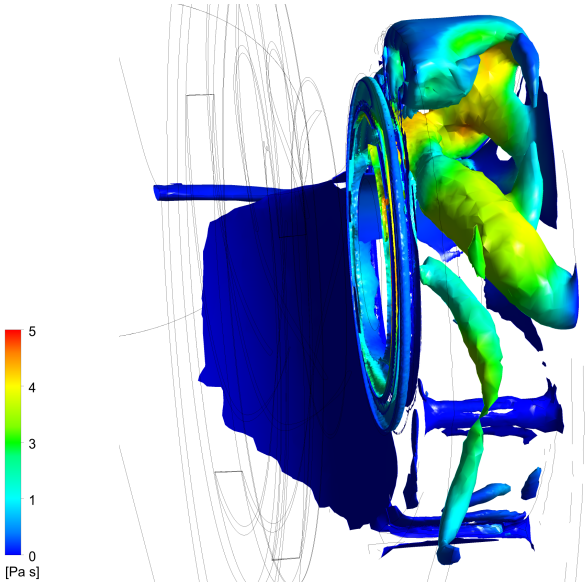
Case 2: Perforated ring not installed $Q = 250m^3/h$ ($Q = 500m^3/h$) $n = 2985RPM$ (clockwise)	Case 2: Perforated ring installed $Q = 250m^3/h$ ($Q = 500m^3/h$) $n = 2985RPM$ (clockwise)



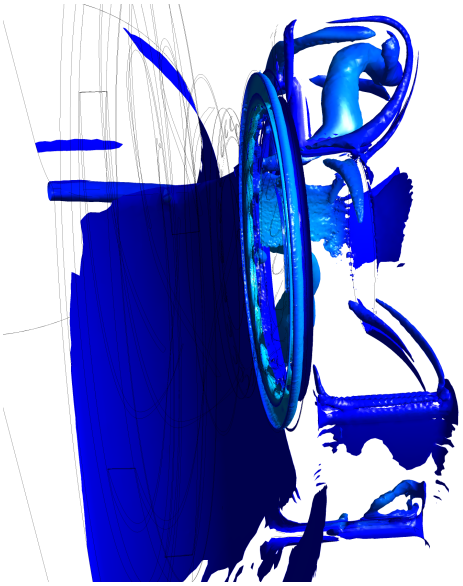
(a) Vortex core identification by means of Q-Criterion, coloured by Eddy Viscosity



(b) Vortex core identification by means of Q-Criterion, coloured by Eddy Viscosity



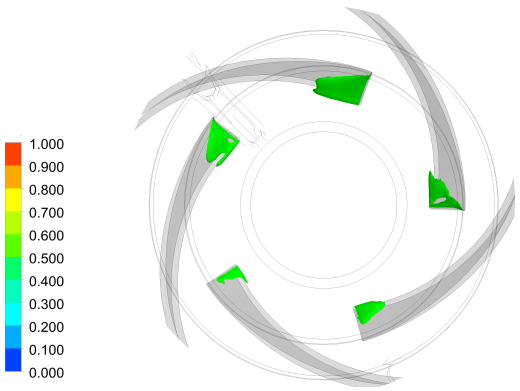
(c) Vortex core identification by means of Q-Criterion (alternate view), coloured by Eddy Viscosity



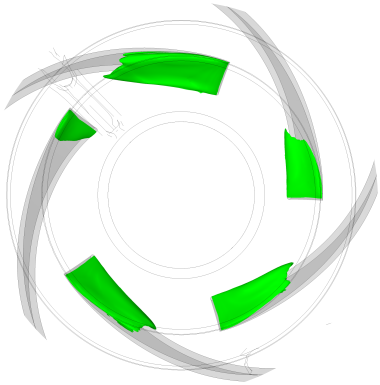
(d) Vortex core identification by means of Q-Criterion (alternate view), coloured by Eddy Viscosity

Figure 14-11. Comparison of vortex core iso-surface regions between the unmodified and modified impeller inlet geometry. Vortex core regions identified by means of the Q-Criterion method and the generated iso-surfaces are colored by Eddy Viscosity

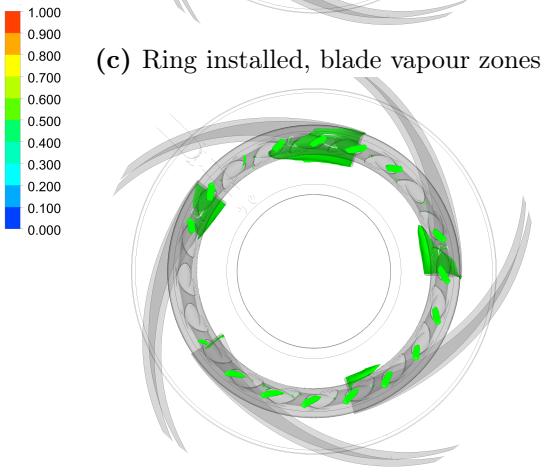
Case 2: Ring design flow rate $Q = 250m^3/h$ ($Q = 500m^3/h$)	Case 1: Best Efficiency Point $Q = 575m^3/h$ ($Q = 1150m^3/h$)
Variable: $(V_{liq} - V_{gas})/V_{liq}$, $n = 2985RPM$ (clockwise), $NPSHA = 16m$	



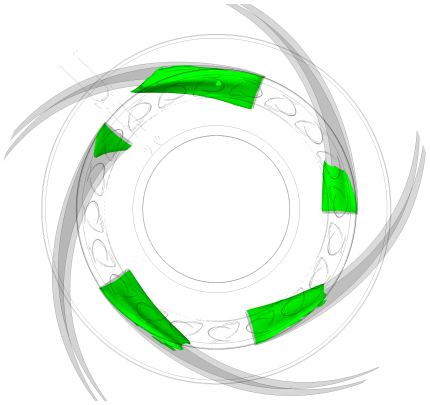
(a) Ring not installed



(b) Ring not installed

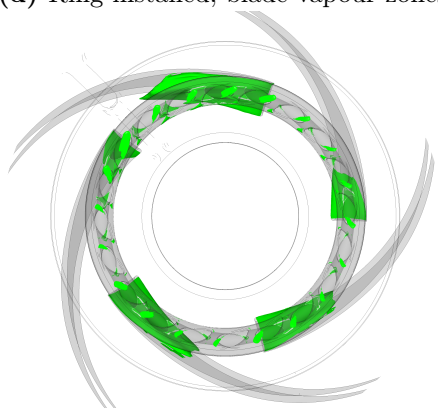


(c) Ring installed, blade vapour zones

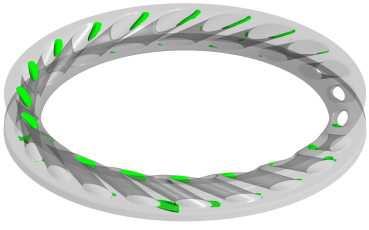


(d) Ring installed, blade vapour zones

(e) Ring installed, all vapour zones



(f) Ring installed, all vapour zones



(g) Ring vapour zones



(h) Ring vapour zones

Figure 14-12. Comparison of the conservative liquid vapour fraction free surface interface between different Cases and eye configurations

15. Conclusion and recommendations

15.1. Conclusion

Due to the stated rationale in this study, a study into the suction recirculation behaviour of a certain pump had been completed and presented in this dissertation. A potential geometric alteration was proposed with the intent of mitigating the suction recirculation at off-design flow regimes without adversely altering the characteristics of the pump setup. A specific requirement of limiting the increase of $NPSHR$ to below 10% was stated to be feasible.

Due to limited computing resources and time constraints, the CFD simulation of the pump was continued on the assumption of a steady state, RANS based, frozen rotor approach. The presented CFD models of both cases were subjected to verification studies by means of the grid refinement procedure developed by Roache (2009). Validation experiments (certified to EN-ISO-9906 (2012)) performed and the impeller performance was compared to a newly developed analytic impeller mean line performance calculation methodology. The verification procedure produced well verified CFD solutions. The comparison of the fine grid CFD solutions to the stated validation tests had been proven to be in close agreement and thus can be accepted. The CFD models presented can thus be confidently accepted as an adequate representation of the real world setups.

A partial volumetric survey of the actual test impeller were also completed although accessibility of the shrouded construction made the evaluation challenging. A representative geometric evaluation of a similar (de-shrouded) pump impeller was completed and significant deviations were found between the idealised 3D solid model (which is based on data from previous reverse engineering projects) and the measured geometries. The deviations can contribute to the observed deviations in results seen in the pump performance tests, as described in the relevant sections detailing the geometric aspects of the pump geometry.

During the second experiment various technical, time and economic constraints (as explained) necessitated the acceptance of a potentially non-calibrated pressure transducer to be used for the second experiment. Some experimental values were scrutinised and found to be misleading - the results are still incorporated with explanation for completeness. The first experiment was judged to be satisfactory.

With the above taken into consideration, the research objectives are considered and the stated hypothesis can be evaluated:

15.1.1. Evaluation of hypothesis

The hypothesis is stated to be: A profiled bulkhead-ring aids in suppressing excessive suction recirculation, and thus aids in relieving the intensity of damaging suction recirculation cavitation.

The hypothesis consists of two parts; the first part of the statement can be partially substantiated. It was proven that for the current observed cases, the tendency of fluid back-flow from the suction eye to the suction volute at the low flow condition was successfully restricted by the

modification. The tendency of the flow to separate from blade congruent conditions at low flows was not successfully mitigated.

The second part of the hypothesis concerns the mitigation of cavitation at the observed low flow conditions relating to recirculation induced cavitation. The current model did not successfully predict suction recirculation cavitation in the true sense of the phenomenon, i.e. cavitation at the vortex center of the separation cell, as described by Fraser (1981*a*); Karassik and McGuire (1997); Gülich (2001). In order to model these effects, more sophisticated solving methodologies and exponentially greater computing power is required. Other cavitation zones were however identified that is more along the lines of classic vaporisation cavitation that is well known to happen at low $NPSHA$. The cavitation intensity/size of the cavitation cloud/zone was modeled well by the setup. It was noted that the modified geometry tended to induce a greater amount of cavitation, when considering the size of the cavitation zones. Additional cavitation nucleation sites were introduced by the ring geometry, this resulted in additional cavitation clouds inside or at close proximity to the perforation flow area, resulting in flow obstruction of these flow areas.

15.1.2. Evaluation of implementation in industrial applications

The current geometry is not considered to be viable for pump applications where a combination of the presence of low $NPSHA$ and a wide operating range is required. The current geometry can be adapted and potentially implemented in feasible pumps with adequate geometric features (large eye diameter which will allow for the optimal drill angle to be implemented in the design without the risk of structural compromise) experiencing high suction recirculation while operating in a defined operating range relating to Q and have adequate $NPSHA$ that will mitigate vaporisation induced cavitation. The stated feasible application requirements will make other, less complex, options viable as well - this diminishes the attractive properties of the current design in lieu of simplicity of design.

15.2. Recommendations for further study

The following recommendations can be made regarding potential further study relating to the current work:

1. In order to more accurately simulate the flow field, it is recommended to conduct a study that details the full transient simulation of the complete pump setup (including both suction eyes and full volute configurations), by means of a sliding mesh technique. The turbulence could potentially be simulated using more rigorous methods such as LES (as applied in similar applications Sagaut (2006), Yamanishi et al. (2007) and Byskov et al. (2003)) or DES based approaches. The transient solution should include the transient simulation of cavitation as well in order to more precisely capture the cavitation zone in the recirculatory vortex cores at low flow conditions.
2. In order to further improve the potential for a more closely validated CFD computational result, further experimental setups could implement the manufacture and testing of an impeller which is produced by more precise manufacturing techniques (in order to ensure more accurate and symmetrical geometry) - e.g. CNC milling from billet, investment casting, additive manufacturing (potentially), etc. The casing flow surfaces could also conditioned in order to conform to a considerably more uniform surface roughness finish, ε. It is recognised that commercial pumps will rarely conform to precise laboratory standards,

especially larger units with complex casting features. The capital expenditure related to upgrading the current geometry will likely be prohibitive.

3. Design exploration could be completed in order to determine the most robust and efficient ring geometry for the widest efficient operating range.

4. Due to the limitations presented by the current study regarding the impeller eye geometry, a similar study could be performed by considering a pump setup with a much larger d_1. The increased diameter would alleviate the geometric constraints imposed by the current geometry on the required β_{1r} dimension, allowing for more optimal drill angles and d_r dimensions to be achieved.

Bibliography

Andrews, M. J. (2011), 'Guidelines for Use of Commercial Software and Diagnostics in Articles for the Journal of Fluids Engineering', *Journal of Fluids Engineering* **133(1)**, 010201.

ANSI-HI-14 (1982), Hydraulic Institute Standards for Centrifugal, Rotary & Reciprocating Pumps, Technical report, Hydraulic Institute, Cleveland, OH.

ANSI-HI-1.6 (2000), American National Standard for Centrifugal Pump Tests, American National Standard, Hydraulic Institute, Parsippany, New Jersey.

ANSYS® (2019*a*), CFX®, Release 2019 R2.

ANSYS® (2019*b*), CFX®, Release 2019 R2, Help System, CFX-Reference Guide, ANSYS, Inc.

ANSYS® (2019*c*), CFX®, Release 2019 R2, Help System, CFX-Solver Modeling Guide, ANSYS, Inc.

ANSYS® (2019*d*), CFX®, Release 2019 R2, Help System, CFX-Solver Theory Guide, ANSYS, Inc.

Antoine, C. (1888), 'Tensions des vapeurs; nouvelle relation entre les tensions et les températures', *Comptes Rendus des Séances de l'Académie des Sciences* **107**, 681–684, 778–780, 836–837.

API-610 (1981), Centrifugal Pumps for Petroleum, Petrochemical and Natural Gas Industries, International Standard 6th, American Petroleum Institute, Washington D.C.

API-610 (2011), Centrifugal Pumps for Petroleum, Petrochemical and Natural Gas Industries, International Standard 11th, Errata, American Petroleum Institute, Washington D.C.

ASME-B94.11M (1993), Twist Drills, American National Standard, The American Society of Mechanical Engineers, New York, NY.

ASME-V&V-20 (2009), Standard for Verification and Validation in Computational Fluid Dynamics and Heat Transfer, American National Standard, The American Society of Mechanical Engineers, New York, NY.

Aungier, R. H. (2000), *Centrifugal Compressors: A Strategy for Aerodynamic Design and Analysis*, ASME Press, New York.

Balasubramanian, R., Sabini, E. and Bradshaw, S. (2011), 'Influence Of Impeller Leading Edge Profiles On Cavitation And Suction Performance', *Turbomachinery Laboratory, Texas A&M University* .

Baumgarten, S., Fritz, J., Knierim, C. and Müller, T. (2001), 'Numerical simulation of the flow in a boiler circulating pump.', *Proceedings of the Institution of Mechanical Engineers, Part A: Journal of Power and Energy* **215**(6), 793–800.

Bloch, H. P. (2011), *Pump Wisdom: Problem Solving for Operators and Specialists*, Wiley, Hoboken, N.J.

Bradie, B. (2006), *A Friendly Introduction to Numerical Analysis*, Pearson Prentice Hall, Upper Saddle River, New Jersey.

Bradshaw, S. (2012), 'Modification Of Bb1 Pump Vibration Characteristics To Meet ISO 13709 2nd Edition (API 610 11th) Limits', *Turbomachinery Laboratory, Texas A&M University* .

Bradshaw, S., Cowan, D. and Liebner, T. (2013), 'Influence Of Impeller Suction Specific Speed On Vibration Performance', *Turbomachinery Laboratories, Texas A&M Engineering Experiment Station* .

Brennen, C. E. (1995), *Cavitation and Bubble Dynamics*, number 44 *in* 'Oxford Engineering Science Series', Oxford University Press, New York.

Breugelmans, F. A. E. and Sen, M. (1982), 'Prerotation And Fluid Recirculation In The Suction Pipe Of Centrifugal Pumps', *Texas A&M University. Turbomachinery Laboratories* .

Budris, A. R. (1993), 'The Shortcomings Of Using Pump Suction Specific Speed Alone To Avoid Suction Recirculation Problems', *Turbomachinery Laboratories, Department of Mechanical Engineering, Texas A&M University* .

Budris, A. R. (2010), 'How to Avoid Damage from Internal Suction Recirculation', *WaterWorld Magazine* .

Busemann, A. (1928), 'Das Förderhöhenverhältnis radialer Kreiselpumpen mit logarithmisch-spiraligen Schaufeln', *ZAMM - Zeitschrift für Angewandte Mathematik und Mechanik* **8**(5), 372–384.

Byskov, R. K., Jacobsen, C. B. and Pedersen, N. (2003), 'Flow in a Centrifugal Pump Impeller at Design and Off-Design Conditions—Part II: Large Eddy Simulations', *Journal of Fluids Engineering* **125**(1), 73–83.

Casey, M. and Wintergerste, T., eds (2000), *Industrial Computational Fluid Dynamics of Single-Phase Flows ERCOFTAC Best Practice Guidelines*, first edn, ERCOFTAC, London.

Celik, I., Ghia, U., Roache, P. J., Freitas, C. J., Coleman, H. W. and Raad, P. E. (2008), 'Procedure for Estimation and Reporting of Uncertainty Due to Discretization in CFD Applications', *J. Fluids Eng.* **130**(7), 078001.

Chalghoum, I., Kanfoudi, H., Elaoud, S., Akrout, M. and Zgolli, R. (2016), 'Numerical Modeling of the Flow Inside a Centrifugal Pump: Influence of Impeller–Volute Interaction on Velocity and Pressure Fields', *Arabian Journal for Science and Engineering* **41**(11), 4463–4476.

Cheah, K. W., Lee, T. S., Winoto, S. H. and Zhao, Z. M. (2007), 'Numerical Flow Simulation in a Centrifugal Pump at Design and Off-Design Conditions', *International Journal of Rotating Machinery* **2007**, 1–8.

Cornish, R. J. (1933), 'Flow of Water through Fine Clearances with Relative Motion of the Boundaries', *Proceedings of the Royal Society A: Mathematical, Physical and Engineering Sciences* **140**(840), 227–240.

Dixon, S. L. and Hall, C. A. (2014), *Fluid Mechanics and Thermodynamics of Turbomachinery*, seventh edition edn, Butterworth-Heinemann is an imprint of Elsevier, Amsterdam ; Boston.

EN-ISO-8062-3 (2007), Geometrical Product Specifications (GPS) – Dimensional and geometrical tolerances for moulded parts – Part 3: General dimensional and geometrical tolerances and machining allowances for castings, European Standard EN-ISO-8062-3:2007, CEN - Comité Européen de Normalisation, Brussels, Belgium.

EN-ISO-9906 (2012), Rotodynamic pumps - Hydraulic performance acceptance tests - Grades 1, 2 and 3, European Standard EN ISO 9906:2012: E, CEN - Comité Européen de Normalisation, Brussels, Belgium.

Feng, J., Benra, F. K. and Dohmen, H. J. (2010), 'Unsteady flow investigation in rotor-stator interface of a radial diffuser pump', *Forschung im Ingenieurwesen* **74**(4), 233–242.

Flownex (2018), *Flownex Library Manual*.

Fraser, W. H. (1981*a*), 'Flow Recirculation In Centrifugal Pumps', *Texas A&M University. Turbomachinery Laboratories* .

Fraser, W. H. (1981*b*), Recirculation in Centrifugal Pumps, *in* 'Materials of Construction of Fluid Machinery and Their Relationship to Design and Performance', American Society of Mechanical Engineers, Washington D.C., pp. 65–86.

Freitas, C. J. (1993), 'Journal of Fluids Engineering Editorial Policy Statement on the Control of Numerical Accuracy', *Journal of Fluids Engineering* **115(3)**, 339–340.

Gopalakrishnan, S. (1988), 'A New Method For Computing Minimum Flow', *Turbomachinery Laboratories, Department of Mechanical Engineering, Texas A&M University* .

Gülich, J. F. (1999), 'Impact of three-dimensional phenomena on the design of rotodynamic pumps', *Proceedings of the Institution of Mechanical Engineers, Part C: Journal of Mechanical Engineering Science* **213**(1), 59–70.

Gülich, J. F. (2001), 'Selection criteria for suction impellers of centrifugal pumps (Part 1 of 3)', *World Pumps Magazine* **414**, 29–32.

Gülich, J. F. (2014), *Centrifugal Pumps*, 3rd edn, Springer-Verlag, Berlin.

Gülich, J. F. (2019), *Centrifugal Pumps*, fourth edn, Springer International Publishing, Villeneuve, Switzerland.

Hergt, P., Nicklas, A., Mollenkopf, G. and Brodersen, S. (1996), 'The Suction Performance Of Centrifugal Pumps Possibilities And Limits Of Improvements', *Texas A&M University. Turbomachinery Laboratories* .

Hermez, M., Jawad, B., Liu, L. and Oklejas, E. (2017), Effects of Inlet Curved Spacer Arrangement on Centrifugal Pump Impellers, *in* 'WCX^{TM} 17: SAE World Congress Experience'.

Hermez, M. Y., Jawad, B. A., Liu, L., Fernandez, V., Yee, K. and Oklejas, E. (2016), Comparison of Inlet Curved Disk Arrangements for Suppression of Recirculation in Centrifugal Pump Impellers, *in* 'Volume 7: Fluids Engineering', ASME, Phoenix, Arizona, USA, p. V007T09A031.

Hirschberger, M. and James, I. (2009), 'A Review Of NSS Limitations: New Opportunities', *Texas A&M University. Turbomachinery Laboratories* .

Huber, M. L., Perkins, R. A., Laesecke, A., Friend, D. G., Sengers, J. V., Assael, M. J., Metaxa, I. N., Vogel, E., Mareš, R. and Miyagawa, K. (2009), 'New International Formulation for the Viscosity of H2O', *Journal of Physical and Chemical Reference Data* **38**(2), 101–125.

Hutchinson, B. R. and Raithby, G. D. (1986), 'A multigrid method based on the additive correction strategy', *Numerical Heat Transfer* **9**(5), 511–537.

IAPWS-R7-97 (2012), Revised Release on the IAPWS Industrial Formulation 1997 for the Thermodynamic Properties of Water and Steam, Technical report, Industrial Formulation for Thermodynamic Properties of Water and Steam.

ISO 10360-12 (2016), Geometrical product specifications (GPS) — Acceptance and reverification tests for coordinate measuring systems (CMS) — Part 12: Articulated arm coordinate measurement machines (CMM), European Standard ISO 10360-12:2016(en), CEN - Comité Européen de Normalisation, Brussels, Belgium.

ISO 10360-8 (2013), Geometrical product specifications (GPS) — Acceptance and reverification tests for coordinate measuring systems (CMS) — Part 8: CMMs with optical distance sensors, European Standard ISO 10360-8:2013, CEN - Comité Européen de Normalisation, Brussels, Belgium.

ISO-14001 (2004), Environmental management systems: An easy-to-use checklist for small bulsiness. Are you ready?, Technical report, International Organization for Standardization, Genève, Switzerland.

ISO-9001 (2015), Quality Management Systems - Requirements, Technical Report 5.

ISO-9906 (1999), Rotodynamic pumps - Hydraulic performance acceptance tests - Grades 1, 2 and 3, International Standard ISO 9906:1999: E, International Organization for Standardization, Genève, Switzerland.

Japikse, D. and Baines, N. (1997), *Introduction to Turbomachinery*, Concepts ETI, Vermont, USA.

Kagawa, S. and Matsushita, N. (2017), Improvement of cavitation surge in a double suction centrifugal pump by use of CFD, *in* 'Proceedings of the ASME 2017 Fluids Engineering Division Summer Meeting', Vol. Volume 1A, Waikoloa, Hawaii, USA, p. 6.

Karassik, I. J. (1987), 'Centrifugal pump operation at off-design conditions - Part 2', *Chemical Processing Magazine* .

Karassik, I. J. and McGuire, T. (1997), *Centrifugal Pumps*, Springer US, Boston, MA.

Karassik, I. J., Messina, J. P., Cooper, P. and Heald, C. C., eds (2008), *Pump Handbook*, 4th ed edn, McGraw-Hill, New York.

Kaye, J. and Elgar, E. (1958), 'Modes of adiabatic and diabatic fluid flow in an annulus with an inner rotating cylinder', *Transactions of ASME* **80**, 753–765.

Kim, D. S., Mamatov, S., Jeon, S. G. and Park, W. G. (2017), 'A study of the performance of a radial diffuser for a multistage high-pressure pump', *Journal of Mechanical Science and Technology* **31**(4), 1693–1700.

Launder, B. E. and Spalding, D. B. (1973), 'The numerical computation of turbulent flows', *Computer Methods in Applied Mechanics and Engineering* **3**, 269–289.

Lewis, R. I. (1996), *Turbomachinery Performance Analysis*, Arnold ; Wiley, London : New York.

Liebner, T., Cowan, D. and Bradshaw, S. (2016), The Influence of Impeller Wear Ring Geometry on Suction Performance, *in* 'Proceedings of the 32nd International Pump Users Symposium', Turbomachinery Laboratories, Texas A&M Engineering Experiment Station, Houston, Texas.

Liu, H. and Pan, H. C. (2012), 'The Influence of Turbulence Model Selection and Leakage Considerations on CFD Simulation Results for a Centrifugal Pump', *Advanced Materials Research* **594-597**, 1940–1944.

Lobanoff, V. S. and Ross, R. R. (1992), *Centrifugal Pumps: Design & Application*, 2nd ed edn, Gulf Pub. Co. in association with Plant Engineering, Houston.

Mason, W. (1983), 'A new method for calculating the Busemann head coefficients for radial impellers', *International Journal of Heat and Fluid Flow* **4**(3), 169–175.

Memardezfouli, M. and Nourbakhsh, A. (2009), 'Experimental investigation of slip factors in centrifugal pumps', *Experimental Thermal and Fluid Science* **33**(5), 938–945.

Menter, F. R. (1994), 'Two-equation eddy-viscosity turbulence models for engineering applications', *AIAA Journal* **32**(8), 1598–1605.

Munson, B. R., Okiishi, T. H., Huebsch, W. W. and Rothmayer, A. P. (2013), *Fundamentals of Fluid Mechanics*, 7th edition edn, John Wiley & Sons, Inc, Hoboken, NJ.

NIST Standard Reference Database Number 69 (2018), *in* P. J. Linstrom and W. G. Mallard, eds, 'NIST Chemistry WebBook', National Institute of Standards and Technology, Gaithersburg MD, 20899.

OHSAS-18001 (2007), Occupational health and safety management systems: Requirements, Technical report, OHSAS Project Group, London.

Paeng, K. S. and Chung, M. K. (2001), 'A new slip factor for centrifugal impellers', *Proceedings of the Institution of Mechanical Engineers, Part A: Journal of Power and Energy* **215**(5), 645–649.

Park, S. H. and Morrison, G. L. (2009), Centrifugal pump pressure pulsation prediction accuracy dependence upon CFD models and boudary conditions, *in* 'Proceedings of the ASME 2009 Fluids Engineering Division Summer Meeting', Vail, Colorado.

Páscoa, J. C., Silva, F. J., Pinheiro, J. S. and Martins, D. J. (2010), 'Accuracy details in realistic CFD modeling of an industrial centrifugal pump in direct and reverse modes', *Journal of Thermal Science* **19**(6), 491–499.

Pembroke, J. P., Sabini, E. P. and Littlefield, D. (1998), CFD analysis of a double suction cooling water pump, *in* 'Proceedings of the 15th International Pump Users Symposium', Texas A&M University. Turbomachinery Laboratories, pp. 11–20.

Plesset, M. S. (1949), 'The dynamics of cavitation bubbles', *Journal of Applied Mechanics* **16**, 277–282.

Pletcher, R. H., Anderson, D. A. and Tannehill, J. C. (2016), *Computational Fluid Mechanics and Heat Transfer*, third edn, CRC Press, Boca Raton, FL.

Qiu, X., Japikse, D., Zhao, J. and Anderson, M. R. (2011), 'Analysis and Validation of a Unified Slip Factor Model for Impellers at Design and Off-Design Conditions', *Journal of Turbomachinery* **133**(4), 041018.

Raw, M. (1996), Robustness of coupled Algebraic Multigrid for the Navier-Stokes equations, *in* '34th Aerospace Sciences Meeting and Exhibit', American Institute of Aeronautics and Astronautics, Reno,NV,U.S.A.

Rayleigh, L. (1917), 'On the pressure developed in a liquid during the collapse of a spherical cavity', *The London, Edinburgh, and Dublin Philosophical Magazine and Journal of Science* **34**(200), 94–98.

Rennels, D. C. and Hudson, H. M. (2012), *Pipe Flow: A Practical and Comprehensive Guide*, Wiley, Hoboken, N.J.

Roache, P. (2003), Error Bars for CFD, *in* '41st Aerospace Sciences Meeting and Exhibit', American Institute of Aeronautics and Astronautics, Reno, Nevada.

Roache, P. J. (1998*a*), *Fundamentals of Computational Fluid Dynamics*, Hermosa Publishers, Albuquerque, N.M.

Roache, P. J. (1998*b*), *Verification and Validation in Computational Science and Engineering*, Hermosa Publishers, Albuquerque, N.M.

Roache, P. J. (2009), *Fundamentals of Verification and Validation*, Hermosa Publishers, Socorro, New Mexico.

S Muttalli, R., Agrawal, S. and Warudkar, H. (2014), 'CFD Simulation of Centrifugal Pump Impeller Using ANSYS-CFX', *International Journal of Innovative Research in Science, Engineering and Technology* **03**(08), 15553–15561.

Sagaut, P. (2006), *Large Eddy Simulation for Incompressible Flows*, Scientific Computation, third edn, Springer-Verlag, Berlin/Heidelberg.

Sayers, A. T. (1990), *Hydraulic and Compressible Flow Turbomachines*, McGraw-Hill, London ; New York.

Schiavello, B. (1993), 'Cavitation And Recirculation Troubleshooting Methodology', *Turbomachinery Laboratories, Department of Mechanical Engineering, Texas A&M University* .

Schiavello, B. and Visser, F. C. (2007), 'Pump Cavitation - Various NPSHR Criteria, NPSHA Margins, Impeller Life Expectancy (Unpublished)', *Texas A&M University. Turbomachinery Laboratories* .

Sloteman, D. P., Cooper, P. and Dussord, J. L. (1984), 'Control Of Backflow At The Inlets Of Centrifugal Pumps And Inducers', *Turbomachinery Laboratories, Department of Mechanical Engineering, Texas A&M University* .

Spence, R. and Amaral-Teixeira, J. (n.d.), A CFD Analysis of a Complete Double Entry Centrifugal Pump, *in* 'Proceedings of the 15th UK Conference of the Association of Computational Mechanics in Engineering'.

Stodola, A. (1924), *Dampf- und Gasturbinen*, sixth edn, Springer Berlin Heidelberg, Berlin, Heidelberg.

Stodola, A. (1927), *Steam and Gas Turbines: With a Supplement on the Prospects of the Thermal Prime Mover*, Vol. 2, McGraw-Hill.

Stoffel, B. and Jaeger, R. (1996), 'Experimental Investigations In Respect To The Relevance Of Suction Specific Speed For The Performance And Reliability Of Centrifugal Pumps', *Texas A&M University. Turbomachinery Laboratories* .

Strongin, M. P. (2015), CFD analysis of te pump performance with different liquid viscosity, *in* 'Proceedings of the ASME-JSME-KSME 2015 Joint Fluids Engineering Conference', Seoul, Korea.

Sun, J. and Tsukamoto, H. (n.d.), 'Off-design performance prediction for diffuser pumps.', *Proceedings of the Institution of Mechanical Engineers, Part A: Journal of Power and Energy* **215**(2), 191–201.

Taylor, G. I. (1923), 'Stability of a Viscous Liquid Contained between Two Rotating Cylinders', *Philosophical Transactions of the Royal Society A: Mathematical, Physical and Engineering Sciences* **223**(605-615), 289–343.

Versteeg, H. K. and Malalasekera, W. (2007), *An Introduction to Computational Fluid Dynamics: The Finite Volume Method*, 2nd ed edn, Pearson Education Ltd, Harlow, England ; New York.

Visser, F. C., Brouwers, J. J. H. and Badie, R. (1994), 'Theoretical analysis of inertially irrotational and solenoidal flow in two-dimensional radial-flow pump and turbine impellers with equiangular blades', *Journal of Fluid Mechanics* **269**, 107–141.

Volk, M. (2013), *Pump Characteristics and Applications*, third edn, CRC Press.

von Backström, T. W. (2006), 'A Unified Correlation for Slip Factor in Centrifugal Impellers', *Journal of Turbomachinery* **128**(1), 1.

Vyavahare, P., Bhaskara Rao, L. and Patil, N. (2017), 'CFD Analysis of Double Suction Centrifugal Pump with Double Volute', *Periodica Polytechnica Mechanical Engineering* **62**(1), 74.

White, F. (1999), *Heat Transfer and Fluid Flow*, Genium Publishing Corporation, New York, NY.

Wiesner, F. J. (1967), 'A review of slip factors for centrifugal impellers.', *ASME Journal of Engineering for Power* **89**(4), 558–566.

Wilcox, D. C. (2008), 'Formulation of the k-w Turbulence Model Revisited', *AIAA Journal* **46**(11), 2823–2838.

Wislicenus, G. F. (1947), *Fluid Mechanics of Turbomachinery*, 1st edn, McGraw-Hill.

Yamada, Y. (1962), 'Resistance of a Flow through an Annulus with an Inner Rotating Cylinder', *Bulletin of JSME* **5**(18), 302–310.

Yamanishi, N., Fukao, S., Qiao, X., Kato, C. and Tsujimoto, Y. (2007), 'LES Simulation of Backflow Vortex Structure at the Inlet of an Inducer', *Journal of Fluids Engineering* **129**(5), 587–594.

Yedidiah, S. (1986), 'Certain Effects of Recirculation on Cavitation in Centrifugal Pumps', *Proceedings of the Institution of Mechanical Engineers, Part A: Power and Process Engineering* **200**(4), 283–292.

Yedidiah, S. (1996), *Centrifugal Pump User's Guidebook Problems and Solutions*, Chapman & Hall, New York, NY.

Annexures

A. Reduced Order Model for a rotating internal annular seal leakage path

CFD analysis of turbomachinery is becoming more common and the problem of efficiently and economically simulating internal leakage through annular seals is of primary concern to the designer. The construction of meshes of adequate quality to capture the leakage flow field accurately requires excessively fine grid setups to account for annular seal clearances between 0.1 to 0.5mm. This annexure proposes the construction of a reduced order model of an annular seal setup that allows for analytical calculation of the mentioned leakage using user scripting in the CFD solver setup, subsequently eliminating the mesh requirement for leakage simulation of close running clearances in large pump flow field computation models. The model has been verified against a commercial fluid dynamics software package and achieved a 2.4% accuracy level with $\sigma = 0.0118$ across a wide operating range. The model has been proven to be accurate and capable of accounting for surface roughness effects and temperature variations. Guidance for the implementation of the ROM in the ANSYS® CFX® solver environment is also provided.

A.1. Introduction

In the turbomachinery environment, the annular seal can be described as a small fluid-filled annular clearance between a stationary outer cylinder and a rotating inner cylinder with a fixed axial length. The seal configuration can be of various designs, including but not limited to: cylindrical, serrated, labyrinth, grooved and stepped.

Annular seals enable centrifugal pumps to operate in a satisfactory manner. The annular seal configuration is present at all wearing surfaces between the rotor and stator interfaces, where a seal is required between two individual high and low pressure chambers. Some examples where effective sealing is required are: impeller wear rings, balance pistons/drums and neck bush interfaces in multi-stage rotor arrangements.

It is of paramount importance for the pump designer (and user) to understand the impact of the annular seal clearance and the variation of such dimensions on the operation and performance of centrifugal pumps in general. The magnitude of internal leakage flow rate are directly related- and very sensitive to the annular seal clearance. When an increase of annular seal clearance is observed, a noticeable influence on the total flow rate through the impeller coupled with an operating point shift to the right of the performance curve, and a subsequent detrimental NPSHR shift has been highlighted in various texts including (Bloch, 2011), (Volk, 2013), (Yedidiah, 1996). One author (Gülich, 2014) states that the amount of observable annular seal leakage increases proportionately with an increase of annular clearance by: $Q_{sp} \propto s^{1.5}$, with a more pronounced effect with low specific speed pump designs.

Although some industry standards like API-610 (2011) do provide guidance with regards to recommended annular seal clearances, most original equipment manufacturers have their own design methodologies and clearance requirements for annular seal arrangements. The specified clearance is in some cases not specified to solely account for an optimal internal leakage restriction, but to counteract various mechanical concerns, such as: shaft deflection and rotordynamic stability,

materials prone to galling in certain services, etc. The preferred seal clearance is subsequently seen as a debatable value among users and their maintenance teams. The modelling of internal leakage through rotating annular seals is thus a primary concern for pump designers in order to enable accurate performance prediction of new and revised machine configurations.

Easily accessible computing resources have resulted in the increasing popularity of the utilization of CFD to aid the pump designer in determining accurate performance data in rapid time. The modelling of rotating annular seals are, however, a major difficulty in full pump 3D CFD applications due to excessive mesh density requirements in the vicinity of the annular seals, as mentioned by (Liebner et al., 2016)(Páscoa et al., 2010), especially when more than one annular seal is modelled, as in the case of multi-stage pumps. In order to aid in less computationally intensive techniques to be applied, an alternative method for computing annular seal leakage flows in large 3D CFD models is required.

This paper will present an approach to accurately model the leakage flow in short annular seals by means of a reduced order model of an existing iterative analytic method. The model was verified by Flownex® and applied as an expression in ANSYS® CFX®.

A.2. Theoretical model

Due to the predicable geometry of most annular seal types currently used in turbomachinery design and construction, computationally expansive CFD modelling requirements, coupled with sufficient available research relating to the flow field characteristics, makes internal leakage through annular seals an attractive candidate for ROM construction. Prior to any ROM construction actions, a reliable theoretical model should be identified to model the system of concern. The selected model and its implementation is explained below.

A.2.1. Method requirements

In order to accurately describe the leakage flow through an annular seal, certain key variables need to be included in the evaluation, including (but not limited to): Inlet- and outlet geometry and the surface roughness of the seal wetted area. The roughness cannot be ignored due to the flow field height to roughness ratio.

The model selected for the calculation of the leakage volumetric flow rate is as presented by Gülich in his published book (Gülich, 2014). The method will be explained and tested for accuracy by comparison to a commercial fluid dynamics software.

A.2.2. Model, as proposed by Gülich

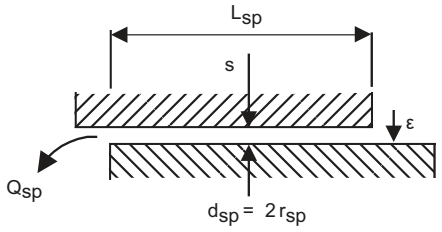


Figure A-1. Geometry of single stage annular seal

In order to calculate the volumetric flow rate through a rotating annular seal, a good understanding of the fluid properties are important. The kinematic viscosity ν is the most important fluid parameter in the current method. Note that the kinematic viscosity can be described by $\nu = \mu/\rho$ (Munson et al., 2013). It is important to take into account that this value will change with temperature and pressure, adequate compensation should be made in order to ensure the accuracy of the model. The model is only valid for fully turbulent flow in the annulus.

$$Q_{sp} = \pi d_{sp} s c_{ax} \tag{A.1}$$

As shown in equation (A.1); the leakage volumetric flow rate Q_{sp} is directly dependent on the OD of the rotating inner cylindrical surface d_{sp}, the measured radial clearance between the rotating and stationary surfaces s, and the axial flow velocity of the fluid in the annulus c_{ax}.

The formulation for the computation of c_{ax} is given in equation (A.2). Note the further dependency of various variables, including the difference in head observed across the annulus ΔH. Although it is possible to approximate this value analytically it is not preferred due to the fact that this variable can be calculated by referencing actual static pressure values during the CFD simulation run-time.

$$c_{ax} = \sqrt{\frac{2g\Delta H}{\zeta_{EA} + \lambda \frac{L_{sp}}{2s}}} \tag{A.2}$$

$$\zeta_{EA} = \zeta_E + \zeta_A \tag{A.3}$$

The annulus inlet pressure loss coefficient (ζ_E) and outlet pressure loss coefficient (ζ_A) were approximated by the included methodology presented in (Gülich, 2014), however these values can be approximated by methods outlined in various authoritative texts on fluid mechanics such as (Rennels and Hudson, 2012). The inlet and outlet loss coefficients were calculated as a sudden contraction and a sudden expansion with rounded edges without a back wall arrangement. These coefficients can have an unexpectedly large impact on the total flow rate computed through the annulus and care should be taken during the design of such devices.

$$\lambda = \underbrace{\left[1 + 0.19\left(\frac{Re_u}{Re}\right)^2\right]^{0.375}}_{\substack{\text{Influence of} \\ \text{rotation}}} \underbrace{\left[\frac{0.31}{\left\{\log\left(A + \frac{6.5}{Re}\right)\right\}^2}\right]}_{\text{Friction coefficient}} \tag{A.4}$$

The hydraulic friction loss coefficient λ, as per equation (A.4), ensures that the friction caused by the surface roughness in the axial direction is taken into account while concurrently compensating for the rotational effect experienced by the fluid as it passes through the rotating annulus setup. The addition of surface roughness effects is extremely beneficial to the analyst and this is one of the main benefits of using the current model.

The model is however highly implicit, equations (A.2), (A.4) and (A.8) are all dependent on each other. There is no way to compute Re without taking the mentioned equations into consideration.

$$A = 0.135\frac{\varepsilon}{s} \tag{A.5}$$

$$u_{sp} = \frac{\pi d_{sp} n}{60} \tag{A.6}$$

$$Re_u = \frac{2su_{sp}}{\nu} \tag{A.7}$$

$$Re = \frac{2sc_{ax}}{\nu} \tag{A.8}$$

In order to determine Re; equation (A.4) is substituted into (A.2), then equation (A.8) is manipulated to isolate c_{ax} and then equated to equation (A.2). The mentioned manipulations culminate to equation (A.9).

$$\frac{Re\nu}{2s} = \sqrt{\frac{2g\Delta H}{\zeta_{EA} + \lambda\frac{L_{sp}}{2s}}} \tag{A.9}$$

Although highly implicit; the reduced and simplified equation (A.9) enables the implementation of numeric root-finding algorithms, as the only truly unknown variable is Re. The root-finding algorithm implemented in the study was the secant method, as detailed in (Bradie, 2006). As can be derived, after the axial Reynolds number, Re, has been determined, simple substitution can be implemented in order to find the remaining dependant variables and finally Q_{sp}.

A.3. Reduced Order Model (ROM)

The main purpose of a ROM is to substitute a complex system of equations/methods/models, often encompassing iterative or numeric methods, with a mathematically equivalent analytic equation (or system of equations) that can be evaluated rapidly and implemented on demand. The effective implementation of ROMs in complex computational simulations (such as CFD analysis) dramatically reduces grid count, ensures better numerical stability and reduces solver run times without sacrificing solution accuracy.

In order to construct a ROM for use in general engineering applications it is required to obtain a large amount of reliable data to use as input to the mathematical model construction. The data required relates to the system being evaluated and the dependence on the particular system to other variables such as temperature, pressure etc.

A.3.1. Variable dependency

In order to construct an accurate ROM it is important to determine which physical parameters will influence the system and how one will effectively incorporate these parameters. The first step is to determine the variable dependency of the chosen model. As can be seen from section A.2.

Variable	Type	Dependency
s	Independent	Fixed geometry
d_{sp}	Independent	Fixed geometry
c_{ax}	Dependent	$Re \rightarrow \nu \rightarrow T, p$
ΔH	Dependent	CFD input

Table A-1. Variable dependency

From table A-1, most variables relating to the geometry of the annular seal installation are independent (i.e. $d_{sp}, s, \varepsilon, L_{sp}$ etc.) while the parameters relating to the fluid flow and the state of the fluid are dependent. It is notable that Q_{sp} is totally dependent on the axial Reynolds number, Re, while Re is in turn dependent on the kinematic viscosity of the fluid, ν, which in turn is directly dependent on the fluid temperature, T and pressure p. The differential head observed across the annular seal arrangement, ΔH, is an unknown, thus will have to be calculated and provided as an input to the model. The model is thus dependent on the main numerical model of the machine being simulated for the final dependent variable. In the current work, the differential head will be calculated by using CEL functions within ANSYS CFX during the solve.

A.3.2. Data generation

In order to generate a representative ROM, ample data relating to the physical system at different operating points are required.

	T_0	T_1	T_2	$\dots$	T_i
ΔH_0	$Q_{sp0,0}$	$Q_{sp0,1}$	$Q_{sp0,2}$	$\dots$	$Q_{sp0,i}$
ΔH_1	$Q_{sp1,0}$	$Q_{sp1,1}$	$Q_{sp1,2}$	$\dots$	$Q_{sp1,i}$
ΔH_2	$Q_{sp2,0}$	$Q_{sp2,1}$	$Q_{sp2,2}$	$\dots$	$Q_{sp2,i}$
$\vdots$	$\vdots$	$\vdots$	$\vdots$		$\vdots$
ΔH_j	$Q_{spj,0}$	$Q_{spj,1}$	$Q_{spj,2}$	$\dots$	$Q_{spj,i}$

Table A-2. Table of data with fixed geometry and ε

Table A-2 depicts a structured approach of data acquisition; with a fixed geometry (inlet and outlet geometry, surface roughness ε, diameters etc.) the model as described in section A.2 is solved for a range of expected ΔH and T values. Upon experimentation with liquid water it can be stated that p has a negligible influence on ν across the expected operating range expected in general turbomachinery related applications and can be safely omitted from the ROM construction.

A.3.3. Regression

The data generated in figure A-2 should be made accessible by means of regression. Regression should be performed per column, thus with fixed ΔH values as a function of T for each increment of ΔH that was determined.

ΔH_0	$x_0 T^y + ... + b_0 T^2 + a_0 T + const_0 = Q_{sp0}$
ΔH_1	$x_1 T^y + ... + b_1 T^2 + a_1 T + const_1 = Q_{sp1}$
ΔH_2	$x_2 T^y + ... + b_2 T^2 + a_2 T + const_2 = Q_{sp2}$
$\vdots$	$\vdots$
ΔH_i	$x_i T^y + ... + b_i T^2 + a_i T + const_i = Q_{spi}$

Table A-3. Polynomial regression at every ΔH to find Q_{sp} as a function of T

Table A-3 describes the intended regression steps and is represented by polynomial equations. Note that all regression formulae should be of the same order/type. The format can be adapted to a scheme that best represents the data provided that all formats are of the same order. After regression of the data had been completed, Q_{sp} can be easily computed at any T (within the modelled range) with a single equation that corresponds to the specified ΔH.

$$\begin{aligned} z_0\Delta H^y + ... + r_0\Delta H^2 + q_0\Delta H + const_0 = &\quad const(\Delta H) \\ z_1\Delta H^y + ... + r_1\Delta H^2 + q_1\Delta H + const_1 = &\quad a(\Delta H) \\ z_2\Delta H^y + ... + b_2\Delta H^2 + a_2\Delta H + const_2 = &\quad b(\Delta H) \\ \vdots & \\ z_i\Delta H^y + ... + b_i\Delta H^2 + a_i\Delta H + const_i = &\quad x(\Delta H) \end{aligned}$$

Table A-4. Polynomial regression of data in table A-3 to find polynomial coefficients as a function of ΔH

In order to enable greater flexibility in the regression functions and to condense the magnitude of equations required, model sensitivity to a range of ΔH needs to be incorporated. Regression of the individual polynomial coefficients are completed as a function of temperature, as shown in table A-4. Here, the order and type of the generated regression equations need not all be similar in form and order.

A.3.4. Final form of ROM

In order to reduce the system of equations generated in tables A-3 and A-4 into a single polynomial function, the functions that represent the polynomial coefficients are incorporated into the form of the regression function in table A-3.

$$x(\Delta H)T^y + b(\Delta H)T^2 + a(\Delta H)T + const(\Delta H) = Q_{sp} \tag{A.10}$$

Equation A.10 is the final form of the ROM. This equation is a function of T and ΔH over the complete range of test data. The annular seal leakage, Q_{sp} can thus be predicted analytically with this single equation that can be easily programmed into a numerical solver environment.

A.4. Verification

A.4.1. Calculated data set

In order to verify the selected mathematical model, it will be tested against existing software. The independent variable inputs to both models are as shown in table A-5.

s $[m]$	d_{sp} $[m]$	n $[RPM]$	L_{sp} $[m]$	ζ_{EA} $[-]$	ε $[m]$
0.00025	0.2655	2985	0.0379	1.1787	0

Table A-5. Input independent variables to the test case

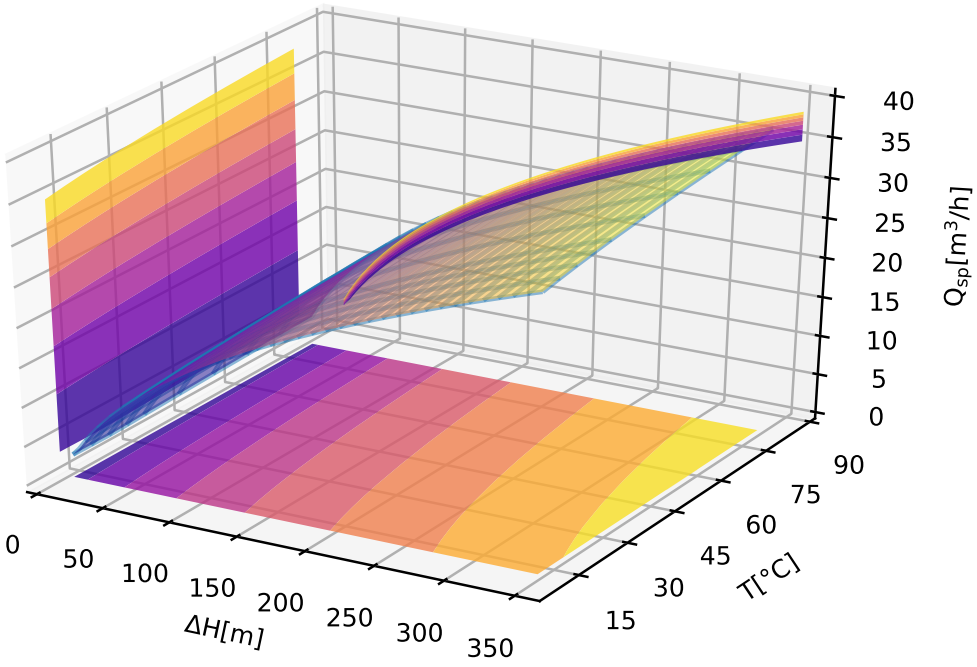


Figure A-2. Calculated Q_{sp} across a range of data as per section A.2

The working fluid was selected to be clean water. The density and dynamic viscosity, μ had been calculated using IAPWS principles, thus; ρ, was calculated using (IAPWS-R7-97, 2012) and the dynamic viscosity, μ, was calculated using (Huber et al., 2009) for each temperature stated. The pressure, p, was taken as the inlet absolute pressure of the pump - as the pressure rise due to the pumping mechanics will impact the fluid properties to an insignificant degree. The kinematic viscosity, ν, was then calculated by the equation $\nu = \mu/\rho$ for each operating point. The calculation was conducted across a range of $[10m \leqslant \Delta H \leqslant 350m]$ and $[283.15K \leqslant T \leqslant 353.15K]$, as depicted in figure A-2.

A.4.2. Flownex-Gülich verification

Table A-5 specifies a surface roughness, ε, of $0m$, this is due to the fact that Flownex cannot implement surface roughness into its evaluation of rotating annular seal leakages at the current time. Thus a base case of $\varepsilon = 0m$ was selected.

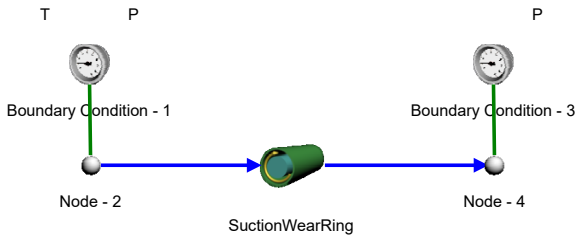


Figure A-3. Model created in Flownex

As per (Flownex, 2018); Flownex calculates the expected annular seal leakage flow by iteration using culminated techniques outlined in the following publications: (Yamada, 1962),(White, 1999),(Taylor, 1923) (Kaye and Elgar, 1958), and (Cornish, 1933). The methods have been verified and is included in the Flownex® 8.9.1.3592 release.

ΔH $[m]$	T $[^\circ C]$	Gülich Q_{sp} $[m^3/h]$	Flownex Q_{sp} $[m^3/h]$	$\frac{\text{Gülich}}{\text{Flownex}}$
45	10	9.516	9.363	1.016
80	15	14.430	14.071	1.025
105	20	17.408	16.967	1.026
135	25	20.539	20.009	1.026
180	30	24.583	23.989	1.025
205	40	26.957	26.346	1.023
225	50	28.827	28.224	1.021
160	60	24.049	23.531	1.022
135	70	22.058	21.586	1.022
105	80	19.250	18.826	1.022

Table A-6. Variable dependency

Figure A-3 depicts the model setup in Flownex®. The specified fluid is the built in fluid: H2O - Water| General (Two Phase Fluids) Master. The inlet and outlet node absolute static pressure values were specified after being calculated with reference to the required differential head, ΔH. The inlet T was adapted as required by the specified test points. The annular seal was divided into 20 elements and reached full program convergence after each step. Table A-6 depicts a (shortened) range of test points, with modified units for Q_{sp} and T to ease interpretation of magnitude and comparison with figure A-2.

Data points	Average	Median	σ
680	1.0238	1.0242	0.0118

Table A-7. Analysis of values; $\frac{\text{Gülich}}{\text{Flownex}}$

Upon evaluation of table A-7; the method as proposed by Gülich generally predicts approximately 2.4% more leakage flow when compared with Flownex® when considering $\varepsilon = 0m$. The model is consistent over a wide range of temperature and differential head and can be considered accurate and fit for use.

A.4.3. Gülich-ROM verification

A ROM was constructed utilizing the method outlined in sections A.2 and A.3. The resulting equations were produced, as shown in equations A.11a to A.11e.

$$d(\Delta H)T^3 + c(\Delta H)T^2 + b(\Delta H)T + a(\Delta H) = Q_{sp} \tag{A.11a}$$

$$\begin{aligned} &1.17449\exp\{-11\}\Delta H^5 - 1.31299\exp\{-8\}\Delta H^4 + ... \\ &+ 5.83278\exp\{-6\}\Delta H^3 - 1.36951\exp\{-3\}\Delta H^2 + ... \\ &+ 0.246651\Delta H + 0.164876 = a(\Delta H) \end{aligned} \tag{A.11b}$$

$$\begin{aligned} &7.51733\exp\{-14\}\Delta H^5 - 7.90636\exp\{-11\}\Delta H^4 + ... \\ &+ 3.18534\exp\{-8\}\Delta H^3 - 6.28108\exp\{-6\}\Delta H^2 + ... \\ &+ 7.70495\Delta H\exp\{-4\} + 0.029208 = b(\Delta H) \end{aligned} \tag{A.11c}$$

$$
\begin{aligned}
&- 6.43846\exp\{-16\}\Delta H^5 + 6.81099\exp\{-13\}\Delta H^4 - ... \\
&- 2.76039\exp\{-10\}\Delta H^3 + 5.45809\exp\{-8\}\Delta H^2 - ... \\
&- 6.56047\Delta H\exp\{-6\} - 2.40868\exp\{-4\} = c(\Delta H)
\end{aligned} \tag{A.11d}
$$

$$
\begin{aligned}
&2.34674\exp\{-18\}\Delta H^5 - 2.50829\exp\{-15\}\Delta H^4 + ... \\
&+ 1.02979\exp\{-12\}\Delta H^3 - 2.06901\exp\{-10\}\Delta H^2 + ... \\
&+ 2.53314\Delta H\exp\{-8\} + 9.80977\exp\{-7\} = d(\Delta H)
\end{aligned} \tag{A.11e}
$$

The independent variables were selected and specified as per section A.4, across the same range as defined in subsection A.4.2. A range of data points were generated and a shortened version of this data is presented in table A-8 with modified units for Q_{sp} and T to ease interpretation of magnitude and comparison with figure A-2.

ΔH $[m]$	T $[°C]$	Gülich Q_{sp} $[m^3/h]$	ROM Q_{sp} $[m^3/h]$	$\frac{\text{Gülich}}{\text{ROM}}$
45	10	9.516	9.465	1.005
80	15	14.430	14.466	0.997
105	20	17.408	17.441	0.998
135	25	20.539	20.530	1.001
180	30	24.583	24.552	1.001
205	40	26.957	26.952	1.001
225	50	28.827	28.845	0.999
160	60	24.049	24.011	1.002
135	70	22.058	22.045	0.919
105	80	19.250	19.296	0.998

Table A-8. Variable dependency

Data points	Average	Median	σ
680	0.9986	1	0.0125

Table A-9. Analysis of values; $\frac{\text{Gülich}}{\text{ROM}}$

Upon evaluation of table A-9; the ROM generally predicts on average 0.14% less leakage flow with a 0% median deviation when compared with the Gülich model when considering $\varepsilon = 0m$. The model is consistent and extremely accurate over a wide range of temperature and differential head and can be considered accurate and fit for use.

A.5. Implementation in ANSYS® CFX®

The method described in section A.2 and verified in section A.4 can be implemented in commercial CFD packages with user scripting capability. An example of such implementation will be made using ANSYS CFX CEL expression language.

Various key variables need to be calculated prior to implementing a ROM of the intended system, the following methodologies and syntax have been tested and is fully functional:

The ΔH variable can be calculated during the solve by specifying the annular seal flow area entrance and exit as a named selection on the discharge- and suction volutes of the pump respectively.

The following expression will be sufficient for the determination of $\Delta H = WearRingdeltaH$ in the ANSYS CFX CEL expression language:

(((**areaAve**(Pressure)@
REGION:DischargeWearRing_Interface)/(g***areaAve**(density)@
REGION:Discharge WearRing_Interface))-((**areaAve**(Pressure)@
REGION:Suction_WearRing_Interface)/(g***areaAve**(density)@
REGION:Suction_WearRing_Interface)))/(1[m])

$T = WearRingInletTemperature$ can be expressed as:

((**areaAve**(T)@**REGION:Discharge WearRing_Interface**)/(1[K]))-273.15

$Q_{sp} = WearRingLeakageROM$ can be expressed as:

(((ROMx3const*WearRingInletTemperature^3)+(ROMx2const*WearRingInletTemperature^2)+
(ROMxconst*WearRingInletTemperature)+(ROMcconst))/60/60)*(1[m3̂/s])*
areaAve(density)@**REGION:Discharge WearRing_Interface**

It should be noted that the equations for ΔH and T should be non-dimentionalized before the implementation of the constructed ROM. After the implementation of the method the answer will be re-dimentionalized for input into the solver. Note that the flow rate required for input to an inlet boundary condition in the CFX solver is kg/s, thus Q_{sp} would require conversion to this unit. The noted variables; $ROMx3const$, $ROMx2const$, $ROMxconst$ and $ROMcconst$ are respectively equal to $d(\Delta H)$, $c(\Delta H)$, $b(\Delta H)$ and $a(\Delta H)$.

A.6. Conclusion

The method presented in this Annexure proved the accuracy of properly constructed ROM's for use in practical CFD analysis. The method proposed will ensure accurate modelling of annular seal flow leakage in centrifugal pumps with single stage cylindrical annular seals with hydraulically smooth surface finish, however; the method described in section A.2 does enable the analyst to account for surface roughness. The model is considered adequate for use with surface roughness effects included. The inclusion of surface roughness makes the proposed model and ROM generation technique superior to techniques focused on hydraulically smooth profiles due to the significant effect of roughness on the leakage rate, Q_{sp}. A method to implement generated ROM's in ANSYS CFX is also presented. The model had been tested and is fully functional when properly applied and verified. The implementation of this model will ensure dramatic mesh size reduction with excellent solution accuracy and an increase of overall solver speed. The methodology can be applied to seals with other designs and fluids.

B. ANSYS® CFX® CEL implementation

The CEL expression language algorithms used in the definition of various boundary condition values and monitor points are discussed in this Annexure. The formulae are written exactly as constructed in CFX-Pre, thus it is the actual working algorithms.

B.1. Annular seal Reduced Order Model

WearRingInletTemperature = ((**areaAve**(T) @ **REGION:Discharge WearRing_Interface**)/(1[K])) - 273.15.

WearRingdeltaH = (((**areaAve**(Pressure) @ **REGION:Discharge WearRing_Interface**)/(g*__areaAve__(density) @ **REGION:Discharge WearRing_Interface**)) - ((**areaAve**(Pressure) @ **REGION:Suction_WearRing_Interface**)/(g*__areaAve__(density) @ **REGION:Suction_WearRing_Interface**)))/(1[m])

ROMcconst = if(WearRingdeltaH <=100,
(((3.50566878725597*10^(-10))*WearRingdeltaH^5) +
((-1.45399126075547*10^(-7))*WearRingdeltaH^4) +
((0.0000261181565507009)*WearRingdeltaH^3) +
((-0.00282097133473297)*WearRingdeltaH^2) + ((0.277225797567424)*WearRingdeltaH) +
(-0.345474063235185)),
(((1.82505965876411*10^(-7))*WearRingdeltaH^3) +
((-0.00019864742795027 5)*WearRingdeltaH^2) + ((0.11999207827543)*WearRingdeltaH) +
(4.10668170563444)))

ROMx2const = if(WearRingdeltaH <=100,
(((-1.12862783929567*10^(-13))*WearRingdeltaH^5) + ((4.02607051715195*10^(-11))*
WearRingdeltaH^4) + ((-5.70949678605405*10^(-9))*WearRingdeltaH^3)
+((4.07284918941674*10^(-7))*WearRingdeltaH^2) +
((-0.0000151091927031241)*WearRingdeltaH) + (-0.00014535997401775)),
(((-4.05097343227527*10^(-13))*WearRingdeltaH^3) +
((4.36844623524572*10^(-10))*WearRingdeltaH^2) +
((-2.39492571451993*10^(-7))*WearRingdeltaH) + (-0.000376754971412105)))

ROMx3const = if(WearRingdeltaH <=100,
(((5.40889680585463*10^(-16))*WearRingdeltaH ^5) + ((-1.93820156454775*10^(-13))*
WearRingdeltaH^4) + ((2.76727047103652*10^(-11))*WearRingdeltaH^3) +
((-1.99645192582853*10^(-9))* WearRingdeltaH^2) + ((7.58388345410361*10^(-8))*
WearRingdeltaH) + (5.0221817027061*10^(-7))),
(((3.43937442958384*10^(-15))*WearRingdeltaH^3) +
((-3.52170870917029*10^(-12))*WearRingdeltaH^2) +
((1.62471920169429*10^(-9))*WearRingdeltaH) + (1.69144292568636*10^(-6))))

ROMxconst = if(WearRingdeltaH <=100,
(((8.62725821688937*10^(-12))*WearRingdeltaH^5)
+((-3.05251287279439*10^(-9))*WearRingdeltaH^4)

+((4.27444595561559*10^(-7))*WearRingdeltaH^3) +
((-0.0000298220382749498)*WearRingdeltaH^2) + ((0.0010525449020497)*WearRingdeltaH)
+(0.0184337726584669)),
(((-1.59827687030638*10^(-11))*WearRingdeltaH^3) +
((1.0781828128422*10^(-8))*WearRingdeltaH^2) +
((1.41636038877302*10^(-6))*WearRingdeltaH) + (0.033686196303166)))

WearRingLeakageROM = (((ROMx3const*WearRingInletTemperature^3) +
(ROMx2const*WearRingInletTemperature^2) + (ROMxconst*WearRingInletTemperature) +
(ROMcconst))/60/60)*(1[m^3/s])* **areaAve**(density) @ **REGION:Discharge**
WearRing_Interface

WearRingOutletV = (WearRingLeakageROM/**areaAve**(density) @ **REGION:Discharge**
WearRing_Interface)/**area**() @ **REGION:Discharge WearRing_Interface**

WearRingPowerLoss = (((9.91213398783052*10^(-6))*WearRingInletTemperature^4) +
(-0.00256954213124583*WearRingInletTemperature^3) +
(0.27514325313904*WearRingInletTemperature^2) +
(-17.7779452022768*WearRingInletTemperature) + (1895.16954883129))*1[kg m^2 s^-3]

B.2. Boundary conditions

myRPM = ((-1)*(2985/60)*2*pi) [s^-1]

myTimescale = 1[rad]/(-1*myRPM)

myTemp = (20+273.15)[K]

myVaporPressure = 100*(10^(5.40221-(1838.675/(-31.737+(myTemp/1[K])))))[kPa]

B.3. Torque

For unmodified geometry:

myTorque = **torque_z**()@**REGION:Entire BLADE** + **torque_z**()@**REGION:Entire**
SHROUD + **torque_z**()@**REGION:Entire HUB** +
torque_z()@**REGION:Impeller_WearRing_Suction_Fillet** +
torque_z()@**REGION:Impeller_Outer** +
torque_z()@**REGION:Suction_ShaftInterface** + (WearRingPowerLoss/(**abs**(myRPM)))

For modified geometry:

myTorque = **torque_z**()@**REGION:Ring_Surface** + **torque_z**()@**REGION:Entire**
BLADE + **torque_z**()@**REGION:Entire SHROUD** + **torque_z**()@**REGION:Entire**
HUB + **torque_z**()@**REGION:Impeller_WearRing_Suction_Fillet** +
torque_z()@**REGION:Impeller_Outer** +
torque_z()@**REGION:Suction_ShaftInterface** + (WearRingPowerLoss/(**abs**(myRPM)))

B.4. Custom monitor points

myEfficiency = **abs**(**massFlow**()@**Inlet_SuctionVolute***myHead*g/myPower)

myHead = (**massFlowAve**(Total Pressure in Stn Frame)@**Outlet_DischargeVolute** - **massFlowAve**(Total Pressure in Stn Frame)@**Inlet_SuctionVolute**)/(g***ave**(Density)@**Inlet_SuctionVolute**)

myHeadImpeller = (**massFlowAve**(Total Pressure in Stn Frame)@**REGION:Entire OUTFLOW** - **massFlowAve**(Total Pressure in Stn Frame)@**REGION:Entire INFLOW**)/(g***ave**(Density)@**REGION:Entire INFLOW**)

myHeadStatic = (**massFlowAve**(Pressure)@**Outlet_DischargeVolute** - **massFlowAve**(Pressure)@**Inlet_SuctionVolute**)/(g***ave**(Density)@**Inlet_SuctionVolute**)

myPower = myTorque***abs**(myRPM)

NPSH = (**massFlowAve**(Total Pressure in Stn Frame)@**Inlet_SuctionVolute**)/(g***ave**(Density)@**Inlet_SuctionVolute**)

C. Assessment of test pump geometry

The accuracy of any CFD analysis is heavily dependent on the geometric accuracy of the physical model under investigation. In order to accurately measure the impeller geometry of the current pump, destructive methods would allow the most accurate measurement. Due to the fact that the equipment is actively used in industrial processes and is considered a high value component, destructive testing of functional components is not allowed.

C.1. Measurement standard

In accordance with EN-ISO-8062-3 (2007), the recommended Dimensional Casting Tolerance Grade (DCTG) range for sand castings that are machine moulded (considering steel/nickel based alloys) for long-series production castings range between DCTG-8 to DCTG-12, the tolerances are shown in table C-1. Additionally, the Geometrical Casting Tolerance Grade (GCTG), which governs geometric features, is recommended to range between GCTG-5 to GCTG-7, the tolerances are shown in table C-2.

Table C-1. Adaptation of EN-ISO-8062-3 (2007) Table 2 - Linear Dimensional Casting Tolerances

Nominal Dimension $[mm]$	DCTG-8 $[\pm mm]$	DCTG-9 $[\pm mm]$	DCTG-10 $[\pm mm]$	DCTG-11 $[\pm mm]$	DCTG-12 $[\pm mm]$
$x \leq 10$	0.5	0.75	1	1.4	2.1
$10 < x \leq 16$	0.55	0.8	1.1	1.5	2.2
$16 < x \leq 25$	0.6	0.85	1.2	1.6	2.3
$25 < x \leq 40$	0.65	0.9	1.3	1.8	2.5
$40 < x \leq 63$	0.7	1	1.4	2	2.8
$63 < x \leq 100$	0.8	1.1	1.6	2.2	3
$100 < x \leq 160$	0.9	1.25	1.8	2.5	3.5
$160 < x \leq 250$	1	1.4	2	2.8	4

Table C-2. Adaptation of EN-ISO-8062-3 (2007) Table 4 and 5 - Casting Tolerances

Nominal Dimension $[mm]$	Table 4 - Flatness GCTG-5 $[\pm mm]$	GCTG-6 $[\pm mm]$	GCTG-7 $[\pm mm]$	Table 5 - Roundness and symmetry GCTG-5 $[\pm mm]$	GCTG-6 $[\pm mm]$	GCTG-7 $[\pm mm]$
$x \leq 10$	0.2	0.3	0.45	0.3	0.45	0.7
$10 < x \leq 30$	0.3	0.45	0.7	0.45	0.7	1
$30 < x \leq 100$	0.45	0.7	1	0.7	1	1.5
$100 < x \leq 300$	0.7	1	1.5	1	1.5	2.25

Complex geometry tolerances are not explicitly specified by EN-ISO-8062-3 (2007) e.g. profile of vane geometry, or the hub curvature. The mentioned geometries will thus be evaluated based on a combination of tolerances detailed in tables C-1 and C-2.

C.2. Measurement equipment and analysis software

The measurements were conducted by utilising a FARO® Quantum^{S} 3.5m FaroArm® 7 axis laser scanner. As per ISO 10360-8 (2013) and ISO 10360-12 (2016); the maximum permissible error of the arm is rated at: volumetric accuracy of the equipment is 0.07mm, with a Single Point Articulation Test (SPAT) repeatability at 0.045mm. The laser scanner was calibrated to 0.021mm error on the probe hole compensation calibration and 0.024mm volumetric error on the laser scanner calibration prior to the measurement being executed. The measurement was executed indoors, at an ambient temperature of 24°C.

The analysis of the results were completed by utilising the following software packages: Geomagic® DesignX^{TM} 19.0.2 and Geomagic® ControlX^{TM} 18.0.1.

C.3. Impeller

C.3.1. Measurement setup

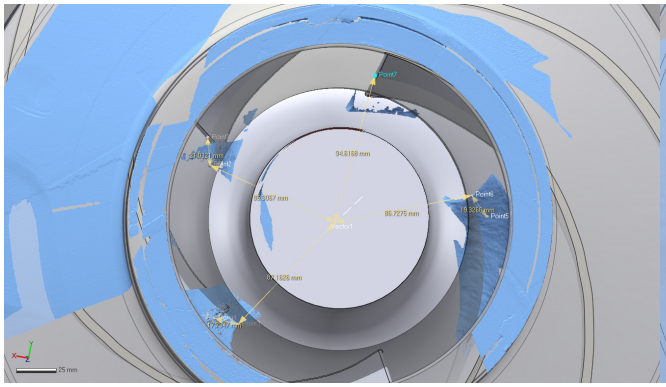


Figure C-1. The setup at time of 3D scanning.

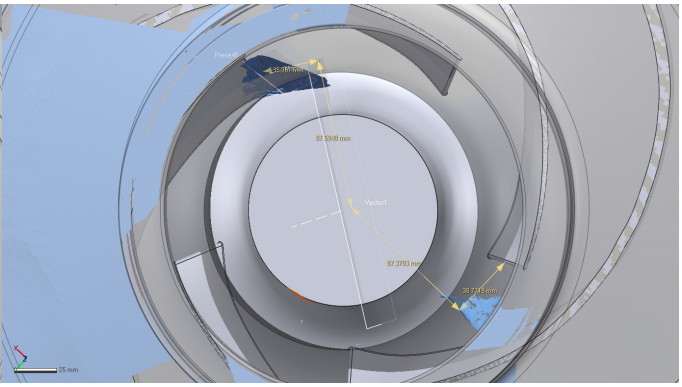
Fig. C-1 depicts the setup of the test pump impeller prior to scan execution. It is to be noted that the (production ready) shaft assembly is supported on two trestles. The figure shows the available scan area. The accessibility of the laser scanning equipment at the two eyes have been severely restricted by the presence of the shaft, nonetheless representative measurements were completed of portions of both eyes and also a portion of the outside diameter of the impeller.

C.3.2. Visual evaluation of measurement results of the impeller used during testing

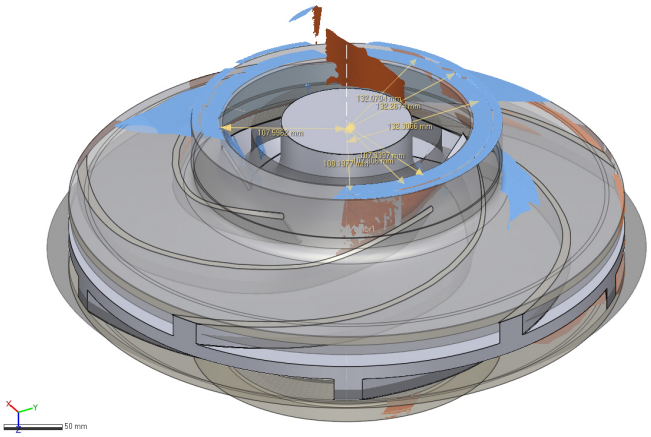
Figure C-2 depicts the comparison between the generated impeller geometry and the partial scan of the actual impeller geometry considered in this study. The major deviations on the vanes are the length of the extension into the eye of the impeller itself. There also exists a difference between the two impeller eyes regarding the vane length as per figs. C-2a and C-2b,



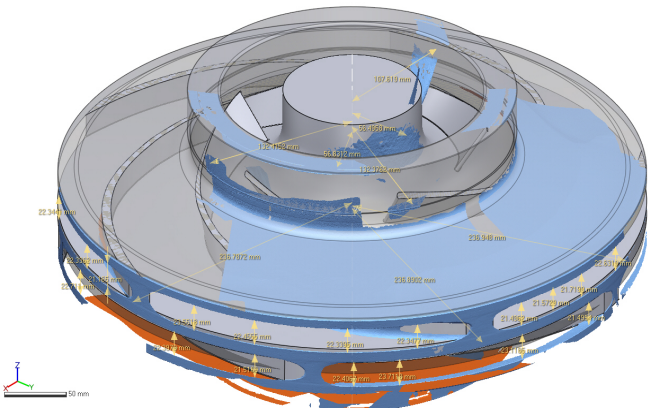
(a) Left impeller half/eye, showing the measured leading edge radius $0.5d_{1b}$ and linear leading edge deviation as measured on the mean line construction surface.



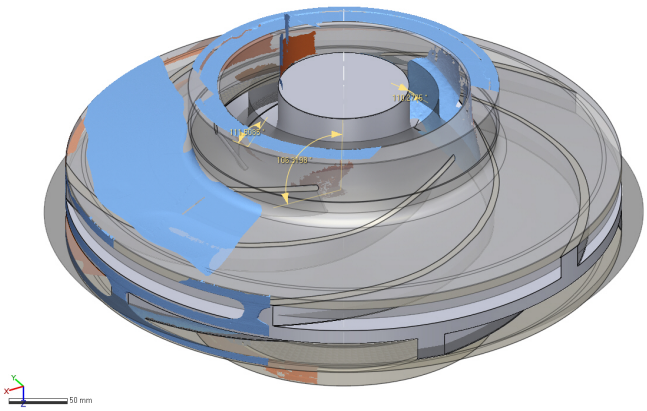
(b) Right impeller half/eye, showing the measured leading edge radius $0.5d_{1b}$ and linear leading edge deviation as measured on the mean line construction surface



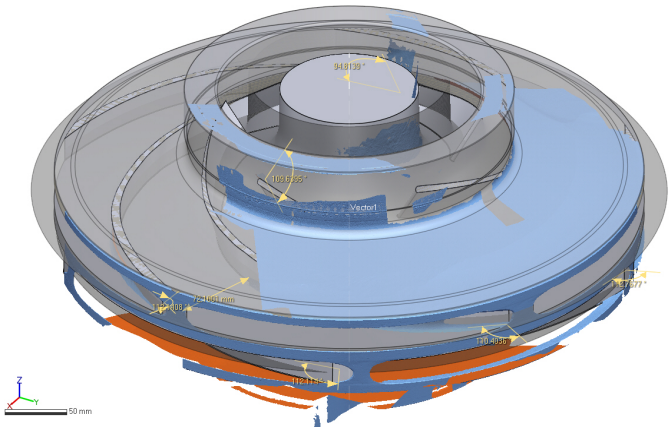
(c) Left impeller half/eye, showing relevant radial and linear measurements.



(d) Right impeller half/eye, showing relevant radial and linear measurements.



(e) Left impeller half/eye, showing relevant vane inlet angle measurements. All measured vane outlet angles are also shown.



(f) Right impeller half/eye, showing relevant vane inlet angle measurements.

Figure C-2. Illustration of the linear and angular measurements taken on the 3D scanned point cloud of the impeller which was used in the pump test. The point cloud measurements are compared to the model geometry.

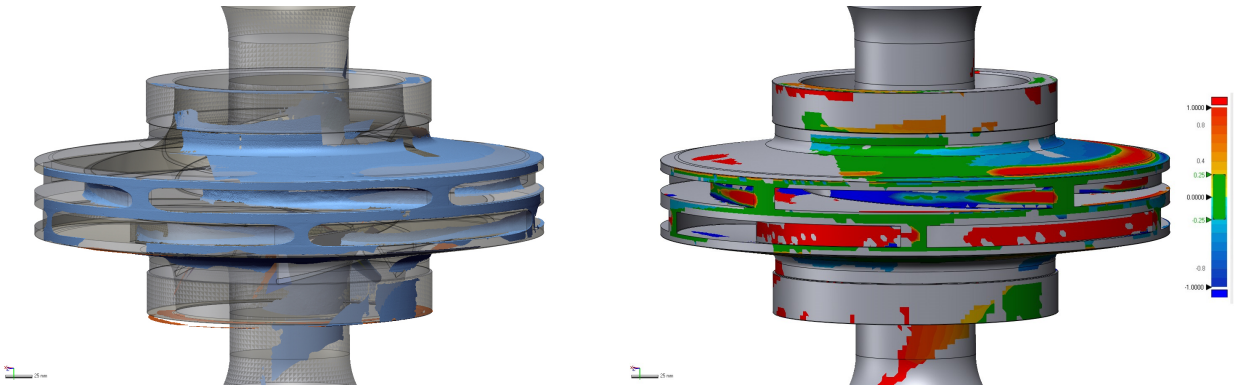
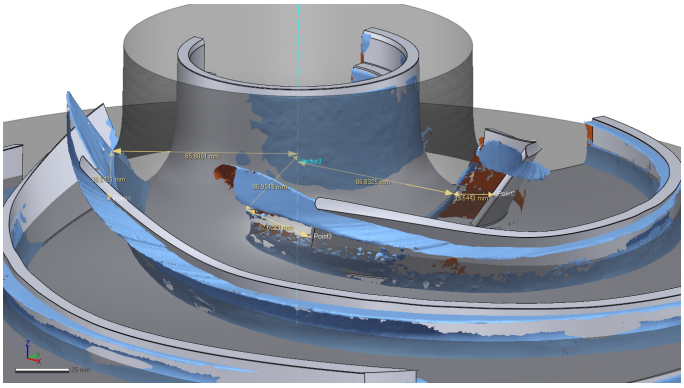
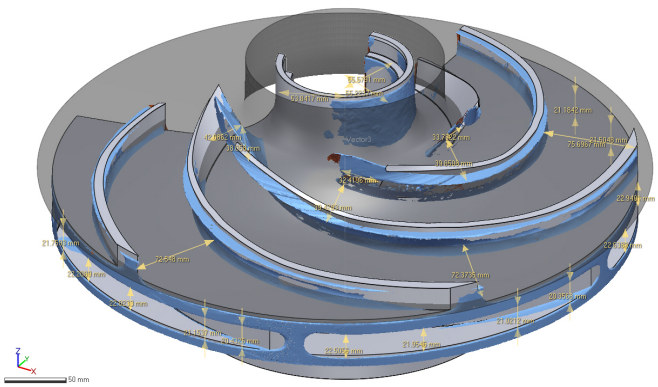


Figure C-3. Partial scan of shrouded (tested) impeller outlet geometry.

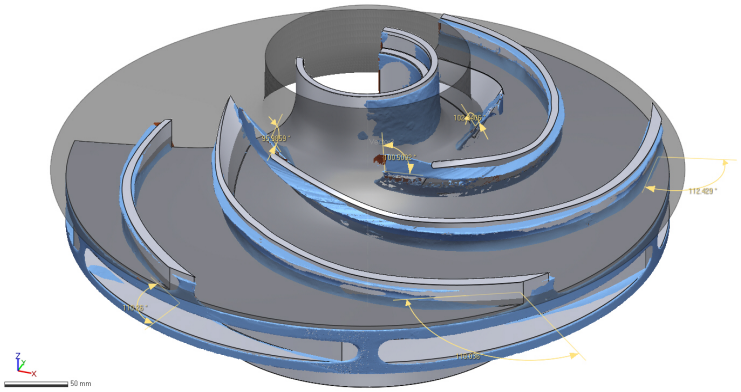
C.3.3. Visual evaluation of measurement results of similar impeller after destructive machining



(a) Right impeller half/eye, showing the measured leading edge radius $0.5d_{1b}$ and linear leading edge deviation as measured on the mean line construction surface



(b) Right impeller half/eye, showing relevant radial and linear measurements.



(c) Right impeller half/eye, showing relevant vane inlet and outlet angle measurements.

Figure C-4. Illustration of the linear and angular measurements taken on the 3D scanned point cloud of a similar impeller which was destroyed for measurement purposes. The point cloud measurements are compared to the model geometry.

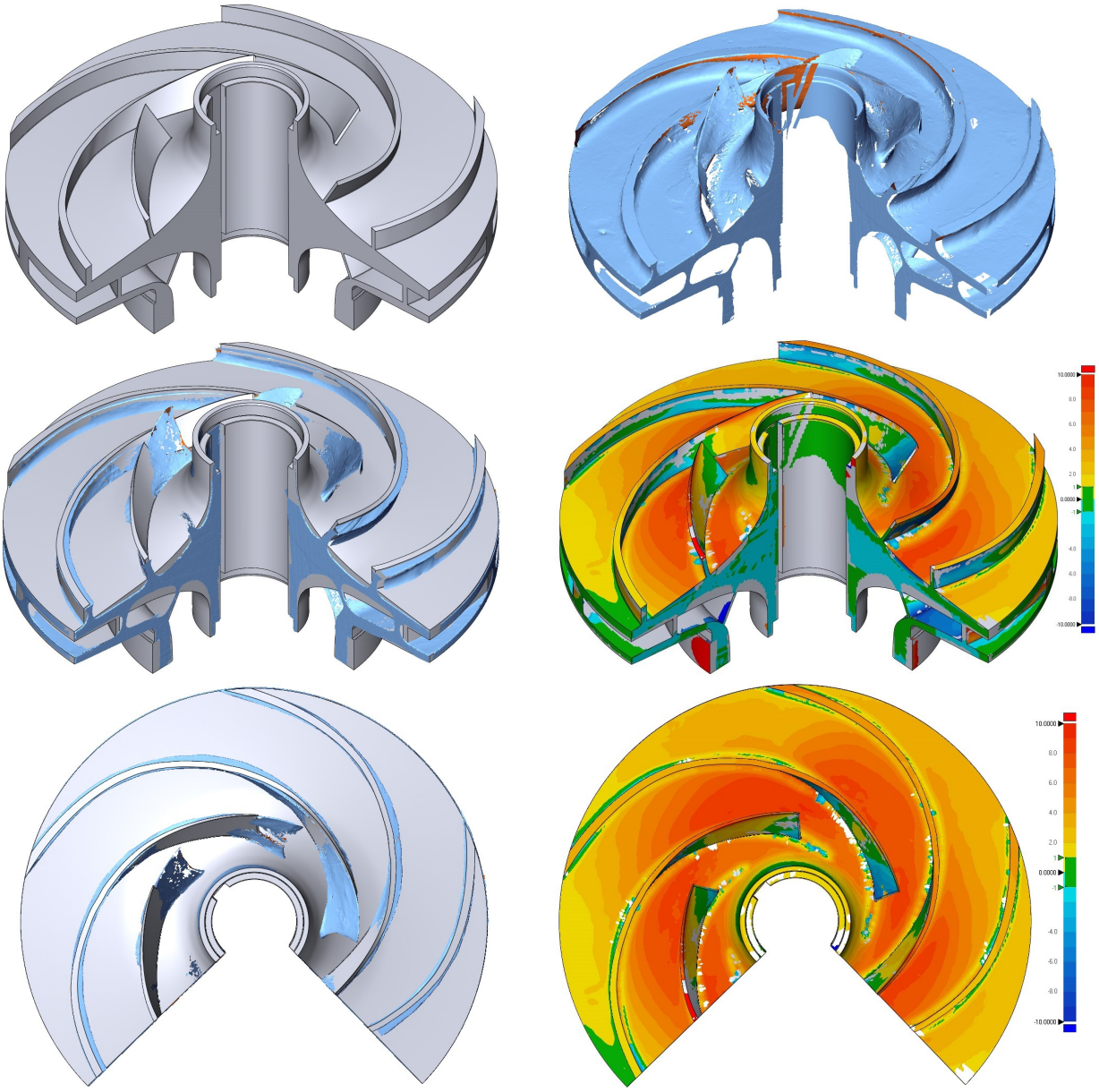


Figure C-5. Accuracy of in site geometry vs ideal design

In order to inspect the hub and bade profiles, a scrapped impeller from the same production facility and production run was deshrouded and accurately surveyed by means of 3D laser scanning. The results of the scan was compared with the modeled (ideal) impeller geometry used during pump testing.

C.3.4. Evaluation to set standard

The measured geometry - as shown in representative figs. C-2, C-3, C-4 and C-5 - were compared with the idealised impeller geometry as used in the CFD analysis. The ideal geometry was measured for acceptability by comparing the deviations to the measured geometry by means of comparing the data with the acceptance standards for industrial castings as stipulated in EN-ISO-8062-3 (2007), and specified in tables C-1 and C-2. Industrial production multi-core large impeller sand castings are known for geometric deviations due to the inherent nature of the process and the complexities of cores, thus the acceptance criteria (as can be reasonably expected from foundries - in the absence of specific specified tolerances) corresponding to the casting material type, as stipulated in EN-ISO-8062-3 (2007), was adopted. The deviations, as acquired by 3D laser scanning, is shown in tables C-3 and C-4.

Considering fig. C-5 and table C-4, the representative internal location, thickness and the shape of the vanes (apart from the leading edge deviations) are accurate within reasonable observation. The representative hub profile, however, is less favourable and the large deviations noted is indicative of casting pattern wear and/or sub-optimal casting control and technique. The throat area will be enlarged, this will in turn cause a slower average flow velocity through the knee of the meridional passage. The shroud seems to be accurate.

As can be observed from tables C-3, and figs. C-2a and C-2b: there exists a substantial difference in the vane leading edge length ΔL_{sch}, even between the two impeller halves of the test impeller. Additionally, there exists a noticeable deviation in the the perceived vane inlet metal angles (β^*_{1B}, as measured on the meanline on the suction side of the vanes) - both between the separate halves and individual blades. The inlet leading edge pitch diameters (d_{1b}) does comply with the roundness requirement. The outlet metal angles, β^*_{2B} (as measured on the pressure side of the vanes), show a much more consistent outlet angle on all measured blades - only marginally outside of the specified value.

The linear dimensions are much more consistent across the entire measured spectrum. When evaluating the linear and roundness magnitudes, see tables C-3 and C-4, most of the critical feature dimensions satisfy the stated criteria. The b_2 measurement falls narrowly outside of the limits (for the measured values), while the $a1$ and $a2$ magnitudes were also narrowly rejectable. The impeller inlet hub, eye and outlet radial diameters and roundness dimensions are also acceptable. The impeller outlet diameter is machined, and thus complies with the specification. Note that the wear ring outside diameter, r_{sp} was measured prior to re-applying the wear resistant coating; the outside diameter of this part was ground to within 0.04mm tolerance of 133mm prior to installation.

When the measured geometry in tables C-3 and C-4 are strictly compared with the limits set in tables C-1 and C-2, the conclusion can be made that the supplied impellers, and the impeller used as the model pump in this study have geometric flaws that renders it subject to rejection on the basis of non-compliance with the limits set in EN-ISO-8062-3 (2007). Although the previous statement is strictly true, EN-ISO-8062-3 (2007) does make provision for the acceptance of castings which does not comply strictly to all dimensions, as stated in paragraph 10 of the mentioned standard: "Unless otherwise stated, workpieces exceeding the general tolerances shall not lead to automatic rejection, provided that the ability of the workpiece to function is not impaired (see C.4)." As the impeller still performs reasonably, there is no direct cause for automatic rejection by the user - even though noticeable geometric inadequacies exist. The detail of measurement performed in this section is not expected to be achieved by artisans which accept the castings, thus the supplied impellers (with all the mentioned geometrical defects) are readily installed and used in the production pumps used in the tests.

Table C-3. Evaluation of unmachined (cast) geometric impeller features vs. the ideal impeller geometry, as per EN-ISO-8062-3 (2007) by means of laser scanning.

Fig.	Feature	Target $x[mm]$ $\theta[°]$	Nom. Dim. $\Delta x[mm]$ $\Delta\theta[°]$	Deviation $\Delta x[mm]$ $\Delta\theta[°]$	DCTG Grade	GCTG Grade	Pass/ Fail
Evaluation to EN-ISO-8062-3 (2007) of the Left Impeller Half							
C-2d	b_2	20.25	$16 < x \leq 25$	$1.25 \leq \Delta x \leq 3.46$	>12	-	Fail
C-2c	r_n	55	$40 < x \leq 63$	-	-	-	-
C-2c	Δr_n	0	$40 < x \leq 63$	-	-	-	-
C-2c	r_1	105.45	$100 < x \leq 160$	$1.89 \leq \Delta x \leq 2.75$	12	-	Pass
C-2c	Δr_1	0	$100 < x \leq 300$	$\Delta x \leq 0.86$	-	<7	Pass
C-2f	β^*_{1B}	11.64	$\theta \leq 2.58$ [1]	$4.68 \leq \Delta\theta \leq 9.87$	-	>7	Fail
C-2f	β^*_{2B}	19.37	$\theta \leq 2.58$ [1]	$\Delta\theta \leq 2.74$	-	>7	Fail
C-2f	$a1$	41.62	$40 < x \leq 63$	-	-	-	-
C-2f	$a2$	68.95	$63 < x \leq 100$	-	-	-	-
C-2d	ΔL_{sch}	0	$x \leq 10$	$17.73 \leq \Delta x \leq 21.03$	>12	-	Fail
C-2a	r_{1b}	94.62	$63 < x \leq 100$	$-9.31 \leq \Delta x \leq 7.46$	>12	-	Fail
C-2a	Δr_{1b}	0	$30 < x \leq 100$	$\Delta x \leq 1.86$	-	>7	Fail
C-2c	r_{sp}	133	$100 < x \leq 160$	$-0.93 \leq \Delta x \leq -0.69$	<8	-	Pass
C-2c	Δr_{sp}	0	$100 < x \leq 300$	$\Delta x \leq 0.24$	-	<5	Pass
C-2c	r_2	236.5	$160 < x \leq 250$	-	-	-	-
C-2c	Δr_2	0	$100 < x \leq 300$	-	-	-	-
C-3	Blade curve[3]	0	$160 < x \leq 250$	$-1.2 \leq \Delta x \leq 1.2$	9	-	Pass
C-3	Blade pitch	72	$\theta \leq 4.02$ [2]	$0.39 \leq \Delta\theta \leq 0.83$	-	<5	Pass
Evaluation to EN-ISO-8062-3 (2007) of the Right Impeller Half							
C-2d	b_2	20.25	$16 < x \leq 25$	$0.91 \leq \Delta x \leq 3.30$	>12	-	Fail
C-2d	r_n	55	$40 < x \leq 63$	$1.50 \leq \Delta x \leq 1.83$	10	-	Pass
C-2d	Δr_n	0	$30 < x \leq 100$	$\Delta x \leq 0.34$	-	6	Pass
C-2d	r_1	105.45	$100 < x \leq 160$	$2.17 \leq \Delta x \leq 2.17$	<8	-	Pass
C-2d	Δr_1	0	$100 < x \leq 300$	-	-	-	-
C-2f	β^*_{1B}	11.64	$\theta \leq 2.58$ [1]	$-6.83 \leq \Delta\theta \leq 8$	-	>7	Fail
C-2f	β^*_{2B}	19.37	$\theta \leq 2.58$ [1]	$1.03 \leq \Delta\theta \leq 3.40$	-	>7	Fail
C-2f	$a1$	41.62	$40 < x \leq 63$	-	-	-	-
C-2f	$a2$	68.95	$63 < x \leq 100$	$\Delta x \leq 3.15$	>12	-	Fail
C-2d	ΔL_{sch}	0	$x \leq 10$	$35.96 \leq \Delta x \leq 38.77$	>12	-	Fail
C-2b	r_{1b}	94.62	$63 < x \leq 100$	$-7.24 \leq \Delta x \leq -7.03$	>12	-	Fail
C-2b	Δr_{1b}	0	$30 < x \leq 100$	$\Delta x \leq 0.22$	-	<5	Pass
C-2d	r_{sp}	133	$100 < x \leq 160$	$-0.62 \leq \Delta x \leq -0.58$	<8	-	Pass
C-2d	Δr_{sp}	0	$100 < x \leq 300$	$\Delta x \leq 0.04$	-	<5	Pass
C-2d	r_2	236.5	$160 < x \leq 250$	$0.29 \leq \Delta x \leq 0.45$	<8	-	Pass
C-2d	Δr_2	236.5	$100 < x \leq 300$	$\Delta x \leq 0.16$	-	<5	Pass
C-3	Blade curve[3]	0	$160 < x \leq 250$	$-1.2 \leq \Delta x \leq 1.2$	9	-	Pass
C-3	Blade pitch	72	$\theta \leq 4.02$ [2]	$\Delta\theta \leq 0.06$	-	<5	Pass

[1] As no indication of angular tolerance is explicitly given in EN-ISO-8062-3 (2007), the limiting angular tolerance was derived from the EN-ISO-8062-3 (2007) Table 4 GCTG-7 limit for flatness. The angle was calculated by assuming a scalene right-angled triangle with a 10mm hypotenuse and 0.45mm opposite side length; the limiting deviation ($\pm\theta$) amounts to 2.58°.
[2] Similar to [1], symmetry of pitch was determined using EN-ISO-8062-3 (2007) Table 5 GCTG-7.
[3] Vane curve radius (mean-line), measured by mesh deviation and EN-ISO-8062-3 (2007) Table 2.

Table C-4. Evaluation of the similar, machined (cast) geometric impeller features vs. the ideal impeller geometry, as per EN-ISO-8062-3 (2007) by means of laser scanning.

Fig.	Feature	Target $x[mm]$ $\theta[°]$	Nom. Dim. $\Delta x[mm]$ $\Delta\theta[°]$	Deviation $\Delta x[mm]$ $\Delta\theta[°]$	DCTG Grade	GCTG Grade	Pass/ Fail
Evaluation to EN-ISO-8062-3 (2007) of the Left Impeller Half							
C-4b	b_2	20.25	$16 < x \leq 25$	$0.11 \leq \Delta x \leq 2.69$	>12	-	Fail
C-4b	r_n	55	$40 < x \leq 63$	$-2.64 \leq \Delta x \leq 0.63$	12	-	Pass
C-4b	Δr_n	0	$30 < x \leq 100$	$\Delta x \leq 2.58$	-	>7	Fail
C-4b	r_1	105.45	$100 < x \leq 160$	-	-	-	-
C-4b	Δr_1	0	$100 < x \leq 300$	-	-	-	-
C-4c	β^*_{1B}	11.64	$\theta \leq 2.58$ [1]	$-5.7 \leq \Delta\theta \leq 0.7$	-	>7	Fail
C-4c	β^*_{2B}	19.37	$\theta \leq 2.58$ [1]	$0.67 \leq \Delta\theta \leq 3.06$	-	>7	Fail
C-4b	$a1$	41.62	$40 < x \leq 63$	$-2.19 \leq \Delta x \leq 0.47$	12	-	Pass
C-4b	$a2$	68.95	$63 < x \leq 100$	$3.42 \leq \Delta x \leq 6.75$	>12	-	Fail
C-4a	ΔL_{sch}	0	$x \leq 10$	$32.62 \leq \Delta x \leq 38.24$	>12	-	Fail
C-4a	r_{1b}	94.62	$63 < x \leq 100$	$-8.82 \leq \Delta x \leq -7.72$	>12	-	Fail
C-4a	Δr_{1b}	0	$30 < x \leq 100$	$\Delta x \leq 1.1$	-	7	Pass
C-5	Blade curve[3]	0	$160 < x \leq 250$	$-2.27 \leq \Delta x \leq 2.65$	11	-	Pass
C-5	Blade pitch	72	$\theta \leq 4.02$ [2]	$0.43 \leq \Delta\theta \leq 0.63$	-	<5	Pass
C-5	Hub curve[4]	0	$160 < x \leq 250$	$-0.43 \leq \Delta x \leq 9.1$	>12	-	Fail

[1] As no indication of angular tolerance is explicitly given in EN-ISO-8062-3 (2007), the limiting angular tolerance was derived from the EN-ISO-8062-3 (2007) Table 4 GCTG-7 limit for flatness. The angle was calculated by assuming a scalene right-angled triangle with a 10mm hypotenuse and 0.45mm opposite side length; the limiting deviation ($\pm\theta$) amounts to 2.58°.
[2] Similar to [1], symmetry of pitch was determined using EN-ISO-8062-3 (2007) Table 5 GCTG-7.
[3] Vane curve radius (mean-line), measured by mesh deviation on the suction side of the vane and EN-ISO-8062-3 (2007) Table 2.
[4] Hub curve radius, measured by mesh deviation normal to the 3D solid model surface, evaluated by EN-ISO-8062-3 (2007) Table 2 limits.

C.3.5. Practical evaluation of impeller measurement and geometry

In order to attempt a rationalisation of the measurements, the average and standard deviation of a various combination of measurements were made as shown in tables C-5 and C-6. It has been highlighted in the mentioned data tables that the standard deviation, σ, of the measured values are quite small - except in the case of the inlet metal angle, β^*_{1B}, and the vane leading edge length difference, ΔL_{sch}. Here it can be seen that there exists some notable variance between impeller sides, and also between individual vanes in the same eye. Similar comments can also be made in the length deviations of the vane leading edges.

with reference to table C-5; On average it can be stated that the left impeller eye's vanes differ by 7.14° from the combined right eyes, with a large standard deviation. Also, on average, the vane leading edge deviation differs by 18.01mm between eyes (where the right-hand eye has the longer vanes).

When considering the averaged view of all available measurement points; table C-6 suggests that the deviation between the generated 3D impeller model and the total average values is relatively small - this includes important values such as the in- and outlet passage throat lengths (a_a and a_2).

Table C-5. Detailed assessment of geometric features of the impeller casting

Dim.	Unit	Test impeller Left eye			Test impeller Right eye			Deshrouded impeller Right eye			3D Model[5]
		n_m	$\bar{x}$	σ	n_m	$\bar{x}$	σ	n_m	$\bar{x}$	σ	
Dimensions related to casting accuracy - non-machined											
b_2	$[mm]$	7	22.48	0.75	10	22.16	0.66	13	21.67	0.78	20.2
r_n	$[mm]$	-	-	-	2	56.66	0.17	6	54.51	1.15	55.77
r_1	$[mm]$	4	107.73	0.31	1	107.62	-	-	-	-	105.72
β^*_{1B}[3]	$[°]$	3	19.37	2.21	2	12.23	7.41	3	9.59	2.69	11.64
β^*_{2B}[4]	$[°]$	1	22.11	-	3	21.77	1	3	20.91	1.08	19.37
a_1	$[mm]$	-	-	-	-	-	-	3	40.46	1.17	41.62
a_2	$[mm]$	-	-	-	1	72.10	-	3	73.54	1.53	68.95
ΔL_{sch} [6]	$[mm]$	3	19.36	1.35	2	37.37	1.41	3	34.80	2.46	-
r_{1b}	$[mm]$	3	86.40	0.79	2	87.49	0.11	3	86.51	0.50	94.62
Dimensions related to machined accuracy											
r_{sp}	$[mm]$	4	132.24	0.1	2	132.4	0.02	-	-	-	133
r_2	$[mm]$	-	-	-	3	236.88	0.07	-	-	-	236.52

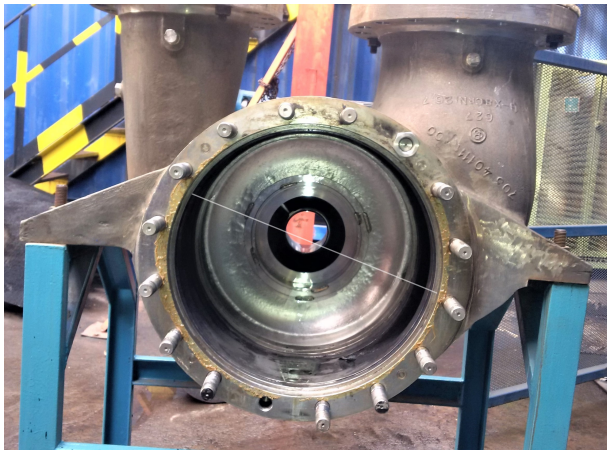
[1] The following diameters were measured as a radius, with reference to the center line vector of the impeller shaft: $d_n = 2r_n$, $d_1 = 2r_1$, $d_{sp} = 2r_{sp}$, $d_2 = 2r_2$ and $d_{1b} = 2r_{1b}$.
[2] All measurements were executed tangent to a constructed meanline surface, except b_2.
[3] β^*_{1B} corresponds to β_{1B} as measured on the suction side vane surface.
[4] β^*_{2B} relates to β_{2B} as measured on the pressure side vane surface.
[5] This column represents the actual 3D geometry used in the CFD, as per original drawings.
[6] The ΔL_{sch} represents a linear length projection between leading edges, on the meanline.

Table C-6. Assessment of geometric features of the impeller casting - averaged approximation

Dim.	Unit	Test impeller Left eye			Combined All right eyes			Combined All measurements			3D Model
		n_m	$\bar{x}$	σ	n_m	$\bar{x}$	σ	n_m	$\bar{x}$	σ	
Dimensions related to casting accuracy - non-machined											
b_2	$[mm]$	7	22.48	0.75	23	21.88	0.77	30	22.02	0.81	20.2
r_n	$[mm]$	-	-	-	8	55.05	1.37	8	55.05	1.37	55.77
r_1	$[mm]$	4	107.73	0.31	1	107.62	-	5	107.71	0.28	105.72
β^*_{1B}	$[°]$	3	19.37	2.21	5	10.65	5.29	8	13.92	6.10	11.64
β^*_{2B}	$[°]$	1	22.11	-	6	21.34	1.13	7	21.45	1.08	19.37
a_1	$[mm]$	-	-	-	3	40.46	1.17	3	40.46	1.17	41.62
a_2	$[mm]$	-	-	-	4	73.18	1.46	4	73.18	1.46	68.95
ΔL_{sch}	$[mm]$	3	19.36	1.35	5	35.83	2.45	8	29.65	8.24	-
r_{1b}	$[mm]$	3	86.40	0.79	5	86.90	0.62	8	86.71	0.73	94.62
Dimensions related to machined accuracy											
r_{sp}	$[mm]$	4	132.24	0.10	2	132.40	0.02	6	132.29	0.11	133
r_2	$[mm]$	-	-	-	3	236.88	0.07	3	236.88	0.07	236.52

[1] to [6] in table C-5 applies.

C.4. Casing



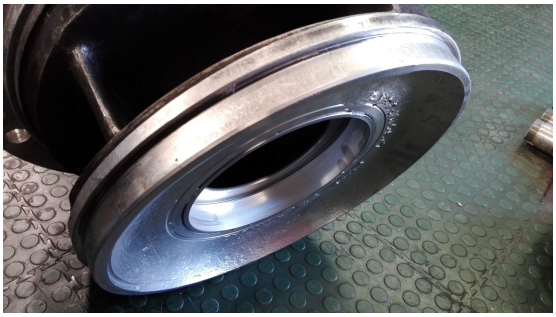
(a) Volute casing, indicating cutwater positions



(b) Inner cutwater, b_{3i}



(c) Outer cutwater, b_{3a}



(d) Casing cover



(e) Outlet nozzle - double volute



(f) Suction splitter rib (casing cover side)

Figure C-6. Depictions of the volute casing and some critical components.

Fig. C-6 shows the casing and it's components - as used during the performance tests. Note that the flow cavity shows signs of general in-service wear - the casting heat number and material grade (cast-in) markings are still clearly visible, as per fig. C-6d. The inner volute cutwater, shown in fig. C-6c and the outer volute cutwater, shown in fig. C-6b are intact and in good operating condition.

Pictures showing high quality casting finishes are shown in figs. C-6e and C-6f. Note that the wetted area has a smooth surface finish and is characteristic of high manufacturing standards. The dimensions of the critical casing features (of this particular casting) were previously determined by high accuracy surveying during a recent client-driven as-built drawing generation exercise, only some critical dimensions were verified and compared to drawing (and thus automatically with the generated 3D geometry).

Refer to tables C-7 and C-8. All but one measurement variance fell within the EN-ISO-8062-3 (2007) limits of acceptability. This can be attributed to complex measurement areas and general in-service wear on the cutwater surfaces, as per figs. C-6c ad C-6b. The geometry after averaging and evaluation as per table C-8 is judged to be accurate when compared with the constructed 3D geometry.

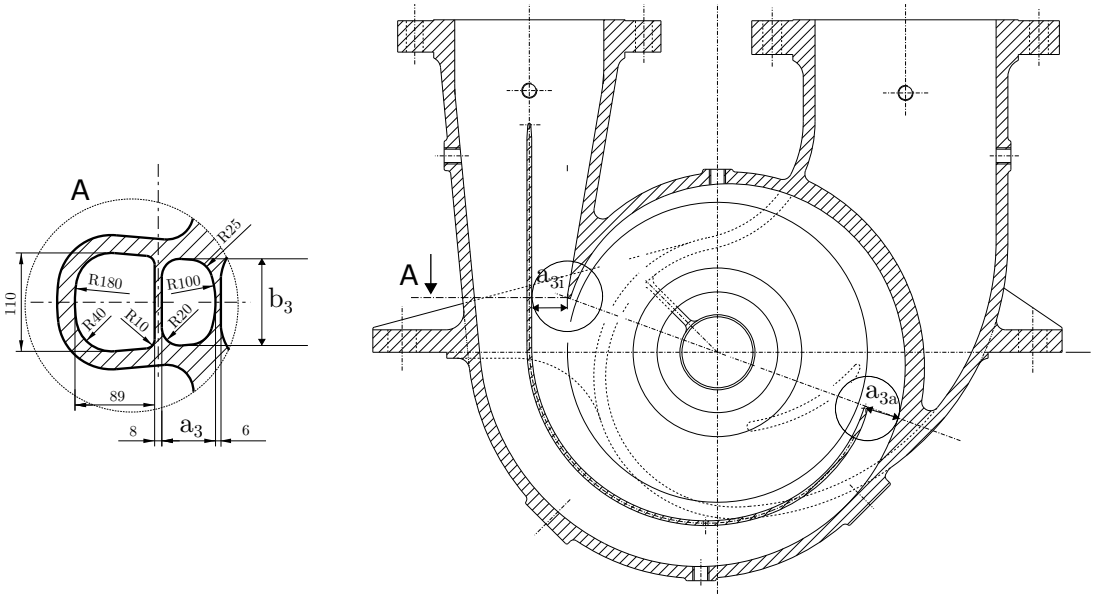


Figure C-7. Representative images showing important casing variables.

Table C-7. Evaluation of the cast geometric casing features vs. the ideal geometry, as per EN-ISO-8062-3 (2007) by means of physical measurement.

Fig.	Feature	Target $x[mm]$ $\theta[°]$	Nom. Dim. $\Delta x[mm]$ $\Delta\theta[°]$	Deviation $\Delta x[mm]$ $\Delta\theta[°]$	DCTG Grade	GCTG Grade	Pass/ Fail
C-7	a_{3i}	58	$40 < x \leq 63$	$0.3 \leq \Delta x \leq 3.2$	>12	-	Fail
C-7	a_{3a}	58	$40 < x \leq 63$	$0 \leq \Delta x \leq 1.5$	11	-	Pass
C-7	b_{3i}	97	$63 < x \leq 100$	$0.55 \leq \Delta x \leq 1.71$	11	-	Pass
C-7	b_{3a}	97	$63 < x \leq 100$	$1.22 \leq \Delta x \leq 2.7$	12	-	Pass

[1] All dimensions were taken as linear measurements utilising manual methods, i.e. inside micrometers, and compared to the limits stated in EN-ISO-8062-3 (2007). Due to the complex geometry, some variance in the measurements were obtained.

Table C-8. Assessment of geometric features of casing

Dim.	Unit	Casing measurements			3D Model
		n_m	$\bar{x}$	σ	
a_{3i}	$[mm]$	6	59.38	0.92	58
a_{3a}	$[mm]$	5	58.89	0.56	58
b_{3i}	$[mm]$	4	98.1	0.43	97
b_{3a}	$[mm]$	5	99.06	0.53	97

[1] Averaged values of all measurements taken, as indicated in fig. C-7.

C.5. Chapter summary

C.5.1. Matters regarding the impeller geometry

The centrifugal pump fleet, operating at present moment, have suffered damage during operation - thus attempts were made during past years to produce and use locally cast impellers (due to cost considerations). Subsequently, locally cast impellers have been observed to be less accurately produced when compared with the original parts. Due to the previously mentioned fact, the impeller that was used in the actual assembly cannot be guaranteed (at the present moment) to be an exact reproduction of the original design and/or to even be an exact replica of other impellers in the fleet and/or inventory. Although a significant effort was made to generate an acceptable 3D geometry for use in the CFD, significant geometric variations were nonetheless discovered on the hub profile, blade length and inlet metal angles. Differences were also found between the mentioned geometry located in the opposing impeller eyes.

Due to the nature of the economic climate in South Africa, and specifically the operating conditions of the pump considered; the procurement of alternative impellers for this application was considered and executed by the equipment owners. The casting quality of the locally sourced parts are of lower geometrical quality when compared with to OEM variant, although not technically rejectable (considering the provisions of EN-ISO-8062-3 (2007), and reasonably expected measurement capabilities of the artisans who maintain the units). As a result, the geometry must be accepted as adequate for the study - as no alternatives were available at the time of execution of the current work.

As discussed earlier in this section; the averaged values of the geometry are considered to be more representative of the current impeller geometric model. The observed deviations between the CFD model and the experiments can largely be attributed to the inaccuracy of the manufactured impeller geometry.

C.5.2. Matters regarding the casing geometry

The casing geometry was generated by using drawings produced by a professional engineering contractor on a previous reverse engineering drive. The verification of certain dimensions were completed in order to determine if the original drawing dimensions were accurate. It was determined that the drawings were accurate, with the casing showing signs of superficial wear, resulting in a recordable loss of wall thickness pertaining to a large percentage of the casing internal areas - the deviations are however still within acceptable ranges when compared to the referenced set standard for new castings. The casing and the 3D generated model thereof was thus accepted to be within reasonable accuracy.

D. Methods regarding the design of the back-flow restricting ring

D.1. Prediction of flow rate at point of suction- and discharge recirculation inception

D.1.1. Discharge recirculation

For the prediction of the flow rate at discharge recirculation, Q_{dr}, the following formula was implemented - as described by Equation D.1 as per Fraser (1981*b*):

$$Q_{dr} = \frac{d_2^2 b_2 n}{6.089 \times 10^9} \cdot \frac{c_{2m}}{u_2} \tag{D.1}$$

where c_{2m}/u_2 was determined from Figure 6 in the paper by Fraser (1981*b*). The curve was converted to an analytical equation and is represented by Equation D.2:

$$\frac{c_{2m}}{u_2} = 0.004596803\beta_2 - 0.010550618 \tag{D.2}$$

D.1.2. Suction recirculation

In order to the volume flow rate at the onset of suction recirculation, Q_{sr}, the method proposed by Fraser (1981*b*) is implemented by Equation D.3:

$$Q_{sr} = \frac{d_1(d_1^2 - d_n^2)n}{2.43 \times 10^{10}} \cdot \frac{c_{1m}}{u_1} \tag{D.3}$$

The method was modified by Gopalakrishnan (1988) for inlet flow angles $10° \leq \beta_1 \leq 30°$ - the value of the factor c_{1m}/u_1 derived from Figure 7 in Fraser (1981*b*) is adapted by Equation D.4:

$$\frac{c_{1m}}{u_1} = \tan\beta_1[1 - 0.2091(\beta_1 - 9.5)^{0.4}] \tag{D.4}$$

For inlet flow angles $30° < \beta_1 \leq 40°$ - the value of the factor c_{1m}/u_1 derived from Figure 7 in Fraser (1981*b*) is adequate and presented by Equation D.5:

$$\frac{c_{1m}}{u_1} = 0.000276443\beta_1^2 - 0.008137061\beta_1 + 0.171295864 \tag{D.5}$$

D.2. Determining the required suction eye diameter

D.2.1. Methodology for determining the inlet throat diameter for an inlet bull ring

A method to calculate the ID of a bull ring (d_r) for a selected flow rate (Q_{La}) is proposed by Gülich (2019) and explained below. Note that the method is implicit and that numeric methods should be applied in order to calculate the proposed diameter. Note - all calculations in this section are made for the outer streamline, the subscript $x_{...,a}$ denotes the requirement in the equations below.

$$k_n = 1 - \frac{d_n^2}{d_r^2} \tag{D.6}$$

$$\tau_{1,a} = \sqrt{\frac{z_{La} e_{1,a}}{\pi d_1 \sin(\beta_{1B,a}) \sin(\lambda_{La_1})}} \tag{D.7}$$

$$\beta'_{1,a} = \arctan\left(\frac{c_{1m,a}\tau_{1,a}}{u_{1,a} - c_{1u,a}}\right) \tag{D.8}$$

$$i'_{1,a} = \beta_{1B,a} - \beta'_{1,a} \tag{D.9}$$

$$d_r = 2.9 \sqrt[3]{\frac{Q_{La}\tau_{1,a}}{f_q n k_n \tan(\beta_{1B,a} - i'_{1,a})}} \quad \text{if} \quad \alpha_1 = 90° \tag{D.10}$$

$$A_{1,dR} = \frac{\pi}{4}\left(d_r^2 - d_n^2\right) \tag{D.11}$$

In order to construct a new $\text{NPSHR}_{3\%}$ vs Q_{La} curve for the newly calculated d_r value, functions describing the physics should be constructed that can be solved across a wide range. The first constructed function is dependent on actual test data of $\text{NPSHR}_{3\%}$ vs Q_{La} during a performance test:

$$\sigma(Q_{La}) = \frac{2g\text{NPSHR}_{3\%}(Q_{La})}{u_1^2} \tag{D.12}$$

Calculate $i'_{1,a}$ with reference to the measured flow rate in the test, Q_{La}, thus $i'_{1,a}(Q_{La})$. This is achieved by computing the inlet velocity triangles at different flow rates, and determining the incidence per flow rate.

Now, relate the new estimated flow rate (Q') to the test flow rate (Q_{La}) through the calculation of the incidence during the initial test. The new $\text{NPSHR}_{3\%}$ vs Q_{La} curves are constructed by using the functions below for $\text{NPSHR}_{3\%}$ and Q_{La} respectively

$$Q'(i'_{1,a}) = \frac{f_q A_{1,dR} u_{1,a}}{\frac{1}{\tan\alpha_1} + \frac{\tau_{1,a}}{\tan(\beta_{1B,a} - i'_{1,a}(Q_{La}))}} \tag{D.13}$$

$$\text{NPSHR}'_{3\%}(Q') = \sigma(Q_{La})\frac{u_{1,a}^2}{2g} \tag{D.14}$$

Note that the above method is applicable to $\alpha_1 = 90°$. As with the nature of the design of turbomachinery, some uncertainty is unavoidable. In the absence of explicit uncertainty limits related to the discussed methodology, similar uncertainty values could be applied as shown in section D.2.2, table D-1 - as applied during the design of new impeller inlet diameters.

D.2.2. A design methodology for a new impeller design - prior to blade development

As can be seen below, a method has been shown which could be used during the design of a new impeller - prior to determining the actual blade inlet angles (incidence). The calculation method, as detailed in Gülich (2019), dictates the methodology used to determine the estimated value of d_1 as per the pump characteristics and the specified flow characteristics.

$$n_{ss} = n\frac{\sqrt{Q/f_q}}{NPSH_{3\%}^{0.75}} \tag{D.15}$$

$$n_{ss}^{**} = \frac{n_{ss}}{\sqrt{k_n}}\left(\frac{n_{q,Ref}}{n_q}\right)^{0.19} \qquad n_{q,Ref} = 27 \quad \text{if} \quad n_q < 170 \tag{D.16}$$

$$k_n = 1 - \frac{d_n^2}{d_1^2} \tag{D.17}$$

$$\varphi_1 = \frac{110^{(1/0.625)}}{n_{ss}} = k_n^{0.8}\left(\frac{110}{n_{ss}}\right)^{1.6}\left(\frac{n_q}{n_{q,Ref}}\right)^{0.3} = \frac{c_{1m}}{u_1} = \tan\beta_1 \tag{D.18}$$

$$d_1 = 2.9\sqrt[3]{\frac{Q_{La}}{f_q n k_n \varphi_1}\left(1 + \frac{\varphi_1}{\tan\alpha_1}\right)} \tag{D.19}$$

As can be seen from eqns. D.16 to D.19, above - the process of finding the optimal d_1 for a specific n_{ss} is an implicit method. In order to solve for eqn. D.19, one has to insert eqn. D.17 into the right hand side of the equation. The variable k_n contains d_1, thus an iterative solving method should be employed.

It is important to note the large variance in the value of d_1. The deviation between the minimum and maximum potential diameters are to be evaluated on a case-by-case basis. The enlargement of d_1 will facilitate a more lenient $NPSHR_{3\%}$ limit - at the expense of making the impeller susceptible to recirculation at flows closer to the BEP.

Table D-1. Detailed assessment of the inlet eye diameter - new impeller design

Q[1]	$\alpha_1 = 80°$				$\alpha_1 = 90°$				$\alpha_1 = 100°$			
$[m^3/h]$	$d_{1_{min}}$ $[mm]$	d_1 $[mm]$	$d_{1_{max}}$ $[mm]$	β_1 $[°]$	$d_{1_{min}}$ $[mm]$	d_1 $[mm]$	$d_{1_{max}}$ $[mm]$	β_1 $[°]$	$d_{1_{min}}$ $[mm]$	d_1 $[mm]$	$d_{1_{max}}$ $[mm]$	β_1 $[°]$
212.35	162.77	169.40	175.82	8.21	161.50	168.25	174.76	5.03	160.20	167.07	173.68	4.96
300[2]	175.85	183.95	191.76	8.27	174.36	182.62	190.55	7.09	172.85	181.26	189.32	6.93
342.54	182.19	191.01	199.50	8.29	180.61	189.59	198.22	8.09	178.99	188.15	196.91	7.89
457.97	190.73	200.44	209.78	11.12	188.82	198.74	208.24	10.76	186.87	197.00	206.67	10.42
579.33[3]	196.76	207.06	216.95	14.09	194.50	205.05	215.14	13.51	192.19	202.99	213.30	12.98
638.08	198.89	209.39	219.47	15.52	196.46	207.22	217.52	14.83	193.96	205.01	215.53	14.19

[1] The flow rates mentioned in this column are equivalent to 50% of the total measured flow rate in the test, in order to represent the flow through a single eye.

[2] This is the selected design flow rate to which the ring will be sized. The linked row values were linearly interpolated from the calculation results that were based on the pump test shown in Chapter 9, and the calculation methodology shown in Annex. D.

[3] This is the best efficiency point (BEP) as determined from the test in Chapter 9. The total flow rate (as measured) is equal to $1158.66m^3/h$ (this value has been rounded off to $1150^3/h$ in the text, for convenience and due to the fact that the stated value was determined through regression.

[4] The calculation of the variance in d_1 (i.e. $d_{1_{min}}$ and $d_{1_{max}}$) was completed by incorporating the standard deviation of $\pm 14\%$ for n_{ss}^{**} - as mentioned in Gülich (2019)

D.3. Determination of geometrical design limits of ring geometry

D.3.1. Design constraints

In order to determine the geometric limit of the possible layout of the perforated ring design, an iterative calculation algorithm was constructed to perform the required calculations and evaluations. The design algorithm is constrained by the following design conditions (refer to D-1):

1. The perforation inlet and outlet should penetrate the ring surfaces at r_{rPCD} (or d_{rPCD}).
2. The metal ligament thickness of the ribs between perforations on r_{rPCD} should be specified and maintained regardless of hole diameter - in this case, $t_{lig} = (e + 0.75\text{mm})$, to compensate for a less resilient material in cavitation prone environments (due to cost, material availability and time constraint).
3. The metal ligament thickness of the ribs between perforations and the ring ID, r_r or d_r, should not be less than t_{lig}, due to the same reasons.
4. There shall be an equal amount of perforations per flow passage, this will ensure that unequal flow distribution does not occur between passages.
5. The diameter of the perforations, r_h or d_h, shall be selected on the basis of standard available drill bits as per ASME-B94.11M (1993) standard sizes for metric twist drills. This is to ensure ease of manufacture.

D.3.2. Mathematical formulation

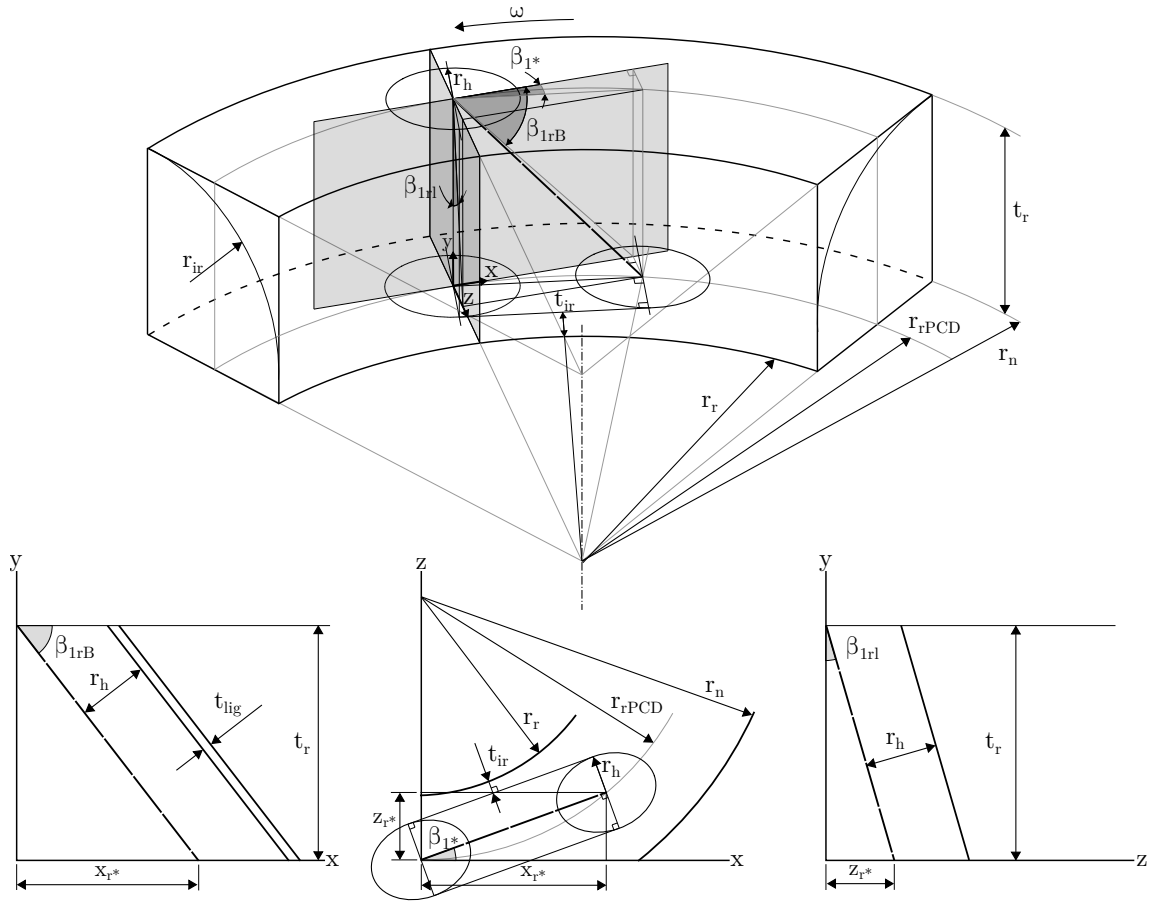


Figure D-1. Nomenclature useful in the ring design algorithm.

With reference to figs. D-1 and 0-1, the following formulations describe the values of interest:

$$x_{r*} = t_{ir}\cot(\beta_{1r}) \tag{D.20}$$

Determine z_{r*} by finding the smallest real root of eqn. D.21:

$$(z_{r*} - r_{rPCD})^2 + {x_{r*}}^2 = {r_{rPCD}}^2 \tag{D.21}$$

Determine the maximum theoretical drill radius, r_h, at the specified β_{1r} by incorporating the stated minimum t_{ir}.

$$r_h = \sqrt{{r_{rPCD}}^2 - \left(0.5\sqrt{{x_{r*}}^2 + {z_{r*}}^2}\right)^2} - r_r - t_{ir} \tag{D.22}$$

Equate the calculated r_h value to the closest (smaller) ASME-B94.11M (1993) standard metric drill bit size. Use the new r_h value in all the subsequent calculations.

Determine the maximum amount of perforations while abiding by the constraints

$$n_h = z_{La}\left\lfloor \frac{\pi d_{rPCD}}{(d_h + t_{lig})\mathrm{cosec}(\beta_{1r})} \cdot \frac{1}{z_{La}} \right\rfloor \tag{D.23}$$

Calculation of the original annular eye flow area of a single impeller eye:

$$A_{or} = \pi[(0.5d_1)^2 - (0.5d_n)^2] = \pi({r_1}^2 - {r_n}^2) \tag{D.24}$$

Calculation of the total combined throat flow area of the perforations:

$$A_{h_{all}} = n_h \pi {r_h}^2 \tag{D.25}$$

Calculation of the flow area obstruction caused by a solid (unmodified) ring with the same diameter as the modified variant:

$$A_{rs} = \pi[(0.5d_1)^2 - (0.5d_r)^2] = \pi({r_1}^2 - {r_r}^2) \tag{D.26}$$

Calculation of the total flow area resulting from the perforated ding modification:

$$A_{flow} = (A_{or} - A_{rs}) + A_{h_{all}} \tag{D.27}$$

Calculation of the ratio between the flow area resulting from the perforated throat flow area vs the unmodified inlet eye flow area:

$$A_{ratio} = \frac{A_{flow}}{A_{or}} \tag{D.28}$$

Calculation of the ratio between the flow area resulting from the perforated throat flow area vs the obstructed area of a solid ring of the same d_r:

$$A_{ratio2} = \frac{A_{h_{all}}}{A_{rs}} \tag{D.29}$$

The methodology highlighted in this section was converted to a functional computer algorithm where results were generated after d_r and β_{1r} were systematically varied. This methodology generates a data set which (when analysed) reflects the limitations of the geometry in terms of throat flow area and minimum allowable perforation drill angle.

D.4. Perforation drill angle design

With the calculated limitations, as per the methodology outlined in paragraph D.3.2 and with reference to fig. 10-6, the following method can be executed and approximate velocity triangles can be generated and evaluated. Note, due to the small flow cavity of the perforations, the short flow path and the inherent uncertainty of the design and lack of cascade test data for similar geometries, the outlet flow deviation (δ_{1r}) was neglected and only ideal outlet vectors were considered.

Determine the average axial flow velocity:

$$c_{sa} = \frac{Q_{La}}{A_{or}} \tag{D.30}$$

Determine the inlet velocity triangle of the ring by means of the following equations, based on ideal velocity triangle theory:

$$c_{1ur} = c_{sa}\cot(\alpha_{1r}) \tag{D.31}$$

$$c_{1r} = \frac{c_{sa}}{\sin(\alpha_{1r})} \tag{D.32}$$

$$w_{1ur} = U_{rPCD} - c_{1ur} \tag{D.33}$$

$$\beta_{1r} = \text{atan}(\frac{c_{sa}}{w_{1ur}}) \tag{D.34}$$

Similarly, the outlet velocity triangle of the ring could be approximated by:

$$\beta_{2r} = \beta_{2rB} \tag{D.35}$$

$$w_{2ur} = \frac{c_{sa}}{\tan\beta_{1rB}} \tag{D.36}$$

$$w_{2r} = \sqrt{{w_{2ur}}^2 + {c_{sa}}^2} \tag{D.37}$$

$$c_{2ur} = U_{rPCD} - w_{2ur} \tag{D.38}$$

$$c_{2r} = \sqrt{{c_{2ur}}^2 + {c_{sa}}^2} \tag{D.39}$$

The incidences of the various blades and perforations can be calculated from:

$$i'_{1r} = \beta_{1rB} - \beta_{1r} \tag{D.40}$$

$$i''_{1} = \beta_{1B} - \beta_{2rB} \tag{D.41}$$

Note that the impeller leading edge metal angle, β_{1B} varies from 16.6° at the hub interface to 13.1° at the shroud. Calculations at different eye diameters should take the change in vane metal angle into account. The method can be applied to multiple arrangements

The following velocity triangle data was generated as per the selected design:

With reference to fig. 10-6, the following calculations were completed:

Table D-2. Calculated velocity triangles for shockless entry per impeller eye (unmodified)

Q_{La}[2] $[m^3/h]$	$\dot{m}$[3] $[kg/s]$	α_{1r} [°]	c_{sa} $[m/s]$	c_{1r} $[m/s]$	c_{1ur} $[m/s]$	w_{1r} $[m/s]$	w_{1ur} $[m/s]$	β_{1r} [°]	i'_1 [°]
250	69.24	80	2.74	2.7	0.48	21.85	21.67	7.21	8.33
250	69.24	90	2.74	2.74	0	22.33	22.16	7.05	8.49
250	69.24	100	2.74	2.7	-0.48	22.81	22.64	6.9	8.64
300	83.08	80	3.29	3.24	0.58	21.83	21.58	8.66	6.88
300	83.08	90	3.29	3.29	0	22.4	22.16	8.44	7.1
300	83.08	100	3.29	3.24	-0.58	22.97	22.74	8.23	7.31
450	124.63	80	4.93	4.86	0.87	21.85	21.29	13.05	2.49
450	124.63	90	4.93	4.93	0	22.7	22.16	12.55	2.99
450	124.63	100	4.93	4.86	-0.87	23.55	23.03	12.09	3.45
575	159.24	80	6.3	6.21	1.11	21.97	21.05	16.67	-1.13
575	159.24	90	6.3	6.3	0	23.04	22.16	15.88	-0.34
575	159.24	100	6.3	6.21	-1.11	24.11	23.27	15.16	0.38

[1] These variable magnitudes are applicable to all considered cases as the impeller geometry remains constant.
[2] This value represents the flow through a single eye, for total pump: $2Q_{La}$
[3] Mass flow calculated at $\rho = 997kg/m^3$ - this corresponds to test conditions.
[4] Calculations performed at $d = 0.5(d_r + d_n)$, $\beta_{1B} = 15.54°$ and $n = 2985$RPM

Table D-3. Calculated perforation velocity triangles for shockless entry (modified)

Q_{La}[2] $[m^3/h]$	$\dot{m}$[3] $[kg/s]$	α_1 [°]	c_{sa} $[m/s]$	c_{1r} $[m/s]$	c_{1ur} $[m/s]$	w_{1r} $[m/s]$	w_{1ur} $[m/s]$	β_{1r} [°]	i'_{1r} [°]
250	69.24	80	4.62	4.55	0.81	29.51	29.15	9	21
250	69.24	90	4.62	4.62	0	30.32	29.96	8.76	21.24
250	69.24	100	4.62	4.55	-0.81	31.12	30.78	8.53	21.47
300	83.08	80	5.54	5.46	0.98	29.51	28.99	10.82	19.18
300	83.08	90	5.54	5.54	0	30.47	29.96	10.48	19.52
300	83.08	100	5.54	5.46	-0.98	31.43	30.94	10.15	19.85
450	124.63	80	8.31	8.19	1.47	29.69	28.5	16.26	13.74
450	124.63	90	8.31	8.31	0	31.1	29.96	15.51	14.49
450	124.63	100	8.31	8.19	-1.47	32.51	31.43	14.82	15.18
575	159.24	80	10.62	10.46[5]	1.87	30.03	28.09	20.71	9.29
575	159.24	90	10.62	10.62[5]	0	31.79	29.96	19.52	10.48
575	159.24	100	10.62	10.46[5]	-1.87	33.56	31.84	18.45	11.55

[1] These variable magnitudes are applicable to all considered cases as the impeller geometry remains constant.
[2] This value represents the flow through a single eye, for total pump: $2Q_{La}$
[3] Mass flow calculated at $\rho = 997kg/m^3$ - this corresponds to test conditions.
[4] Calculations performed at $d = d_{rPCD}$, $\beta_{1B} = 13.79°$ and $n = 2985$RPM
[5] Refer fig. I-2f: perforation axial inlet flow velocity calculated by CFD: ($c_{1m} = c_{sa}$ in this case) $10m/s < c_{1m} < 13m/s$

Table D-4. Calculated perforation outlet velocity triangle angles, and inlet velocity triangles to impeller (modified)

Q_{La}[2] $[m^3/h]$	$\dot{m}$[3] $[kg/s]$	α_{2r} [°]	c_{sa} $[m/s]$	c_{2r} $[m/s]$	c_{2ur} $[m/s]$	w_{2r} $[m/s]$	w_{2ur} $[m/s]$	β_{2r} [°]	i''_1 [°]
250	69.24	11.87	4.62	22.45	21.97	9.24	8	30	-16.21
300	83.08	15.22	5.54	21.11	20.37	11.08	9.6	30	-16.21
450	124.63	28.11	8.31	17.65	15.57	16.63	14.4	30	-16.21
575	159.24	42.57	10.62	15.7	11.57	21.25	18.4	30	-16.21

[1] These variable magnitudes are applicable to all considered cases as the impeller geometry remains constant.
[2] This value represents the flow through a single eye, for total pump: $2Q_{La}$
[3] Mass flow calculated at $\rho = 997kg/m^3$ - this corresponds to test conditions.
[4] Calculations performed at $d = d_{rPCD}$, $\beta_{1B} = 13.79°$ and $n = 2985$RPM

Table D-5. Calculated velocity triangle data for unaffected portion of impeller blades (modified)

Q_{La}[2] $[m^3/h]$	$\dot{m}$[3] $[kg/s]$	α_1 [°]	c_{sa} $[m/s]$	c_{2r} $[m/s]$	c_{2ur} $[m/s]$	w_{2r} $[m/s]$	w_{2ur} $[m/s]$	β_{2r} [°]	i_1* [°]
250	69.24	80	4.62	0.81	21.84	21.34	22.16	12.21	3.33
250	69.24	90	4.62	0	22.63	22.16	22.16	11.77	3.77
250	69.24	100	4.62	-0.81	23.43	22.97	22.16	11.37	4.17
300	83.08	80	5.54	0.98	21.89	21.18	22.16	14.66	0.88
300	83.08	90	5.54	0	22.84	22.16	22.16	14.04	1.5
300	83.08	100	5.54	-0.98	23.79	23.13	22.16	13.47	2.07
450	124.63	80	8.31	1.47	22.3	20.69	22.16	21.89	-6.35
450	124.63	90	8.31	0	23.67	22.16	22.16	20.57	-5.03
450	124.63	100	8.31	-1.47	25.04	23.62	22.16	19.39	-3.85
575	159.24	80	10.62[5]	1.87	22.9	20.28	22.16	27.64[6]	-12.1
575	159.24	90	10.62[5]	0	24.57	22.16	22.16	25.61[6]	-10.07
575	159.24	100	10.62[5]	-1.87	26.27	24.03	22.16	23.85[6]	-8.31

[1] These variable magnitudes are applicable to all considered cases as the impeller geometry remains constant.
[2] This value represents the flow through a single eye, for total pump: $2Q_{La}$
[3] Mass flow calculated at $\rho = 997kg/m^3$ - this corresponds to test conditions.
[4] Calculations performed at $d = 0.5(d_r + d_n)$, $\beta_{1B} = 15.54°$ and $n = 2985$RPM
[5] Refer fig. I-2d: impeller eye axial inlet flow velocity calculated by CFD: ($c_{1m} = c_{sa}$ in this case) $8m/s < c_{1m} < 13m/s$
[6] Refer fig. I-4b surface contours at top of image (inlet): perforation axial inlet flow velocity calculated by CFD: ($\beta_1 = \beta_{2r}$ in this case) $24° < \beta_1 < 27°$

E. Grid Convergence Index formulation

The following formulations were extracted and adapted directly from the Journal of Fluids Engineering Editorial Policy Statement on the Control of Numerical Accuracy, as per Freitas (1993) and subsequently by the referenced work by Celik et al. (2008):
Three different grids are generated, and the representative grid size for each separate 3D grid is determined by eq. (E.1):

$$h = \left[\frac{1}{N}\sum_{i=1}^{N}\right]^{1/3} \tag{E.1}$$

In order to calculate the grid refinement factor, the following is true, eq. (E.2):

$$r_{21} = \frac{h_2}{h_1} \tag{E.2a}$$

$$r_{32} = \frac{h_3}{h_2} \tag{E.2b}$$

The apparent order of convergence is calculated numerically below. It should be noted that a certain amount of oscillatory convergence is tolerated.

$$p_o = \frac{1}{\ln(r_{21})}\left|\ln\left|\frac{\varepsilon_{32}}{\varepsilon_{21}}\right| + q(p_o)\right| \tag{E.3a}$$

$$q(p) = \ln\left(\frac{r_{21}^{p_o} - s_o}{r_{32}^{p_o} - s_o}\right) \tag{E.3b}$$

$$s_o = 1 \cdot \mathrm{sgn}\left(\frac{\varepsilon_{32}}{\varepsilon_{21}}\right) = 1 \cdot \mathrm{sgn}\left(\frac{\phi_3 - \phi_2}{\phi_2 - \phi_1}\right) \tag{E.3c}$$

The extrapolated values of the observed variable ϕ is determined by a technique based on Richardson extrapolation, and can be obtained by solving eq. (E.4):

$$\phi_{ext}^{21} = \frac{r_{21}^{p_o}\phi_1 - \phi_2}{r_{21}^{p_o} - 1} \tag{E.4a}$$

$$\phi_{ext}^{32} = \frac{r_{32}^{p_o}\phi_1 - \phi_2}{r_{32}^{p_o} - 1} \tag{E.4b}$$

The approximate relative error is calculated by:

$$e_a^{21} = \left|\frac{\phi_1 - \phi_2}{\phi_1}\right| \tag{E.5}$$

The extrapolated relative error, is calculated by solving the following equation:

$$e_{ext}^{21} = \left|\frac{\phi_{ext}^{12} - \phi_1}{\phi_{ext}^{12}}\right| \tag{E.6}$$

thus, the fine grid convergence index is obtained by:

$$GCI_{fine}^{21} = \frac{F_s e_a^{21}}{r_{21}^{p_o} - 1} \tag{E.7a}$$

$$GCI_{fine}^{32} = \frac{F_s e_a^{32}}{r_{32}^{p_o} - 1} \tag{E.7b}$$

Roache (2009) also states that the coarse grid GCI could be calculated by:

$$GCI_{coarse}^{21} = r^{p_o} GCI_{fine}^{21} \tag{E.8a}$$

$$GCI_{coarse}^{32} = r^{p_o} GCI_{fine}^{32} \tag{E.8b}$$

Roache (2009) states that the asymptotic region has been achieved if the following holds true, if the exact solution is not known:

$$AR = \frac{GCI_{fine}^{32}}{r^{p_o} GCI_{fine}^{21}} \tag{E.9}$$

F. Additional discussion relating to the analytic calculation of the impeller mean-line

F.1. Analytic solution methodology

F.1.1. Calculation methodology and principles

The conceptual use of velocity triangles in order to calculate the theoretical head rise and related parameters of a grossly simplified impeller geometry is widely explained in literature.
The assumptions that enable the classic one dimensional theory to be valid under ideal circumstances include the following assumptions, as mentioned by Sayers (1990):

1. The blades shall represent a logarithmic spiral layout. Thus no changes to the tangential metal angle relative to the axis of rotation, β_{2B}, is allowed between inlet- and outlet diameters. The internal geometry between the inlet and outlet are thus ignored.
2. An infinite amount of infinitely thin blades are assumed to be present, in essence; the assumption that no secondary flows and velocity gradients in any other direction (except the radial direction) are present.
3. losses in the throat of the impeller are neglected, thus it is assumed that the fluid will abruptly change direction from the axial to the radial direction, without any losses.

The ideal assumption thus reduces the complex 3D geometry of a centrifugal impeller to a flat rotating disk, with an infinite blade count while maintaining no loss operation. The hypothetical geometry is thus insensitive to any flow and geometry related loss sources such as slip and pressure and velocity gradients caused by secondary flow phenomena. In order to more accurately approximate the physical performance of centrifugal impellers, a more rigorous method that considers a greater amount of geometrical detail should be implemented.

Rigorous method for centrifugal impeller mean line calculation

In order to (partially) address the concerns raised in the previous paragraph; a rigorous method of calculation was devised. The method is explained by means of the algorithm shown in Figure F-1. The method builds on classic Euler pump theory by extending its applicability from considering only logarithmic spiral shaped blades to ensuring compatibility with custom blade geometries and actual impeller meridional geometry.

The algorithm executes by first collecting and processing the available impeller geometry data into usable data sets that describe the impeller hub, shroud and blade profiles. Important geometrical features (such as the 3D blade length, blade angles at all positions, blade lean angles, etc) are then derived from this data by means of numerical analysis and processing. After the initial data processing step has been completed, the inlet velocity triangle is calculated and the output of this subroutine is then passed to the iterative portion of the algorithm in the form of inputs and starting criteria. The iterative loop then automatically discretizes the entire blade and meridional geometry into a certain amount of finite parts/partitions. The theoretical head rise per discretized element/partition is systematically calculated by using the calculated outlet velocity triangle data from the previous partition as input to the next, etc. The slip factor is considered for all elements after the calculated point R_{slip}, see Figure 0-1, by utilising the theory

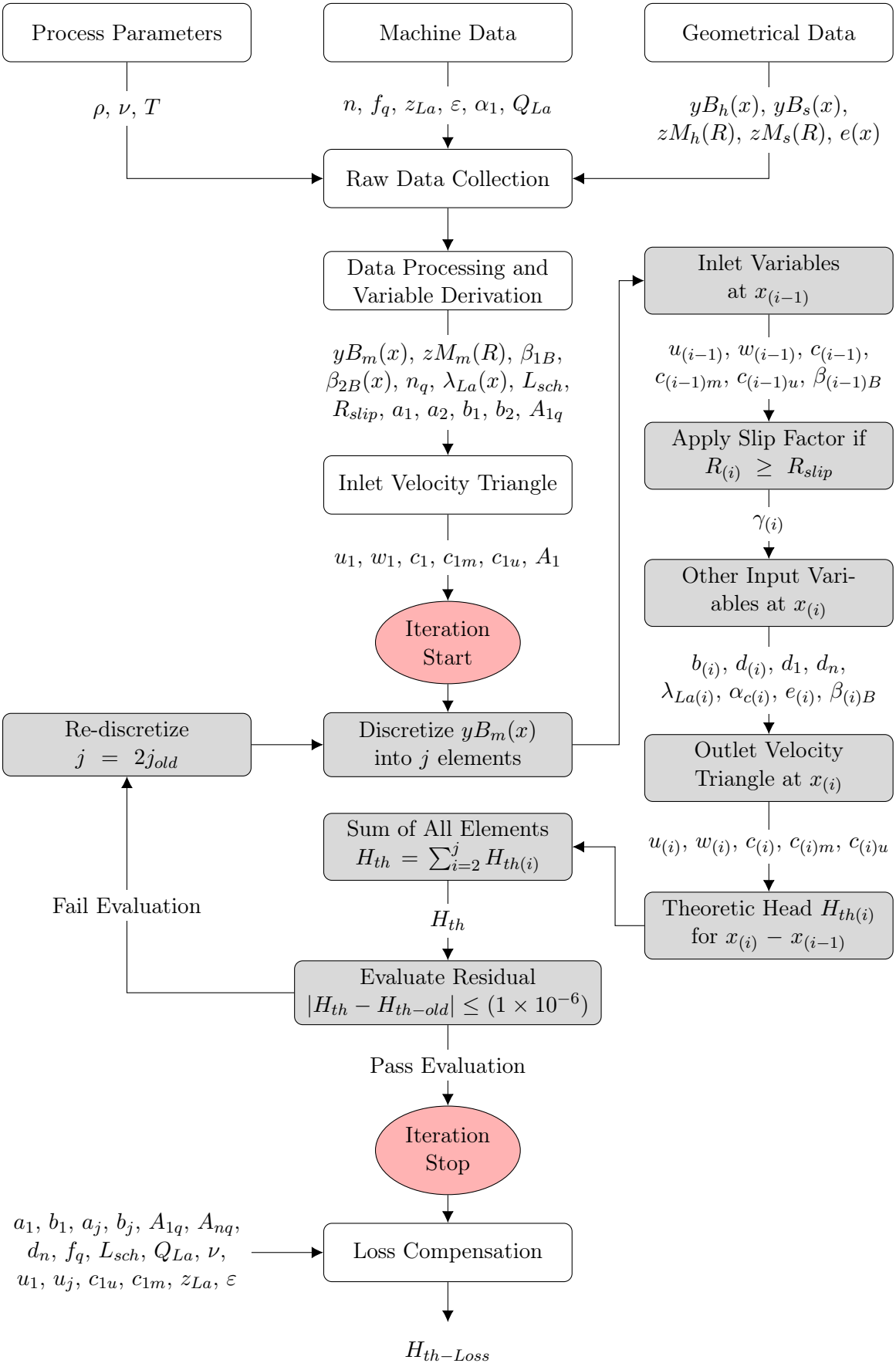


Figure F-1. Impeller meanline calculation algorithm

proposed by Gülich (2014) that slip starts to impede the flow field after this point (the grey shaded area in Figure 0-1. The selection of the appropriate slip model is discussed in paragraph F.1.2. The sum of all the discrete elements is then determined to be the theoretical head produced by the impeller (neglecting losses). The calculated theoretical head is then compared with the previous iteration result; should the difference between the two values not meet the designated stopping criteria, the geometry is automatically re-discretized by doubling the amount of elements and the iteration step is re-initialized and executed. The loop is terminated when the stopping criteria is satisfied. After the converged theoretical head is determined, the losses are evaluated by using the method outlined in Gülich (2014) for centrifugal impellers. The predicted theoretical head rise (loss compensated) can be judged to be more representative of actual impeller geometries with varying blade and meridional geometries when compared to the basic methodology as discussed in the previous section.

F.1.2. Slip factor

The slip factor is one of the most important parameters to consider during impeller design. The slip factor, as described by various texts including (Dixon and Hall, 2014) and (Lewis, 1996), is expressed fundamentally in the following way (refer to Figure 0-1):

$$\gamma = \frac{c_{2u}}{c_{2u\infty}} = 1 - \frac{\Delta c_{2u}}{c_{2u\infty}} \tag{F.1}$$

Thus, the slip factor can be defined as the deviation of a streamline from a blade-congruent flow path (ideal) as it exits through the outlet flow area of a particular rotating impeller. This deviation is described by the angle $\delta = \beta_{2B} - \beta_2$ in Figure 0-1. As can be observed, the δ angle directly impacts the outlet velocity triangle and will cause a shift in the ratio of absolute (c_2) and relative (w_2) outlet velocity components, this will directly impact the ability of the impeller to produce a certain differential head (ΔH). The accurate determination of the slip factor is thus of much importance to the impeller designer.

The following sections will briefly describe using a literature survey of the field, different slip factor models considered during this particular study.A particular slip factor model will also be selected.

Comparison of considered slip factor models

One of the most well known classical formulations applicable to centrifugal impellers with back-swept vanes was introduced by Stodola (1924), see Equation G.1. Stodola (1924) formulated a fully mathematical treatment of slip and introduced the concept of the existence of a relative eddy in the flow passage between blades. The model is simple and is still in wide usage today due to this fact.

Busemann (1928) developed a slip model that requires extensive mathematical effort but is credited as being one of the most exact commercially available formulations. Although this formulation had been developed for 2D impellers with logarithmic spiral blade configurations, the data produced by the Busemann model is still frequently used as reference when modern formulations are developed. Mason (1983) has since produced a simplified mathematical method to determine the constants required for the execution of the Busemann (1928) exact method, this work enables accurate determination of the mentioned constants without incorporating the noted errors in the correlations of other authors when producing user-friendly graphs of the values, and with considerably simpler mathematical treatment.

Wiesner (1967) proposed a simple empirical model that fits the model of Busemann (1928) up to a very satisfactory point across the whole range of applicability, see Equation G.2 - this publication can be considered as one of the greatest influencing works in the field of slip modeling. The

Table F-1. Comparison of different slip models

Slip Model [1]	Model range of validity for β_{2B} [°] [2] (≤ 5 | 20 | 30 | 40 | 45 | 80 | 90 | 90 <)	z_{La}	$\frac{d\beta'_{2B}}{dM'}$	Oper. Point [3]	Prin./ Verif.[4]
Stodola[5]		> 6 [8]	N [10]	BC	RE/T
Busemann[6]		≥ 2	N	BC	Ex/T
Stanitz[7]		> 22 [9]	N	BC	RE/T
Wiesner		≥ 3	N	BC	C/B
Aungier			N	BC	W/B
Gülich			N	BC	W/B
v.Backström			N	BC	C/B
Paeng		≥ 3	N	BC	RE/V
Qui			Y	Range	RE/B

[1] The slip models are evaluated based on centrifugal impeller design only.
[2] Valid (black), reasonable (grey) and invalid (white) application ranges.
[3] The operating point of most models require Blade Congruent (BC) flow, achieved at ≈ BEP.
[4] Principle/Verification: RE=Relative Eddy, Ex=Explicit Method, T=Testing, C=Correlation, B=Busemann data, W=Wiesner data, V=Visser exact solution
[5] Prefered range by Sayers (1990) due to ease of use and accuracy in this range.
[6] Sayers (1990) specified range, although generally applicable.
[7] Applicable to radial blade profiles, will not be considered further in this study.
[8] Evaluate the operable range
[9] Evaluate the operable range
[10] Wislicenus (1947) proposed a method of using the average outlet metal angle.

Wiesner slip model has since become a fundamental formulation from where many other models have been generated by slight modification of the base model. Models that were developed that utilize the Wiesner formulation include (but is not limited to) the models by Aungier (2000), Equation see G.5, and Gülich (2014), see Equation G.6.

von Backström (2006) proposed a completely new mathematical model which produces accurate results compared with the classical models of Busemann (1928) and Wiesner (1967). The von Backström/SRE slip model is applicable across a wide range of vane angles and attempts to consolidate the most accurate classical slip models into a single formulation that is universally applicable to centrifugal impellers, without the calculation of a limiting radius ratio, see Equation G.4.

Some modern slip models have implemented an analytic approach by reviving and expanding on the classical relative eddy concept. Paeng and Chung (2001), see Equation G.7, developed a convenient model that improves the work of Visser et al. (1994) with regards to the accuracy of slip factor approximation across a wider range of impeller designs and configurations. A recent slip factor model Qiu et al. (2011), see Equation G.8, have demonstrated clear advantages over previous correlations due to the incorporation of the outlet blade turning rate and the impeller flow rate into the mathematical treatment of the slip velocity. The incorporation of the mentioned factors enable the accurate estimation of slip for impellers (even with blades that are not logarithmic in design while considering special outlet blade angle changes) across the entire operating range of the impeller. The model by Qiu et al. (2011) exhibits an additional advantage due to the ability of the model to calculate radial (back-swept, straight, and forward-swept vane configurations), mixed-flow and axial impeller layouts.

Table F-1 attempts to condense and compare the considered slip factor models with each other. It can be observed that the majority of the models considered are in some way related to the early (and ground breaking) work by Busemann (1928) and the directly related work of Wiesner (1967), however all models are appropriate if applied responsibly to the posed problem. The different slip models will be compared upon calculation of the impeller mean-line; invariably some models will be more suited to certain situations when compared to its peers; the most suitable model for comparison with the CFD results is selected below.

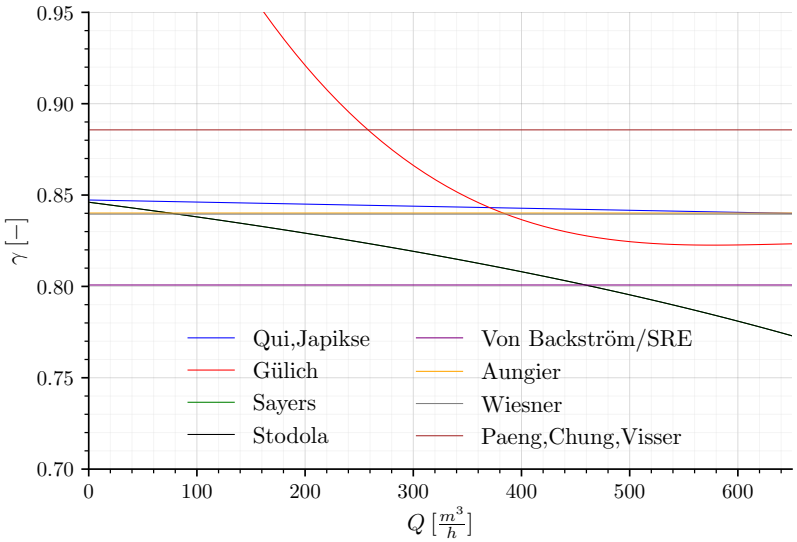


Figure F-2. Calculation of slip factor in the range of evaluation with regards to the current geometry of the unmodified impeller.

Figure F-2 depict representative values of the slip factor γ versus flow rate in the representative range of this study per impeller eye. It can be seen that the majority of the considered flip factors are constant and is not a function of flow rate. The more modern method as defined by Qiu et al. (2011) does take the effect of flow rate into account while considering the geometry of the blades. Another claim of the authors is that off-design operating regimes are better predicted compared with other (classic) slip models.

Considering the data produced in fig. 9-2 and table 9-4, it is possible to determine the most accurate slip model for the application. The models that produce the best overall results are the Qiu et al. (2011), Aungier (2000) and Wiesner (1967) formulations. The Wiesner (1967) formulation was selected as the best slip factor for the application, based on its historical accuracy (due to the fact that is it based almost purely on the work of Busemann (1928)) and due to its proven superior performance in the current study.

G. Slip factor formulations

Every section below provides a self-contained algorithm to calculate slip factors for centrifugal impellers as per the method defined by its individual author. Note all specified limits of applicability. The formulations shown below have been implemented for back-swept blade designs.

G.1. Stodola's slip model

(Stodola, 1924)

$$\beta'_{2B} = 90° - \beta_{2B} \tag{G.1a}$$

$$\phi_2 = \frac{c_{2m}}{u_2} \tag{G.1b}$$

$$\gamma = 1 - \frac{\frac{\pi}{z_{La}} cos(\beta'_{2B})}{1 - \phi_2 tan(\beta'_{2B})} \tag{G.1c}$$

G.2. Wiesner's slip model

(Wiesner, 1967)

$$\epsilon_{lim} = e^{[\frac{-8.16 sin(\beta_{2B})}{z_{La}}]} \tag{G.2a}$$

$$\gamma = 1 - \sqrt{\frac{sin(\beta_{2B})}{z_{La}^{0.7}}} \quad \text{where} \quad \frac{d_{1b}}{d_{2b}} \leq \epsilon_{lim} \tag{G.2b}$$

$$\gamma = 1 - \sqrt{\frac{sin(\beta_{2B})}{z_{La}^{0.7}}} \left[1 - \left(\frac{\frac{d_{1b}}{d_{2b}} - \epsilon_{lim}}{1 - \epsilon_{lim}}\right)^3\right] \quad \text{where} \quad \frac{d_{1b}}{d_{2b}} > \epsilon_{lim} \tag{G.2c}$$

G.3. Stanitz slip model

$$\beta'_{2B} = 90° - \beta_{2B} \tag{G.3a}$$

$$\phi_2 = \frac{c_{2m}}{u_2} \tag{G.3b}$$

$$\gamma = 1 - \frac{0.63\pi}{z_{La}[1 - \phi_2 tan(\beta'_{2B})]} \quad \text{where} \quad 45° < \beta_{2B} \leq 90° \tag{G.3c}$$

G.4. von Backström/SRE slip model

(von Backström, 2006)

$$\beta'_{2B} = 90° - \beta_{2B} \tag{G.4a}$$

$$RR = max\left(\frac{r_i}{0.5d_{2b}}, 0.5\right) \tag{G.4b}$$

$$F_0 = 5 \tag{G.4c}$$

$$\gamma = 1 - \left[1 + F_0 \frac{z_{La}(1 - RR)}{2\pi cos(\beta_{2B})^{0.5}}\right]^{-1} \tag{G.4d}$$

G.5. Aungier slip model

(Aungier, 2000)

$$\delta_\gamma = 1 - \sqrt{\frac{sin(\beta_{2B})sin(\alpha_{c2})}{z_{La}^{0.7}}} \tag{G.5a}$$

$$\delta^*_\gamma = sin(19° + 0.2\beta_{2B}) \tag{G.5b}$$

$$\epsilon_{lim} = \frac{\delta_\gamma - \delta^*_\gamma}{1 - \delta^*_\gamma} \tag{G.5c}$$

$$\gamma = \delta_\gamma \quad \text{where} \quad \frac{d_{1b}}{d_{2b}} \leq \epsilon_{lim} \tag{G.5d}$$

$$\gamma = \delta_\gamma \left[1 - \left(\frac{\frac{d_{1b}}{d_{2b}} - \epsilon_{lim}}{1 - \epsilon_{lim}}\right)^3\right]^{\sqrt{0.1\beta_{2B}}} \quad \text{where} \quad \frac{d_{1b}}{d_{2b}} > \epsilon_{lim} \tag{G.5e}$$

G.6. Gülich slip model

(Gülich, 2014)

$$\epsilon_{lim} = e^{\left[\frac{-8.16sin(\beta_{2B})}{z_{La}}\right]} \tag{G.6a}$$

$$d_{1m} = \sqrt{0.5(d_1^2 + d_n^2)} \tag{G.6b}$$

$$d_2 = \sqrt{0.5(d_{2a}^2 + d_{2i}^2)} \tag{G.6c}$$

$$d^*_{1m} = \frac{d_{1m}}{d_2} \tag{G.6d}$$

$$k_w = 1 - \left(\frac{d^*_{1m} - \epsilon_{lim}}{1 - \epsilon_{lim}}\right)^3 \quad \text{where} \quad d^*_{1m} \leq \epsilon_{lim} \tag{G.6e}$$

$$k_w = 1 \quad \text{where} \quad d^*_{1m} > \epsilon_{lim} \tag{G.6f}$$

$$f_1 = 1.02 + 1.2 \times 10^{-3}(n_q - 50) \quad \text{for semi-axial impellers} \tag{G.6g}$$

$$f_1 = 0.98 \quad \text{for radial impellers} \tag{G.6h}$$

$$\gamma = f_1 \left[1 - \left(\frac{\sqrt{sin\beta_{2B}}}{z_{La}^{0.7}}\right)\right] k_w \quad \text{where} \quad z_{La} \geq 3 \tag{G.6i}$$

G.7. Paeng-Chung-Visser slip model

(Paeng and Chung, 2001)

$$\beta'_{2B} = 90° - \beta_{2B} \tag{G.7a}$$

$$f_0 = 0.833 + 0.21e^{\frac{-z_{La}^3}{32.3}} \tag{G.7b}$$

$$A_z = 0.024\left(1 - e^{\frac{-z_{La}^{4.1}}{336}}\right) \tag{G.7c}$$

$$B_z = 24.2\left(1 - e^{\frac{-z_{La}^{1.31}}{3.04}}\right) \tag{G.7d}$$

$$f = f_0 + A_z e^{\frac{\beta'_{2B}}{B_z}} \tag{G.7e}$$

$$\alpha = \frac{sin(\frac{\pi}{z_{La}})cos\beta'_{2B}}{1 + sin(\frac{\pi}{z_{La}}cos\beta'_{2B})} \tag{G.7f}$$

$$\epsilon_{lim} = 1 - \frac{2sin(\frac{\pi}{z_{La}}cos\beta'_{2B})}{1 + sin(\frac{\pi}{z_{La}}cos\beta'_{2B})} \tag{G.7g}$$

$$\gamma = 1 - f\alpha \quad \text{where} \quad \frac{d_{1b}}{d_{2b}} < \epsilon_{lim} \tag{G.7h}$$

$$\gamma = (1 - f\alpha)\left[1 - \left(\frac{d_{1b}}{d_{2b}}\right)^{\left(\frac{z_{La}}{cos\beta'_{2B}}\right)^{0.85}}\right] \quad \text{where} \quad \frac{d_{1b}}{d_{2b}} \geq \epsilon_{lim} \tag{G.7i}$$

G.8. Qiu-Japikse slip model

(Qiu et al., 2011)

$$\beta'_{1B} = \beta_{1B} - 90^\circ \tag{G.8a}$$

$$\beta'_{RMSB} = \beta_{RMSB} - 90^\circ \tag{G.8b}$$

$$\beta'_{2B} = \beta_{2B} - 90^\circ \tag{G.8c}$$

$$\phi_2 = \frac{c_{2m}}{u_2} \tag{G.8d}$$

$$s_2 = \frac{\pi d_{2b}}{z_{La}} \tag{G.8e}$$

$$\Delta M' = 0.5\sqrt{\frac{d_{2b}^2 - d_{1b}^2}{2}} \quad \text{where } \beta_{RMSB} \text{ is known} \tag{G.8f}$$

$$\frac{\mathrm{d}\beta'_{2B}}{\mathrm{d}M'} = \frac{\beta'_{2B} - \beta'_{RMSB}}{\Delta M'} \quad \text{where } \beta_{RMSB} \text{ is known} \tag{G.8g}$$

$$\Delta M' = 0.5(d_{2b} - d_{1b}) \quad \text{where } \beta_{RMSB} \text{ is not known} \tag{G.8h}$$

$$\frac{\mathrm{d}\beta'_{2B}}{\mathrm{d}M'} = \frac{\beta'_{2B} - \beta'_{1B}}{\Delta M'} \quad \text{where } \beta_{RMSB} \text{ is not known} \tag{G.8i}$$

$$F = 1 - sin\left(\frac{\pi}{z_{La}}\right) sin\left(\frac{\pi}{z_{La}} + \beta'_{2B}\right) cos\beta'_{2B} sin\alpha_{c2} - \frac{e_2}{s_2 cos\beta'_{2B}} \frac{\mathrm{d}\beta'_{2B}}{\mathrm{d}M'} \tag{G.8j}$$

$$\sigma_\gamma = 1 - \frac{F\pi cos\beta'_{2B} sin\alpha_{c2}}{z_{La}} - \frac{F s_2 \phi_2}{4 cos\beta'_{2B}} \tag{G.8k}$$

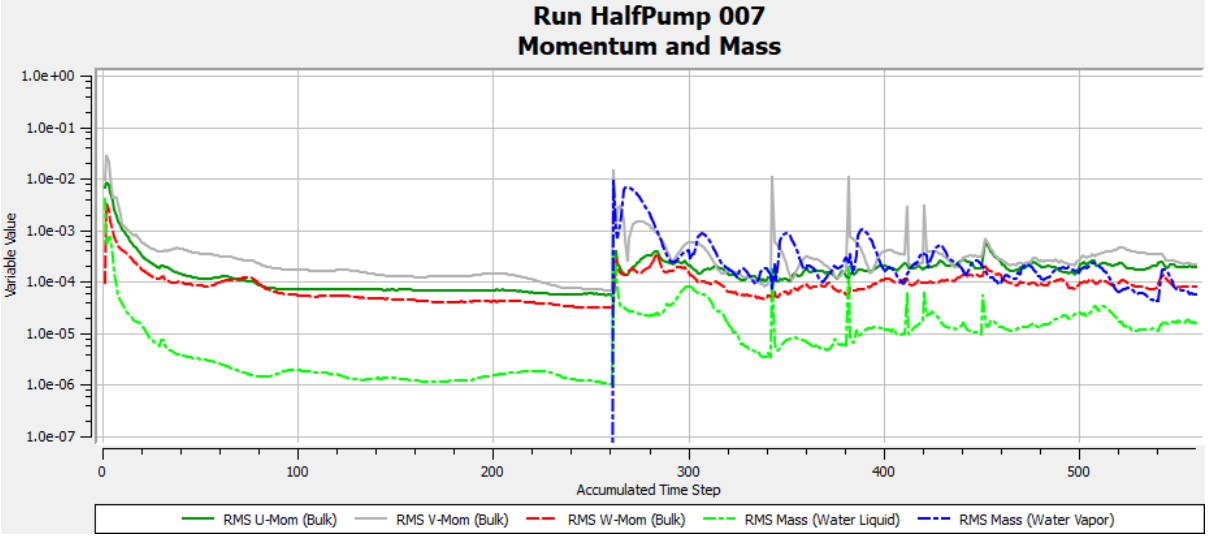
$$\epsilon_{lim} = e^{\left[\frac{-8.16 sin(\beta_{2B})}{z_{La}}\right]} \tag{G.8l}$$

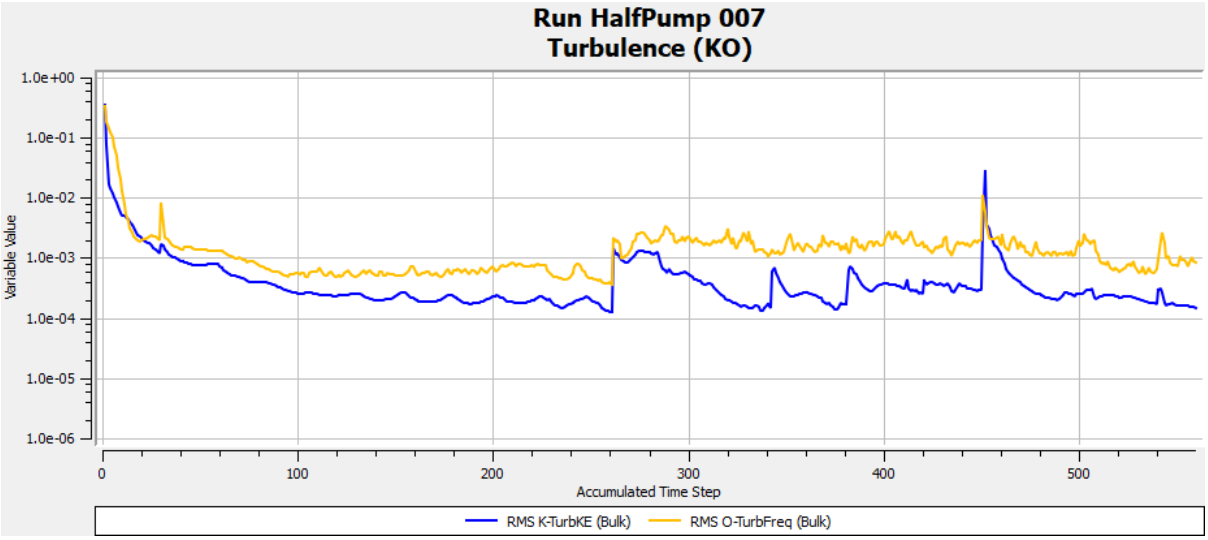
$$\gamma = \sigma_\gamma \quad \text{where} \quad \frac{d_{1b}}{d_{2b}} \leq F \tag{G.8m}$$

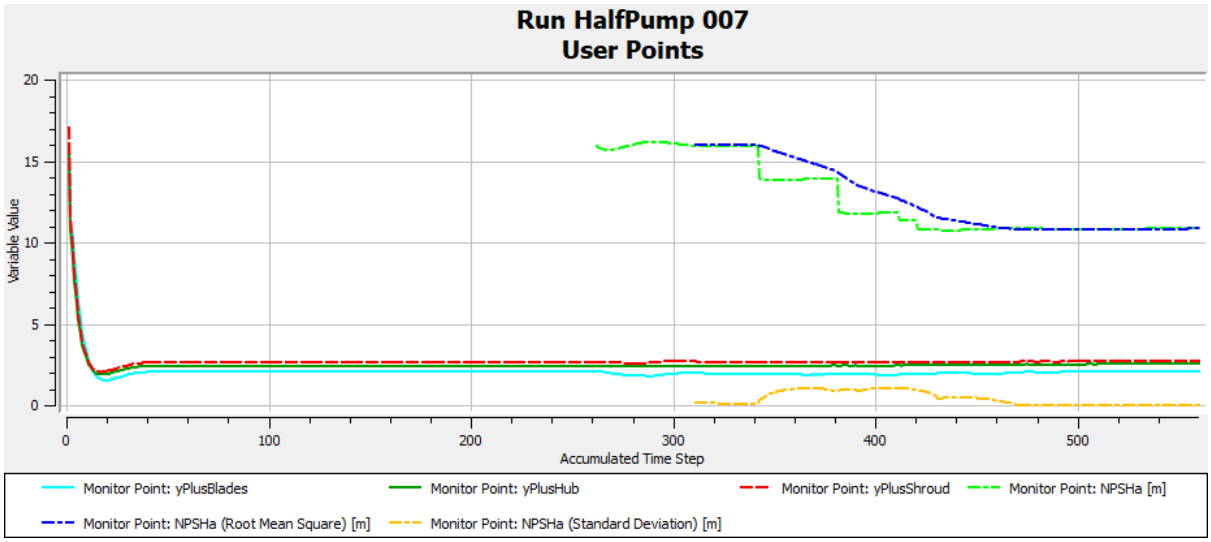
$$\gamma = \sigma_\gamma \left[1 - \left(\frac{\frac{d_{1b}}{d_{2b}} - \epsilon_{lim}}{1 - \epsilon_{lim}}\right)^3\right] \quad \text{where} \quad \frac{d_{1b}}{d_{2b}} > F \tag{G.8n}$$

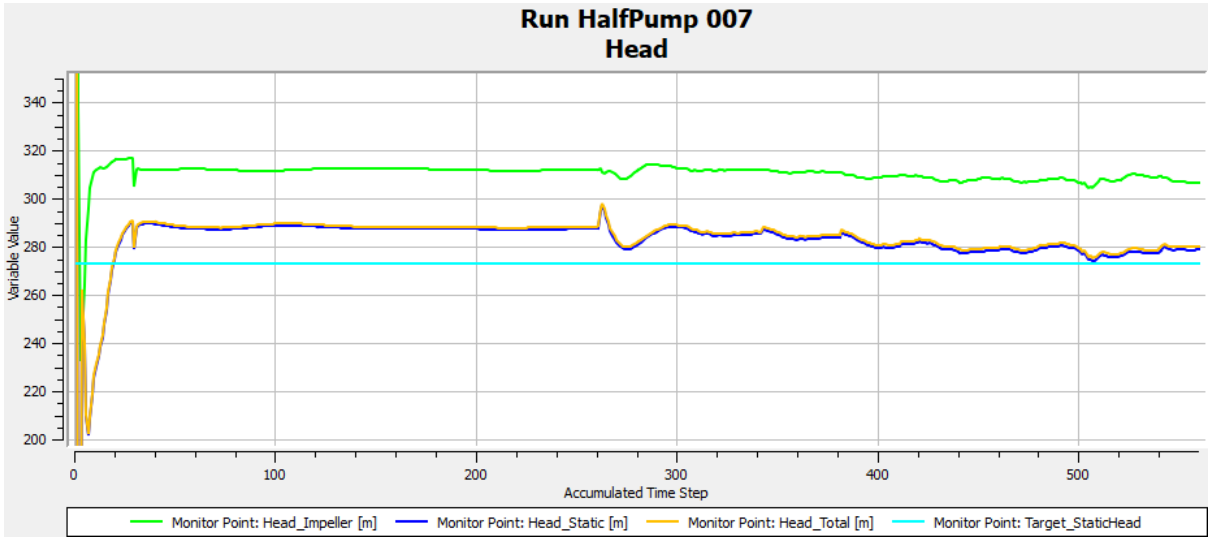
H. Example monitor and residual plots

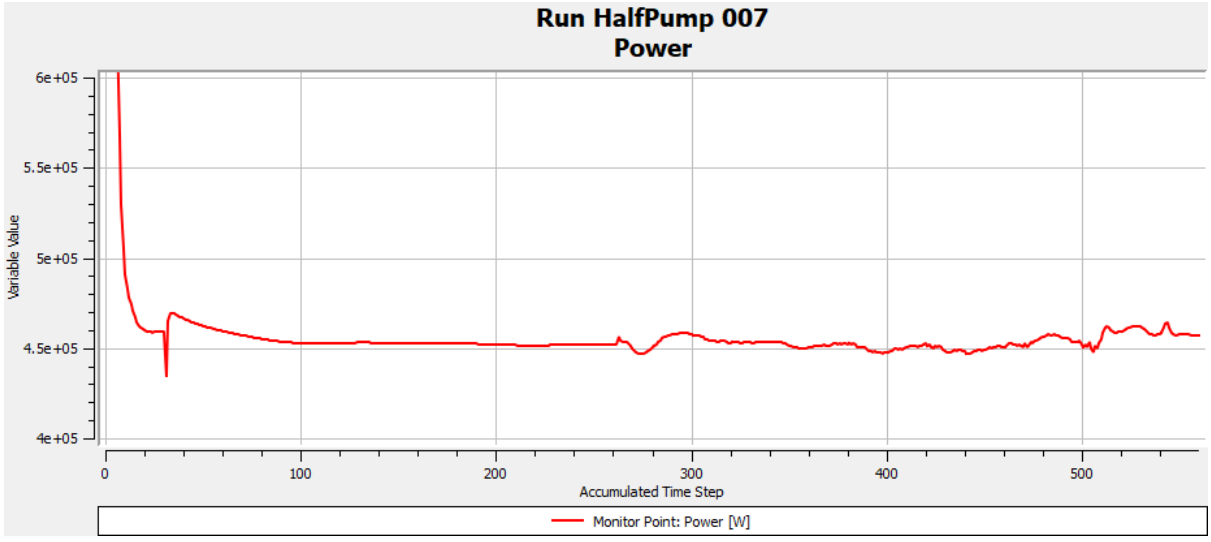
The following plots were typical monitoring points during a CFD run. The example is of a $127.215 kg/s$ case. The first part of the graphs are a non-cavitating case, followed by the cavitation model turned on and then the systematic reduction of suction pressure until a 3% reduction of ΔH_{tot} is observed.

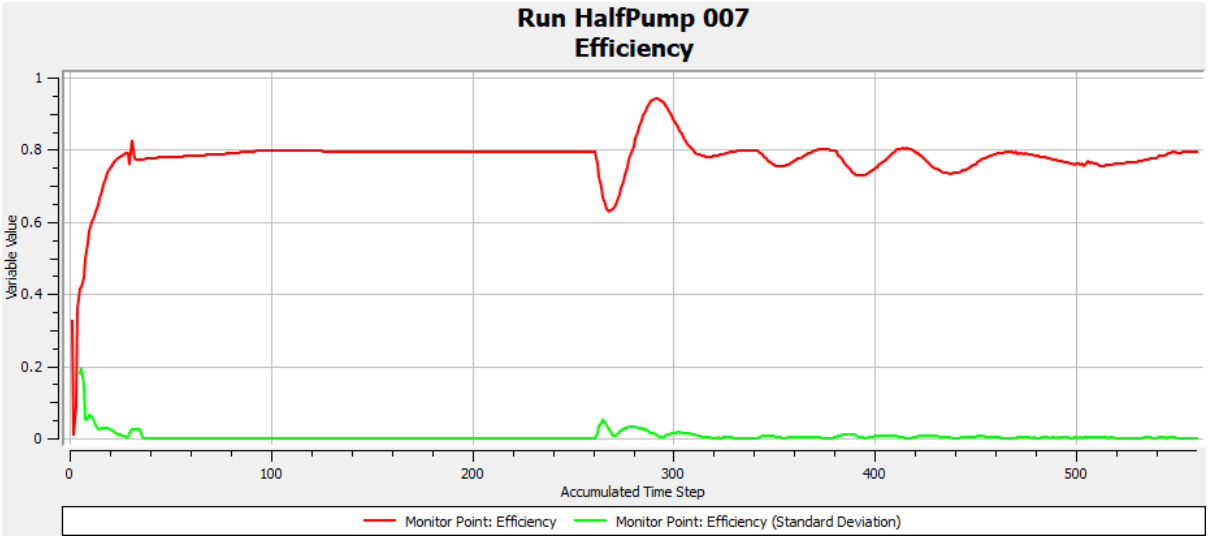


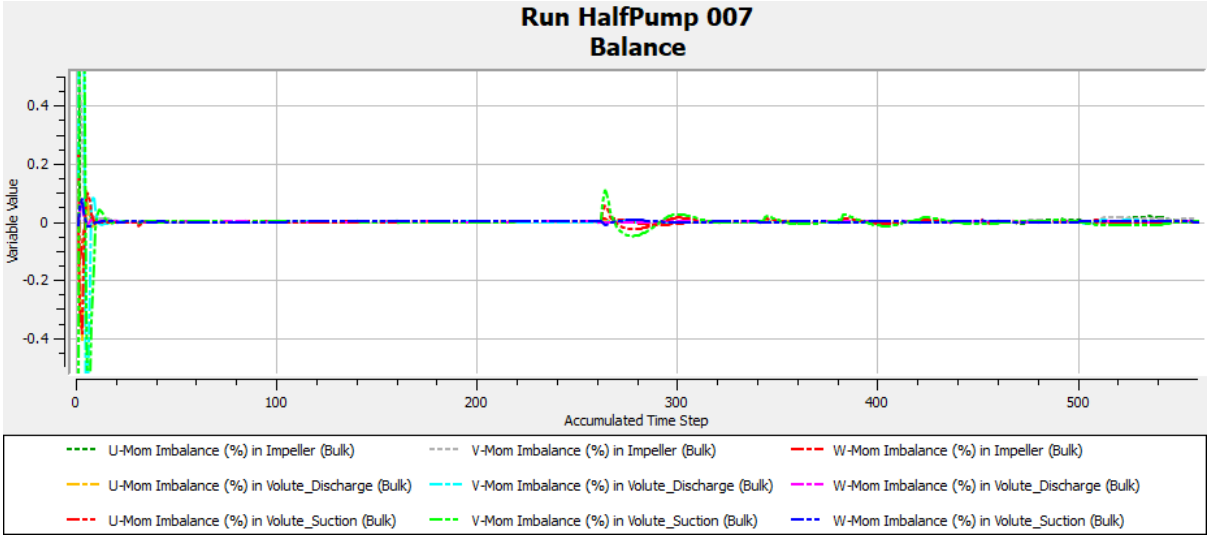


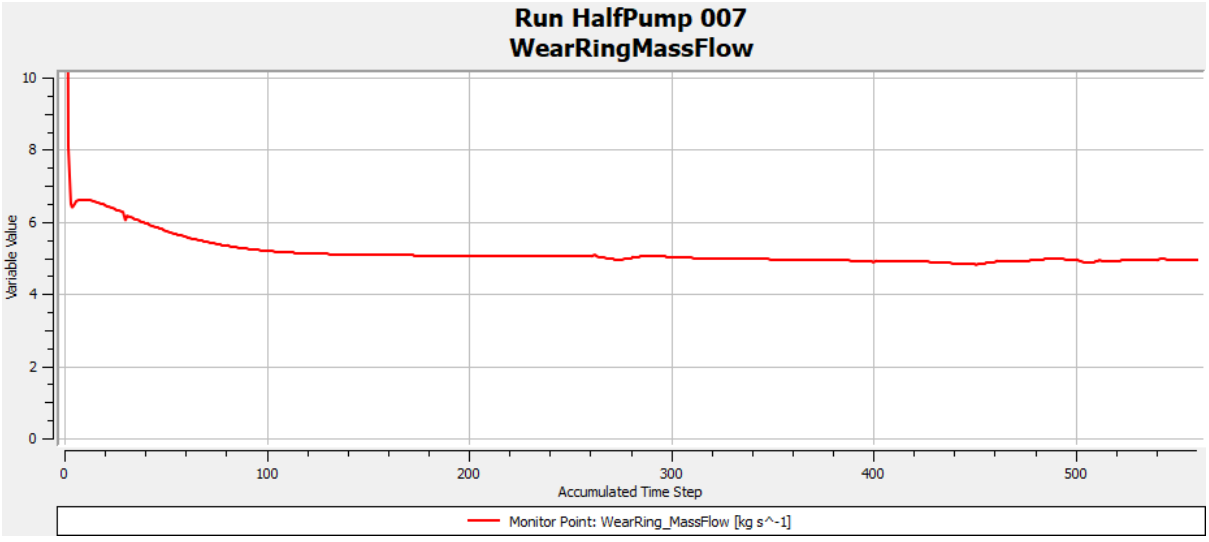

Run HalfPump 007
User Points
Variable Value
Accumulated Time Step
Monitor Point: yPlusBlades
Monitor Point: yPlusHub
Monitor Point: yPlusShroud
Monitor Point: NPSHa [m]
Monitor Point: NPSHa (Root Mean Square) [m]
Monitor Point: NPSHa (Standard Deviation) [m]


Run HalfPump 007
Head
Variable Value
Accumulated Time Step
Monitor Point: Head_Impeller [m]
Monitor Point: Head_Static [m]
Monitor Point: Head_Total [m]
Monitor Point: Target_StaticHead


Run HalfPump 007
Power
Variable Value
Accumulated Time Step
Monitor Point: Power [W]

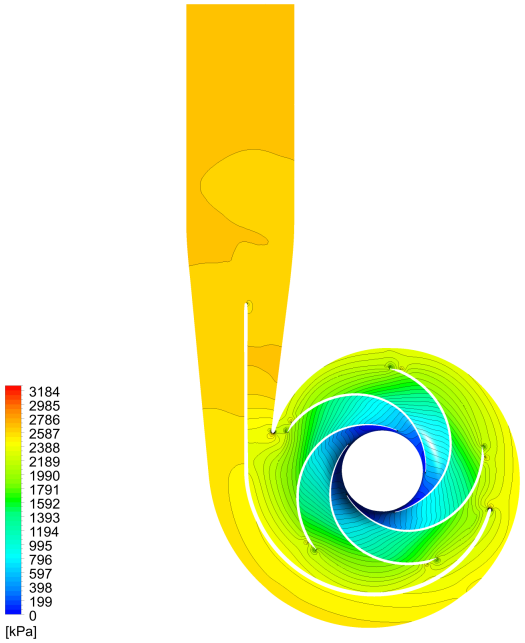

Run HalfPump 007
Efficiency
Variable Value
Accumulated Time Step
Monitor Point: Efficiency
Monitor Point: Efficiency (Standard Deviation)


Run HalfPump 007
Balance
Variable Value
Accumulated Time Step
U-Mom Imbalance (%) in Impeller (Bulk)
V-Mom Imbalance (%) in Impeller (Bulk)
W-Mom Imbalance (%) in Impeller (Bulk)
U-Mom Imbalance (%) in Volute_Discharge (Bulk)
V-Mom Imbalance (%) in Volute_Discharge (Bulk)
W-Mom Imbalance (%) in Volute_Discharge (Bulk)
U-Mom Imbalance (%) in Volute_Suction (Bulk)
V-Mom Imbalance (%) in Volute_Suction (Bulk)
W-Mom Imbalance (%) in Volute_Suction (Bulk)

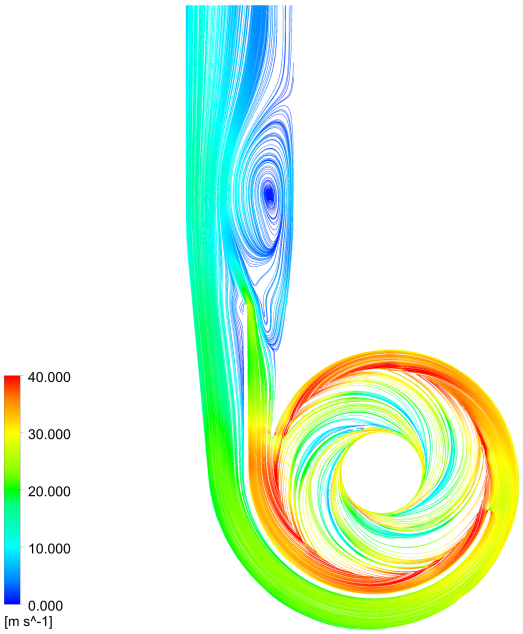

Run HalfPump 007
WearRingMassFlow
Variable Value
Accumulated Time Step
Monitor Point: WearRing_MassFlow [kg s^-1]

I. Best Efficiency Point CFD Data

Case 1: Best Efficiency Point flow rate
$n = 2985RPM$ (clockwise), $Q = 575m^3/h$ ($Q = 1150m^3/h$ for full pump)



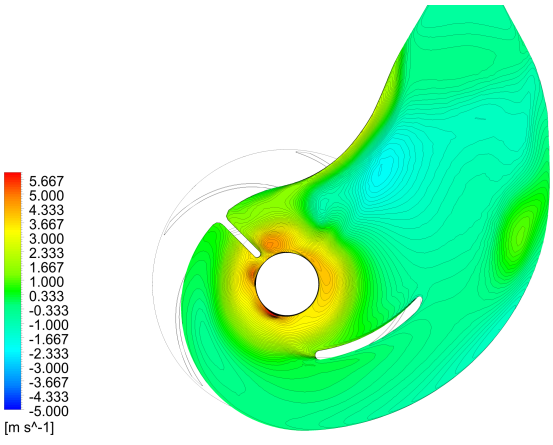
(a) Absolute pressure, Plane I



(b) Velocity magnitude (relative/Stationary), Plane I



(c) Total pressure in stationary frame, Plane C*

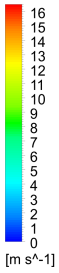


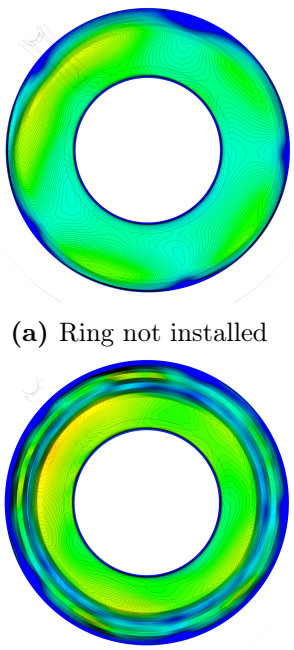
(d) Axial flow velocity in stationary frame, Plane C*

Figure I-1. Comparison of BEP (initial) conditions for Case 1

Plane E	Plane F	Plane G

Case 1: Best Efficiency Point flow rate
$n = 2985RPM$ (clockwise), $Q = 575m^3/h$ ($Q = 1150m^3/h$ for full pump)
Measured variable: c_{1m}, direction of normal flow: into page

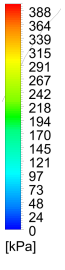


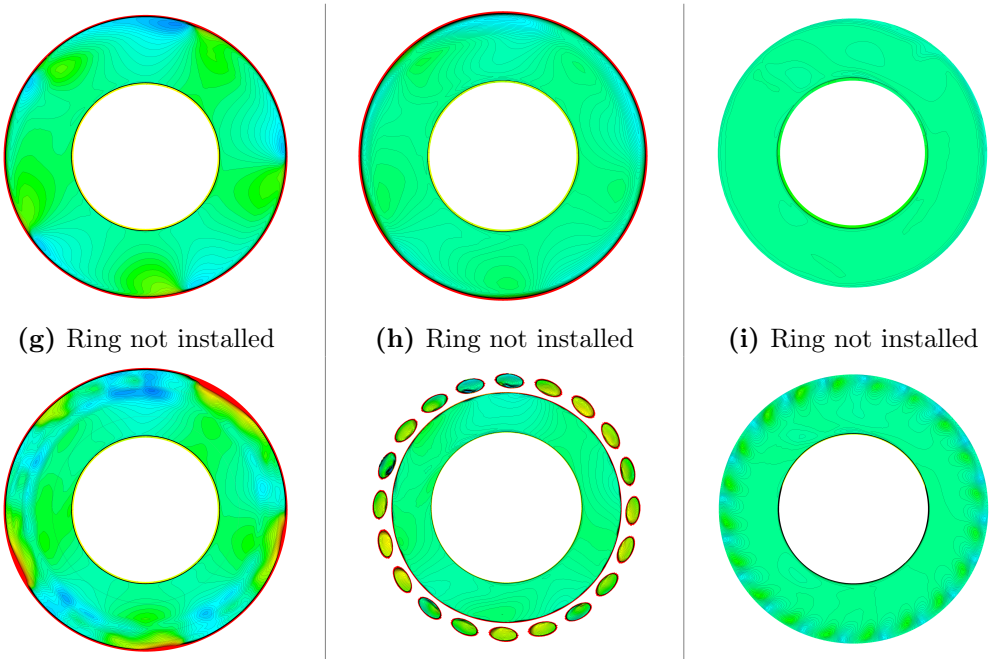


(a) Ring not installed **(b)** Ring not installed **(c)** Ring not installed

(d) Ring installed **(e)** Ring installed **(f)** Ring installed

Case 1: Best Efficiency Point flow rate
$n = 2985RPM$ (clockwise), $Q = 575m^3/h$ ($Q = 1150m^3/h$ for full pump)
Measured variable: p_{Ts}, direction of normal flow: into page





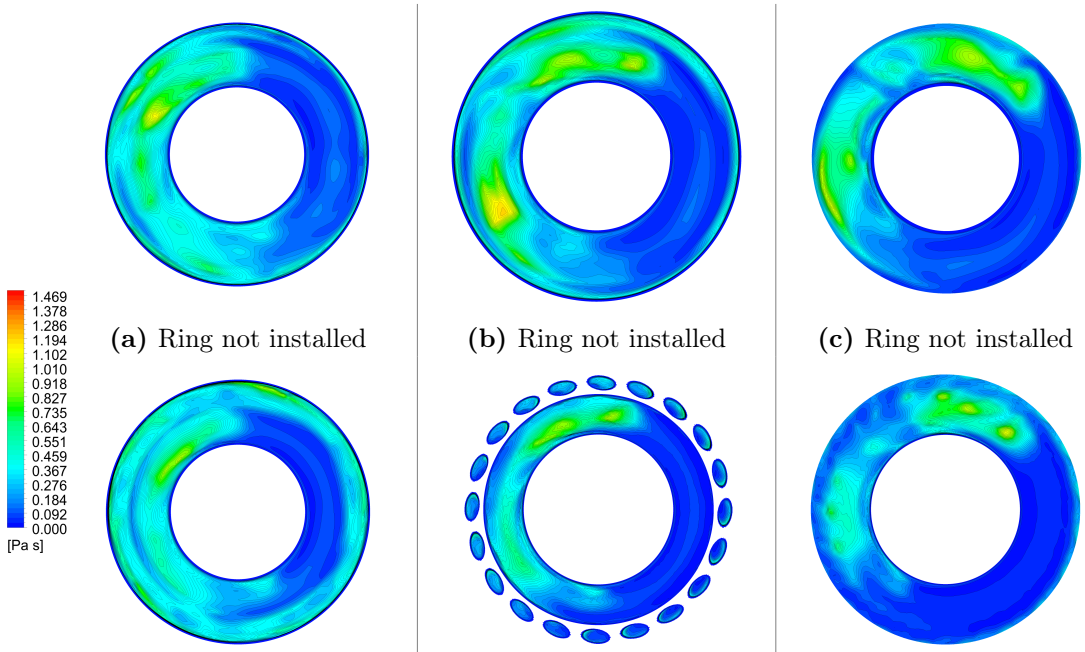
(g) Ring not installed **(h)** Ring not installed **(i)** Ring not installed

(j) Ring installed **(k)** Ring installed **(l)** Ring installed

Figure I-2. Comparison of p_{Ts} between different Cases and eye configurations

Plane E	Plane F	Plane G

Case 1: Best Efficiency Point flow rate
$n = 2985RPM$ (clockwise), $Q = 575m^3/h$ ($Q = 1150m^3/h$ for full pump)
Measured variable: p_{Ts}, direction of normal flow: into page



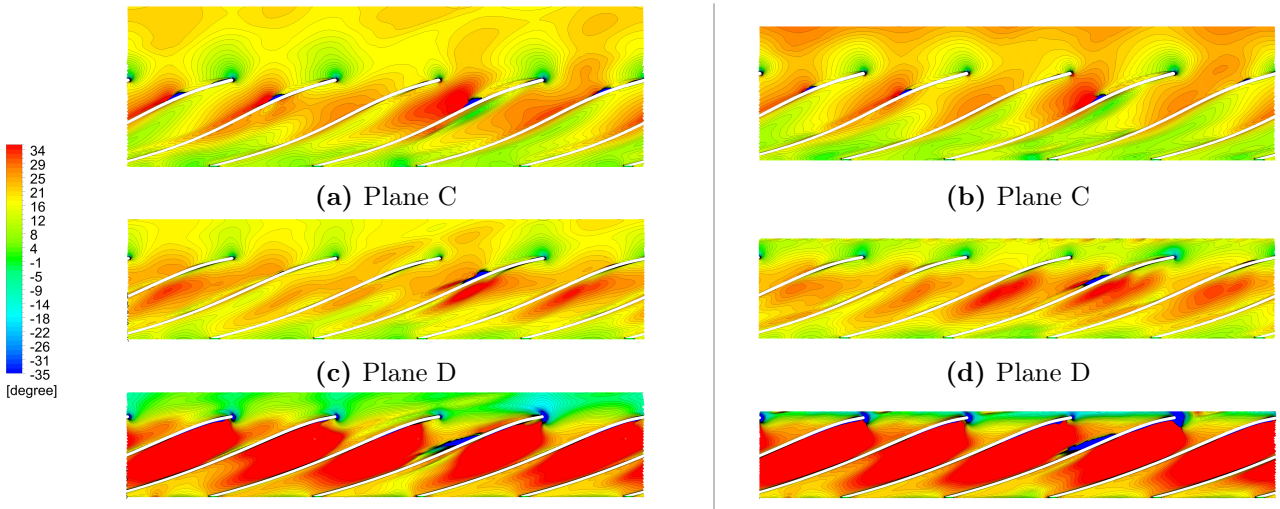
(a) Ring not installed **(b)** Ring not installed **(c)** Ring not installed

(d) Ring installed **(e)** Ring installed **(f)** Ring installed

Figure I-3. Comparison of μ_t between different Cases and eye configurations

No Ring installed	Ring Installed

Case 1: Ring design flow rate
$n = 2985RPM$ (clockwise), $Q = 575m^3/h$ ($Q = 1150m^3/h$ for full pump)
Measured variable: Inlet flow angle, β_1



(a) Plane C **(b)** Plane C

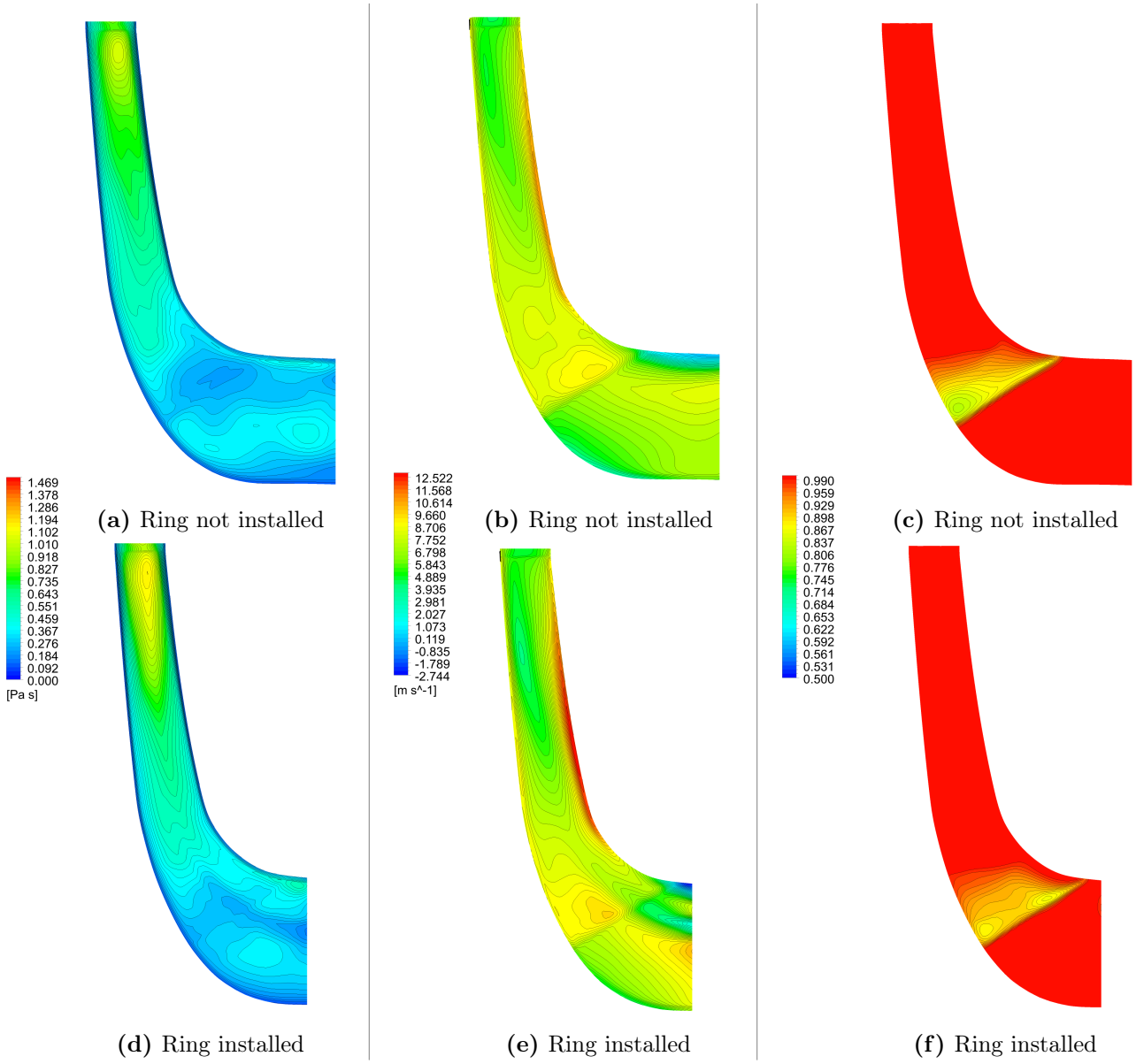
(c) Plane D **(d)** Plane D

(e) Shroud **(f)** Shroud

Figure I-4. Comparison of impeller inlet flow angle between different Cases and eye configurations

Case 1: BEP flow rate
$n = 2985RPM$ (clockwise), $Q = 575m^3/h$ ($Q = 1550m^3/h$ for full pump)
Measured variable: μ_t, direction of normal flow: into page

Eddy Viscosity	Streamwise velocity	Conservative liquid volume fraction



(a) Ring not installed **(b)** Ring not installed **(c)** Ring not installed

(d) Ring installed **(e)** Ring installed **(f)** Ring installed

Figure I-5. Comparison of area-averaged, circumferential meridional data

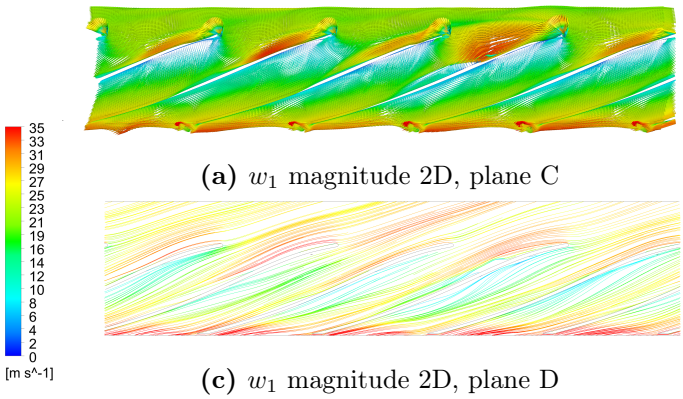
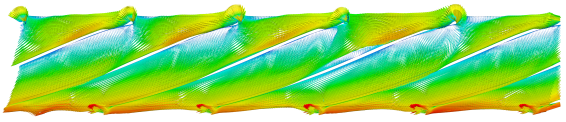
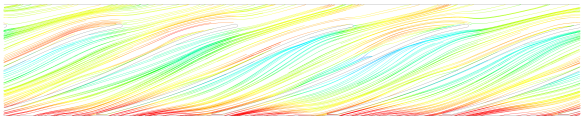
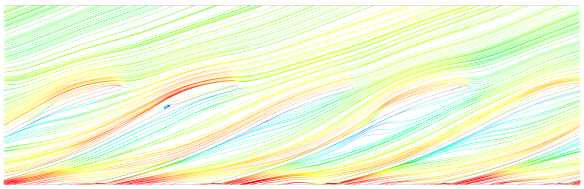
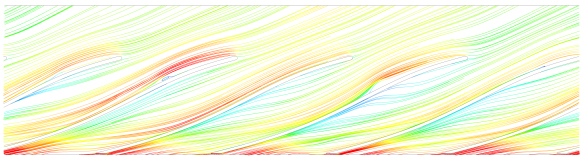
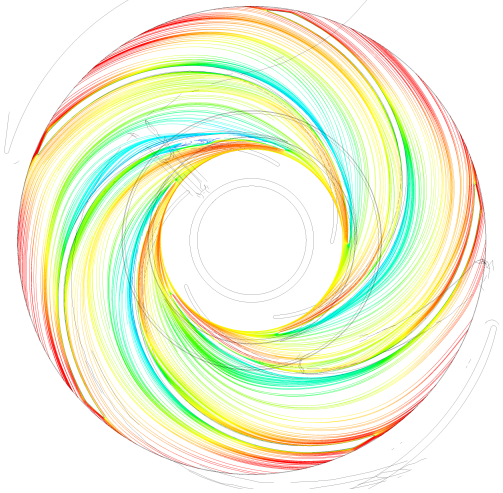
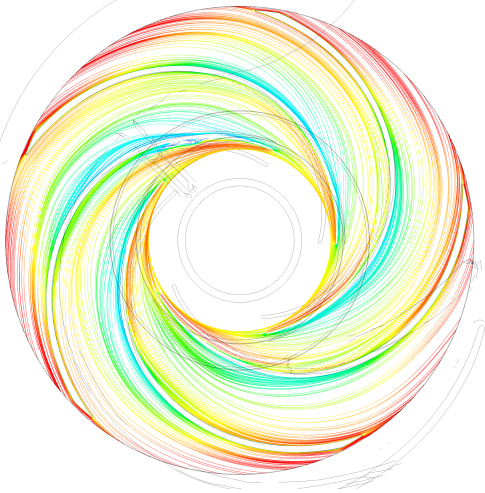
Case 1: Perforated ring not installed $Q = 575m^3/h$ ($Q = 1150m^3/h$) $n = 2985RPM$ (clockwise)	Case 1: Perforated ring installed $Q = 575m^3/h$ ($Q = 1150m^3/h$) $n = 2985RPM$ (clockwise)
	
(a) w_1 magnitude 2D, plane C	**(b)** w_1 magnitude 2D, plane C
	
(c) w_1 magnitude 2D, plane D	**(d)** w_1 magnitude 2D, plane D
	
(e) w_1 magnitude 2D, Shroud	**(f)** w_1 magnitude 2D, Shroud
	
(g) Velocity magnitude 2D streamline, plane C	**(h)** Velocity magnitude 2D streamline, plane C

Figure I-6. Comparison of 2D plane unmodified and modified impeller inlet geometry.